Design and Development of Iridium based Dinuclear Complexes for Photodynamic Therapy and Optoelectronic Applications

by

NISHNA N.

10CC18J39004

A thesis submitted to the
Academy of Scientific & Innovative Research
for the award of the degree of
DOCTOR OF PHILOSOPHY
in
SCIENCE

Under the supervision of
Dr. JOSHY JOSEPH

CSIR-National Institute for Interdisciplinary Science and Technology (CSIR-NIIST), Thiruvananthapuram – 695 019

Academy of Scientific and Innovative Research
AcSIR Headquarters, CSIR-HRDC campus
Sector 19, Kamla Nehru Nagar,
Ghaziabad, U. P. – 201 002, India

October 2024

The thesis is dedicated to

My Family

National Institute for Interdisciplinary Science and Technology (CSIR-NIIST)
Council of Scientific & Industrial Research (CSIR)
Industrial Estate P. O., Trivandrum - 695 019
Kerala, INDIA

Dr. Joshy Joseph
Principal Scientist
Chemical Sciences and Technology Division

Tel: +91-471-2515 476
Mob: +91-9495611444
E-mail: joshy@niist.res.in

October 21, 2024

CERTIFICATE

This is to certify that the work incorporated in this Ph.D. thesis entitled, *"**Design and Development of Iridium based Dinuclear Complexes for Photodynamic Therapy and Optoelectronic Applications**"*, submitted by ***Ms. Nishna N.*** to the Academy of Scientific and Innovative Research (AcSIR) in fulfilment of the requirements for the award of the Degree of ***Doctor of Philosophy in Science***, embodies original research work carried out by the student. We, further certify that this work has not been submitted to any other University or Institution in part or full for the award of any degree or diploma. Research materials obtained from other sources and used in this research work have been duly acknowledged in the thesis. Images, illustrations, figures, tables etc., used in the thesis from other sources, have also been duly cited and acknowledged.

21/10/24

Nishna N.

21.10.2024

Dr. Joshy Jospeh

(Thesis Supervisor)

STATEMENTS OF ACADEMIC INTEGRITY

I Nishna N., a Ph.D. student of the Academy of Scientific and Innovative Research (AcSIR) with Registration No. 10CC18J39004 hereby undertake that, the thesis entitled "***Design and Development of Iridium based Dinuclear Complexes for Photodynamic Therapy and Optoelectronic Applications***" has been prepared by me and that the document reports original work carried out by me and is free of any plagiarism in compliance with the UGC Regulations on *"Promotion of Academic Integrity and Prevention of Plagiarism in Higher Educational Institutions (2018)"* and the CSIR Guidelines for "*Ethics in Research and in Governance (2020)*".

21/10/24

Nishna N.

October 21, 2024
Thiruvananthapuram

It is hereby certified that the work done by the student, under my supervision, is plagiarism-free in accordance with the UGC Regulations on *"Promotion of Academic Integrity and Prevention of Plagiarism in Higher Educational Institutions (2018)"* and the CSIR Guidelines for "*Ethics in Research and in Governance (2020)*".

21/10/24

October 21, 2024
Thiruvananthapuram

21/10/24

Dr. Joshy Joseph

DECLARATION

I, Nishna N., AcSIR Registration No. 10CC18J39004 declare that my thesis entitled, ***"Design and Development of Iridium based Dinuclear Complexes for Photodynamic Therapy and Optoelectronic Applications"*** is plagiarism-free in accordance with the UGC Regulations on *"Promotion of Academic Integrity and Prevention of Plagiarism in Higher Educational Institutions (2018)"* and the CSIR Guidelines for "*Ethics in Research and in Governance (2020)*".

I would be solely held responsible if any plagiarised content in my thesis is detected, which is violative of the UGC regulations 2018.

21/10/24

Nishna N.

October 21, 2024

Thiruvananthapuram

ACKNOWLEDGEMENTS

I would like to express my deepest gratitude to my thesis guide, Dr. Joshy Joseph, for his invaluable guidance, unwavering support, and encouragement throughout this journey. His mentorship has been instrumental in the successful completion of this thesis, and I am truly thankful for his steadfast belief in my abilities.

I am also immensely grateful to Dr. Kaustabh Kumar Maiti for his expertise, encouragement, and thoughtful advice, all of which played a crucial role in shaping this work.

I wish to extend my sincere thanks to Dr. C. Anandharamakrishnan, Director, and Dr. A. Ajayaghosh, former Director of the CSIR-National Institute for Interdisciplinary Science and Technology, Thiruvananthapuram, for providing the necessary facilities to carry out this research.

My sincere thanks to

- *DAC members : Dr. Narayanan Unni K. N., Dr. V. Karunakaran., Dr. Suresh C. H.*
- *HODs (CSTD): Dr. K.V. Radhakrishnan, Dr. Sujatha Devi P., Dr. K. R. Gopidas, and Dr. Narayanan Unni K. N.*
- *AcSIR coordinators: Dr. Jayamurthy P., Dr. V. Karunakaran, Dr. Suresh C. H., and Dr. Luxmi Varma.*
- *Discussions and Suggestions:. Dr. Jubi. John and Dr. Sreejith Shankar.*
- *All scientists in CSTD Division*
- *Dr. Shih-Chun Lo, Dr. Ebnazar Namdas*
- *Dr. Sarah KM McGregor, Dr. Ilene Allison and Dr. Nicholle Wallwork*
- *Technical Support: Mr. Robert Philip, Mr. Nidhin, Mr. Jerin, Mr. Merin, Ms. Gayathri, Mr. Prasad, Ms. Viji*
- *Dr. Shyamjith S., Dr. Vishnu Priya Murali, Ms. Chandhana R.*
- *Mr. Vibhu Darshan, Ms. Kavya Rajeev, Ms. Roopasree O J.*
- *Dr. Sreejith, Dr. Shameel, Dr. Sajena, Dr. Anjali, Dr. Shibna, Pavitra, Anagha, Arjun, Jomon, Hrishi, Darshana, Brija and former group members*
- *M.Sc. Project students Alkha, Reshma*
- *Shibu, Indu, Susu, Sheba, Vishnu, Neethi, Hasna and all other present and former members of CSTD*
- *CSIR for CSIR-JRF and CSIR-SRF Fellowship*
- *SERB Overseas Visiting Doctoral Fellowship, 2018−19 supported by the Science and Engineering Research Board (SERB), Department of Science and Technology (DST) (SERB/F/6000/2019-20)*
- *Jijo, Parents, Nishma, Jithin and FRIDAY*

Nishna N.

TABLE OF CONTENTS

Certificate		i
Statements of Academic Integrity		ii
Declaration		iii
Acknowledgments		iv
Table of Contents		vi
List of Abbreviations		viii
Preface		xiii
CHAPTER 1	**Iridium(III) Complexes and their Applications in Optoelectronics and Cancer Biology: An Overview**	**1-59**
1.1.	Abstract	1
1.2.	Introduction	4
1.3.	Fundamentals of Photoluminescence and Electroluminescence	7
1.3.1.	Photoluminescence	7
1.3.1.1.	Emission Quantum yield and Lifetime	9
1.3.1.2.	Electronically Excited States in Transition Metal Complexes	10
1.3.2.	Electroluminescence	11
1.4.	Iridium Complexes	13
1.5.	Photodynamic Therapy (PDT)	18
1.5.1.	Generation of Singlet Oxygen	20
1.5.2.	Types of Photosensitizers	22
1.5.3.	Photosensitizers based on Transition Metal Complexes	23
1.5.4.	Iridium Complexes as Effective Generators of Singlet Oxygen	24
1.5.5.	Applications of Iridium(III) Complexes in Biological Systems	25
1.5.5.1.	Cellular Uptake of Iridium(III) Complexes	26
1.5.5.2.	Activatable Photosensitizers for Imaging and Therapy	27
1.5.5.3.	Key Organelle-Targeting Strategies for Iridium Complexes	28
1.5.6.	Literature Review	29
1.6.	Organic Light Emitting Diode (OLED)	38
1.6.1.	General Structures and Working Principles	39
1.6.2.	Device Architecture and Fabrication	40
1.6.3.	Device Lifetime	42
1.6.4.	Device Efficiency	43
1.6.5.	Phosphorescent Materials as Emitting Layer for OLED application	44
1.6.6.	Iridium(III) Complexes for OLED application	47
1.7.	Dinuclear Iridium based Phosphorescent Emitters	51
1.7.1.	NΛN- type bridged Iridium(III) Complexes	53
1.7.2.	NΛO- type bridged Iridium(III) Complexes	55

1.7.3.	CΛN- type bridged Iridium(III) Complexes	57
1.8.	Objectives and Methodologies for the Present Investigation	59
1.9.	References	59
CHAPTER 2	**Exploring a Mitochondria Targeting, Dinuclear Cyclometalated Iridium (III) Complex for Image-Guided Photodynamic Therapy in Triple-negative Breast Cancer Cells**	**81-124**
2.1.	Abstract	81
2.2.	Introduction	83
2.3.	Results and Discussion	88
2.3.1.	Synthesis of IR-MO and IR-DI Complexes	88
2.3.2.	Photophysical Properties	89
2.3.3.	*In vitro* Assessment of Photodynamic Therapy	98
2.3.3.1.	Cytotoxicity, Internalization, and Mitochondrial Targeting of IR-DI in MDA-MB-231 cells	98
2.3.3.2.	Photoactivation and PDT studies of IR-DI in MDA-MB 231 cells	103
2.3.3.3.	Cell death mechanism of IR-DI in MDA-MB 231 cells	104
2.4.	Conclusion	111
2.5.	Experimental Section	111
2.5.1.	Materials and General Instruments	111
2.5.2.	Photophysical Measurements	112
2.5.3.	*In vitro* studies	113
2.5.4.	Synthesis and Characterization of the Molecules	117
2.5.5.	NMR and Mass Spectrum	120
2.6.	References	124
CHAPTER 3	**Mitochondria-Targeted Dinuclear Iridium(III) Photosensitizer with Intrinsic Viscosity Sensing for Activatable Photodynamic Therapy Mitochondria-Targeted Dinuclear Iridium (III) Photosensitizer with Intrinsic Viscosity Sensing for Activatable Photodynamic Therapy**	**131-165**
3.1.	Abstract	131
3.2.	Introduction	133
3.3.	Results and Discussion	138
3.3.1.	Design and Synthesis of IR-ISO and IR-IMO Complexes	138
3.3.2.	Photophysical Properties	139
3.3.3.	*In vitro* studies	145
3.3.3.1.	Internalisation and Cytotoxicity of IR-ISO in SK-BR-3 and MCF-10A	145

3.3.3.2.	Mitochondria Targeting, Photoactivation, and PDT Studies of IR-ISO in SK-BR-3 Cells	149
3.3.3.3.	Cell Death Mechanism of IR-ISO in SK-BR-3 Cells	151
3.4.	Conclusion	154
3.5.	Experimental Section	155
3.5.1.	Materials and General Instruments	155
3.5.2.	Photophysical Measurements	155
3.5.3.	*In vitro* studies	157
3.5.4.	Synthesis and Characterization of the Molecules	159
3.5.5.	NMR and Mass Spectrum	162
3.6.	References	165

CHAPTER 4	**Development of Dinuclear Cyclometalated Iridium Complexes (III) with Non-innocent Bridging Ligand for OLED Applications**	**169-200**

4.1.	Abstract	169
4.2.	Introduction	171
4.3.	Results and Discussion	175
4.3.1.	Design and Synthesis of IR-BIB and IR-DPP Complexes	175
4.3.2.	Photophysical and Electrochemistry Properties	177
4.3.3.	Electroluminescent (EL) Properties of IR-BIB	182
4.4.	Conclusion	188
4.5.	Experimental Section	189
4.5.1.	Materials and General Instruments	189
4.5.2.	Photophysical and Electrochemical Measurements	189
4.5.3.	OLED Fabrication and Measurements	190
4.5.4.	Synthesis and Characterization of Molecules	191
4.5.5.	NMR and Mass Spectrum	195
4.6.	References	200

Abstract of the Thesis	203
List of Publications	205
List of Posters Presented in Conference	206
Abstracts of papers/posters presented	207
Attachment of the publication	213

LIST OF ABBREVIATIONS

A	Ampere
ABDA	9,10-Anthracenediyl-bis(methylene)dimalonic acid
ACQ	Aggregation-Caused Quenching
acac	Acetylacetonate
AgCl	Silver(I) chloride
AIE	Aggregation Induced Emission
Al	Aluminium
AO-EB	Acridine Orange-Ethidium Bromide
Ar	Argon
C	Carbon
cd	Candela
cP	Centipoise
$CDCl_3$	Deuterated chloroform
CE	Current Efficiency
CH_2Cl_2	Dichloromethane
CH_3CN	Acetonitrile
$CHCl_3$	Chloroform
CIE	Commission Internationale de l'Éclairage
cm	Centimeter
CO_2	Carbon dioxide
CV	Cyclic Voltammetry
Cyt c	Cytochrome C
DCM	Dichloromethane
DMEM	Dulbecco's Modified Eagle Medium
DMF	Dichloromethane
DMSO	Dimethyl sulfoxide
DPBF	1,3-Diphenylisobenzofuran
EL	Electroluminescence
E_g	Band gap
EML	Emission Layer
ESI	Electrospray ionization
ET	Energy Transfer
ETL	Electron Transport Layer

EtOH	Ethanol
et al.	Et alia
EQE	External Quantum Efficiency
eV	Electron volt
fac	facial
Fc	Ferrocene
FITC	Fluorescein Isothiocyanate
FRET	Förster Resonance Energy Transfer
g	Gram
GAPDH	Glyceraldehyde 3-Phosphate Dehydrogenase
h	Hour
H_2O	Water
HBL	Hole Blocking layer
HIL	Hole-Injecting Layer
HOMO	Highest Occupied Molecular Orbital
HRMS	High Resolution Mass Spectrometry
HTL	Hole Transport Layer
IC	Internal Conversion
IC_{50}	Inhibitory Concentration at 50%
ICPMS	Inductively Coupled Plasma Mass Spectrometry
ICT	Internal Charge Transfer
IL	Inter Connector Layers
ILCT	Intra-Ligand Charge Transfer
ILET	Inter-Ligand Energy Transfer (ILET)
IQE	Internal Quantum Efficiency
Ir	Iridium
ISC	Inter System Crossing (ISC)
ITO	Indium doped tin oxide
J	Current Density
knr	Non radiative rate
kr	Radiative rate
L	Luminance
LC	Ligand-Centered transitions
LE	Luminous Efficiency
LE	Locally Excited

LEEC	Light-Emitting Electrochemical Cell
LED	Light Emitting Diode
LLCT	Ligand-to-Ligand Charge Transfer
LMCT	Ligand-to-Metal Charge Transfer
LMMCT	Ligand–Metal-to-Metal Charge Transfer
lm	lumen
LUMO	Lowest Unoccupied Molecular Orbital
M	Molar
m	meter
MC	Metal-Centered transitions
MeOH	Methanol
mer	meridional
Mito	Mitochondria
min	Minute
MLCT	Metal-to-Ligand Charge Transfer
mL	Millilitre
MMLCT	Metal–Metal-to-Ligand Charge Transfer
mM	Millimolar
MO	Molecular Orbitals
mol	Mole
N	Nitrogen
NaCl	Sodium chloride
Na_2CO_3	Sodium Carbonate
NH_4PF_6	Ammonium hexafluorophosphate
NIR	Near-Infra Red
NMR	Nuclear Magnetic Resonance
nm	Nanometer
ns	Nanosecond
O	Oxygen
$^1O_2$	Singlet Oxygen
OCE	Out-Coupling Efficiency
OLED	Organic Light Emitting Diode
PACT	Photoactivated Chemotherapeutic agents
PBS	Phosphate-Buffered Saline
PCC	Pearson's Correlation Coefficient

PDT	Photodynamic Therapy
$Pd(PPh_3)_4$	Tetrakis(triphenylphosphine)palladium(0)
PE	Power Efficiency
PEDOT	Poly(3,4-ethylenedioxythiophene)
PeT	Photo-induced Electron Transfer
PHOLED	Phosphorescent OLEDs
PI	Propidium Iodide
PL	Photoluminescence
PLIM	Phosphorescence Lifetime Imaging
PLQY	Photoluminescence Quantum Yield
ppy	phenylpyridine
PS	Photosensitizer
PTT	Photothermal Therapy
PVK	Poly(9-vinyl carbazole)
QE	Quantum Efficiency
ROS	Reactive Oxygen Species
Ru	Ruthenium
s	Second
S_0	Singlet ground state
S_1	Singlet excited state
Si-DMA	Silicon Dimethylacetamide
SOC	Spin-Orbit Coupling
SOQY	Singlet Oxygen Quantum Yield
T	Temperature
T_0	Triplet ground state
T_1	Triplet excited state
TLC	Thin Layer Chromatography
TMS	Tetramethylsilane
TPA	Two-Photon Absorption
TPE	Two-Photon Excitation
TTA	Triplet-Triplet Annihilation
UV	Ultra Violet
UV-vis	Ultra Violet-visible
V	Voltage
W	Watt

Xe	Xenon
δ	Delta
ε	Molar extinction coefficient
η_{ext}	External Quantum Efficiency
η_{int}	Internal Quantum Efficiency
η_J	Power Efficiency
η_L	Current Efficiency
η_P	Luminous Efficiency
λ	Wavelength
λ_{em}	Wavelength of emission
λ_{ex}	Wavelength of excitation
$\Delta\lambda$	Change in wavelength
μL	Microliter
μM	Micromolar
ξ	Spin-orbit coupling constant
τ	Excited state lifetime
Φ	Quantum yield
Φ_p	Photoluminescence Quantum yield
Φ_s	Singlet Oxygen Quantum yield
%	Percentage
°C	Degree Celsius

PREFACE

In recent years, there has been considerable interest in iridium(III) complexes within both academic and industrial research due to their diverse applications in areas such as cellular imaging, photodynamic therapy (PDT), organic light-emitting diodes (OLEDs), catalysis, photochemical sensors, and biomarkers. These complexes are noted for their high photoluminescence quantum yields, adjustable emission wavelengths, excellent light stability, significant Stokes shifts, and prolonged luminescence lifetimes. These advantageous properties primarily arise from the efficient spin-orbit coupling (SOC) associated with the iridium metal, facilitating effective inter-system crossing between singlet and triplet states.

In therapeutic applications, especially in PDT, iridium complexes have shown potential as photosensitizers. PDT is a non-invasive approach that uses light-activated reactions between a photosensitizer and molecular oxygen to generate reactive oxygen species (ROS), which can induce cancer cell death. This method has gained attention as a clinical option for treating various diseases, particularly cancer and actinic keratosis. While mononuclear Ir(III) complexes have been previously utilized as sensitizers in PDT, di- and multi-nuclear Ir(III) complexes have not been extensively studied. In addition to their biomedical applications, iridium complexes are also used as emitters in optoelectronic devices like OLEDs. OLEDs consist of multiple layers, including electron transport, hole transport, and hole injection layers, arranged between two electrodes. When an appropriate voltage is applied, electrons and holes are injected into the emissive layer, where they recombine to form excitons, leading to light emission. This thesis focuses on the design and development of new and efficient Ir(III)-based photosensitizers and emissive materials. It aims to explore the properties of dinuclear iridium-based complexes and their structure-property relationships. The research includes the synthesis of various iridium complexes, their characterization, and an investigation of their photophysical properties, along with their therapeutic and optoelectronic applications.

The thesis is organised into four chapters, of which the **Chapter 1** provides an overview and literature review of the chemistry of iridium complexes and current advancements in PDT and OLEDs. The usage of cyclometalated iridium (III) metal complexes as photosensitizers for PDT and emissive layers in lighting devices are discussed in detail.

In the **Chapter 2**, we discuss the imaging and photodynamic therapeutic effect of a new dinuclear iridium complex (**IR-DI**). PDT is a rapidly advancing treatment approach utilizing laser-triggered photosensitizers for combating cancer and iridium-based photosensitizers show promise for their ability to both image and treat cancer. In this chapter, we report a dinuclear Ir(III) complex (**IR-DI**) along with a structurally similar monomer complex (**IR-MO**) having 2-(2,4-difluorophenyl)pyridine and 4′-methyl-2,2′-bipyridine ligands. The comparative investigation of the mononuclear and dinuclear Ir(III) complexes showed similar absorption profiles, but the dinuclear derivative **IR-DI** exhibited a higher photoluminescence quantum yield (Φ_p) of 0.70 compared to that of **IR-MO** (Φ_p = 0.47). Further, **IR-DI** showed a higher singlet oxygen generation quantum yield (Φ_s) of 0.49 compared to **IR-MO** (Φ_s = 0.28), signifying the enhanced potential of the dinuclear derivative for image-guided photodynamic therapy. *In vitro* assessments indicate that **IR-DI** shows efficient cellular uptake and significant photocytotoxicity in the triple-negative breast cancer cell line MDA-MB-231. In addition, the presence of a dual positive charge on the dinuclear system facilitates the inherent mitochondria targeting ability without the need for a specific targeting group. Subcellular singlet oxygen generation by **IR-DI** was confirmed using Si-DMA, and light-activated cellular apoptosis via ROS-mediated PDT was verified through various live-dead assays performed in the presence and absence of the singlet oxygen scavenger NaN_3. Further, the mechanism of cell death was elucidated by an Annexin V-FITC/PI flow cytometric assay and by investigating the cytochrome c release from mitochondria using Western blot analysis.

Chapter 3 of the thesis focuses on the design and development of a cationic cyclometalated Ir(III) complex (**IR-ISO**) with 1-phenylisoquinoline as the cyclometalating ligand and 4′-methyl-2,2′-bipyridine as the bridging ligand for viscosity activated PDT applications. Intracellular viscosity has been demonstrated as a vital contributor or indicator for diabetes, atherosclerosis and even cell malignancy, because these disease conditions could affect protein–protein interactions in cellular membranes. Thus, it is imperative to develop an instantaneous and non-destructive viscosity sensing probe for imaging and therapeutic application. In this regard, we developed a new viscosity sensitive dinuclear iridium complex which freely rotates and shows weak luminescence in a low-viscosity environment, while in viscous media due to restricted intermolecular rotation (RIR), exhibit significantly enhanced luminescence. The Ir(III) based viscosity probe, **IR-ISO** showed a higher singlet oxygen generation quantum yield (Φ_s) of 0.90 in neat glycerol

compared to that in neat methanol (Φ_s= 0.67), signifying the enhanced activity of dinuclear complex in viscous environment. *In vitro* experiments demonstrated that **IR-ISO** exhibited enhanced cellular luminescence in breast cancer cell line SK-BR-3, while comparatively faint luminescence was observed in normal cell line MCF-10A. The selectivity of **IR-ISO** towards breast cancer cell line SK-BR-3 and subsequent enhancement in luminescence and singlet oxygen quantum yields validate the possibility of viscosity assisted, enhanced PDT. Further, the generation of subcellular singlet oxygen by **IR-ISO** was confirmed using singlet oxygen sensor green (SOSG), while light-triggered cellular apoptosis via ROS-mediated PDT was validated through various live-dead assays. Additionally, the mechanism of cell death was clarified using an Annexin V-FITC/PI flow cytometric assay and cell cycle analysis.

Chapter 4 discusses the synthesis and optoelectronic applications of two iridium dinuclear complexes with 2-(4-tert-butylphenyl)pyridine as the cyclometalating ligands and bibenzimidazole (**IR-BIB**) or DPP (**IR-DPP**) as the bridging ligand. These molecules are specifically designed to exhibit efficient luminescence in the solid state and hence can be used as emissive layers in OLED devices. The **IR-BIB** and **IR-DPP** complexes exhibited PLQYs of 0.75 and 0.27, respectively. The OLED device fabrication was proceeded with high PLQY derivative, **IR-BIB** and the performance of the OLED devices were optimized by several parameters, including current efficiency, power efficiency, luminescence intensity and EQE. Optimized devices of **IR-BIB** alone and **IR-BIB** doped in PVK showed luminescence maximum of 150 cd/m^2 and 6,300 cd/m^2, respectively. The OLED device incorporating **IR-BIB** doped PVK demonstrated higher EQE of 5.85%, while the **IR-BIB** alone device exhibited an EQE of 0.028%. This chapter highlights the application of the dinuclear iridium complexes as a excellent emitting layers in OLED and demonstrates the potential of these materials for optoelectronic applications.

CHAPTER 1

Iridium(III) Complexes and their Applications in Optoelectronics and Cancer Biology: An Overview

1.1. Abstract

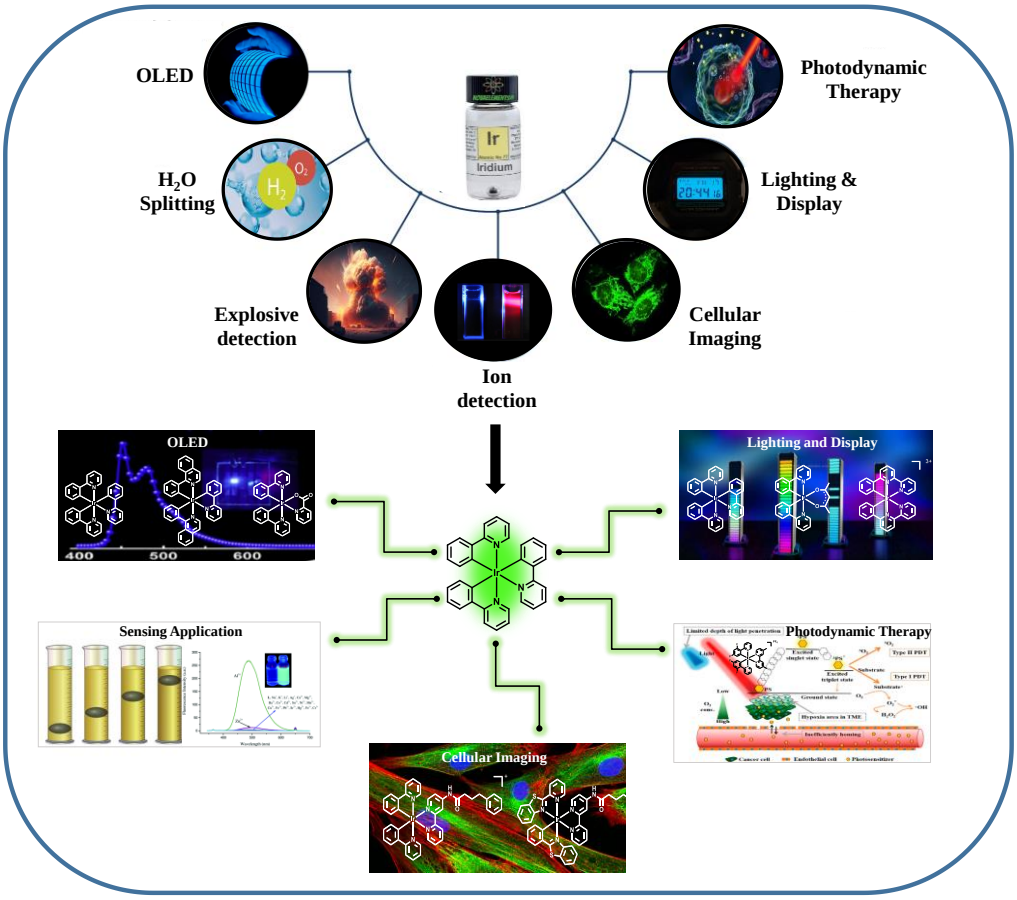

Iridium based transition metal complexes have attracted significant interest in recent years due to their unique combination of photophysical and chemical properties. These complexes exhibit remarkable photoluminescence, stability, and electron transfer capabilities, making them highly versatile for various applications. Iridium based materials show great promise in organic light-emitting diodes (OLEDs) for enhancing electroluminescence efficiency, as well as in water-splitting catalysts for sustainable

hydrogen production. Their luminescent properties enable their use in ion detection and cellular imaging, while their photosensitizing capabilities are crucial in photodynamic therapy (PDT) for generating reactive oxygen species (ROS) to target cancer cells. Additionally, iridium complexes play a vital role in lighting and display technologies due to their tunable emission properties. Most iridium complexes employed in these applications have traditionally been mononuclear. However, recent research has increasingly focused on dinuclear iridium(III) complexes, which provide distinct advantages through their metal-metal interactions. These interactions enhance photophysical performance by increasing photoluminescence efficiency, tuning excited-state lifetimes, and improving emission properties. Furthermore, dinuclear iridium complexes exhibit stronger spin-orbit coupling, facilitating efficient intersystem crossing and enhancing emission quantum yields.

In the realm of photodynamic therapy (PDT), dinuclear iridium complexes are emerging as powerful photosensitizers. When activated by light, these complexes can efficiently generate singlet oxygen species, leading to localized cell death in cancerous tissues thereby providing a minimally invasive alternative to traditional cancer treatments. The presence of an additional metal center allows dinuclear systems to achieve higher photoluminescence and singlet oxygen generation quantum yields, rendering them superior to mononuclear iridium complexes. In addition to therapeutic applications, dinuclear iridium complexes show promise in cellular sensing and imaging, particularly for detecting biologically relevant ions and molecules. Their luminescent response to environmental changes can be utilized for real-time monitoring in biological systems, enhancing the functionality of these versatile materials. Furthermore, the high photoluminescence characteristics make the iridium(III) complexes well-suited for organic light-emitting

diodes (OLEDs), where high brightness, color purity, and energy efficiency are crucial for next-generation displays and lighting solutions.

This thesis aims to explore the synthesis, characterization, and application of dinuclear iridium(III) complexes in three key areas: PDT, sensing, and OLEDs. By studying the relationship between ligand design, coordination geometry, and photophysical behavior, this research seeks to optimize the performance of dinuclear iridium complexes for multifunctional roles. The findings are expected to contribute to the development of advanced iridium based materials, offering solutions to current challenges in optoelectronics and cancer therapy. These studies also provide insights into future directions for the design of functional materials in related fields.

1.2. Introduction

In recent years, luminescent transition-metal complexes have emerged as a focal point across multiple scientific fields, with wide-ranging applications in optoelectronics, anticancer therapies, bio-sensing, and bio-imaging. Complexes formed primarily by second- and third-row transition metal ions coordinated with organic ligands display diverse excited states - such as metal-to-ligand charge transfer (MLCT), ligand-to-ligand charge transfer (LLCT), intra-ligand charge transfer (ILCT), ligand-to-metal charge transfer (LMCT), metal–metal-to-ligand charge transfer (MMLCT), and ligand–metal-to-metal charge transfer (LMMCT)—which contribute to their exceptional emission properties.[1-3] Notably, these photophysical characteristics can be fine-tuned by modifying the coordination ligands. Among transition metal complexes, iridium complexes have garnered particular attention due to their outstanding photophysical properties and the relative ease with which they can be synthesized.

Iridium (Ir) is a group 9 transition metal situated in period 6, following cobalt and rhodium, with an atomic number of 77 and an electronic configuration of [Xe] $4f^{14}\,5d^{7}\,6s^{2}$. Discovered in 1804 by English chemist Smithson Tennant, it was identified as a trace element within platinum.[4] Iridium is notable for its remarkable chemical and physical properties, being both inert and resistant to corrosion. The chemistry of iridium is highly diverse and fascinating, displaying a range of oxidation states from -1 to +9, three coordination numbers (4, 5, and 6), and multiple coordination geometries. The most prevalent oxidation states for iridium complexes are +1 and +3. In the +1 oxidation state, iridium, with a d^{8} electron configuration, forms either tetra-coordinate or penta-coordinate compounds, with square planar or trigonal bipyramidal geometries, respectively. In the +3 oxidation state, iridium has a $5d^{6}$ electron configuration and almost exclusively forms

hexacoordinate, octahedral complexes.[4] These complexes exhibit remarkable photostability, high PL quantum yields at room temperature, shorter excited-state lifetimes, favorable cell-membrane permeability, and a tunable fluorescence wavelength spanning the blue to near-infrared region.[5-11] Moreover, their substantial Stokes shift minimizes self-quenching, and their extended phosphorescence lifetimes offer advantages in reducing unwanted autofluorescence in biological systems through techniques such as time-gated imaging and photoluminescence lifetime imaging. [12, 13]

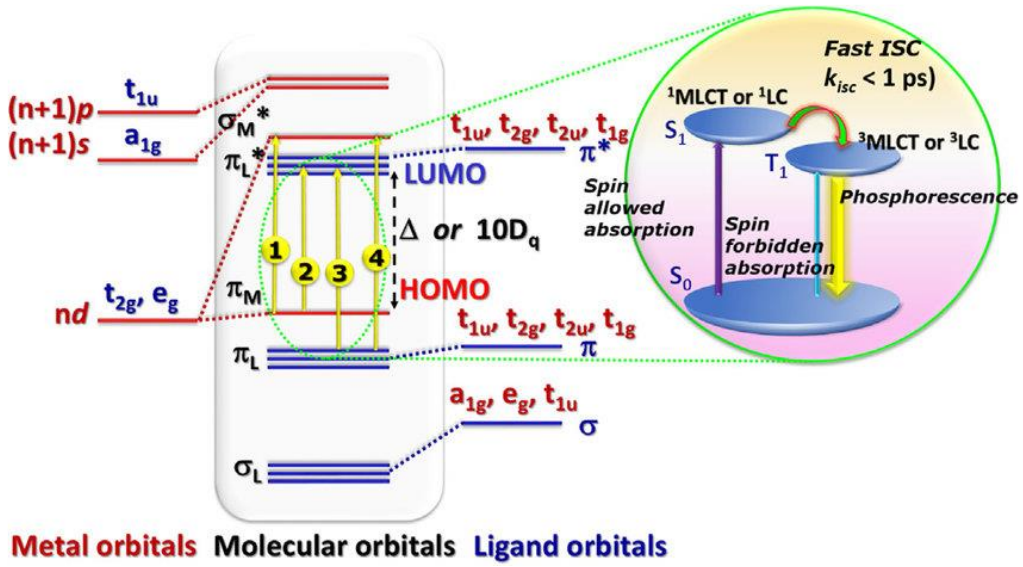

Figure 1.1. Molecular orbital diagram for iridium(III) complexes in octahedral coordination: (1) MC (Metal centred ligand field transition); (2) MLCT (Metal to ligand charge transfer); (3) ILCT (Intra ligand charge transfer) or LLCT (Ligand to ligand charge transfer); (4) LMCT (Ligand to metal charge transfer) and Room temperature phosphorescence accompanied by rapid intersystem crossing is shown in the inset. Figure adapted from reference 1.

The efficiency of phosphorescent emission in iridium complexes is closely tied to the strong spin-orbit coupling facilitated by the 5d orbitals of the Ir^{3+} ion (ξIr = 4430 cm^{-1}).[6, 14] This coupling allows for efficient intersystem crossing (ISC) from singlet to triplet states, enabling the spin-forbidden relaxation process that promotes radiative decay from the triplet state. This decay mainly arises from triplet metal-to-ligand charge transfer (^{3}MLCT) or a combination of ^{3}MLCT and ligand-centered (^{3}LC) transitions.[3, 15-18]

Additionally, various interesting processes such as intramolecular inter-ligand energy transfer (ILET) and ligand-to-ligand charge transfer (LLCT) are observed in certain iridium complexes (**Figure 1.1**).[19] The energy of the excited states can be adjusted by changing the substituents in the cyclometalating or ancillary ligand systems, resulting in a broad range of emission colors. This versatility renders phosphorescent iridium(III) complexes highly valuable for various applications, such as organic light-emitting diodes (OLEDs), photodynamic therapy (PDT), light-emitting electrochemical cells (LEECs), photosensitizers for water-splitting, and biological labelling. Additionally, they are utilized in electro-generated chemiluminescence, dye-sensitized solar cells, singlet oxygen sensitizers, luminescent sensitizers for DNA charge-transfer reactions, photocatalysis for organic synthesis and CO_2 reduction, chemosensors, metallo-pharmaceuticals, and nonlinear optics (**Figure 1.2**).[20-43] The extensive exploration of these compounds underscores their potential impact across diverse technological and scientific domains.

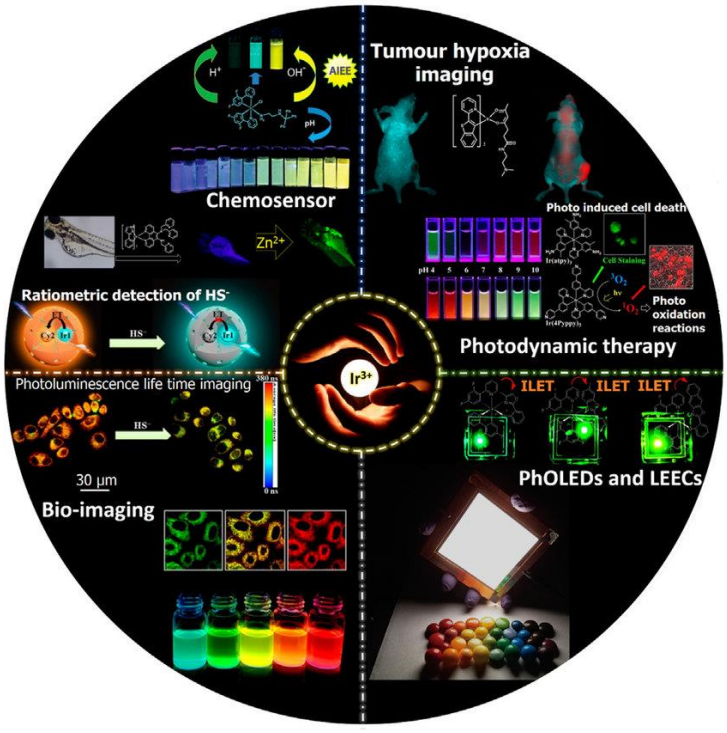

Figure 1.2. Applications of cyclometalated iridium(III) complexes. Figure adapted from reference 1.

1.3. Fundamentals of Photoluminescence and Electroluminescence

1.3.1. Photoluminescence

Luminescence refers to the light emitted by a substance resulting from an electronically excited state.[44] When a molecule absorbs energy such as light, it gets excited to a higher electronic state and returns to the ground state by radiative or non-radiative decay. When the energy is lost radiatively, the process is known as photoluminescence. Based on the nature of the excited state, luminescence is typically categorized as either fluorescence or phosphorescence. **Figure 1.3** shows a Jablonski diagram illustrating different photoluminescent processes. In the diagram, the states labelled "S" represent singlet states, where electrons have anti-parallel spins, while the states labelled "T" denote triplet states, where electrons have parallel spins. The vertical lines indicate radiative transitions between these states.[45]

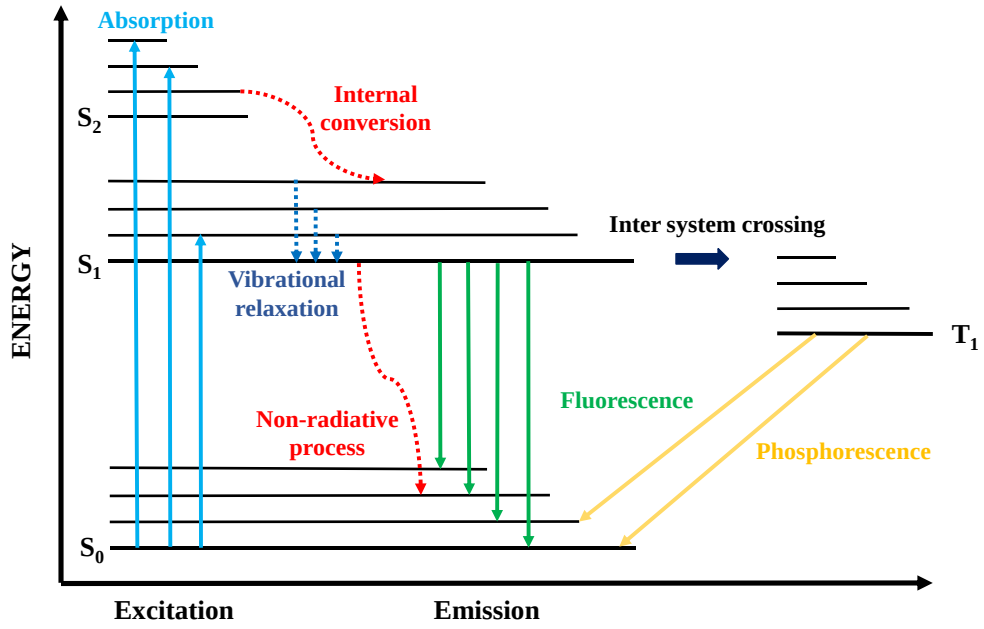

Figure 1.3. Perrin-Jablonski diagram highlighting fluorescence and phosphorescence. Figure adapted from reference 45.

Typically, an electron rapidly transitions to a lower energy vibrational state within the same excited electronic state, a phenomenon referred to as vibrational relaxation.[46] Non-radiative relaxation to lower energy electronic states with the same multiplicity is called internal conversion (IC). In contrast, intersystem crossing is another type of non-radiative decay that occurs between excited states with different multiplicities, such as from the singlet state S_1 to the triplet state T_1. This transition is forbidden in traditional organic compounds due to the need for a change in spin multiplicity.[44, 45]

The fluorescence and phosphorescence can be distinguished based on the spin states of the involved electrons and the timescales of their emissions. Fluorescence, characterized by its rapid emission, occurs when an electron in an excited singlet state returns to the ground state, typically within a few nanoseconds. This spin-allowed transition results in the emission of a photon, making fluorescence a fast process with a high decay rate. The efficiency of fluorescence can be quantified by the photoluminescence quantum yield (PLQY) and the fluorescence lifetime. In contrast, phosphorescence involves a transition from an excited triplet state to the ground state. Due to the same spin orientation of electrons in the triplet state, this transition is spin-forbidden, resulting in a much slower process compared to fluorescence. Phosphorescence lifetimes can range from milliseconds to several seconds, and in some cases, even minutes. The efficiency of phosphorescence, similar to fluorescence, can be described by the phosphorescence PLQY and the phosphorescence lifetime. [44, 47]

The discovery that heavy metal complexes can enhance phosphorescence has been a significant advancement in the field of luminescent materials. Heavy metals like iridium, platinum, and osmium exhibit strong spin-orbit coupling (SOC), which is the interaction between an electron's spin and its orbital motion around the nucleus. This strong SOC in

heavy atoms leads to more efficient intersystem crossing (ISC) from the singlet to the triplet state, breaking down the spin selection rules that typically govern these transitions in organic molecules.[48-51] As a result, the presence of heavy metal complexes facilitates the transition from the triplet state to the ground state, enabling faster and more efficient phosphorescence. This has led to the development of phosphorescent emitters with high PLQYs and reduced lifetimes to the order of microseconds.[47] The enhancement of phosphorescence through heavy metal complexes has significant implications for the design and development of advanced luminescent materials, enabling their use in a wide range of applications that require efficient and long-lasting emission properties.

1.3.1.1. Emission Quantum yield and Lifetime

The non-radiative decay pathway competes with luminescence and can reduce the quantum yield of photoluminescence in the emitting species. This reduction happens because deactivation occurs through vibrational (thermal) processes rather than radiative dissipation. The quantum yield, defined as the ratio of emitted photons to absorbed photons, is associated with the rates of radiative (k_r) and non-radiative (k_{nr}) processes, as shown in Equation (1)[44, 52]

$$\text{PLQY} = \frac{kr}{(kr + \text{knr})} \qquad \text{Equation (1)}$$

The lifetime of the excited states can be defined as the inverse of the total of radiative and non-radiative decay rates, as shown in Equation (2)[44, 52]

$$\frac{1}{\tau} = k_r + k_{nr} \qquad \text{Equation (2)}$$

The excited state lifetime (τ), defined as the average time taken between the excitation and return to the ground state, is generally in the order of 10^{-9} s for the fluorescence and 10^{-6} to 10^{-3} s for the phosphorescence.[44]

1.3.1.2. Electronically Excited States in Transition Metal Complexes

In transition metal complexes, the metal atom causes mixing of its d orbitals with the conjugated ligands of π-character. Consequently, photoexcitation of these compounds can lead to various electronic transitions, depending on the nature of the molecular orbitals (MOs). As a result, there are four principal types of excited states possible (**Figure 1.4**): d-d, d- π*, π- π* and π-d.[44, 52]

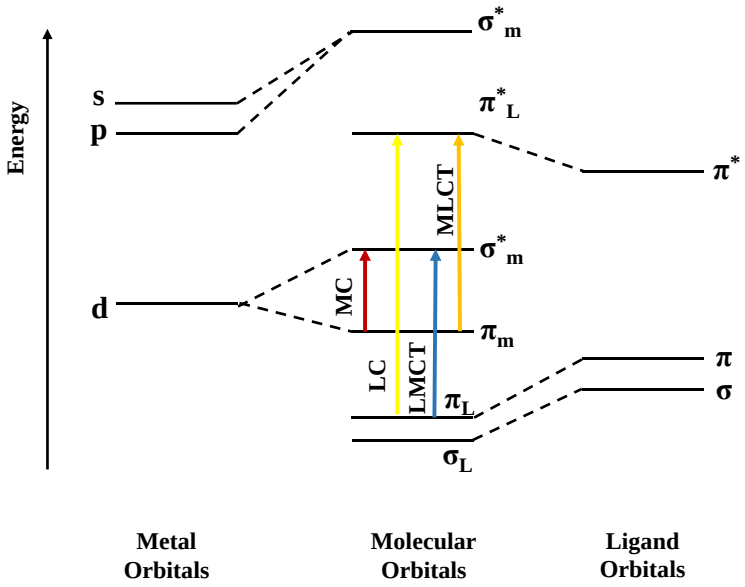

Figure 1.4. Simplified molecular orbital diagram in a coordination complex. M denotes the metal and L denotes ligand. Figure adapted from reference 52.

(i) d-d transition state - The metal-centered (MC) transitions, where the excited state results from transitions involving only the metal's occupied and unoccupied d orbitals.

(ii) π- π* transition state - The ligand-centered (LC) transitions, occurring when an electron moves from a π-bonding or non-bonding orbital to higher anti-bonding π* orbitals within the ligands. If these orbitals are situated on different ligands, the excitation involves inter-ligand or ligand-to-ligand charge transfer (ILCT or LLCT).

(iii) π-d transition state - The ligand-to-metal charge transfer (LMCT) transitions, where electrons are excited from a ligand π orbital to an orbital that is predominantly based on the metal.

(iv) d-π* transition state - The metal-to-ligand charge transfer (MLCT) transitions, which involve the excitation of electrons from a metal-centered d orbital to a ligand π* orbital.

The relative energy levels of these states are essential in determining the photophysical properties of organometallic complexes. These properties can be effectively adjusted through careful selection of the ligand system and the central metal atom.

1.3.2. Electroluminescence

Electroluminescence refers to the emission of light from organic or semiconducting materials when a voltage is applied. In photoluminescence, electrons are excited from the ground state to excited singlet states by absorbing light. In contrast, electroluminescence involves the injection of charge carriers with random spin orientations, leading to the formation of excitons with various spin states upon recombination.[53] According to spin-statistics calculations (**Figure 1.5**), electrical excitation typically produces one singlet exciton for every three triplet excitons. Singlet excitons, which have an antisymmetric spin configuration and a total spin quantum number (S) of zero, can decay to the ground state

through spin-allowed transitions. Conversely, triplet excitons have a spin quantum number (S) of one, making their transition to the ground state spin-forbidden.[53]

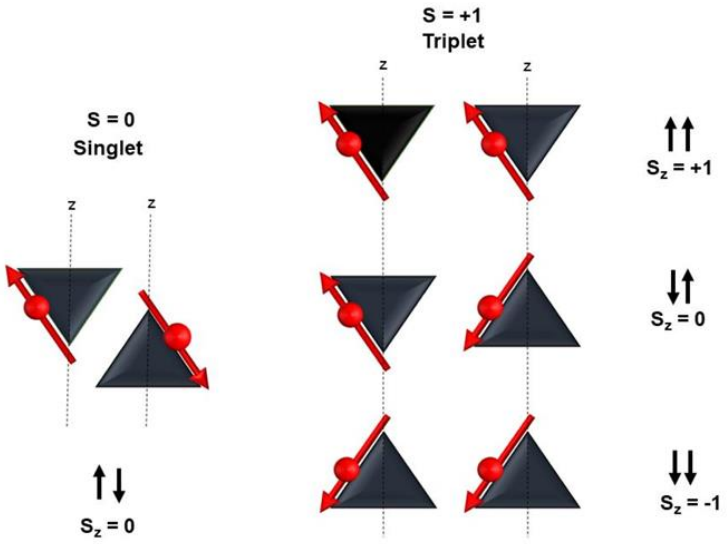

Figure 1.5. Vector representation of the four spin states of the two electrons. Figure adapted from reference 53.

In fluorescent emitters, triplet excitons typically decay non-radiatively to the ground state. Since 75% of the excitons generated are triplet excitons, the internal quantum efficiency (IQE) of a fluorescent emitter is restricted to 25%. In contrast, phosphorescent emitters can utilize 100% of the excitons due to strong spin-orbit coupling (SOC) caused by the heavy atom effect.[54] Under electrical excitation, singlet excitons can convert to triplet states through intersystem crossing (ISC), allowing emission from the triplet state. This ability to harvest both singlet and triplet excitons enables phosphorescent emitters to attain maximum IQE of 100% (**Figure 1.6**).[54]

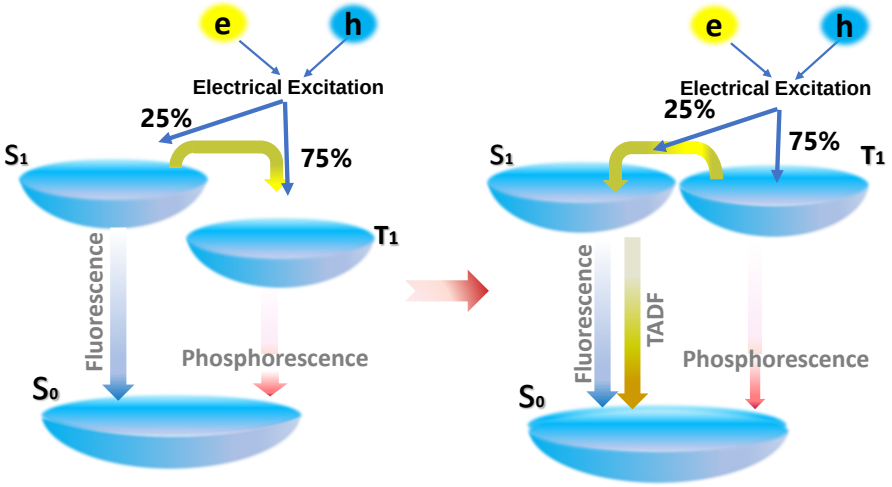

Figure 1.6. Schematic representation of singlet and triplet excitons in the electroluminescence process. Figure adapted from reference 54.

1.4. Iridium Complexes

The transition metal ions are placed within an octahedral ligand environment, their d orbitals undergo a splitting into two sets: three degenerate orbitals termed t_{2g} and two degenerate orbitals termed e_g (**Figure 1.7**). The energy separation between these sets (Δ) is affected by several factors: (i) the oxidation state of the metal, where higher oxidation states result in a larger Δ; (ii) the spatial extent of the d orbitals, which is relatively small for 3d metals and progressively larger for 4d and 5d metals; and (iii) the strength of the ligand field. When Δ is sufficiently large, the metal ion prefers a low-spin electron configuration (t_{2g}^6 e_g^0), a behaviour commonly seen in Ir(III) complexes. Consequently, Ir(III) complexes have a singlet ground state, characterized by no unpaired electrons, while their excited states can be either singlet or triplet.[52, 55]

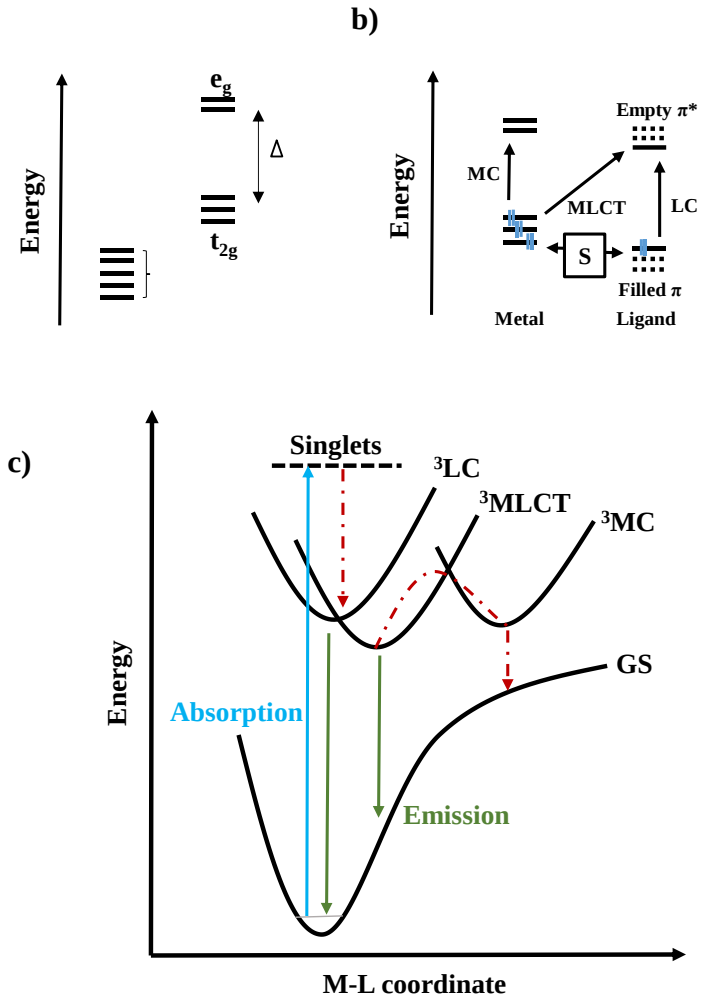

Figure 1.7. (a) Splitting of d orbitals, in an octahedral environment; (b) Orbital representation of the MLCT, LC, and MC transitions and (c) Electronic transitions involving MLCT, LC and MC excited states. Figure adapted from reference 52.

The strong spin-orbit coupling (SOC) in Ir(III) complexes, combined with their efficient photoluminescence, can be primarily attributed to the high ligand-field splitting energy of the d orbitals. The energy is further enhanced by the use of high-field cyclometalating ligands.[56] This leads to a significant energy gap between the d-d orbitals in cyclometallated Ir(III) complexes, reducing the chances of non-radiative metal-centered (MC) transitions.[12] As a result, the triplet state (T_1) typically acts as the lowest energy emitting state, often arising from a mix of triplet levels that include both ^{3}MLCT and ^{3}LC state, or a combination of both (**Figure 1.7b**).[52, 55] This blending of excited states is a direct

result of SOC, which not only integrates states of similar energies but also generates new mixed states. The MLCT or LC emission, depends on the energy levels of the ligand's π/π* orbitals. Therefore, the choice or design of the cyclometalating ligand plays a crucial role in determining both the nature of the emitting state and the color of the emission.[12, 52, 57]

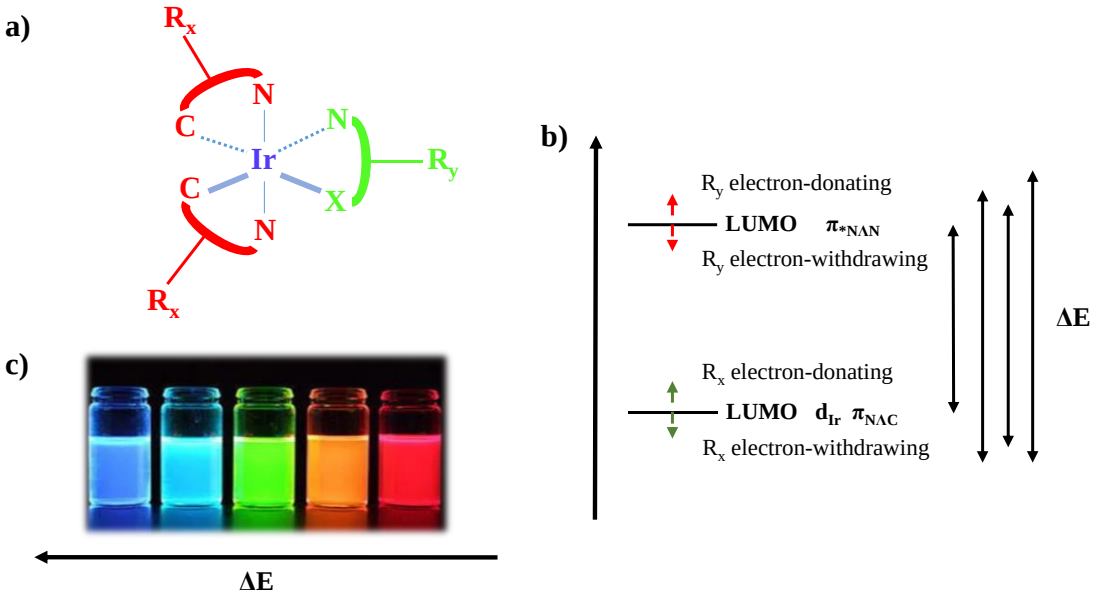

Figure 1.8. (a) The general structure of an iridium(III) complex; (b) Adjusting the ΔE energy between the HOMO and LUMO states by adding electron donating and withdrawing groups to the C^N and N^N ligands and (c) Examples of the range of emission colors achieved through molecular engineering of Ir(III) complexes. Figure adapted from reference 52.

The color and nature of the excited state in Ir(III) complexes can be modified through molecular engineering. By combining phenyl-pyridine ligands (C^N ligands), which coordinate with Ir(III) via carbon and nitrogen atoms, with bipyridine or phenanthroline ligands (N^N ligands) that bind through nitrogen atoms, different emission colors can be achieved.[4] The C^N ligands, which are anionic, primarily contribute to the HOMO, while the neutral N^N ligands, with their lower energy antibonding π* orbitals, are associated with the LUMO. To achieve blue emission, the energy difference between the HOMO and LUMO needs to be increased. This can be done by adding electron-

withdrawing groups, such as fluorine, to the C^N ligands, which stabilizes the HOMO and results in higher energy (blue) emission. Similarly, adding electron-donating groups to the N^N ligands can achieve the same result. Conversely, the addition of electron-donating groups to the C^N ligands or electron-withdrawing groups to the N^N ligands shifts the emission toward red emission (**Figure 1.8**).[4, 52]

The Ir(III) complexes are generally classified as homoleptic tris-cyclometalated ($Ir(C^N)_3$) and heteroleptic bis-cyclometalated [$Ir(C^N)_2(L^X)$] complexes, where C^N represents a cyclometalating ligand and L^X denotes an ancillary ligand. These complexes demonstrate remarkable thermal stability and substantial electronic interactions due to the robust Ir–C bond, which is comparable to a covalent bond. This leads to extensive electronic interactions between the iridium d-orbitals and the π-orbitals of ligand.[4] The synthesis of these complexes usually consists of two-step process. Initially, the HC^N ligand reacts with iridium chloride ($IrCl_3.nH_2O$), forming a dichloro-bridged dinuclear dimer $[Ir(C^N)_2(\mu\text{-}Cl)]_2$ through the Nonoyama reaction (**Figure 1.9a**).[58] This dimer is a versatile precursor for synthesizing various complexes due to its compatibility with a wide range of ligands. Further reaction of the dichloro-bridged dimer with an additional cyclometalating ligand results in the formation of tris-cyclometalated complexes. These can be homoleptic if the C^N ligands are identical, forming $[Ir(C^N)_3]$, or heteroleptic if a different C^N ligand is used (**Figure 1.9b, c**).

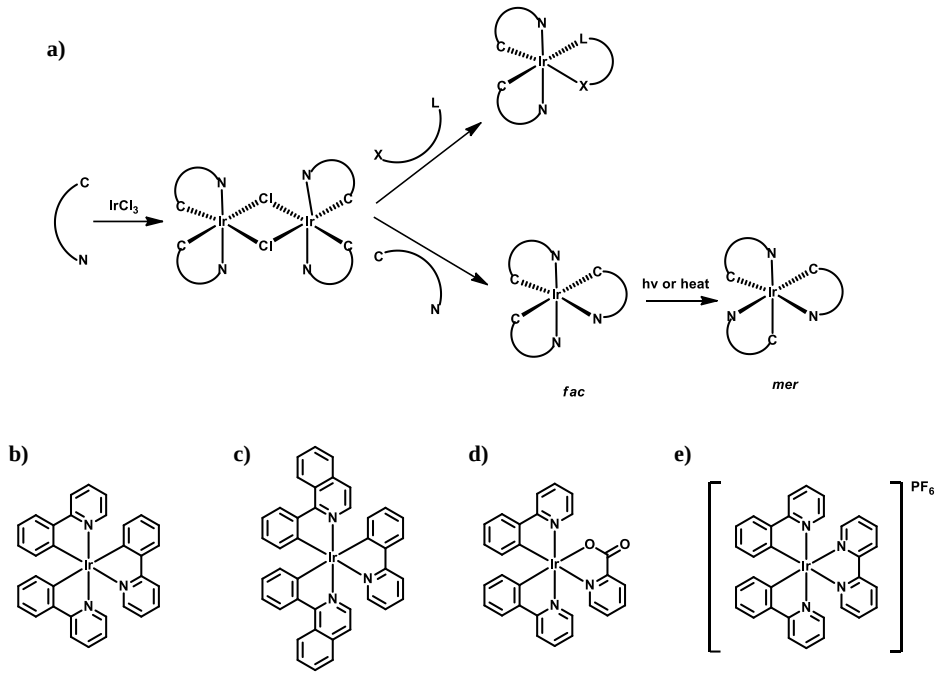

Figure 1.9. (a) Generalized synthetic scheme of iridium(III) complexes: Examples for (b) Homoleptic tris-cyclometalated iridium(III) complex; (c) Heteroleptic tris-cyclometalated iridium(III) complex; (d) Neutral heteroleptic bis-cyclometalated iridium complex and (e) Cationic heteropeptic bis-cyclometlated iridium(III) complex. Figure adapted from reference 52.

For tris-cyclometalated Ir(III) complexes, two isomeric forms can occur: facial (*fac*) and meridional (*mer*) **(Figure 1.9a)**.[4, 59-64] The *mer* isomer can be isomerized to the more stable *fac* isomer through thermal or photochemical processes. The chloride dimer can also react with chelating ligands to form a wide array of neutral bis-cyclometalated complexes $[Ir(C\text{^}N)_2(L\text{^}X)]$, where L^X are anionic ligands like β-diketonates, picolinates, and pyridineazolates **(Figure 1.9d)**, or charged complexes $[Ir(C\text{^}N)_2(L\text{^}L)]^+$ with neutral ligands such as diimine or phosphines **(Figure 1.9e)**.[4, 50, 65-67] Researchers have developed a range of neutral and ionic mono-, bis-, and tris-cyclometalated Ir(III) complexes that emit light across the visible spectrum.[68, 69]

1.5. Photodynamic Therapy (PDT)

Photodynamic therapy (PDT) has attracted considerable interest as an alternative cancer treatment because of its ability to selectively target and destroy tumor cells while preserving healthy cells. In the last decade, the clinical application of PDT has grown significantly. Although PDT has been used for over 30 years to treat bacterial and fungal infections, its application in cancer therapy has seen notable growth.[70-74] PDT works by producing reactive and toxic oxygen species when a photosensitizer is activated, which then destroys tumor tissue. It has several clear advantages over traditional treatments: it is non-invasive, highly selective, and allows multiple treatments without the risk of resistance or dose limits, as seen in radiotherapy. Additionally, it promotes faster healing with little to no scarring, can be done on an outpatient basis, and generally has fewer side effects.

PDT involves four main stages (**Figure 1.10**).[75-77]

- The first stage is the introduction of the photosensitizer into the body.
- In second stage, the photosensitizer selectively accumulates around the tumor tissue during a period of incubation.
- The third stage involves irradiating the tumour tissue with a light stimulus, which excites the photosensitizer and generates cytotoxic reactive oxygen species (ROS).
- Finally, in the fourth stage, these ROS react with biological substrates such as nucleotides, amino acids, proteins, and lipids, disturbing normal cell functions and inducing cell death.

A photosensitizer in PDT can be considered a "stimuli-responsive system," remaining dormant in the dark and becoming active only when exposed to light of selective wavelength.

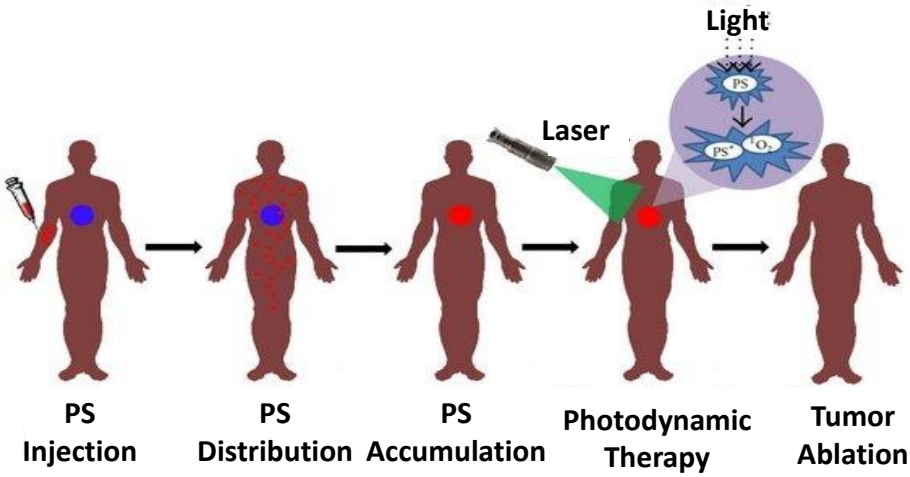

Figure 1.10. Schematic representation of different stages of PDT. Figure adapted from 75.

Photodynamic therapy (PDT), typically dependent on oxygen, can still occur in low-oxygen (hypoxic) environments. PDT is categorized into two types based on its photochemical reactions: type I and type II (**Figure 1.11**).[78-80] Upon light activation, the photosensitizer (PS) transitions from its ground singlet state (S_0) to an excited singlet state (S_1), and then to an excited triplet state (T_1). This triplet state initiates photochemical reactions through two distinct pathways: type I and type II. In type I PDT, the triplet state photosensitizer (T_1) engages in electron transfer processes, reacting directly with biological substrates to produce free radicals. These free radicals can further interact with triplet oxygen ($^3O_2$) and water to form superoxide ($O_2^{\bullet-}$), hydroxyl ($^{\bullet}OH$), and hydrogen peroxide (H_2O_2). Conversely, in type II PDT, the triplet state photosensitizer (T_1) converts surrounding triplet oxygen ($^3O_2$) into cytotoxic singlet oxygen ($^1O_2$) through direct energy transfer. Thus, type II PDT is more effective in oxygen-rich environments, while type I PDT can operate in hypoxic conditions.[80-83]

The mechanism of cell death induced by PDT-either apoptosis or necrosis-depends on the photosensitizer's location in the cell and the quantity of singlet oxygen generated.

Several literature reports indicate that photosensitizers primarily localized in the mitochondria or endoplasmic reticulum are more likely to induce apoptosis. In contrast, those in the plasma membrane or lysosomes tend to promote necrosis. Additionally, PDT triggers acute local inflammation, which stimulates an immune response against cancer cells.[79, 84-86] Type I PDT's ability to function under hypoxic conditions and type II PDT's effectiveness in well-oxygenated environments allow PDT to be versatile in various physiological conditions.[87] The localization of the photosensitizer within cellular structures helps in determining the pathway of cell death and influences the overall therapeutic outcome.[80] Moreover, the immune response elicited by the localized inflammation adds another layer of effectiveness to PDT as a cancer treatment strategy.[79]

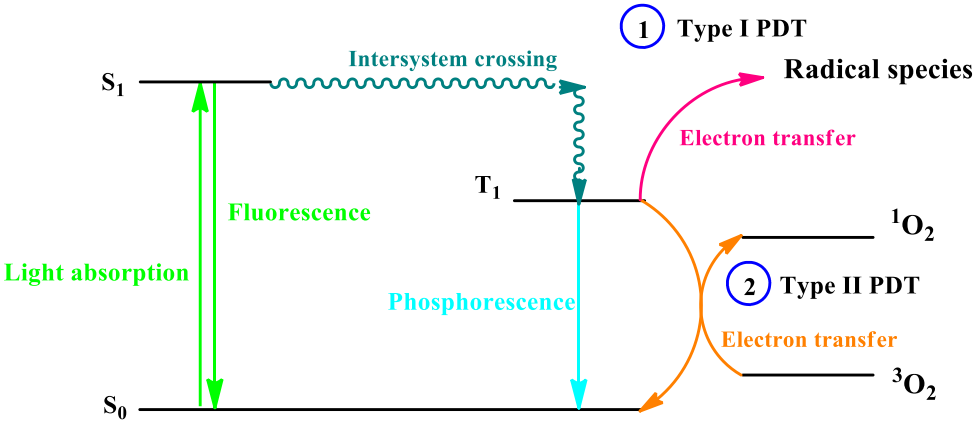

Figure 1.11. Schematic representation of type I and type II PDT. Figure adapted from reference 92.

1.5.1. Generation of Singlet Oxygen

Photosensitized generation is an efficient and controllable method for producing singlet oxygen (($^1O_2$) and requires oxygen, light of a specific wavelength, and a photosensitizer (PS) that can absorb and utilize this energy to excite oxygen to its singlet state. The PS is crucial in photodynamic therapy (PDT) as it generates reactive oxygen species (ROS) upon irradiation with light of a selected wavelength. Typically, a PS is a

single, stable chemical compound with high purity. An ideal PS should exhibit high efficiency in ISC from the singlet to triplet state, very low toxicity in the absence of light (dark toxicity), minimal phototoxicity to normal tissues, and strong absorption at longer wavelengths.[88]

The primary photophysical processes involved in reaching the triplet excited state (S_0-S_1-T_1 or S_0-S_1-T_n-T_1) are generally quantum mechanically forbidden. Achieving the triplet state in an organic compound requires a non-radiative transition from S_1 to T_n or S_1 to T_1, known as intersystem crossing (ISC).[79] As previously mentioned, this transition involves changing spin states, and during ISC, both energy and total angular momentum (comprising orbital and spin components) must be conserved. The key interaction facilitating the coupling of two spin states and the conservation of total angular momentum is the spin-orbit coupling (SOC), where the electron spin couples with orbital angular momentum.[89]

Several factors enhance ISC, including:

- The heavy atom effect, where the presence of heavy atoms increases SOC.
- Low-lying n-π^* transitions that facilitate spin-state changes.
- Exciton coupling, where interactions between excitons can promote ISC.
- Intramolecular spin conversion, where spin states are converted within the molecule.

These factors contribute to the efficiency and effectiveness of photosensitizers in producing singlet oxygen, making them essential for the success of PDT.

The heavy atom effect plays a crucial role in enhancing spin-orbit coupling (SOC) and intersystem crossing (ISC). Atoms with high atomic numbers, such as iridium (Ir) and

platinum (Pt), create significant SOC due to their high positive nuclear charge (Z), which accelerates electrons to relativistic speeds and intensifies the coupling between their spin and orbital magnetic moments. This effect scales with Z^4 (where Z is the nuclear charge) and is observable in elements like ruthenium (Ru) and osmium (Os).[90-93] In addition to the heavy atom effect, ISC can be enhanced by low-lying n-π transitions. Transitions between non-bonding and anti-bonding (n-π*) states have a small energy gap between singlet (S_1) and triplet (T_1) states, which facilitates ISC. El-Sayed's selection rule supports this, as transitions from S_1 (n, π*) to T_1 (π-π*) are allowed due to their small energy gap and angular momentum conservation.[90] Exciton coupling also contributes to ISC enhancement. When two identical chromophores are close together, their transition dipole moments interact, forming delocalized excited states from a single local singlet excitation. If these singlet states are near the energy of the triplet state, ISC is promoted.[79]

1.5.2. Types of Photosensitizers

Different classes of photosensitizers that can generate singlet oxygen include organic dyes and aromatic hydrocarbons, which absorb UV-vis light and are commonly used in biological applications. Porphyrins, phthalocyanines, and related tetrapyrroles are notable for their strong absorption in the visible spectrum and their ability to generate singlet oxygen.[80] However, porphyrins and organic photosensitizers suffer from poor solubility and photostability (prone to degradation with prolonged light exposure). Additionally, they may have limited absorption range, reducing overall efficiency. To address this, transition metal complexes, particularly those containing heavy metals, were introduced for their strong ability to generate singlet oxygen.

1.5.3. Photosensitizers based on Transition Metal Complexes

The limitations of organic, and porphyrin photosensitizers have prompted the investigation of transition metal-based photosensitizers. These inorganic complexes, particularly those incorporating heavy atoms, offer promising alternatives due to their enhanced photophysical properties. Transition metal complexes, such as those containing Pt(II), Ir(III), and Ru(II), can be designed to exhibit strong absorption in the visible region and produce effective triplet states for singlet oxygen generation.[94, 95] Ir(III) complexes, in particular, have shown significant advantages over Ru (II) and Pt (II) complexes.[95, 96] They exhibit high photostability, long lifetimes, high phosphorescence quantum yields, substantial Stokes shifts, and tunable emission colors.[97] These properties make Ir(III) complexes effective in generating reactive oxygen species (ROS) under both normoxic and hypoxic conditions, which is beneficial for both imaging and therapeutic applications in cancer treatment. Consequently, Ir(III) complexes are increasingly recognized as promising candidates for photodynamic therapy (PDT), with ongoing research focusing on their potential for cancer diagnosis and therapy. **Figure 1.12** illustrates common class of Ir(III) complexes used in PDT and imaging, demonstrating their versatility and effectiveness in medical research.[79]

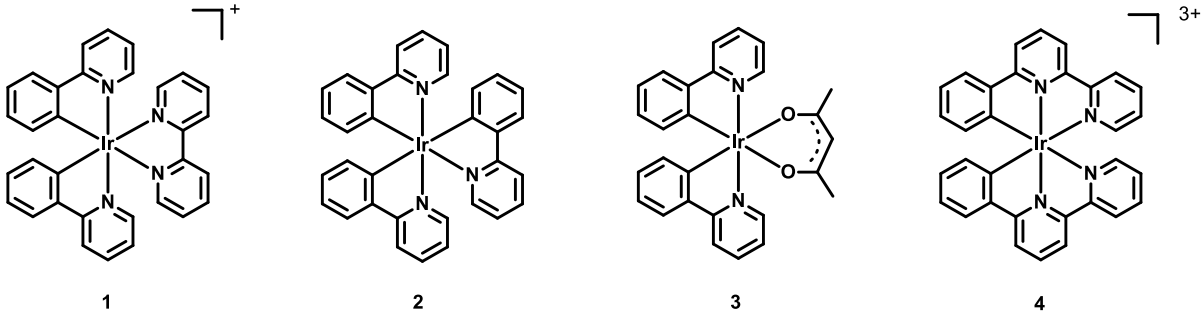

Figure 1.12. Structure of common iridium complexes used as photosensitizers for PDT.

1.5.4. Iridium Complexes as Effective Generators of Singlet Oxygen

Recent advancements in the development of Ir(III) complexes for singlet oxygen generation have demonstrated promising potential in photodynamic therapy (PDT) and related applications (**Figure 1.13**).[98] The rapid growth in the chemistry and application of cyclometalated Ir(III) complexes, as highlighted in reviews by You and Nam, underscores their significance in this area.[99] Certain Ir(III) complexes have achieved remarkable singlet oxygen quantum yields (Φ_Δ) approaching unity. Various Ir(III) complexes featuring two cyclometalated ligands and an ancillary diketonate (e.g., $[Ir(C^N)_2(O^O)]$) (**complex 1**) have been investigated for their capacity to generate singlet oxygen through both energy and electron transfer pathways.[100] For instance, Murata's studies on Ir(III) complexes revealed a range of Φ_Δ values, from 0.26 for $[Ir(pip)_2(acac)]$ (where pip = 2-phenylimidazo-4,5-f-1,10-phenanthroline) to 0.97 for $[Ir(ppy)_2(bpy)]$ (where ppy = 2-phenylpyridine) (**complexes 2** and **3**). These variations in singlet oxygen generation efficiency are attributed to differences in the oxidation potential of the sensitizer and the triplet energy levels.[101] In another study, Pope *et al.*, explored the photooxidation properties of the first pyrene-based Ir(III) complex (**complex 4**). They reported both neutral cyclometalated $[Ir(C^N)_3]$ and heteroleptic cationic $[Ir(C^N)_2(N^N)]^+$ complexes, with the cationic species showing superior singlet oxygen photogeneration performance.[102] Recent modifications to Ir(III) complexes have further enhanced their efficiency. For example, Maggioni and colleagues developed a polymer complex by incorporating bis(cyclometalated) $Ir(ppy)_2^+$ fragments into phenanthroline pendants of a poly-(amidoamine) copolymer (**complex 5**).[103] The corresponding molecular complex $[Ir(ppy)_2(bap)]^+$ was also synthesized for comparison (**complex 6**). In aqueous solutions, the polymer complex formed nano-aggregates that sensitized singlet oxygen generation, although it exhibited a lower quantum yield than the molecular complex. Photodynamic therapy examination indicated that both complexes

induced cell apoptosis upon light exposure, with the molecular **complex 6** yielding higher apoptotic cell fractions. However, the polymer complex displayed lower levels of necrosis and reduced toxicity in the absence of irradiation. These findings suggest that conjugating iridium sensitizers to polymers may mitigate cellular damage, providing a promising approach for developing effective and safer PDT agents.

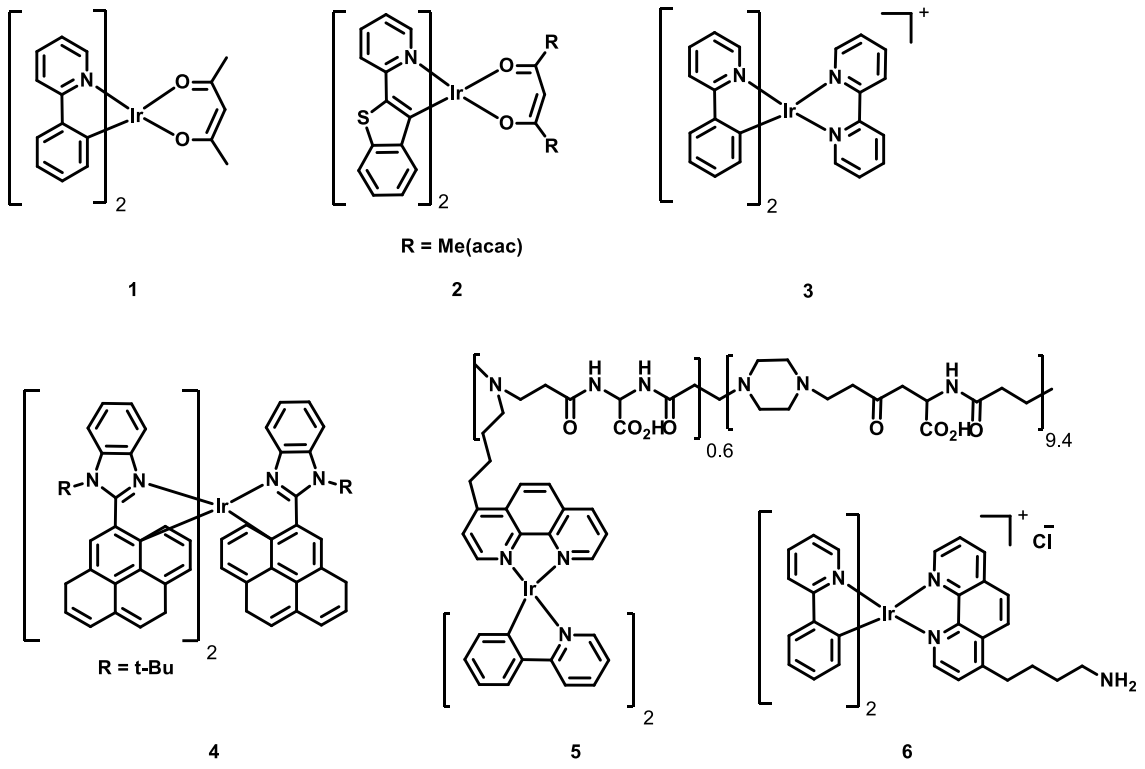

Figure 1.13. Structure of various iridium complexes **(1-6)** reported for singlet oxygen generation.

1.5.5. Applications of Iridium(III) Complexes in Biological Systems

To effectively utilize the synthesized complex in biological systems, several requirements must be satisfied, and modifications to the ligand can significantly enhance its efficiency. Below, three primary criteria are discussed that are essential for optimizing the complex's performance in biological applications.

1.5.5.1 Cellular Uptake of Iridium(III) Complexes

For effective intracellular photodynamic therapy (PDT) and imaging, it is essential that the reagent is taken up by cells efficiently and at a controlled rate. Cyclometalated Ir(III) polypyridine complexes show better cellular uptake than their chlorinated parts. This improved uptake is due to the enhanced lipophilicity resulting from the cyclometalation and polypyridine structures.[104] Research by Velders *et al.*, has highlighted the impact of different amino acid substituents on the uptake efficiency of a series of Ir(III) complexes. Among these, Ir(III) complexes conjugated with lysine generally show greater uptake compared to those with glycine or alanine. This variation is likely due to differences in lipophilicity, as evidenced by the range of lipophilicity values observed for complexes with aliphatic alkyl chains. Interestingly, while higher lipophilicity is often associated with increased cellular uptake, the most lipophilic complex in this series showed lower efficiency in cellular internalization due to its tendency to self-aggregate in aqueous solutions, hindering its cellular uptake.[105, 106] The mechanism of cellular uptake for Ir(III) polypyridine complexes has been further explored through studies involving temperature variations and uptake inhibitors. For instance, the complex $[Ir(ppy)_2(bpy\text{-}(C_4)_2]^+$, upon internalization into HeLa cells at 37 °C, forms a diffuse emissive background with cytoplasmic granules.[107] The disappearance of these cytoplasmic foci at lower temperatures (4 °C) or in the presence of endocytic inhibitors suggests that the complex enters cells via both passive diffusion and endocytosis. The interaction of biological substrates with Ir(III) polypyridine complexes also affects their intracellular distribution and uptake mechanisms.[108, 109] For example, indole-substituted complexes internalize through an energy-dependent process such as endocytosis. Further investigations by Mao *et al.*, with bis-cyclometalated Ir(III) complexes revealed that cellular uptake can be reduced at lower temperatures and in the presence of metabolic inhibitors, though endocytosis inhibitors did

not impact uptake.[110] This indicates that the complexes penetrate the cell membrane through an energy-dependent mechanism, bypassing endocytic pathways. These findings underscore the complexity of cellular uptake mechanisms and the influence of chemical modifications on the efficacy of Ir(III) complexes in PDT and imaging applications.

1.5.5.2. Activatable Photosensitizers for Imaging and Therapy

Photosensitizers are not limited to therapeutic applications like singlet oxygen generation; they also play a crucial role in imaging, especially in the near-infrared (NIR) spectrum. This capability makes them valuable for both therapy and diagnostic imaging, a concept known as theranostics.[76, 111] Theranostics merges therapeutic and diagnostic functions to enhance drug efficacy and accurately target tumor sites. This dual functionality allows for the assessment of chemotherapy by visualizing tumor progression and provides real-time feedback on therapeutic outcomes. Additionally, fluorescence from photosensitizers can serve as a non-invasive optical biopsy tool, distinguishing between benign and malignant cells without the need for traditional histological methods. The fluorescence signal also helps monitor treatment success; a decrease in fluorescence indicates effective cell destruction, offering a dosimetric guide for adjusting therapy in real time.[76] Photosensitizers with luminescent properties can reveal their localization and the extent of their uptake by diseased tissues. This characteristic is particularly useful for developing photosensitizers that become active only in the presence of specific target molecules, thereby minimizing non-specific phototoxicity. Ideally, activatable photosensitizers provide precise imaging by differentiating target cells from normal cells. Furthermore, photosensitizers can be conjugated with agents from other imaging modalities, such as radio-labeled or MRI contrast agent-conjugated photosensitizers, creating multifunctional probes that offer combined imaging and therapeutic

capabilities.[112] Many of iridium(III) complexes, exhibit intense, long-lived, and environmentally sensitive emissions. This makes them excellent reporters for monitoring local biological events and intracellular dynamics. Techniques such as laser scanning confocal microscopy enable detailed tracking of these complexes within cells, while phosphorescence lifetime imaging (PLIM) leverages their long-lived phosphorescence for highly sensitive measurements.[112]

1.5.5.3. Key Organelle-Targeting Strategies for Iridium Complexes

Moving forward, metal complexes have been designed to target specific organelles within cells, enhancing therapeutic precision. Organelles like the cytomembrane, lysosome, mitochondrion, golgi apparatus, endoplasmic reticulum, and nucleus are crucial for cellular function, and their dysfunction can lead to diseases such as cancer, Parkinson's, Alzheimer's, and diabetes.[113, 114] The clinical success of cisplatin has catalyzed the development of metal-based anticancer agents targeting organelles to improve therapeutic outcomes.[115-119] Two primary strategies for targeting organelles involve attaching metal centers to organelle-specific moieties or adjusting the metal complex's properties to meet organelle-targeting requirements.[120, 121] Peptides and small molecules are common targeting moieties, though peptides can be degraded by enzymes, unlike more stable small molecules. Another approach is to modify the ligands of a metal complex to enhance its organelle targeting. For example, lysosome targeting, complexes may incorporate moieties like amines that become protonated in the acidic lysosomal environment, leading to accumulation within lysosomes.[122, 123] Alternatively, hydrophilic cationic metal complexes can utilize the endocytic pathway to reach lysosomes.

1.5.6. Literature Review

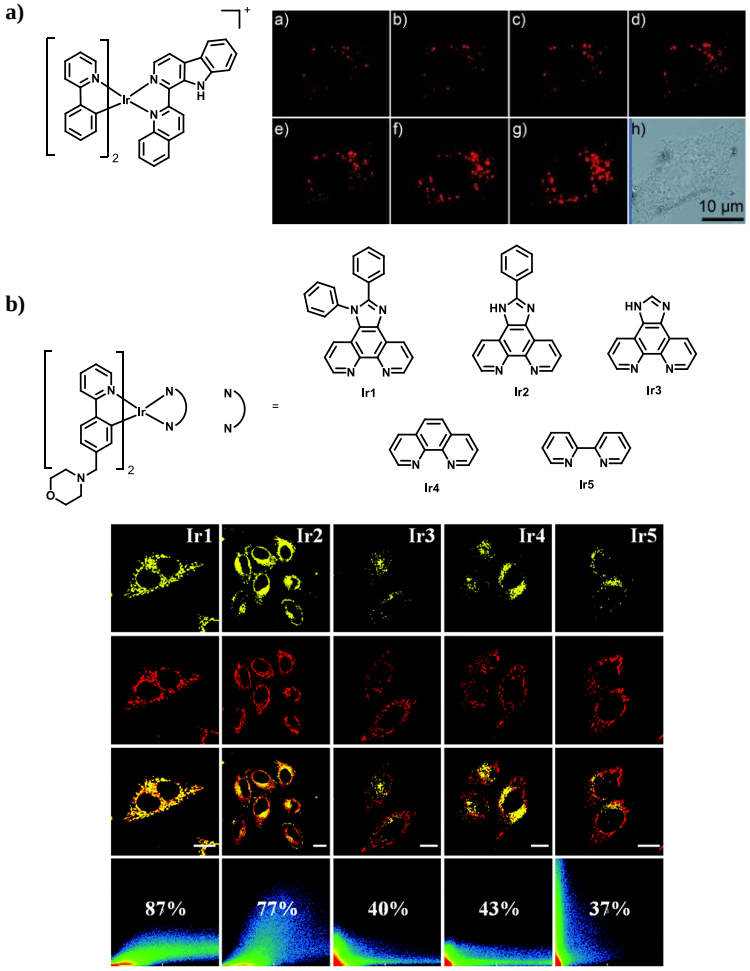

Figure 1.14. (a) Structure of lysosome targeting Ir(III) probe and corresponding real time tracking of two photon excited lysosomes in A549 cell line and (b) Structure of mitochondria targeting Ir(III) probes with the corresponding confocal images of probe colabelled with mitotracker red in HeLa cell lines. Figure adapted from 124 and 125.

Recent advances include Ir(III) complexes developed by Mao *et al.*, which specifically target lysosomes and induce autophagic responses in live cells (**Figure 1.14a**).[124] These complexes not only facilitate lysosome imaging but also enhance sensitivity through their two-photon absorption (TPA) properties, making them compatible with various staining methods and reducing background noise. Chao *et al.*, reported a series of mitochondria targeting iridium complexes (**Ir1**-**Ir5**) for hypoxic tumors (**Figure 1.14b**).[125] The overall positive charge and lipophilic nature of iridium complexes help them

to get localized in the mitochondria of cells even without having any specific targeting group.[80, 126] These complexes serve as effective theranostic agents, offering both imaging and therapeutic applications.

Williams's group investigated two cyclometalated iridium(III) complexes, both featuring 2-pyridylbenzimidazole ligands.[127] **Complex 1** displayed green emission, whereas **complex 2** exhibited emission at 590 nm (**Figure 1.15**). However, when incubated with CHO cells, their emissions became nearly identical due to a protonation equilibrium influenced by local pH, with **complex 1** being dominant at pH 7.4 and **complex 2** forming in the acidic environment of lysosomes. Both complexes showed low cytotoxicity, with IC_{50} values exceeding 200 µM. The positive charge of these iridium complexes makes them effective for staining mitochondria, as they have a strong affinity for the electrical potential of the mitochondrial membrane, which is an important consideration for mitochondrial staining techniques.

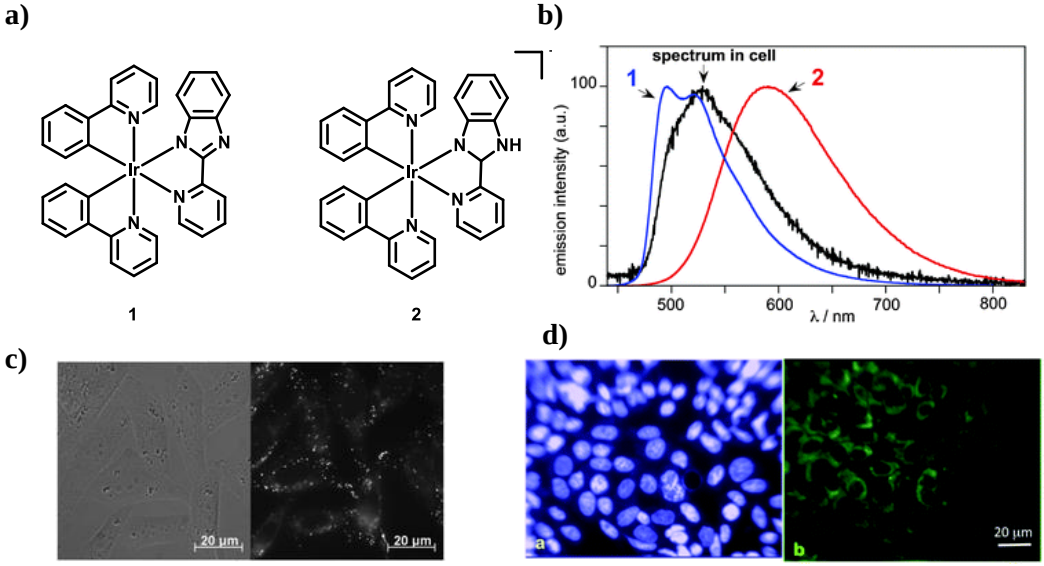

Figure 1.15. (a) Structure of iridium **complexes 1** and **2**; (b) Emission profile of complexes **1** and **2**; (c) Bright filed and fluorescence images of **complex 1** incubated CHO cells and (d) Fluorescence microscopy images of live CHO cells co-stained with **complex 1** and Hoechst. Figure adapted from reference 127.

Lo and his team developed a series of bioconjugate iridium(III) complexes **(1a-4a** and **1b to 4b)** that incorporate D-glucose or D-galactose units linked by polyethylene glycol to enhance uptake in cancer cells (**Figure 1.16**).[128] By modifying the π conjugation of cyclometalated ligands, they aimed to increase cellular uptake, taking advantage of the higher expression of glucose transporters (GLUTs) and hexokinases in cancer cells. The study revealed that **complexes 1a** and **1b** exhibited slightly higher lipophilicity and cellular uptake in HeLa cell lines. These complexes get localized in mitochondria through an energy-dependent pathway. This innovative approach holds promise for developing targeted cancer therapies using sugar-modified iridium(III) complexes.

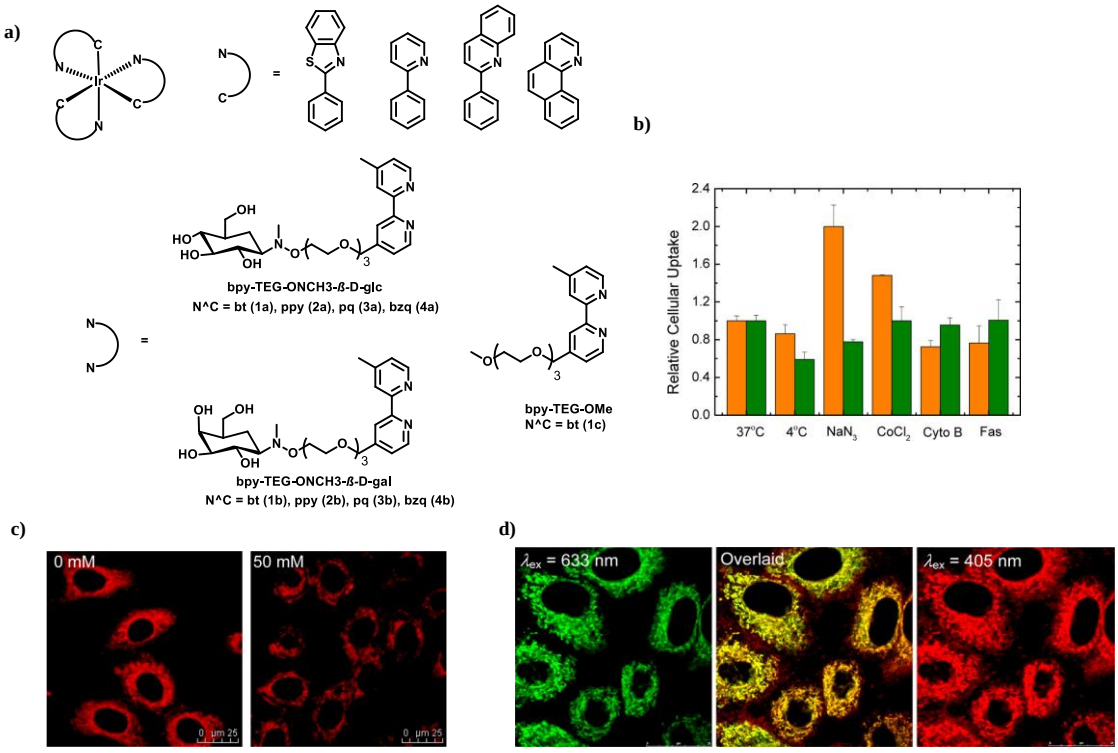

Figure 1.16. (a) Structure of iridium complexes used for imaging; (b) Relative cellular uptake of iridium associated with in HeLa cell upon incubation with **complexes 1a** (orange) and **1b** (green); (c) Laser-scanning confocal microscopy images of HeLa cells upon incubation with **complex 1a** and (d) Laser-scanning confocal microscopy images of HeLa cells upon incubation with MitoTracker Deep Red and **complex 1a**. Figures adapted from reference 128.

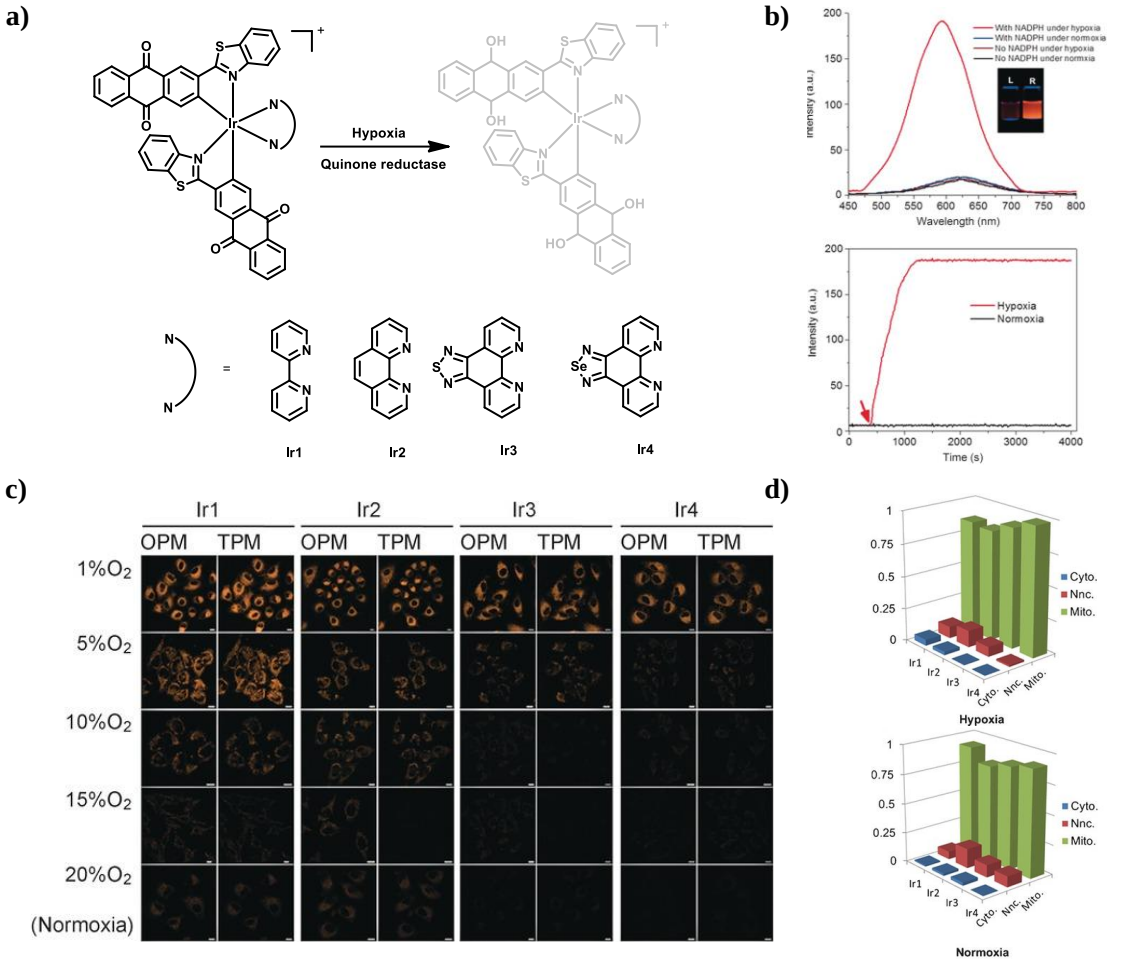

Figure 1.17. (a) Structure of the iridium **complexes (1-4)**; (b) Fluorescence turn-on of the complex under hypoxic condition in solution state; (c) Confocal images of adherent A549 cells treated with probes under normoxic as well as hypoxic condition and (d) The quantification of the sub-cellular distribution of the complexes. Figure adapted from reference 129.

Chao *et al.*, reported several anthraquinone-based iridium(III) complexes (**Ir1**-**Ir4**) designed to enhance hypoxia detection through a two-photon absorption mechanism (**Figure 1.17**).[129] These complexes feature an anthraquinone component that typically quenches iridium emission under normal conditions. However, in hypoxic environments, it transitions to an active hydroquinone state, producing a detectable light signal. When introduced into A549 cells, these complexes are reduced by NAD(P)H and cellular reductase enzymes, which significantly boosts their emission intensity under hypoxic conditions. Complexes **Ir1**-**Ir4** exhibit varying sensitivities to oxygen levels, with complex

Ir1 responding at 5% oxygen and complexes 2-4 at 1% or lower. These probes, which localize in mitochondria, demonstrate minimal cytotoxicity, maintaining over 80% cell viability under both normoxic and hypoxic conditions after 12 hours at a concentration of 10 µM. This study underscores their potential for cellular imaging and oxygen sensing.

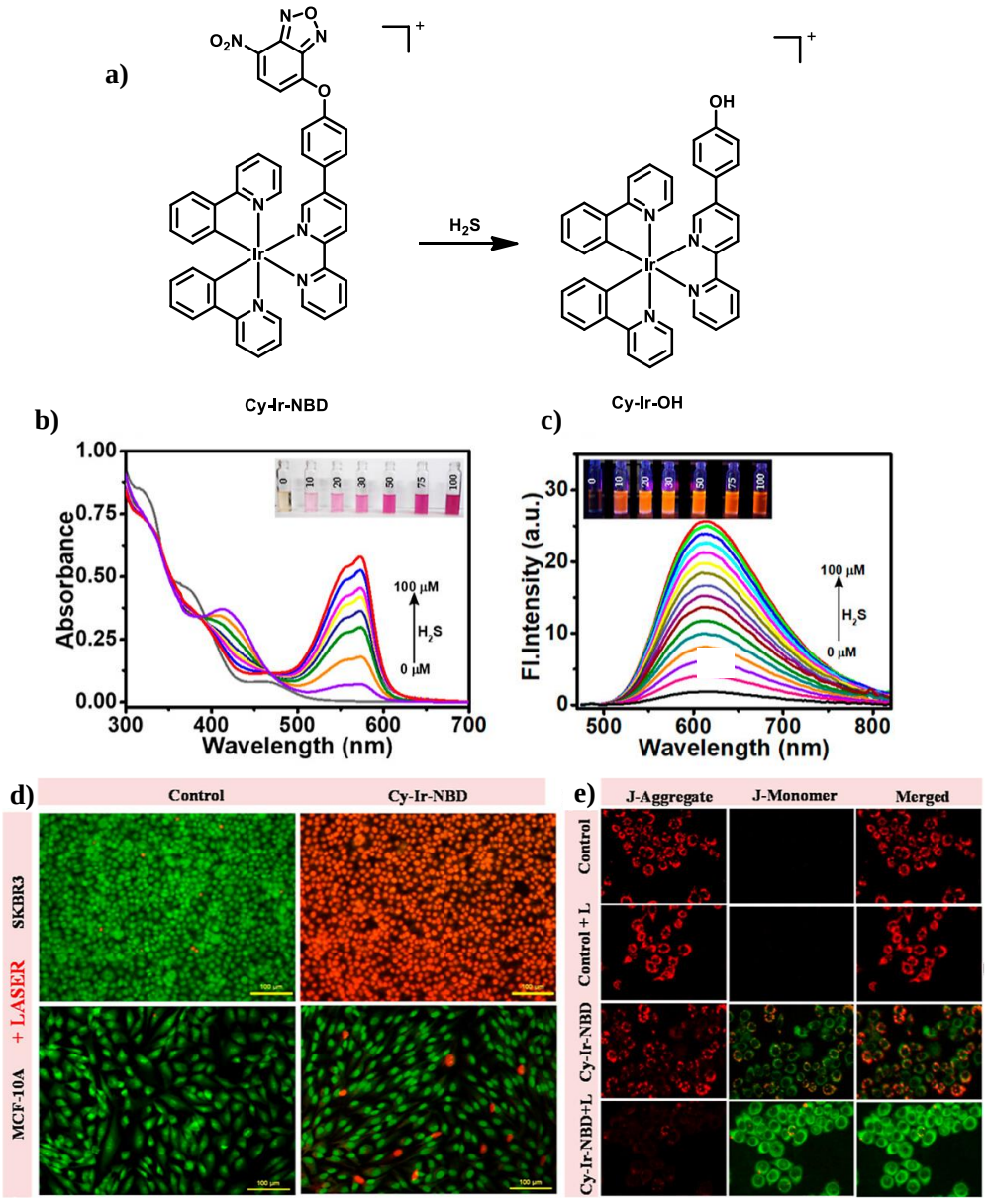

Figure 1.18. (a) Structure of iridium **Cy-Ir-NBD** and **Cy-Ir-OH**; (b) Change in absorption signals induced by iridium complex across different concentrations of Na_2S; (c) Fluorescence change in iridium **complex 1** across different concentrations of Na_2S; (d) Apoptotic evaluation of PDT using the AO/PI dual staining assay in SK-BR-3 cells and normal MCF-10A cells and e) Depolarization of mitochondria membrane potential after PDT were confirmed using the JC-1 assay. Figure adapted from reference 130.

In a separate study by Maiti *et al.*, a novel iridium complex-based photosensitizer, designated as **Cy-Ir-NBD**, was developed for precise targeting in cancer therapy. This complex includes a component that responds to hydrogen sulfide (H_2S) and a photosensitizer moiety (**Cy-Ir-OH**).[130] Under normal conditions, the iridium complex remains inactive, keeping photodynamic therapy (PDT) in an "off" state. When it encounters H_2S, which is abundant in certain cancer cells, the complex activates into a functional photosensitizer. The effectiveness of this treatment was confirmed using imaging techniques such as SERS and fluorescence (**Figure 1.18**).

Yanli Zhao *et al.*, developed two micelles, referred to as **FIr 1** and **FIr 2**, that integrate chemotherapy and photodynamic therapy (PDT) to enhance cancer treatment. These micelles contain Ir(III) complexes linked to the chemotherapy drug camptothecin (CPT) via a glutathione (GSH)-responsive bond. The micelles are encapsulated with pluronic F127 and have folic acid on their surface for targeted delivery to cancer cells. When GSH levels are high in tumor cells, the micelles release CPT, while visible light activates them to produce singlet oxygen for PDT. The targeted micelles are more effective at killing cancer cells, especially in folate receptor-rich HeLa cells, compared to non-targeted systems. This makes them a promising tool for cancer therapy and imaging (**Figure 1.19**).[131]

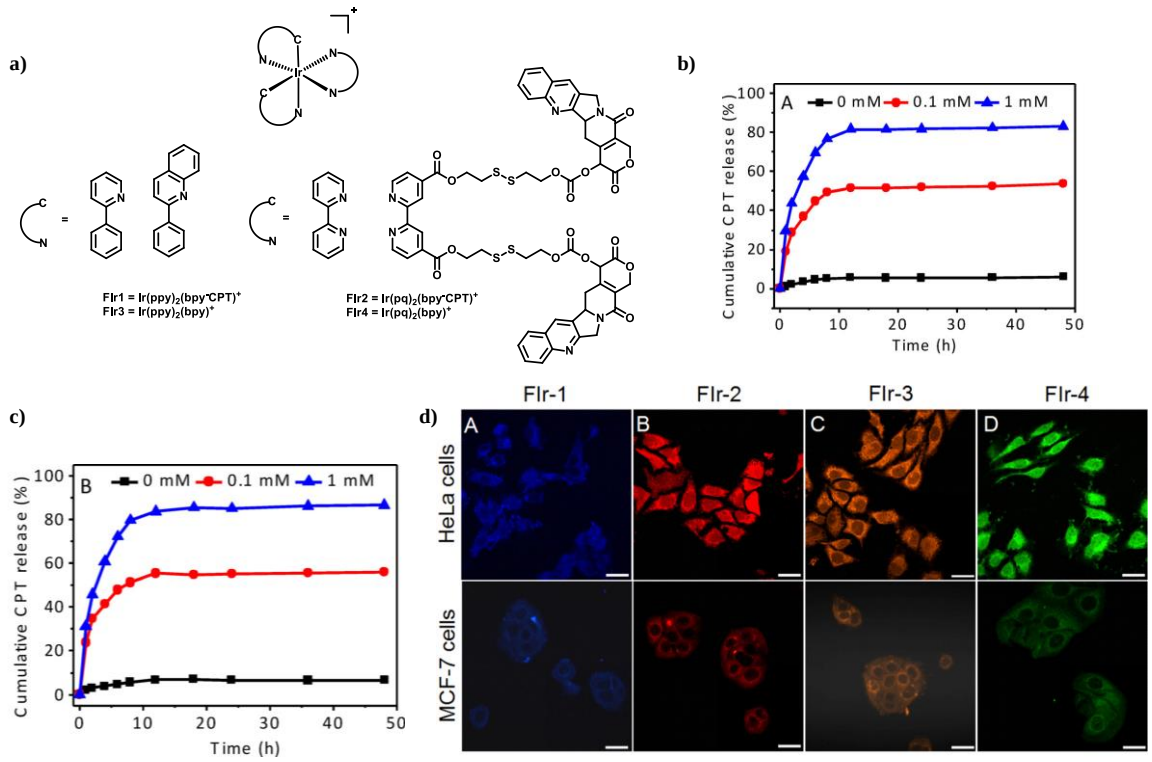

Figure 1.19. (a) Structure of the iridium complexes used; (b, c) CPT release plot of micelles (A) **Fir1** and (B) **Fir2** in the absence and presence of GSH and (d) Confocal microscopy images of HeLa and MCF-7 cells treated with **complexes FIr1-FIr4**. Figure adapted from reference 131.

Zhao and colleagues developed an iridium based photosensitizer, complex **Ir-1**, featuring benzyl-appended pyridinium groups that facilitate photo-induced electron transfer (PeT), specifically designed to respond to glutathione (GSH), which is present in high concentrations in cancer cells (**Figure 1.20**). [132] Upon interacting with glutathione, the photosensitizers undergo nucleophilic substitution, leading to changes in their phosphorescence properties, including intensity, wavelength, and lifetime. This sensitivity to GSH allows for targeted imaging and enhanced photodynamic therapy (PDT) in cancer cells due to their high GSH levels. The effectiveness of this strategy was further demonstrated by developing a new derivative, **Ir-2**, which showed improved emission properties and higher singlet oxygen production by replacing the pyridinium group with a hydroxyl group.

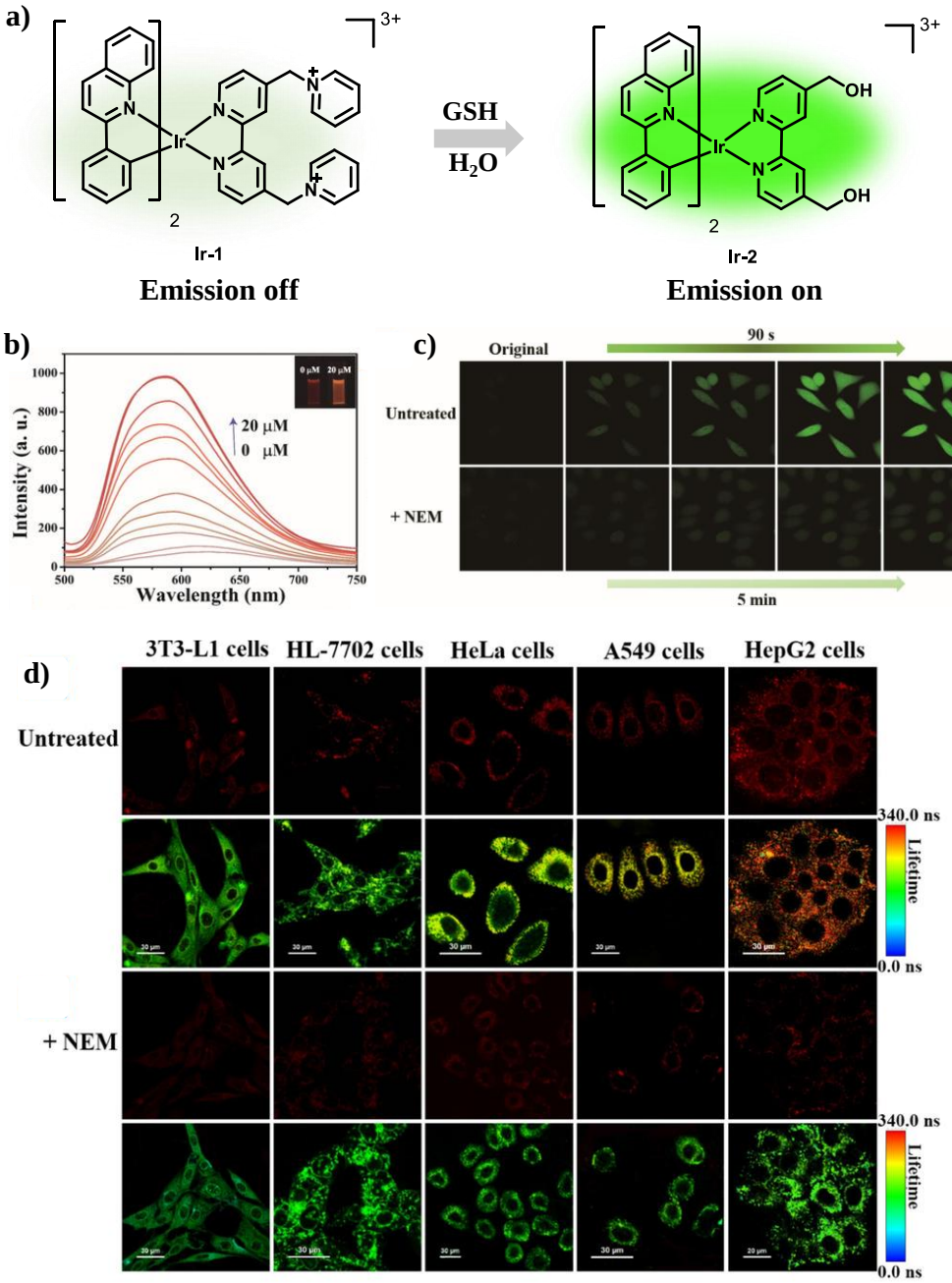

Figure 1.20. (a) The structure of iridium complexes (**Ir-1** and **Ir-2**) and mechanism of GSH activation; (b) Emission spectra of **Ir-1** under different GSH concentrations; (c) Confocal microscopy images showing DCHF-DA assays of intracellular ROS generation of **Ir-1** and (d) Confocal luminescent images and PLIM images of different types of cells incubated with the **Ir-1**. Figure adapted from reference 132.

Gou *et al.*, reported an iridium(III) complex (**IrDAD**)featuring a unique Donor–Acceptor–Donor ligand that exhibits strong absorption in the near-infrared region and demonstrates efficient Intramolecular Charge Transfer (ICT) **(Figure 1.21)**.[133] Unlike

conventional aggregation-caused quenching (ACQ) dyes, this iridium complex generates Reactive Oxygen Species (ROS) predominantly when in an aggregated state. This unique characteristic, combined with its low radiative transition rate, enhances its capability to convert light energy into reactive oxygen species and heat, making it suitable for both photodynamic therapy (PDT) and photothermal therapy (PTT). Additionally, the iridium complex was transformed into nanoparticles conjugated with polyethylene glycol (PEG), which exhibited preferential accumulation in tumors and significant tumor regression in vivo, underscoring its potential for advanced cancer treatment.

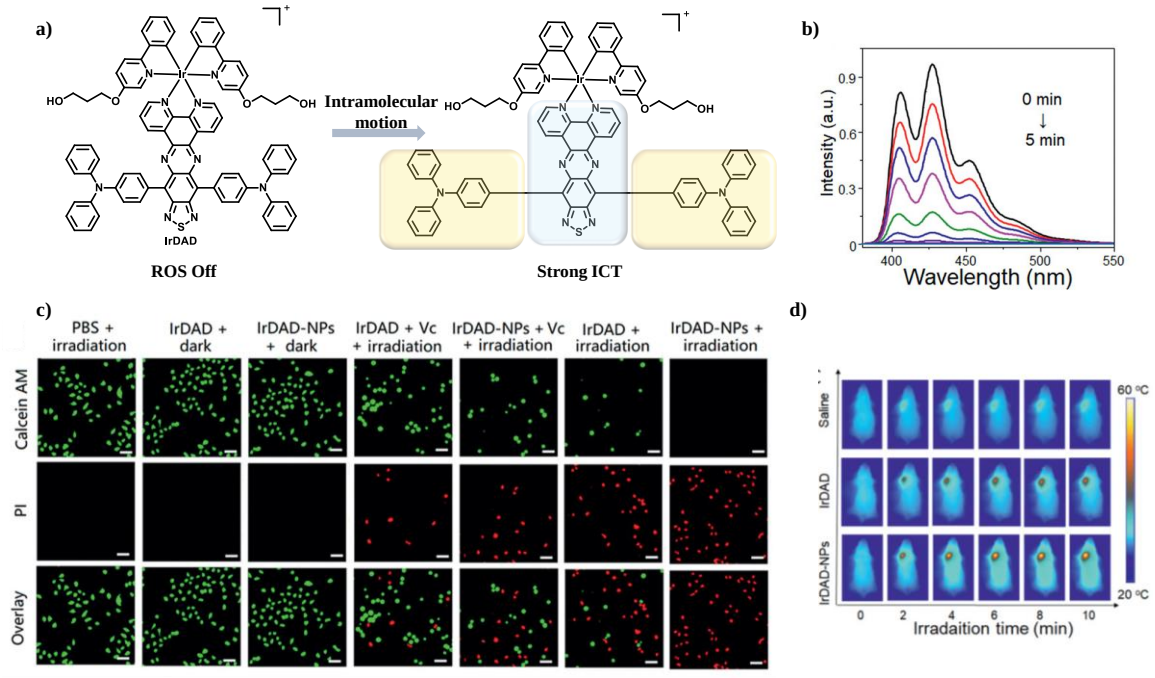

Figure 1.21. (a) The structure of the iridium complex **IrDAD**; (b) The time-dependent fluorescence spectra of ABDA irradiated in the presence of iridium complex; (c) Confocal fluorescence images of calcein AM /propidium iodide, co-stained A549 cells after treatment with iridium complex in the presence or absence of laser irradiation and (d) Thermal images of A549 tumor-bearing mice under laser irradiation for different times. Figure adapted from reference 133.

1.6. Organic Light Emitting Diode (OLED)

Thomas A. Edison's invention of the incandescent bulb in 1879 marked a significant advancement in lighting technology, utilizing a tungsten filament heated to produce light. Despite its revolutionary impact, the incandescent bulb is notably inefficient, converting only about 5% of electrical energy into visible light, with the remainder lost as heat.[134] This inefficiency leads to high energy consumption and significant heat generation, presenting challenges in both cost and safety.[135] The need for more energy-efficient lighting solutions became increasingly evident as global energy demands grew. In the 1980s, fluorescent lamps emerged as a promising alternative. These lamps function by passing an electric current through mercury vapor, which emits ultraviolet light that excites a phosphor coating inside the lamp, resulting in visible light. Fluorescent lamps are much more efficient than incandescent bulbs, with typical energy efficiencies ranging from 60 to 70 lumens per watt (lm/W).[136] However, despite their improved efficiency, fluorescent lamps have drawbacks.[137, 138] They produce a lower quality of light, often with a harsh or flickering effect, and contain mercury, a toxic element that raises environmental and health concerns. This combination of factors led to a decline in the popularity of fluorescent lamps as more advanced technologies became available. The development of light-emitting diodes (LEDs) represented another major leap in lighting technology. LEDs operate based on electroluminescence, where a semiconductor material emits light when an electric current passes through it. This technology offers significantly higher energy efficiency compared to both incandescent and fluorescent lamps. Modern LEDs can achieve efficiencies exceeding 100 lm/W, far surpassing the performance of earlier lighting technologies. Additionally, LEDs have the advantage of a longer lifespan, reduced heat output, and greater durability. They also provide superior color rendering and can be designed in various forms, including compact and flexible designs. This makes LEDs

suitable for a wide range of applications, from general lighting to specialized uses in electronics and displays. Light-emitting diodes (LEDs) have become a more eco-friendly and efficient alternative, surpassing fluorescent lamps with efficiencies exceeding 100 lm/W.[139]

A significant advancement was the development of organic light-emitting diodes (OLEDs), which use organic materials to emit light when electrically stimulated, offering advantages like flexibility and reduced weight compared to traditional LEDs.[140-142] In 2019, Wei Li *et al.*, introduced a highly flexible white OLED with a power efficiency of 126.6 lm/W, maintaining 80% efficiency after 3000 bending cycles.[143] OLEDs are now available commercially, offering high efficiency, longevity, and excellent color quality, although their production cost remains high, around $250-300 per square meter.[144] To reduce costs, researchers are exploring novel materials and solution-processing techniques for manufacturing.[145]

1.6.1 General Structures and Working Principles

OLEDs can be classified into single-layer or multilayer designs based on their architecture. A single-layer OLED features an organic emissive material, either as a pure emitter or doped into a host material, situated between two electrodes: a metal cathode with a low work function (like Al, Ca, Ba, or Mg) and a transparent anode (such as indium tin oxide) on a substrate like plastic or glass.[146, 147] When a voltage is applied across the electrodes, holes from the anode and electrons from the cathode are injected into the highest occupied molecular orbital (HOMO) and lowest unoccupied molecular orbital (LUMO) of the emissive layer, respectively. This results in the migration of these charges through the emissive layer, where they recombine to form excitons (**Figure 1.22**).[148, 149] These excitons can be either singlet or triplet states, with a 1:3 ratio of singlet to triplet excitons according

to spin statistics.[150] The excitons then return to their ground state through either light emission (electroluminescence) or non-radiative processes that produce heat. The color of the emitted light is determined by the energy gap between the HOMO and LUMO of the emissive material.[150]

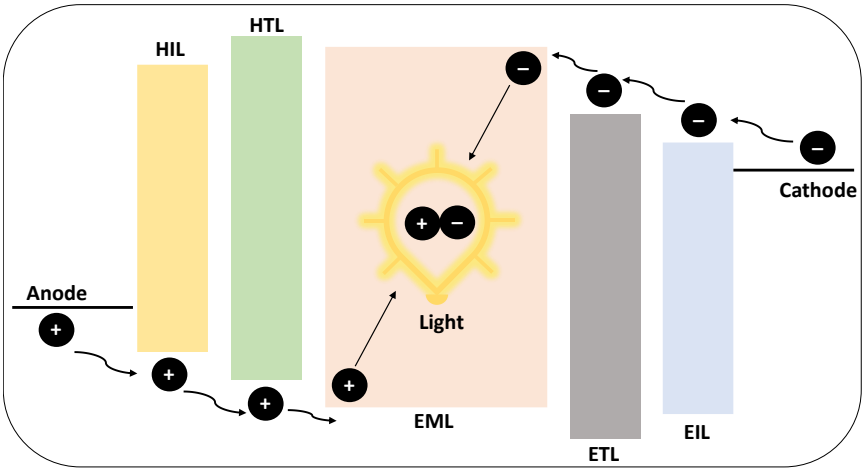

Figure 1.22. Schematic illustration of the working principle of OLED.

For efficient electroluminescence, recombination of charges should occur in the center of the emissive layer. Achieving this requires balanced and high charge mobility. If charge mobility is unequal, recombination may happen near the electrodes, causing exciton quenching and reduced efficiency. Although single-layer OLEDs generally struggle with efficiency, a notable exception is a recent study from the Max Planck Institute for Polymer Research, which developed a single-layer OLED with a high power efficiency of 82 lm/W at 1000 Cd/m^2.[151] Given the challenges in balancing charge injection and mobility, multilayer OLEDs were introduced to improve upon the limitations of single-layer devices.

1.6.2 Device Architecture and Fabrication

Since their inception, small-molecule organic light-emitting diodes (SMOLEDs) have evolved from simple monolayer designs to complex multilayer structures, often comprising 7 to 9 layers.[152] Each layer serves a specific role: the hole-injecting layer (HIL),

hole transport layer (HTL), hole-blocking layer (HBL), and electron transport layer (ETL) (**Figure 1.23**).[153] Tang and his team were pioneers in demonstrating that adding an HTL could significantly enhance the performance of monolayer devices.[140] To further boost efficiency, additional buffer layers, such as ETLs and HBLs, were introduced between the anode and HTL, and an interlayer between the cathode and ETL was also implemented.[153-157] However, increasing the number of layers often results in higher driving voltages for OLEDs and shorter device lifetimes due to higher driving currents. To address this, chemical doping was introduced. For example, Huang *et al.*, reported a device featuring an emission layer sandwiched between p-type doped HTL and n-type doped ETL, which showed high brightness and efficiency at very low operating voltages.[158] More recent advancements include tandem OLED architectures, which consist of multiple emission layers stacked vertically and connected by interconnector layers (ILs). These interconnector layers are essential for device performance as they facilitate charge generation and ensure smooth current flow between units.[159-161] When a voltage is applied, electrons and holes are generated from the interconnector layer and injected into the neighboring ETL and HTL, respectively, where they recombine and emit light. Typical ILs include electrically doped organic semiconductors, ultrathin metal layers, transparent conductive oxides, or transition metal oxides.[162, 163]

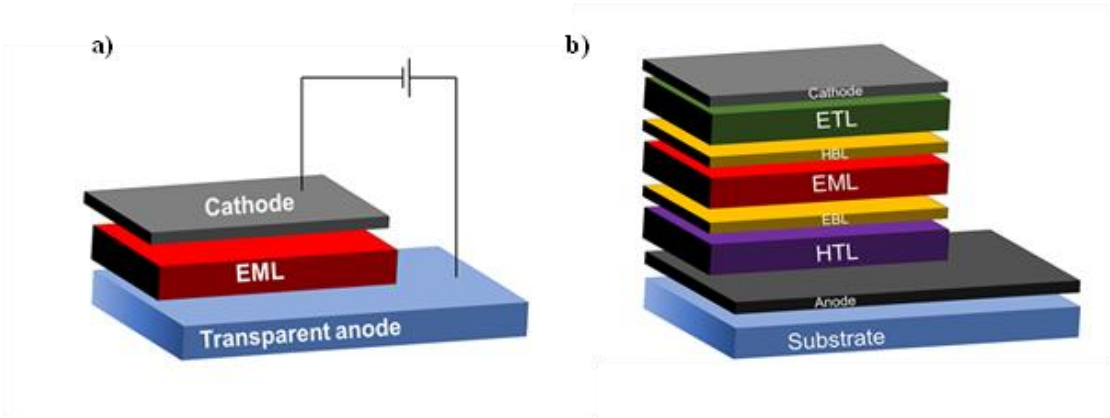

Figure 1.23. General structures of a) single layer OLED and b) multilayer OLED.

A significant advantage of tandem OLED is the ability to achieve the same brightness as single devices while operating at half the current density, leading to improved stability and prolonged lifespan. This design also reduces color shifts compared to conventional single-unit devices. OLEDs can be fabricated using two main methods: (i) thermal evaporation in a high vacuum, which provides high efficiency and precise control over deposition and layer thickness but is costly due to significant organic material waste (70-80%), and (ii) solution-processing techniques, which are more cost-effective and suitable for large-scale manufacturing but face challenges such as solubility issues, layer damage during coating, and defects affecting device efficiency.[164-167]

1.6.3. Device Lifetime

A key challenge for OLED technology is ensuring device stability and longevity, particularly due to the uneven aging of primary colors, where the efficiency of different colored pixels degrades at different rates. The lifetime of an OLED can be categorized into two types: shelf life and operational lifetime.[168] Shelf life refers to the duration an OLED can be stored before performance deteriorates, while operational lifetime (T_{50}) is the time it takes for the device to reach half its original brightness.[169] Although standardized measurement methods are still lacking, a typical benchmark for display applications is a lifespan exceeding 20,000 hours with a minimum brightness of 100 cd/m².[170] OLED performance and durability are influenced by both intrinsic and extrinsic factors. Intrinsic factors include low thermal stability, instability of the host materials, flawed device design, and diffusion of electrode metals. Extrinsic factors encompass environmental elements like atmospheric oxygen and moisture. Degradation in OLEDs typically leads to reduced luminance over time. In small-molecule OLEDs (SMOLEDs), three primary degradation mechanisms have been identified: (i) dark-spot degradation, (ii) catastrophic failure, and

(iii) intrinsic degradation.[171] Dark-spot degradation is associated with electrode issues and results in non-emissive regions, diminishing device luminance.[172, 173] Catastrophic failure involves defects in the organic layers that can cause electrical shorts and reduced currents. Intrinsic degradation manifests as a gradual decrease in brightness during operation without visible changes in the device's appearance. While the first two types of degradation can be managed by optimizing fabrication processes and encapsulation, intrinsic degradation remains a significant challenge.[174] Researchers are actively working on developing new materials and improved encapsulation and fabrication methods to address these issues.

1.6.4. Device Efficiency

In evaluating OLED technology, key metrics of efficiency include: (i) quantum efficiency (QE), (ii) current efficiency (CE/η_L), and (iii) luminous efficiency (η_P) or power efficiency (PE). Quantum Efficiency encompasses two main parameters: external quantum efficiency (EQE) and internal quantum efficiency (IQE). EQE represents the ratio of emitted photons to injected charges and is calculated as per Equation (3).[175]

$$\eta_{ext} = \eta_r \chi \phi \eta_{ext} = \frac{\eta_{int}}{\eta_{out}} \qquad \text{Equation (3)}$$

where, η_r is the probability of recombination of holes and electrons into excitons. For triplet emitters, this combination can approach 100%, as singlet excited states (25%) can convert to the lowest triplet state via intersystem crossing (ISC), making the probability close to 1 when charge balance is maintained. Φ is the photoluminescence quantum yield (PLQY), which can be nearly 100% in well-chosen doped systems.[176] χ represents the likelihood of radiative decay, while η_{out} is the light out-coupling efficiency (OCE), which indicates the fraction of photons escaping the device. IQE and operational voltage depend on the materials and device design, whereas OCE is affected by total internal reflection (TIR).

Typically, OCE is less than 20%, as estimated by $\eta_{out} = 1/ (2n^2)$, where n is the refractive index of the emitting material.[177, 178] According to classical ray optics, about 70% of photons are trapped inside the OLED, with 50-60% remaining within the device due to variations in refractive indices of the organic materials, and 20-30% lost to TIR at the glass-air interface.[179] Consequently, experimentally determined EQE values have generally been limited to under 30% without additional out-coupling components. Efforts to enhance EQE include the integration of microcavities, the use of specially shaped substrates, index-matching mediums, and controlling molecular dipole orientations in the layers.[180-186]

Current efficiency (η_L) is defined as the ratio of luminance (L) to the current density (J) applied to the OLED. Luminous efficiency (η_P) is the ratio of optical output to electrical input, calculated as per Equation (4):

$$\eta_p = \frac{L\pi}{fV} = \frac{\eta_L \pi}{V} \qquad \text{Equation (4)}$$

where, V represents the operating voltage. Therefore, high luminous efficiency in devices requires, achieving a high quantum efficiency (or current efficiency) with a low operating voltage. The efficiency of η_L and η_P is influenced by the eye's photopic response, which peaks in the green spectrum. Consequently, even with equivalent quantum efficiency and voltage, current efficiency or luminous efficiency tends to be lower in the blue and red regions of the spectrum compared to green.

1.6.5. Phosphorescent Materials as Emitting Layer for OLED Application

The initial generation of OLEDs utilized fluorescent materials with singlet emitters, where the internal quantum efficiency (IQE) is limited to 25% due to spin statistics. In contrast, phosphorescent OLEDs (PHOLEDs) can achieve a theoretical IQE of 100% by harnessing both singlet 25% excitons and 75% triplet excitons.[187] However, the

phosphorescent nature of these materials involves long-lived triplet states with extended lifetimes, typically in the microsecond range. This can lead to triplet-triplet annihilation (TTA) and cause excitons to diffuse over long distances (greater than 100 nm), which increases the chance of exciton quenching in neighboring layers.[186] To mitigate these issues, it is beneficial to dilute phosphorescent emitters in host matrices.

In PHOLEDs, the operation involves injecting holes and electrons into the doped emission layer (EML). The emission from the dopant in these host-guest systems can occur via one of three mechanisms: (i) the singlet exciton is transferred to the phosphor via Förster or Dexter energy transfer (ET), converted to triplet excitons through ISC, and then emitted as phosphorescence; (ii) triplet excitons generated in the host are transferred to the phosphor via Dexter ET and then radiatively decay; or (iii) electrons and holes recombine on the phosphorescent guest molecules, generating triplet excitons that relax to the ground state through charge trapping in the phosphors, resulting in phosphorescence (**Figure 1.24**).[188] Förster ET is a rapid process (10^{-12} s) effective over long distances (up to 10 nm) requiring significant overlap between the host's emission and the dopant's absorption spectra. Dexter ET, on the other hand, involves electron exchange interactions that require orbital overlap and operate over shorter distances (1.5 nm - 2.0 nm). This process also requires energy matching between the excitons on the host and the dopant. Dexter ET typically dominates in PHOLEDs.[188]

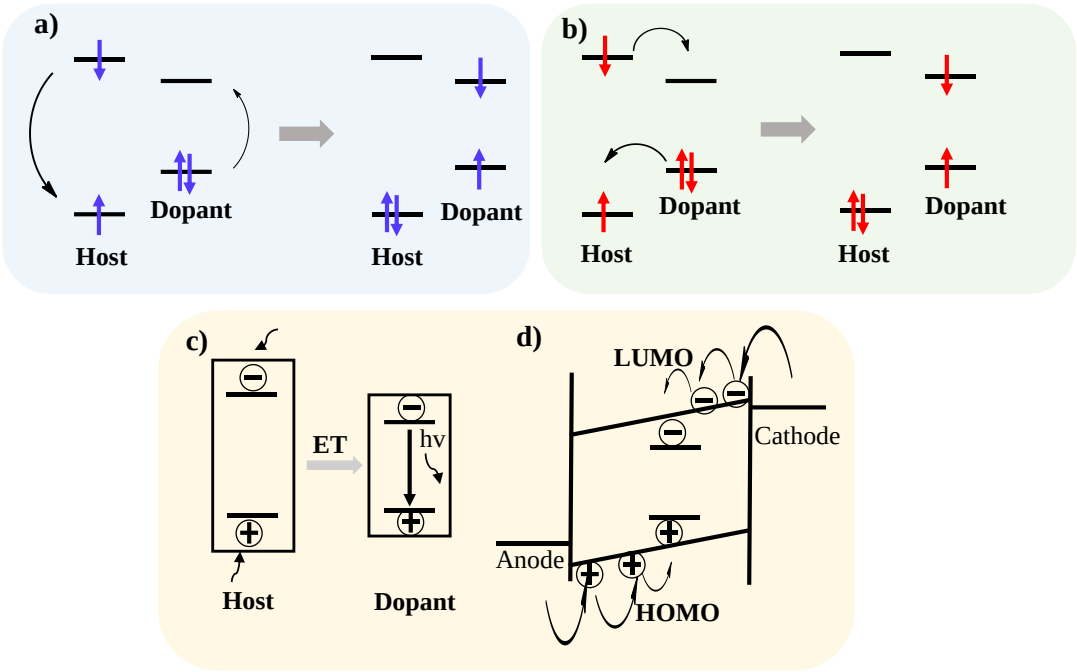

Figure 1.24. (a) Schematic representation of Forster energy transfer; (b) Schematic representation of Dexter energy transfer; (c) Energy transfer in host-dopant systems and (d) Charge trapping for dopant emission in host-dopant system. Figure adapted from reference 52.

The phosphorescent emitter plays a critical role in PHOLEDs, impacting emission energy and electroluminescence (EL) performance. ***Ideal phosphorescent emitters should have short phosphorescence lifetimes to minimize TTA, high phosphorescence quantum yields for efficient light emission, reversible redox properties for stability during charge injection, and good stability overall to enhance device lifespan.*** The color and purity of emission from phosphorescent emitters are also crucial. The emission color is governed by the triplet state energy of the emitter, whereas the purity of the color is affected by the morphology of the film. Film aggregation and phase separation can reduce color purity and may lead to unintended emission colors.[189]

1.6.6. Iridium(III) Complexes for OLED Application

Iridium(III) complexes have garnered significant interest as phosphorescent emitters due to several advantageous properties: their robust chemical and thermal stability, potential for nearly 100% photoluminescence quantum yield (PLQY), relatively short triplet lifetimes, and color tunability. A large library of iridium complexes has been reported as an emitting layer for OLED over the years. Initially, the green-emitting homoleptic complex fac-tris(2-phenylpyridine)iridium(III) [$Ir(ppy)_3$] (**complex 1**), developed by M. E. Thompson and his team, has been extensively studied for its excellent electroluminescent properties (**Figure 1.25**).[5] It exhibited a solution PLQY of 40 ±4%, and a photoluminescence lifetime of approximately 1 μs for $Ir(ppy)_3$, when doped into 4,4'-N,N'-dicarbazole-biphenyl (CBP). Further, it showed an external quantum efficiency (EQE) of 8.0% and a power efficiency of 31 lm/W. Subsequent studies revealed that the PLQY of $Ir(ppy)_3$ could reach about 100%, suggesting that earlier measurements might have been conducted on a non-deoxygenated solution.[190]

Following Thompson's work, Adachi *et al.*, introduced a green-emitting heteroleptic complex, bis(2-phenylpyridine)iridium(III) acetylacetonate $Ir(ppy)_2(acac)$ (**complex 2**) (**Figure 1.25**).[191] This complex, when doped into NTAZ [3-phenyl-4-(1'-naphthyl)-5-phenyl-1,2,4-triazole], achieved an EQE of approximately 15% and a luminous efficiency of around 40 lm/W due to the increased outcoupling efficiency from the perpendicular dipole orientation of the anisotropic emissive chromophore. Further optimization in a bipolar host, m-CF-PhCz [7-(3-(9H-carbazole-9-yl)phenyl)-9,9-dimethyl-9H-fluorene-2-carbonitrile], enhanced the EQE to 20%, attributed to improved charge balance.[192] J.J. Kim and colleagues demonstrated a high-efficiency OLED using $Ir(ppy)_2(acac)$ (**complex 2**) in an exciplex-forming co-host system of TCTA [4,4′,4″-tri(N-

carbazolyl)triphenylamine] and B3PYMPM [4,6-bis(3,5-di(pyridin-3-yl)phenyl)-2-methylpyrimidine], achieving an EQE of 29.1%. This device exhibited minimal efficiency roll-off with increasing current density, indicating excellent electron-hole balance.[193]

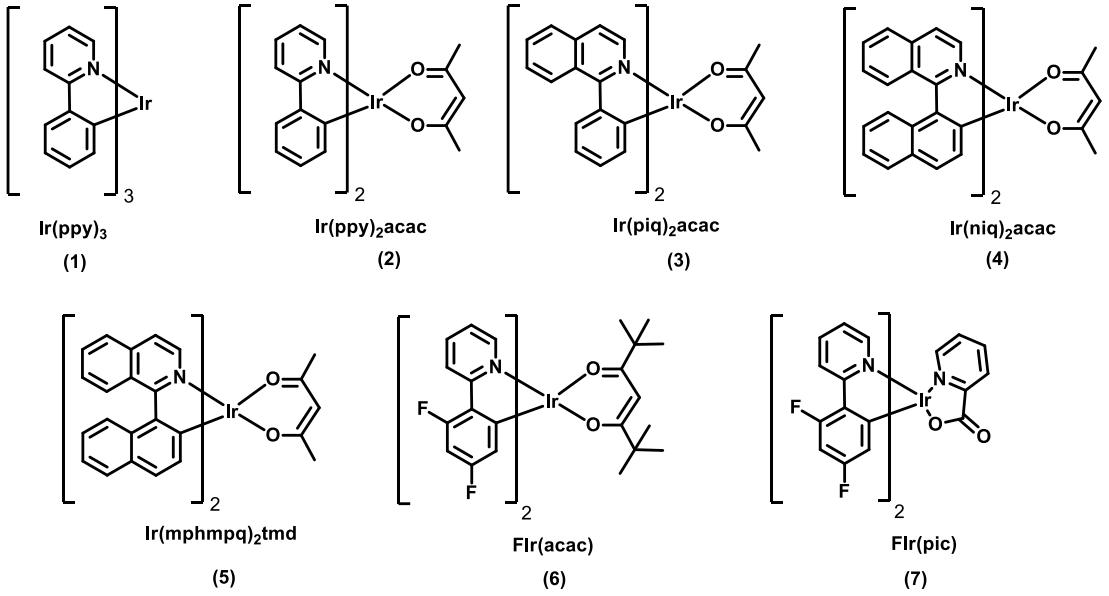

Figure 1.25. Examples of cyclometalated iridium(III) complexes.

The emission wavelength of iridium(III) complexes can be tuned by modifying the cyclometalating ligands, which affects the HOMO and LUMO energy gaps. In these complexes, the LUMO is generally located on the π orbitals of the ligand, while the HOMO comprises both ligand π orbitals and Ir-d orbitals. For example, the emission maxima of $Ir(ppy)_2(acac)$ (**complex 2**), bis(1-phenylisoquinoline)iridium(III) acetylacetonate $Ir(piq)_2(acac)$ (**complex 3**), and bis(1-(2'-naphthyl)isoquinolinato)iridium(III) acetylacetonate $Ir(niq)_2(acac)$ (**complex 4**) were found to be 520 nm, 622 nm, and 664 nm, respectively (**Figure 1.25**).[194, 195] Extending the conjugation of the C^N ligand by adding an extra phenyl ring reduces the HOMO-LUMO energy gap, resulting in a redshift of emission.[65, 196]

Initially, achieving high efficiency in red phosphorescent emitters was challenging, but recent advancements have improved performance. For instance, the heteroleptic red phosphorescent emitter bis (4-methyl-2-(3,5-dimethylphenyl)quinoline)) Ir(III) (tetramethylheptadionate) $Ir(mphmq)_2(tmd)$ (**complex 5**) (**Figure 1.25**) has demonstrated an EQE of 34.1% with an exciplex-forming co-host system, and a device lifetime (LT_{90}) of 2249 hours at a brightness of 1000 cd/m².[197]

Modifying ligands to introduce electron-withdrawing groups can shift emission colors. For example, in **FIr(acac)** (**complex 6**), the introduction of two fluorine atoms into the ortho-position of the metalated phenyl ring resulted in a 38 nm blue-shift compared to the non-fluorinated $Ir(ppy)_2(acac)$ **(Figure 1.25)**.[198] Replacing the acetylacetonate ligand with pinacolate in FIr(pic) (**complex 6**) achieved an additional 20 nm blue shift, and blending FIr(pic) with a bipolar host, 26DCzPPy [2,6-bis(3-(carbazol-9-yl)phenyl)pyridine], improved the EQE to 24% (**Figure 1.25**). J.J. Kim and his team developed an exciplex-forming co-host system using mCP [N,N′-dicarbazolyl-3,5-benzene] and B3PYMPM with FIr(pic), resulting in an efficient OLED with a maximum EQE of approximately 30% and a current efficiency of 62.2 cd/A.[193]

Hou *et al.*, synthesized the Ir(III) complex **$Ir(ppy)_2$(dipba)**, (with N,N'-diisopropyl benzamidinate(dipba) ligand) which exhibited bright yellow emission with a peak at 543 nm (**Figure 1.26**).[199] The corresponding non-doped PHOLED using this complex achieved excellent performance with a low turn-on voltage of 2.4 V and a power efficiency (PE) of 32.5 lm/W, which remained high at different brightness levels. The superior performance was attributed to the effective charge carrier balance and triplet exciton confinement within the emitting layer. Similarly, Liu *et al.*, replaced the dipba ligand with N,N'-diisopropyl-diisopropylguanidinate (dipig) to create a new iridium complex **$Ir(ppy)_2$(dipig)**, which

emitted at 558 nm with a phosphorescent quantum yield of 43% (**Figure 1.26**).[200] The device incorporating this complex achieved a low turn-on voltage of 2.2 V, a maximum luminance of 96,500 cd/m², and efficiencies over 70 lm/W for PE and 18% for EQE, benefiting from the complex's balanced charge transport capabilities.

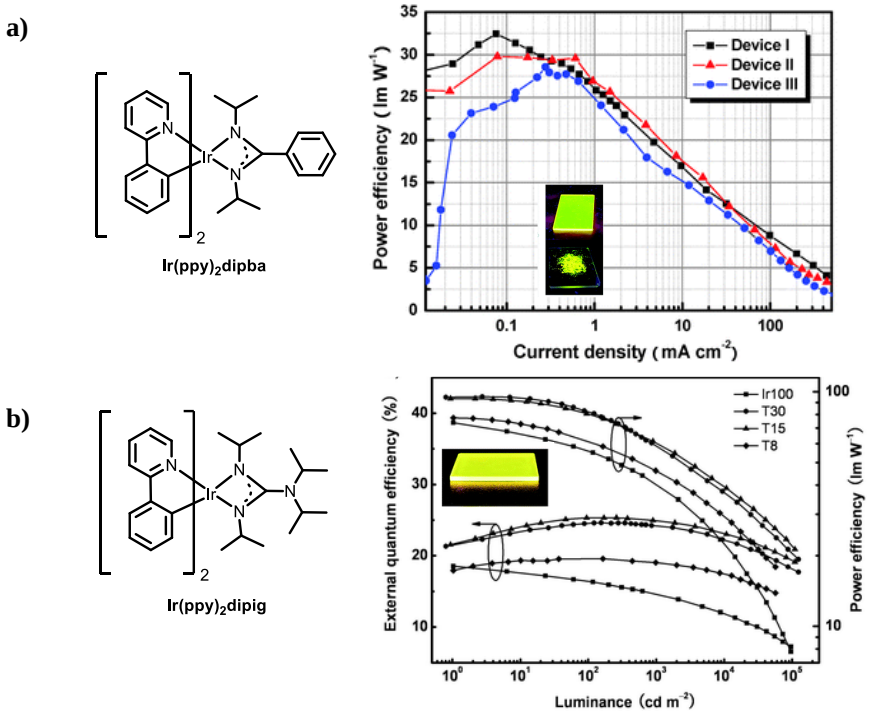

Figure 1.26. (a) Structure of iridium complex **Ir(ppy)₂(dipba)** and the power efficiency – current density curves of device doped with **Ir(ppy)₂(dipba)** and (b)Structure of iridium complex **Ir(ppy)₂(dipig)** and the external quantum efficiency –luminance curve of device doped with **Ir(ppy)₂(dipig)**. Figure adapted from references 199 and 200.

J. J Kim developed deep-blue emitting Iridium(III) complexes (**Ir1, Ir2** and **Ir3**) with horizontally oriented emitting dipoles by modifying the ancillary ligand.[201] The main ligand used is 2′,6′-difluoro-4-(trimethylsilyl)-2,3′-bipyridine (dfpysipy), which contributes to the increased bandgap and results in deep-blue emission due to the incorporation of a trimethylsilyl group at the pyridine and nitrogen at the difluoropyrido group. By adding a methyl group (mpic) to a picolinate (pic) ancillary ligand or substituting the acetate structure of pic with a perfluoromethyl-triazole (fptz) structure, the horizontal

component of the emitting dipoles is enhanced, in the order of mpic (86%) > fptz (77%) > pic (74%). The OLED featuring the Ir complex with the mpic ancillary ligand demonstrated the highest external quantum efficiency of 31.9% among reported blue OLEDs **(Figure 1.27)**.

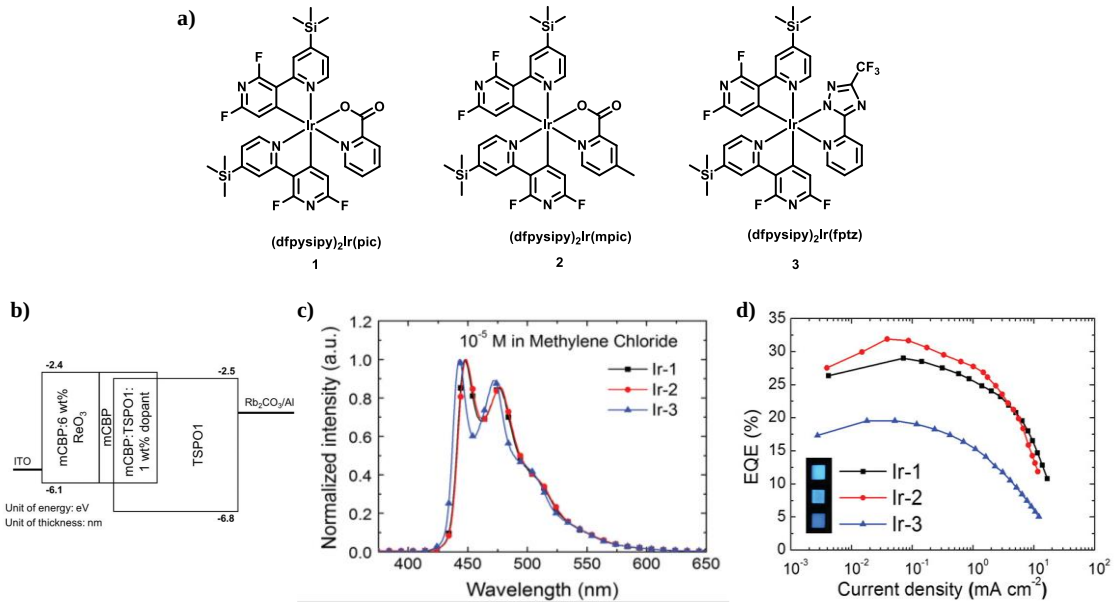

Figure 1.27. (a) Chemical structures of the iridium complexes (**Ir1, Ir2** and **Ir3**); (b) Optimized device structure of deep-blue OLEDs; (c) Current–Voltage–Luminance plot of iridium complex doped OLEDs and (d) EQE of the OLEDs as a function of current density. Figure adapted from reference 201.

1.7. Dinuclear Iridium based Phosphorescent Emitters

The development of mononuclear iridium complexes has been exhaustive, but the exploration of dinuclear Ir(III) systems is relatively limited. Dinuclear iridium complexes are characterized by their relatively large molecular weights, which prevent them from being thermally evaporated to form thin films, necessitating solution processing instead.[202] The majority of research into luminescent Ir(III) complexes has concentrated on vacuum-processed OLEDs, which explains why dinuclear systems have garnered less attention than their monoiridium counterparts. Additionally, the synthesis of dinuclear iridium complexes

is often complicated by the presence of diastereomers, making the synthetic protocols more challenging. Moreover, dinuclear complexes, which incorporate various bridging ligands, typically exhibit photoluminescence quantum yields (PLQYs) that are lower than those of their mononuclear analogs. This has contributed to the prevailing view that dinuclear iridium complexes are inferior emitters, regardless of the intended application.[203-215] Therefore, while mononuclear iridium complexes have been rigorously developed, the fundamental chemistry and practical applications of dinuclear iridium complexes remain underexplored.

Recent careful molecular design has demonstrated that poor photophysical properties are not an intrinsic limitation of dinuclear complexes. For example, in the solid state, highly efficient emission, with aggregation-induced emission and mechanochromic luminescence properties, can be acheived in a dinuclear iridium system via selection of a flexible Schiff base bridging ligand.[216-232] Further, single-molecule white-light emission has been achieved in a dinuclear iridium polymer by using two distinct Ir(III) cores with a bulky conjugated bridging ligand. Williams, Kozhevnikov, and their colleagues have reported a series of dinuclear iridium complexes with nearly 100% photoluminescence quantum yields (PLQYs) in solution, while Zhou and his team have documented solution-processed phosphorescent organic light-emitting devices (OLEDs) with external quantum efficiencies (EQEs) exceeding 10% for dinuclear iridium(III) emitters.[218, 225, 226, 232, 233] The inclusion of a bridging ligand and an additional Ir center introduces unique design possibilities for diiridium complexes, distinguishing them from mono iridium systems. This design approach offers several potential benefits: (i) the ability to explore new structural chemistry by adjusting the bridge flexibility to control aggregation-induced phosphorescent emission (AIPE); (ii) the introduction of intramolecular π–π interactions; (iii) enhanced spin-orbit coupling from multiple metal centers, potentially increasing the

radiative rate constant (*kr*); (iv) an increased chelate effect from the bridging ligand, which could improve complex stability, although this has yet to be demonstrated; (v) improved access to efficient red emitters due to highly conjugated bridging units and (vi) the possibility of dual emission arising from the lowest energy excited states of mixed character.[216, 217, 232, 234-237] Thus, advancing the development of novel dinuclear iridium complexes is of considerable importance.

1.7.1. NΛN- type bridged Iridium(III) Complexes

De Cola *et al.*, introduced two cationic dinuclear iridium(III) complexes, **complex 1** and **2** which employ 2,2'-bipyridine chelates linked by oligo-p-phenylene units (**Figure 1.28**).[238] These complexes were synthesized through on-complex Suzuki dimerization of brominated monoiridium precursors. **Complex 2**, which features the longer linker, achieved the highest solution photoluminescence quantum yield (PLQY) of 17.5% in acetonitrile. The bridging units' extensive conjugation results in the excited state being predominantly localized on the bridge. OLEDs were tested using a straightforward configuration: ITO/PEDOT (100 nm)/PVK: Ir complex (70 nm)/Ba (5 nm)/Al (100 nm) with dopant concentrations of 5 wt% and 30 wt%. However, the devices demonstrated low efficiencies, with the maximum EQE and current CE values of 0.1% and 0.23 cdA^{-1}, respectively.

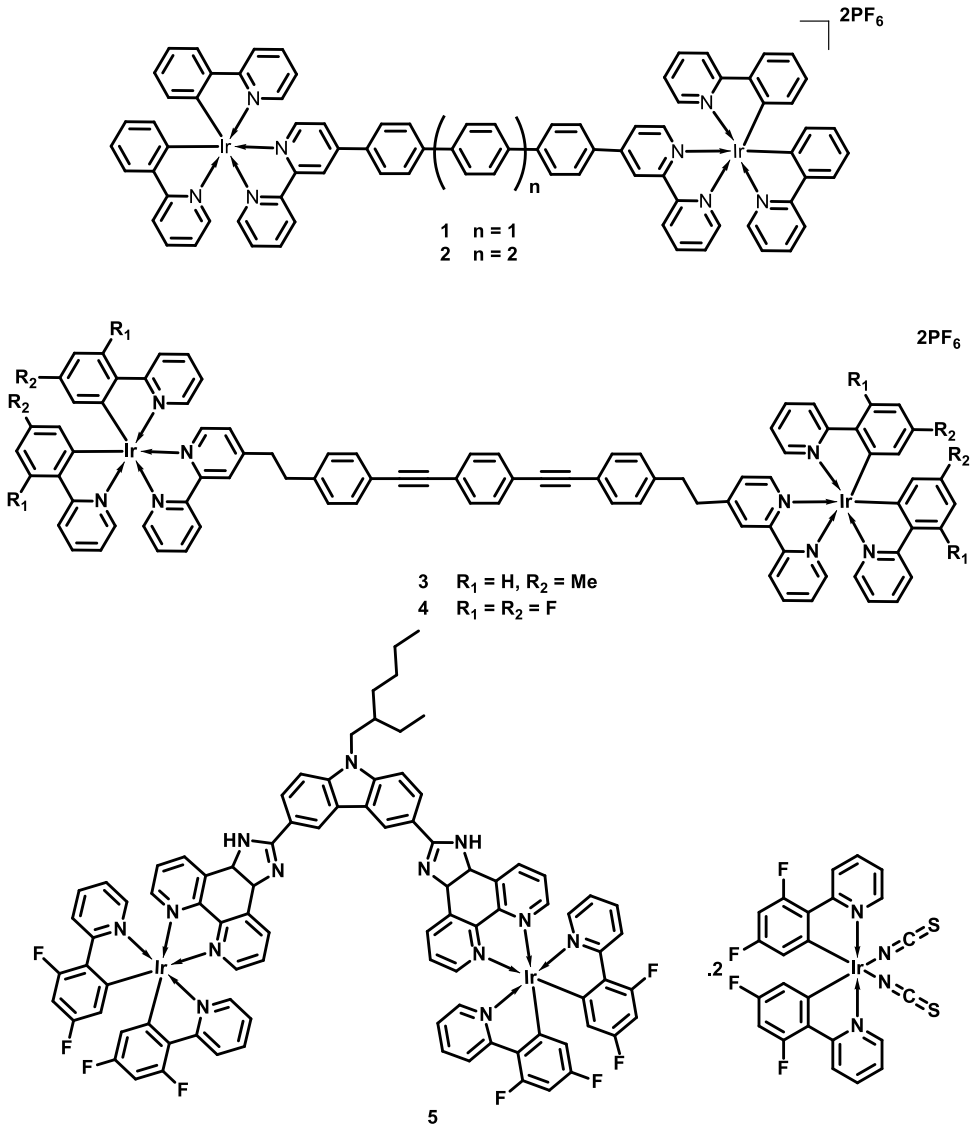

Figure 1.28. Dinuclear iridium complexes with a NΛN-type bridging ligands.

In 2010, **complexes 3** and **4** (**Figure 1.28**) featuring oligo(phenyleneethynylene) and ethylene bridging units were introduced by Henk *et al*.[239] These complexes exhibited photoluminescence quantum yields (PLQYs) of 0.9% and 0.7%, respectively, which are notably low compared to their mononuclear counterparts, which had PLQYs of 14% and 18%. Simple two-layer light-emitting electrochemical cells (LECs) were constructed with the following structure: ITO/PEDOT (100 nm)/**complex 3** or **4**/ionic liquid (IL) with a 1:1 molar ratio (80 nm)/Al. The peak external quantum efficiencies (EQEs) for LECs with **complexes 3** and **4** were 0.16% and 0.13%, respectively. Although these efficiencies are

quite low, the results suggest that self-quenching in the devices was minimized. In 2011, Mayer *et al.*, presented an unusual dinuclear iridium **complex 5** that was non-emissive in solution but exhibited strong red emission in a neat film, achieving a PLQY of 37%.[240] An additional notable feature of this complex was its short lifetime of 48 ns. OLEDs were fabricated using a simple configuration: ITO/PEDOT (40 nm)/PVK (20 nm)/Ir complex/Ca (300 nm)/Al (60 nm). However, the device performance was poor, likely due to self-quenching or energy/electron transfer to the conjugated bridging ligands.

1.7.2. NΛO- type bridged Iridium(III) Complexes

In 2014, Monkman *et al.*, introduced cyclometalated dinuclear iridium(III) complexes bridged by diarylhydrazide ligands, referred to as **complex 6** (**Figure 1.29**).[226] These complexes achieved a photoluminescence quantum yield (PLQY) of 38%. OLEDs were fabricated with the following structure: ITO/PEDOT (50 nm)/ [PVK (40%) **complex 6** (5%)] (90 nm)/Ba (4 nm)/Al (100 nm). The best-performing device used **complex 6** and exhibited peak CE, PE, and EQE values of 37 cdA^{-1}, 14 lmW^{-1}, and 11%, respectively. The same research group also explored the impact of substituents on the bridging and cyclometalating ligands, leading to the design and synthesis of iridium **complexes 7** and **8** (**Figure 1.29**).[219] These complexes showed minimal emission in solution due to non-radiative quenching associated with the mobility of the bridging units. However, when incorporated into a poly(methyl methacrylate) (PMMA) host, they became highly emissive with PLQYs ranging from 42% to 68%. In 2017, Bryce *et al.*, demonstrated two additional dinuclear iridium **complexes**, **9** and **10** (**Figure 1.29**).[241] In a 2-MeTHF (2-Methyltetrahydrofuran) solution, these complexes displayed strong green emission with PLQYs of 73% and 63%, and peak emission wavelengths of 529 nm and 522 nm, respectively. OLEDs with the configuration ITO/PEDOT (45 nm)/PVK (40%) Ir complex

(5%) (70 nm)/TPBi (30 nm)/LiF/Al exhibited bright green electroluminescence with luminance levels exceeding 25,000 cd m^{-2}.

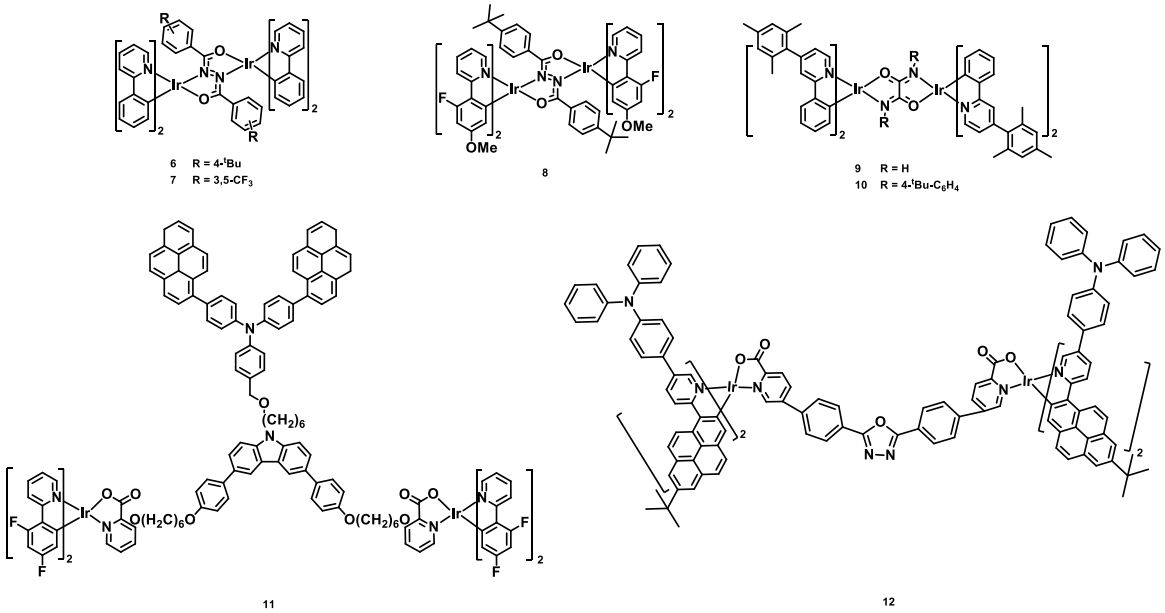

Figure 1.29. Dinuclear Iridium complexes with a NΛO-type bridging ligands.

In 2016, Zhu and colleagues reported iridium based **complex 11** (**Figure 1.29**) as a phosphorescent dopant for white organic light-emitting devices (WOLEDs).[242-244] The solution-processed device featuring **complex 11** emitted near-white light with a CIE color coordinate of (0.29, 0.33). The blue emission was attributed to the 4,4'-di(pyren-1-yl)triphenylamine (DPy(TPA)) group on the bridge, while the remaining emission originated from the rest of the complex. Despite the relatively low device performance, with a maximum luminance of 961 cdm^{-2} and a maximum CE of 0.24 cdA^{-1}, and the non-conjugated nature of the bridging ligand to the Ir centers, this study demonstrates the potential for designing dinuclear iridium systems with dual emission capabilities.

In 2017, Yu Liu and team introduced dinuclear iridium **complex 12** (**Figure 1.29**), successfully developing a novel near-infrared (NIR) emitting complex.[245] They also designed a mono iridium based complex that achieved an EQE of 1.29% at a low current

density of 3.5 $mAcm^{-2}$. In comparison, **complex 12** exhibited a lower EQE of 0.41%, but it showed negligible efficiency roll-off at higher current densities. This work highlighted how a bulky ancillary ligand can effectively prevent molecular aggregation, thereby enhancing device performance.

1.7.3. CΛN- type bridged Iridium(III) Complexes

In 2014, Williams, Kozhevnikov, and colleagues introduced **complexes 13-16** (**Figure 1.30**), which features a cyclometalated bis-tridentate bridge. In a dichloromethane (DCM) solution, this complex showed red emission of 622 nm, a photoluminescence quantum yield (PLQY) of 65%, and excited state lifetimes of τ = 730 ns.[232] Studies comparing a mononuclear analog suggest that the shorter lifetimes are due to the second iridium center. This likely enhances spin-orbit coupling, either because of a stronger heavy atom effect or a reduction in exchange energies, as observed experimentally.

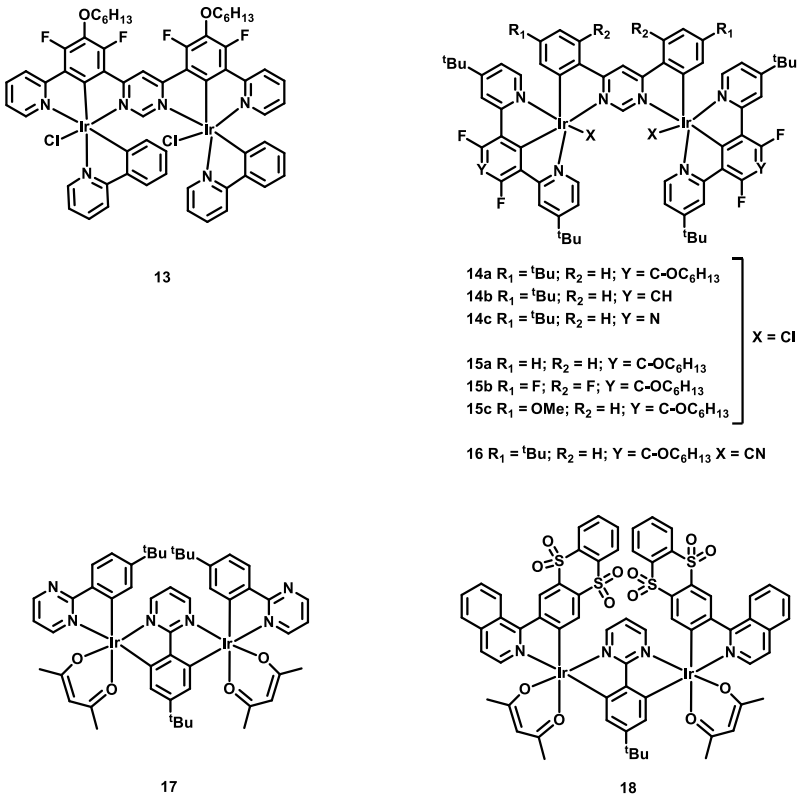

Figure 1.30. Dinuclear iridium complexes with a CΛN-type bridging ligands.

In 2016, Kozhevnikov and colleagues reported a series of non-stereogenic diiridium complexes, which exhibited photoluminescence quantum yields (PLQYs) close to unity and very short phosphorescence lifetimes (τ = 360 ns – 590 ns). [218] These complexes exhibited the highest photophysical performance recorded so far for diiridium complexes in their respective color range. In the same year, Zhou, Wong, and their team introduced a dinuclear iridium(III) complex, designated as **complex 17**, which showed bright phosphorescence with a red shift compared to its mononuclear counterpart **(Figure 1.30)**.[225] OLEDs were constructed with the following structure: ITO/PEDOT (45 nm)/(3.0, 5.0, and 7.0 wt%) complex 17 (30 nm)/TPBi (45 nm)/LiF (1:100 nm). The device using **complex 17** at 5 wt% achieved an external quantum efficiency (EQE) of 14.4%, a current efficiency (CE) of 27.2 cdA^{-1}, and a power efficiency (PE) of 19.5 lmW^{-1}, which are among the highest efficiencies reported for dinuclear iridium(III) complex OLEDs. In 2019, Zhaoxin Wu and colleagues introduced a novel neutral iridium complex **complex 18**, which exhibited a PLQY of 78% and a lifetime of 0.24 μs (**Figure 1.30**).[246] The OLEDs based on this complex were fabricated with the configuration: ITO/PEDOT (45 nm)/4 wt% iridium complex (30 nm)/TPBI (45 nm)/LiF (1 nm)/Al (100 nm). The relatively low solubility of **complex 18** led to a low doping concentration, resulting in insufficient energy transfer, particularly at high current densities, and causing significant efficiency roll-off. Nevertheless, the device with **complex 18** demonstrated deep-red emission with CIE coordinates of approximately (0.69, 0.30), which closely matches the NTSC-recommended standard red CIE coordinates of (0.67, 0.33). This indicates the potential of using such dinuclear Ir(III) complex frameworks for developing deep-red emitters. The device based on **complex 18** achieved a peak EQE of 18%, showing promise for future research with these types of complexes.

1.8. Objectives and Methodologies for the Present Investigation

Continuous efforts are being made to enrich the iridium complexes by exploring new molecular design and improving their properties such as photoluminescence quantum yield, excited state lifetime, colour purity and stability. Even though a wide range of mononuclear iridium complexes were reported for various applications, the properties of di/multi-nuclear iridium complexes remain less explored. The synthetic difficulties of dinuclear iridium complexes may be a reason for them being initially overlooked. However, studies on di/multi-nuclear iridium complexes used in optoelectronic applications have since highlighted their advantages over monomers. In this context, development of iridium complexes with multiple metal centres pose an enormous opportunity. Typically, multiple metal centres are expected to enhance spin-orbit coupling (SOC) in di/multi-nuclear iridium complexes, resulting in enhanced luminescence quantum yields and ROS generation. The inclusion of an extra Ir(III) metal centre can promote effective intersystem crossing (ISC) and result in a high population of the triplet excited states. Furthermore, the right selection of cyclometalating and bridging ligands aid the iridium based dinuclear derivatives to outperform the respective monomer systems. The main objectives of the current thesis include the design and development of new phosphorescent di-nuclear iridium complexes, investigation of their photophysical properties and demonstration of their potential use in PDT and optoelectronic applications.

1.9. References

1. Das, K. S. B. M., Design and Development of Novel Phosphorescent Iridium (III) Complexes for Lighting and Sensing Applications. **2016**.

2. Chou, P.-T.; Chi, Y.; Chung, M.-W.; Lin, C.-C., Harvesting luminescence via harnessing the photophysical properties of transition metal complexes. *Coordination Chemistry Reviews* **2011,** *255* (21), 2653-2665.

3. Huang, K.; Wu, H.; Shi, M.; Li, F.; Yi, T.; Huang, C., Reply to comment on 'aggregation-induced phosphorescent emission (AIPE) of iridium(iii) complexes': origin of the enhanced phosphorescence. *Chemical Communications* **2009,** (10), 1243-1245.

4. Longhi, E.; De Cola, L., Iridium(III) Complexes for OLED Application. In *Iridium(III) in Optoelectronic and Photonics Applications*, 2017; pp 205-274.

5. Baldo, M. A.; Lamansky, S.; Burrows, P. E.; Thompson, M. E.; Forrest, S. R., Very high-efficiency green organic light-emitting devices based on electrophosphorescence. *Applied Physics Letters* **1999,** *75* (1), 4-6.

6. Chi, Y.; Chou, P.-T., Transition-metal phosphors with cyclometalating ligands: fundamentals and applications. *Chemical Society Reviews* **2010,** *39* (2), 638-655.

7. Fan, C.; Yang, C., Yellow/orange emissive heavy-metal complexes as phosphors in monochromatic and white organic light-emitting devices. *Chemical Society Reviews* **2014,** *43* (17), 6439-6469.

8. Wagenknecht, P. S.; Ford, P. C., Metal centered ligand field excited states: Their roles in the design and performance of transition metal based photochemical molecular devices. *Coordination Chemistry Reviews* **2011,** *255* (5), 591-616.

9. Wong, W.-Y.; Zhou, G.-J.; Yu, X.-M.; Kwok, H.-S.; Lin, Z., Efficient Organic Light-Emitting Diodes based on Sublimable Charged Iridium Phosphorescent Emitters. **2007,** *17* (2), 315-323.

10. Wong, W.-Y.; Zhou, G.-J.; Yu, X.-M.; Kwok, H.-S.; Tang, B.-Z., Amorphous Diphenylaminofluorene-Functionalized Iridium Complexes for High-Efficiency Electrophosphorescent Light-Emitting Diodes. **2006,** *16* (6), 838-846.

11. Yang, C.-H.; Su, W.-L.; Fang, K.-H.; Wang, S.-P.; Sun, I. W., Studies of the 5'-Substituted Phenylisoquinoline-Based Iridium Complexes Using Density Functional Theory. *Organometallics* **2006,** *25* (19), 4514-4519.

12. Zanoni, K. P. S.; Coppo, R. L.; Amaral, R. C.; Murakami Iha, N. Y., Ir(iii) complexes designed for light-emitting devices: beyond the luminescence color array. *Dalton Transactions* **2015,** *44* (33), 14559-14573.

13. Zhou, G.; Wong, W.-Y.; Yao, B.; Xie, Z.; Wang, L., Triphenylamine-Dendronized Pure Red Iridium Phosphors with Superior OLED Efficiency/Color Purity Trade-Offs. **2007,** *46* (7), 1149-1151.

14. Flamigni, L.; Barbieri, A.; Sabatini, C.; Ventura, B.; Barigelletti, F., Photochemistry and Photophysics of Coordination Compounds: Iridium. In *Photochemistry and Photophysics of Coordination Compounds II*, Balzani, V.; Campagna, S., Eds. Springer Berlin Heidelberg: Berlin, Heidelberg, 2007; pp 143-203.

15. Zhao, Q.; Li, F.; Liu, S.; Yu, M.; Liu, Z.; Yi, T.; Huang, C., Highly Selective Phosphorescent Chemosensor for Fluoride Based on an Iridium(III) Complex Containing Arylborane Units. *Inorganic Chemistry* **2008,** *47* (20), 9256-9264.

16. Zhang-Jin, L.; Tong-Jun, S. H. U.; Bao-Xiu, M. I.; Zhi-Qiang, G. A. O.; Qu-Li, F. A. N.; Wei, H., Molecular Iridium(III) Complexes and Their Corresponding Electrophosphorescent Devices. *Progress in Chemistry* **2011,** *23* (8), 1627-1643.

17. You, Y.; Park, S. Y., Inter-Ligand Energy Transfer and Related Emission Change in the Cyclometalated Heteroleptic Iridium Complex: Facile and Efficient Color Tuning over the Whole Visible Range by the Ancillary Ligand Structure. *Journal of the American Chemical Society* **2005,** *127* (36), 12438-12439.

18. Duan, H.-S.; Chou, P.-T.; Hsu, C.-C.; Hung, J.-Y.; Chi, Y., Photophysics of Heteroleptic Iridium(III) Complexes Of Current Interest; a Closer Look on Relaxation Dynamics. *Inorganic Chemistry* **2009,** *48* (14), 6501-6508.

19. Reddy, M. L. P., *JPhCPhB C Photochemistry Review*. 2018.

20. Zhao, Q.; Huang, C.; Li, F., Phosphorescent heavy-metal complexes for bioimaging. *Chemical Society Reviews* **2011,** *40* (5), 2508-2524.

21. Baggaley, E.; Weinstein, J. A.; Williams, J. A. G., Lighting the way to see inside the live cell with luminescent transition metal complexes. *Coordination Chemistry Reviews* **2012,** *256* (15), 1762-1785.

22. Guerchais, V.; Fillaut, J.-L., Sensory luminescent iridium(III) and platinum(II) complexes for cation recognition. *Coordination Chemistry Reviews* **2011,** *255*, 2448–2457.

23. Reddy, M. L. P.; Bejoymohandas, K. S., Evolution of 2, 3′-bipyridine class of cyclometalating ligands as efficient phosphorescent iridium(III) emitters for applications in organic light emitting diodes. *Journal of Photochemistry and Photobiology C: Photochemistry Reviews* **2016,** *29*, 29-47.

24. Li, Y.; Tan, C. P.; Zhang, W.; He, L.; Ji, L. N.; Mao, Z. W., Phosphorescent iridium(III)-bis-N-heterocyclic carbene complexes as mitochondria-targeted theranostic and photodynamic anticancer agents. *Biomaterials* **2015,** *39*, 95-104.

25. Whang, D. R.; Sakai, K.; Park, S. Y., Highly efficient photocatalytic water reduction with robust iridium(III) photosensitizers containing arylsilyl substituents. *Angew Chem Int Ed Engl* **2013,** *52* (44), 11612-11615.

26. Thomsen, J. M.; Huang, D. L.; Crabtree, R. H.; Brudvig, G. W., Iridium-based complexes for water oxidation. *Dalton Transactions* **2015,** *44* (28), 12452-12472.

27. DiSalle, B. F.; Bernhard, S., Orchestrated Photocatalytic Water Reduction Using Surface-Adsorbing Iridium Photosensitizers. *Journal of the American Chemical Society* **2011,** *133* (31), 11819-11821.

28. He, L.; Tan, C.-P.; Ye, R.-R.; Zhao, Y.-Z.; Liu, Y.-H.; Zhao, Q.; Ji, L.-N.; Mao, Z.-W., Theranostic Iridium(III) Complexes as One- and Two-Photon Phosphorescent Trackers to Monitor Autophagic Lysosomes. **2014,** *53* (45), 12137-12141.

29. Zhou, J.; Liu, Q.; Feng, W.; Sun, Y.; Li, F., Upconversion Luminescent Materials: Advances and Applications. *Chemical Reviews* **2015,** *115* (1), 395-465.

30. Le Bozec, H.; Guerchais, V., Photochromic bipyridyl metal complexes: Photoregulation of the nonlinear optical and/or luminescent properties. *Comptes Rendus Chimie* **2013,** *16* (12), 1172-1182.

31. Liu, Z.; He, W.; Guo, Z., Metal coordination in photoluminescent sensing. *Chemical Society Reviews* **2013,** *42* (4), 1568-1600.

32. Bejoymohandas, K. S.; Kumar, A.; Sreenadh, S.; Varathan, E.; Varughese, S.; Subramanian, V.; Reddy, M. L. P., A Highly Selective Chemosensor for Cyanide Derived from a Formyl-Functionalized Phosphorescent Iridium(III) Complex. *Inorganic Chemistry* **2016,** *55* (7), 3448-3461.

33. Bejoymohandas, K. S.; George, T. M.; Bhattacharya, S.; Natarajan, S.; Reddy, M. L. P., AIPE-active green phosphorescent iridium(iii) complex impregnated test strips for the vapor-phase detection of 2,4,6-trinitrotoluene (TNT). *Journal of Materials Chemistry C* **2014,** *2* (3), 515-523.

34. Lu, L.; Zhong, H.-J.; He, B.; Leung, C.-H.; Ma, D.-L., Development of a luminescent G-quadruplex-selective iridium(III) complex for the label-free detection of adenosine. *Scientific Reports* **2016,** *6* (1), 19368.

35. Liu, Z.; Sadler, P. J., Organoiridium Complexes: Anticancer Agents and Catalysts. *Accounts of Chemical Research* **2014,** *47* (4), 1174-1185.

36. Ma, D.-L.; Chan, D. S.-H.; Leung, C.-H., Group 9 Organometallic Compounds for Therapeutic and Bioanalytical Applications. *Accounts of Chemical Research* **2014,** *47* (12), 3614-3631.

37. Shao, F.; Elias, B.; Lu, W.; Barton, J. K., Synthesis and Characterization of Iridium(III) Cyclometalated Complexes with Oligonucleotides: Insights into Redox Reactions with DNA. *Inorganic Chemistry* **2007,** *46* (24), 10187-10199.

38. Shao, F.; Barton, J. K., Long-Range Electron and Hole Transport through DNA with Tethered Cyclometalated Iridium(III) Complexes. *Journal of the American Chemical Society* **2007,** *129* (47), 14733-14738.

39. Sun, J.; Zhao, J.; Guo, H.; Wu, W., Visible-light harvesting iridium complexes as singlet oxygen sensitizers for photooxidation of 1,5-dihydroxynaphthalene. *Chemical Communications* **2012,** *48* (35), 4169-4171.

40. Ruggi, A.; van Leeuwen, F. W. B.; Velders, A. H., Interaction of dioxygen with the electronic excited state of Ir(III) and Ru(II) complexes: Principles and biomedical applications. *Coordination Chemistry Reviews* **2011,** *255* (21), 2542-2554.

41. Schulz, G. L.; Holdcroft, S., Conjugated Polymers Bearing Iridium Complexes for Triplet Photovoltaic Devices. *Chemistry of Materials* **2008,** *20* (16), 5351-5355.

42. Yang, C.-M.; Wu, C.-H.; Liao, H.-H.; Lai, K.-Y.; Cheng, H.-P.; Horng, S.-f.; Meng, H.-F.; Shy, J. T., Enhanced photovoltaic response of organic solar cell by singlet-to-triplet exciton conversion. *Applied Physics Letters* **2007,** *90*, 133509-133509.

43. Liu, Z.; Qi, W.; Xu, G., Recent advances in electrochemiluminescence. *Chemical Society Reviews* **2015,** *44* (10), 3117-3142.

44. Lakowicz, J. R., Introduction to Fluorescence. In *Principles of Fluorescence Spectroscopy*, Lakowicz, J. R., Ed. Springer US: Boston, MA, 1999; pp 1-23.

45. Schweizer, T.; Kubach, H.; Koch, T., Investigations to characterize the interactions of light radiation, engine operating media and fluorescence tracers for the use of qualitative light-induced fluorescence in engine systems. *Automotive and Engine Technology* **2021,** *6*, 1-13.

46. Ebata, T., Time-Resolved Study on Vibrational Energy Relaxation of Aromatic Molecules and Their Clusters in the Gas Phase. In *Physical Chemistry of Cold Gas-Phase Functional Molecules and Clusters*, Ebata, T.; Fujii, M., Eds. Springer Singapore: Singapore, 2019; pp 257-286.

47. Yang, X.; Zhou, G.; Wong, W.-Y., Functionalization of phosphorescent emitters and their host materials by main-group elements for phosphorescent organic light-emitting devices. *Chemical Society Reviews* **2015,** *44* (23), 8484-8575.

48. Kasha, M., Collisional Perturbation of Spin-Orbital Coupling and the Mechanism of Fluorescence Quenching. A Visual Demonstration of the Perturbation. *The Journal of Chemical Physics* **1952,** *20* (1), 71-74.

49. Karplus, M., Contact Electron-Spin Coupling of Nuclear Magnetic Moments. *The Journal of Chemical Physics* **1959,** *30* (1), 11-15.

50. Lamansky, S.; Djurovich, P.; Murphy, D.; Abdel-Razzaq, F.; Lee, H.-E.; Adachi, C.; Burrows, P. E.; Forrest, S. R.; Thompson, M. E., Highly Phosphorescent Bis-Cyclometalated Iridium Complexes: Synthesis, Photophysical Characterization, and Use in Organic Light Emitting Diodes. *Journal of the American Chemical Society* **2001,** *123* (18), 4304-4312.

51. Yarnell, J. E.; De La Torre, P.; Castellano, F. N., Efficient Phosphorescence from Naphthalenebenzimidizole-Coordinated Iridium(III) Chromophores. **2017,** *2017* (44), 5238-5245.

52. Vilela, R. R. D. C., Luminescent host-guest systems based on coordination compounds: synthesis, characterization, and applications.

. *Thesis* **2023**.

53. Eschrig, M., Spin-polarized supercurrents for spintronics: A review of current progress. *Reports on progress in physics. Physical Society (Great Britain)* **2015,** *78*.

54. Sekine, C.; Tsubata, Y.; Yamada, T.; Kitano, M.; Doi, S., Recent progress of high performance polymer OLED and OPV materials for organic printed electronics. *Science and Technology of Advanced Materials* **2014,** *15*, 034203.

55. Flamigni, L.; Barbieri, A.; Sabatini, C.; Ventura, B.; Barigelletti, F., Photochemistry and Photophysics of Coordination Compounds: Iridium. 2007; Vol. 281, pp 143-203.

56. Moore, S. A.; Davies, D. L.; Karim, M. M.; Nagle, J. K.; Wolf, M. O.; Patrick, B. O., Photophysical behaviour of cyclometalated iridium(iii) complexes with phosphino(terthiophene) ligands. *Dalton Transactions* **2013,** *42* (34), 12354-12363.

57. Zanoni, K. P. S.; Ravaro, L. P.; de Camargo, A. S. S., Host–guest luminescent materials based on highly emissive species loaded into versatile sol–gel hosts. *Dalton Transactions* **2018,** *47* (37), 12813-12826.

58. Nonoyama, M., Benzo[h]quinolin-10-yl-N Iridium(III) Complexes. *Bulletin of the Chemical Society of Japan* **2006,** *47* (3), 767-768.

59. Tamayo, A. B.; Alleyne, B. D.; Djurovich, P. I.; Lamansky, S.; Tsyba, I.; Ho, N. N.; Bau, R.; Thompson, M. E., Synthesis and characterization of facial and meridional tris-cyclometalated iridium(III) complexes. *J Am Chem Soc* **2003,** *125* (24), 7377-87.

60. Dedeian, K.; Shi, J.; Shepherd, N.; Forsythe, E.; Morton, D. C., Photophysical and electrochemical properties of heteroleptic tris-cyclometalated iridium(III) complexes. *Inorg Chem* **2005,** *44* (13), 4445-7.

61. Karatsu, T.; Ito, E.; Yagai, S.; Kitamura, A., Radiative and nonradiative processes of meridional and facial isomers of heteroleptic iridium-trischelete complexes. *Chemical Physics Letters* **2006,** *424* (4), 353-357.

62. McDonald, A. R.; Lutz, M.; von Chrzanowski, L. S.; van Klink, G. P. M.; Spek, A. L.; van Koten, G., Probing the mer- to fac-Isomerization of Tris-Cyclometallated Homo- and Heteroleptic (C,N)3 Iridium(III) Complexes. *Inorganic Chemistry* **2008,** *47* (15), 6681-6691.

63. Tsuchiya, K.; Ito, E.; Yagai, S.; Kitamura, A.; Karatsu, T., Chirality in the Photochemical mer→fac Geometrical Isomerization of Tris(1-phenylpyrazolato,N,C2′)iridium(III). **2009,** *2009* (14), 2104-2109.

64. Colombo, M. G.; Brunold, T. C.; Riedener, T.; Guedel, H. U.; Fortsch, M.; Buergi, H.-B., Facial tris cyclometalated rhodium(3+) and iridium(3+) complexes: their synthesis, structure, and optical spectroscopic properties. *Inorganic Chemistry* **1994,** *33* (3), 545-550.

65. Li, J.; Djurovich, P. I.; Alleyne, B. D.; Yousufuddin, M.; Ho, N. N.; Thomas, J. C.; Peters, J. C.; Bau, R.; Thompson, M. E., Synthetic Control of Excited-State Properties in Cyclometalated Ir(III) Complexes Using Ancillary Ligands. *Inorganic Chemistry* **2005,** *44* (6), 1713-1727.

66. Lowry, M. S.; Bernhard, S., Synthetically Tailored Excited States: Phosphorescent, Cyclometalated Iridium(III) Complexes and Their Applications. **2006,** *12* (31), 7970-7977.

67. Ulbricht, C.; Beyer, B.; Friebe, C.; Winter, A.; Schubert, U. S., Recent Developments in the Application of Phosphorescent Iridium(III) Complex Systems. **2009,** *21* (44), 4418-4441.

68. Mao, H.-T.; Li, G.-F.; Shan, G.-G.; Wang, X.-L.; Su, Z.-M., Recent progress in phosphorescent Ir(III) complexes for nondoped organic light-emitting diodes. *Coordination Chemistry Reviews* **2020,** *413*, 213283.

69. Yusoff, A. R. B. M.; Huckaba, A. J.; Nazeeruddin, M. K., Phosphorescent Neutral Iridium (III) Complexes for Organic Light-Emitting Diodes. In *Photoluminescent Materials and Electroluminescent Devices*, Armaroli, N.; Bolink, H. J., Eds. Springer International Publishing: Cham, 2017; pp 111-140.

70. Lo, K. K.-W.; Ng, D. C.-M.; Chung, C.-K., First Examples of Luminescent Cyclometalated Iridium(III) Complexes as Labeling Reagents for Biological Substrates. *Organometallics* **2001,** *20* (24), 4999-5001.

71. Lo, K. K.-W.; Hui, W.-K.; Chung, C.-K.; Tsang, K. H.-K.; Lee, T. K.-M.; Li, C.-K.; Lau, J. S.-Y.; Ng, D. C.-M. J. C. c. r., Luminescent transition metal complex biotin conjugates. **2006,** *250* (13-14), 1724-1736.

72. Stinner, C.; Wightman, M. D.; Kelley, S. O.; Hill, M. G.; Barton, J. K. J. I. c., Synthesis and Spectroelectrochemistry of Ir (bpy)(phen)(phi) 3+, a Tris (heteroleptic) Metallointercalator. **2001,** *40* (20), 5245-5250.

73. Barry, N. P.; Sadler, P. J. J. C. S. R., Dicarba-closo-dodecarborane-containing half-sandwich complexes of ruthenium, osmium, rhodium and iridium: biological relevance and synthetic strategies. **2012,** *41* (8), 3264-3279.

74. Kastl, A.; Wilbuer, A.; Merkel, A. L.; Feng, L.; Di Fazio, P.; Ocker, M.; Meggers, E. J. C. C., Dual anticancer activity in a single compound: visible-light-induced apoptosis by an antiangiogenic iridium complex. **2012,** *48* (13), 1863-1865.

75. Celli, J. P.; Spring, B. Q.; Rizvi, I.; Evans, C. L.; Samkoe, K. S.; Verma, S.; Pogue, B. W.; Hasan, T. J. C. r., Imaging and photodynamic therapy: mechanisms, monitoring, and optimization. **2010,** *110* (5), 2795-2838.

76. Lovell, J. F.; Liu, T. W.; Chen, J.; Zheng, G. J. C. r., Activatable photosensitizers for imaging and therapy. **2010,** *110* (5), 2839-2857.

77. Xu, J.; Gao, J.-Q.; Wei, Q., Combination of Photodynamic Therapy with Radiotherapy for Cancer Treatment. *Journal of Nanomaterials* **2016,** *2016*, 1-7.

78. Shen, Y.; Shuhendler, A. J.; Ye, D.; Xu, J.-J.; Chen, H.-Y. J. C. S. R., Two-photon excitation nanoparticles for photodynamic therapy. **2016,** *45* (24), 6725-6741.

79. V, S. K., Luminescent Probes for Organelle Targeted Imaging, Photodynamic Therapy and Theranostic Applications. *Thesis* **2018**.

80. Neelambaran, N.; Shamjith, S.; Murali, V. P.; Maiti, K. K.; Joseph, J., Exploring a Mitochondria Targeting, Dinuclear Cyclometalated Iridium (III) Complex for Image-Guided Photodynamic Therapy in Triple-Negative Breast Cancer Cells. *ACS Applied Bio Materials* **2023,** *6* (12), 5776-5788.

81. Bevernaegie, R.; Doix, B.; Bastien, E.; Diman, A.; Decottignies, A.; Feron, O.; Elias, B., Exploring the Phototoxicity of Hypoxic Active Iridium(III)-Based Sensitizers in 3D Tumor Spheroids. *Journal of the American Chemical Society* **2019,** *141* (46), 18486-18491.

82. Tavakkoli Yaraki, M.; Liu, B.; Tan, Y. N., Emerging Strategies in Enhancing Singlet Oxygen Generation of Nano-Photosensitizers Toward Advanced Phototherapy. *Nano-Micro Letters* **2022,** *14* (1), 123.

83. Yu, H.; Chen, B.; Huang, H.; He, Z.; Sun, J.; Wang, G.; Gu, X.; Tang, B. Z., AIE-Active Photosensitizers: Manipulation of Reactive Oxygen Species Generation and Applications in Photodynamic Therapy. **2022,** *12* (5), 348.

84. Spring, B. Q.; Rizvi, I.; Xu, N.; Hasan, T. J. P.; sciences, p., The role of photodynamic therapy in overcoming cancer drug resistance. **2015,** *14* (8), 1476-1491.

85. Bottone, M. G.; Santin, G.; Aredia, F.; Bernocchi, G.; Pellicciari, C.; Scovassi, A. I. J. C., Morphological features of organelles during apoptosis: an overview. **2013,** *2* (2), 294-305.

86. Zhou, Z.; Song, J.; Nie, L.; Chen, X., Reactive oxygen species generating systems meeting challenges of photodynamic cancer therapy. *Chemical Society Reviews* **2016,** *45* (23), 6597-6626.

87. Lv, W.; Zhang, Z.; Zhang, K. Y.; Yang, H.; Liu, S.; Xu, A.; Guo, S.; Zhao, Q.; Huang, W. J. A. C. I. E., A mitochondria-targeted photosensitizer showing improved photodynamic therapy effects under hypoxia. **2016,** *55* (34), 9947-9951.

88. McKenzie, L. K.; Bryant, H. E.; Weinstein, J. A., Transition metal complexes as photosensitisers in one- and two-photon photodynamic therapy. *Coordination Chemistry Reviews* **2019,** *379*, 2-29.

89. Zhao, J.; Wu, W.; Sun, J.; Guo, S. J. C. S. R., Triplet photosensitizers: from molecular design to applications. **2013,** *42* (12), 5323-5351.

90. Turro, N. J.; Ramamurthy, V.; Scaiano, J. C., *Principles of Molecular Photochemistry: An Introduction*. University Science Books: 2009.

91. Gorman, A.; Killoran, J.; O'Shea, C.; Kenna, T.; Gallagher, W. M.; O'Shea, D. F. J. J. o. t. A. C. S., In vitro demonstration of the heavy-atom effect for photodynamic therapy. **2004,** *126* (34), 10619-10631.

92. Yogo, T.; Urano, Y.; Ishitsuka, Y.; Maniwa, F.; Nagano, T. J. J. o. t. A. C. S., Highly efficient and photostable photosensitizer based on BODIPY chromophore. **2005,** *127* (35), 12162-12163.

93. Awuah, S. G.; Polreis, J.; Biradar, V.; You, Y. J. O. L., Singlet oxygen generation by novel NIR BODIPY dyes. **2011,** *13* (15), 3884-3887.

94. Abrahamse, H.; Hamblin, Michael R., New photosensitizers for photodynamic therapy. *Biochemical Journal* **2016,** *473* (4), 347-364.

95. Wu, Y.; Li, S.; Chen, Y.; He, W.; Guo, Z., Recent advances in noble metal complex based photodynamic therapy. *Chemical science* **2022,** *13* (18), 5085-5106.

96. Huang, H.; Banerjee, S.; Sadler, P., Recent Advances in the Design of Targeted Iridium(III) Photosensitizers for Photodynamic Therapy. *ChemBioChem* **2018,** *19*.

97. Szymaszek, P.; Tyszka-Czochara, M.; Ortyl, J., Iridium(III) complexes as novel theranostic small molecules for medical diagnostics, precise imaging at a single cell level and targeted anticancer therapy. *European Journal of Medicinal Chemistry* **2024,** *276*, 116648.

98. Stacey, O. J.; Pope, S. J. A., New avenues in the design and potential application of metal complexes for photodynamic therapy. *RSC Advances* **2013,** *3* (48), 25550-25564.

99. Ruggi, A.; van Leeuwen, F. W.; Velders, A. H. J. C. C. R., Interaction of dioxygen with the electronic excited state of Ir (III) and Ru (II) complexes: principles and biomedical applications. **2011,** *255* (21-22), 2542-2554.

100. Djurovich, P. I.; Murphy, D.; Thompson, M. E.; Hernandez, B.; Gao, R.; Hunt, P. L.; Selke, M., Cyclometalated iridium and platinum complexes as singlet oxygen photosensitizers: quantum yields, quenching rates and correlation with electronic structures. *Dalton Transactions* **2007,** (34), 3763-3770.

101. Takizawa, S.-y.; Aboshi, R.; Murata, S. J. P.; Sciences, P., Photooxidation of 1, 5-dihydroxynaphthalene with iridium complexes as singlet oxygen sensitizers. **2011,** *10* (6), 895-903.

102. Hallett, A. J.; White, N.; Wu, W.; Cui, X.; Horton, P. N.; Coles, S. J.; Zhao, J.; Pope, S. J. J. C. C., Enhanced photooxidation sensitizers: the first examples of cyclometalated pyrene complexes of iridium (III). **2012,** *48* (88), 10838-10840.

103. Moromizato, S.; Hisamatsu, Y.; Suzuki, T.; Matsuo, Y.; Abe, R.; Aoki, S., Design and Synthesis of a Luminescent Cyclometalated Iridium(III) Complex Having N,N-Diethylamino Group that Stains Acidic Intracellular Organelles and Induces Cell Death by Photoirradiation. *Inorganic Chemistry* **2012,** *51* (23), 12697-12706.

104. Yu, M.; Zhao, Q.; Shi, L.; Li, F.; Zhou, Z.; Yang, H.; Yi, T.; Huang, C. J. C. C., Cationic iridium (III) complexes for phosphorescence staining in the cytoplasm of living cells. **2008,** (18), 2115-2117.

105. Steunenberg, P.; Ruggi, A.; van den Berg, N. S.; Buckle, T.; Kuil, J.; van Leeuwen, F. W. B.; Velders, A. H., Phosphorescence Imaging of Living Cells with Amino Acid-Functionalized Tris(2-phenylpyridine)iridium(III) Complexes. *Inorganic Chemistry* **2012,** *51* (4), 2105-2114.

106. Lo, K. K.-W.; Lee, P.-K.; Lau, J. S.-Y. J. O., Synthesis, characterization, and properties of luminescent organoiridium (III) polypyridine complexes appended with an alkyl chain and their interactions with lipid bilayers, surfactants, and living cells. **2008,** *27* (13), 2998-3006.

107. Zhang, K. Y.; Lo, K. K.-W. J. I. c., Synthesis, properties, and live-cell imaging studies of luminescent cyclometalated iridium (III) polypyridine complexes containing two or three biotin pendants. **2009,** *48* (13), 6011-6025.

108. Lau, J. S.-Y.; Lee, P.-K.; Tsang, K. H.-K.; Ng, C. H.-C.; Lam, Y.-W.; Cheng, S.-H.; Lo, K. K.-W. J. I. C., Luminescent cyclometalated iridium (III) polypyridine indole complexes synthesis, photophysics, electrochemistry, protein-binding properties, cytotoxicity, and cellular uptake. **2009,** *48* (2), 708-718.

109. Liu, H.-W.; Zhang, K. Y.; Law, W. H.-T.; Lo, K. K.-W. J. O., Cyclometalated iridium (III) bipyridine complexes functionalized with an n-methylamino-oxy group as novel phosphorescent labeling reagents for reducing sugars. **2010,** *29* (16), 3474-3476.

110. Cao, J.-J.; Tan, C.-P.; Chen, M.-H.; Wu, N.; Yao, D.-Y.; Liu, X.-G.; Ji, L.-N.; Mao, Z.-W., Targeting cancer cell metabolism with mitochondria-immobilized phosphorescent cyclometalated iridium(iii) complexes. *Chemical science* **2017,** *8* (1), 631-640.

111. Celli, J. P.; Spring, B. Q.; Rizvi, I.; Evans, C. L.; Samkoe, K. S.; Verma, S.; Pogue, B. W.; Hasan, T., Imaging and Photodynamic Therapy: Mechanisms, Monitoring, and Optimization. *Chemical Reviews* **2010,** *110* (5), 2795-2838.

112. Qiu, K.; Zhu, H.; Rees, T. W.; Ji, L.; Zhang, Q.; Chao, H., Recent advances in lysosome-targeting luminescent transition metal complexes. *Coordination Chemistry Reviews* **2019,** *398*, 113010.

113. Satori, C. P.; Henderson, M. M.; Krautkramer, E. A.; Kostal, V.; Distefano, M. M.; Arriaga, E. A. J. C. r., Bioanalysis of eukaryotic organelles. **2013,** *113* (4), 2733-2811.

114. Thomas, J. A. J. C. S. R., Optical imaging probes for biomolecules: an introductory perspective. **2015,** *44* (14), 4494-4500.

115. Rosenberg, B.; Vancamp, L.; Trosko, J. E.; Mansour, V. H., Platinum Compounds: a New Class of Potent Antitumour Agents. *Nature* **1969,** *222* (5191), 385-386.

116. Mandal, S.; Poria, D. K.; Ghosh, R.; Ray, P. S.; Gupta, P. J. D. T., Development of a cyclometalated iridium complex with specific intramolecular hydrogen-bonding that acts as a fluorescent marker for the endoplasmic reticulum and causes photoinduced cell death. **2014,** *43* (46), 17463-17474.

117. Happ, B.; Winter, A.; Hager, M. D.; Schubert, U. S. J. C. S. R., Photogenerated avenues in macromolecules containing Re (I), Ru (II), Os (II), and Ir (III) metal complexes of pyridine-based ligands. **2012,** *41* (6), 2222-2255.

118. Ma, D.-L.; Wang, M.; Liu, C.; Miao, X.; Kang, T.-S.; Leung, C.-H. J. C. c. r., Metal complexes for the detection of disease-related protein biomarkers. **2016,** *324*, 90-105.

119. Lo, K. K.-W. J. A. o. c. r., Luminescent rhenium (I) and iridium (III) polypyridine complexes as biological probes, imaging reagents, and photocytotoxic agents. **2015,** *48* (12), 2985-2995.

120. Ma, D.-L.; Lin, S.; Wang, W.; Yang, C.; Leung, C.-H., Luminescent chemosensors by using cyclometalated iridium(iii) complexes and their applications. *Chemical science* **2017,** *8* (2), 878-889.

121. Kumar, N.; Bhalla, V.; Kumar, M. J. C. C. R., Recent developments of fluorescent probes for the detection of gasotransmitters (NO, CO and H2S). **2013,** *257* (15-16), 2335-2347.

122. Galindo, F.; Burguete, M. I.; Vigara, L.; Luis, S. V.; Kabir, N.; Gavrilovic, J.; Russell, D. A. J. A. C. I. E., Synthetic macrocyclic peptidomimetics as tunable pH probes for the fluorescence imaging of acidic organelles in live cells. **2005,** *44* (40), 6504-6508.

123. Huang, H.; Yu, B.; Zhang, P.; Huang, J.; Chen, Y.; Gasser, G.; Ji, L.; Chao, H., Highly Charged Ruthenium(II) Polypyridyl Complexes as Lysosome-Localized Photosensitizers for Two-Photon Photodynamic Therapy. **2015,** *54* (47), 14049-14052.

124. He, L.; Tan, C. P.; Ye, R. R.; Zhao, Y. Z.; Liu, Y. H.; Zhao, Q.; Ji, L. N.; Mao, Z. W. J. A. C., Theranostic iridium (III) complexes as one-and two-photon phosphorescent trackers to monitor autophagic lysosomes. **2014,** *126* (45), 12333-12337.

125. Qiu, K.; Liu, Y.; Huang, H.; Liu, C.; Zhu, H.; Chen, Y.; Ji, L.; Chao, H. J. D. T., Biscylometalated iridium (III) complexes target mitochondria or lysosomes by regulating the lipophilicity of the main ligands. **2016,** *45* (41), 16144-16147.

126. Cao, L.; Zhang, R.; Zhang, W.; Du, Z.; Liu, C.; Ye, Z.; Song, B.; Yuan, J. J. B., A ruthenium (II) complex-based lysosome-targetable multisignal chemosensor for in vivo detection of hypochlorous acid. **2015,** *68*, 21-31.

127. Murphy, L.; Congreve, A.; Pålsson, L.-O.; Williams, J. A. G., The time domain in co-stained cell imaging: time-resolved emission imaging microscopy using a protonatable luminescent iridium complex. *Chemical Communications* **2010,** *46* (46), 8743-8745.

128. Law, W. H.; Lee, L. C.; Louie, M. W.; Liu, H. W.; Ang, T. W.; Lo, K. K., Phosphorescent cellular probes and uptake indicators derived from cyclometalated iridium(III) bipyridine complexes appended with a glucose or galactose entity. *Inorg Chem* **2013,** *52* (22), 13029-41.

129. Sun, L.; Chen, Y.; Kuang, S.; Li, G.; Guan, R.; Liu, J.; Ji, L.; Chao, H., Iridium(III) Anthraquinone Complexes as Two-Photon Phosphorescence Probes for Mitochondria Imaging and Tracking under Hypoxia. **2016,** *22* (26), 8955-8965.

130. Shamjith, S.; Murali, V. P.; Joesph, M. M.; T S, F.; Chandana, R.; Jayarajan, R. O.; Maiti, K. K., Hydrogen Sulfide-Induced Activatable Photodynamic Therapy Adjunct to Disruption of Subcellular Glycolysis in Cancer Cells by a Fluorescence-SERS Bimodal Iridium Metal–Organic Hybrid. *ACS Applied Materials & Interfaces* **2024,** *16* (21), 27114-27126.

131. Xiang, H.; Chen, H.; Tham, H. P.; Phua, S. Z. F.; Liu, J.-G.; Zhao, Y., Cyclometalated Iridium(III)-Complex-Based Micelles for Glutathione-Responsive Targeted Chemotherapy and Photodynamic Therapy. *ACS Applied Materials & Interfaces* **2017,** *9* (33), 27553-27562.

132. Huang, T.; Yu, Q.; Liu, S.; Zhang, K. Y.; Huang, W.; Zhao, Q., Rational Design of Phosphorescent Iridium(III) Complexes for Selective Glutathione Sensing and Amplified Photodynamic Therapy. **2019,** *20* (4), 576-586.

133. Zhao, J.; Yan, K.; Xu, G.; Liu, X.; Zhao, Q.; Xu, C.; Gou, S., An Iridium (III) Complex Bearing a Donor–Acceptor–Donor Type Ligand for NIR-Triggered Dual Phototherapy. **2021,** *31* (11), 2008325.

134. Steele, R., The story of a new light source. *Nature Photonics* **2007,** *1*, 25-26.

135. CIE Standard Colorimetric System. In *Colorimetry*, 2005; pp 63-114.

136. Thejokalyani, N.; Dhoble, S. J., Novel approaches for energy efficient solid state lighting by RGB organic light emitting diodes – A review. *Renewable and Sustainable Energy Reviews* **2014,** *32*, 448-467.

137. Johnson, N. C.; Manchester, S.; Sarin, L.; Gao, Y.; Kulaots, I.; Hurt, R. H., Mercury Vapor Release from Broken Compact Fluorescent Lamps and In Situ Capture by New Nanomaterial Sorbents. *Environmental Science & Technology* **2008,** *42* (15), 5772-5778.

138. Hu, Y.; Cheng, H., Mercury risk from fluorescent lamps in China: current status and future perspective. *Environment international* **2012,** *44*, 141-50.

139. Narukawa, Y.; Sano, M.; Sakamoto, T.; Yamada, T.; Mukai, T., Successful fabrication of white light emitting diodes by using extremely high external quantum efficiency blue chips. **2008,** *205* (5), 1081-1085.

140. Tang, C. W.; VanSlyke, S. A., Organic electroluminescent diodes. *Applied Physics Letters* **1987,** *51* (12), 913-915.

141. Chwang, A.; Hack, M.; Brown, J., Flexible OLED display development: Strategy and status. *Journal of The Society for Information Display - J SOC INF DISP* **2005,** *13*.

142. Lee, S. M.; Kwon, J. H.; Kwon, S.; Choi, K. C., A Review of Flexible OLEDs Toward Highly Durable Unusual Displays. *IEEE Transactions on Electron Devices* **2017,** *64* (5), 1922-1931.

143. Li, W.; Li, Y.-Q.; Shen, Y.; Zhang, Y.-X.; Jin, T.-Y.; Chen, J.-D.; Zhang, X.-H.; Tang, J.-X., Releasing the Trapped Light for Efficient Silver Nanowires-Based White Flexible Organic Light-Emitting Diodes. **2019,** *7* (21), 1900985.

144. Pattison, M.; Hansen, M.; Bardsley, N.; Thomson, G. D.; Gordon, K.; Wilkerson, A.; Lee, K.; Nubbe, V.; Donnelly, S. *2022 Solid-State Lighting R&D Opportunities*; Guidehouse, Inc., Washington, DC (United States): 2022.

145. Zhao, F.; Ma, D., Approaches to high performance white organic light-emitting diodes for general lighting. *Materials Chemistry Frontiers* **2017,** *1* (10), 1933-1950.

146. Nuyken, O.; Jungermann, S.; Wiederhirn, V.; Bacher, E.; Meerholz, K., Modern Trends in Organic Light-Emitting Devices (OLEDs). *Monatshefte für Chemie - Chemical Monthly* **2006,** *137*, 811-824.

147. Yersin, H., Triplet Emitters for OLED Applications. Mechanisms of Exciton Trapping and Control of Emission Properties. In *Transition Metal and Rare Earth Compounds: Excited States, Transitions, Interactions III*, Yersin, H., Ed. Springer Berlin Heidelberg: Berlin, Heidelberg, 2004; pp 1-26.

148. Bredas, J.-L., Mind the gap! *Materials Horizons* **2014,** *1* (1), 17-19.

149. Liang, W. J. P. E., Excitons. **1970,** *5* (4), 226.

150. Waser, R., Nanoelectronics and Information Technology. Citeseer: 2005.

151. Kotadiya, N.; Blom, P.; Wetzelaer, G.-J., Efficient and stable single-layer organic light-emitting diodes based on thermally activated delayed fluorescence. *Nature Photonics* **2019,** *13*.

152. He, G.; Schneider, O.; Qin, D.; Zhou, X.; Pfeiffer, M.; Leo, K., Very high-efficiency and low voltage phosphorescent organic light-emitting diodes based on a p-i-n junction. *Journal of Applied Physics* **2004,** *95* (10), 5773-5777.

153. Adamovich, V.; Cordero, S.; Djurovich, P.; Tamayo, A.; Thompson, M.; D'Andrade, B.; Forrest, S., New charge-carrier blocking materials for high efficiency OLEDs. *Organic Electronics* **2003,** *4*, 77-87.

154. Shirota, Y.; Kuwabara, Y.; Inada, H.; Wakimoto, T.; Nakada, H.; Yonemoto, Y.; Kawami, S.; Imai, K., Multilayered organic electroluminescent device using a novel starburst molecule, 4,4′,4″-tris(3-methylphenylphenylamino)triphenylamine, as a hole transport material. *Applied Physics Letters* **1994,** *65* (7), 807-809.

155. Hung, L. S.; Tang, C. W.; Mason, M. G., Enhanced electron injection in organic electroluminescence devices using an Al/LiF electrode. *Applied Physics Letters* **1997,** *70* (2), 152-154.

156. Kido, J.; Iizumi, Y., Fabrication of highly efficient organic electroluminescent devices. *Applied Physics Letters* **1998,** *73* (19), 2721-2723.

157. Wu, Y.-L.; Chen, C.; Huang, Y.-H.; Lu, Y.-J.; Chou, C.-H.; Wu, C.-C., Highly efficient tandem organic light-emitting devices utilizing the connecting structure based on n-doped electron-transport layer/HATCN/hole-transport layer. *Applied Optics* **2014,** *53*.

158. Huang, J.; Pfeiffer, M.; Werner, A.; Blochwitz, J.; Leo, K.; Liu, S., Low-voltage organic electroluminescent devices using pin structures. *Applied Physics Letters* **2002,** *80* (1), 139-141.

159. Sun, J. X.; Zhu, X. L.; Peng, H. J.; Wong, M.; Kwok, H. S., Effective intermediate layers for highly efficient stacked organic light-emitting devices. *Applied Physics Letters* **2005,** *87* (9).

160. Chang, C.-C.; Chen, J.-F.; Hwang, S.-W.; Chen, C. H., Highly efficient white organic electroluminescent devices based on tandem architecture. *Applied Physics Letters* **2005,** *87* (25).

161. Chen, C.-W.; Lu, Y.-J.; Wu, C.-C.; Wu, E. H.-E.; Chu, C.-W.; Yang, Y., Effective connecting architecture for tandem organic light-emitting devices. *Applied Physics Letters* **2005,** *87* (24).

162. Meyer, J.; Kröger, M.; Hamwi, S.; Gnam, F.; Riedl, T.; Kowalsky, W.; Kahn, A., Charge generation layers comprising transition metal-oxide/organic interfaces: Electronic structure and charge generation mechanism. *Applied Physics Letters* **2010,** *96*.

163. Hamwi, S.; Meyer, J.; Kröger, M.; Winkler, T.; Witte, M.; Riedl, T.; Kahn, A.; Kowalsky, W., The Role of Transition Metal Oxides in Charge-Generation Layers for Stacked Organic Light-Emitting Diodes. **2010,** *20* (11), 1762-1766.

164. Lee, T.-W.; Noh, T.; Shin, H.-W.; Kwon, O.; Park, J.-J.; Choi, B.-K.; Kim, M.-S.; Shin, D. W.; Kim, Y.-R., Characteristics of Solution-Processed Small-Molecule Organic Films and Light-Emitting Diodes Compared with their Vacuum-Deposited Counterparts. **2009,** *19* (10), 1625-1630.

165. Jou, J.-H.; Hsu, M.-F.; Wang, W.-B.; Chin, C.-L.; Chung, Y.-C.; Chen, C.-T.; Shyue, J.-J.; Shen, S.-M.; Wu, M.-H.; Chang, W.-C.; Liu, C.-P.; Chen, S.-Z.; Chen, H.-Y., Solution-Processable, High-Molecule-Based Trifluoromethyl-Iridium Complex for Extraordinarily High Efficiency Blue-Green Organic Light-Emitting Diode. *Chemistry of Materials* **2009,** *21* (13), 2565-2567.

166. Chen, J.; Shi, C.; Fu, Q.; Zhao, F.; Hu, Y.; Feng, Y.; Ma, D., Solution-processable small molecules as efficient universal bipolar host for blue, green and red phosphorescent inverted OLEDs. *Journal of Materials Chemistry* **2012,** *22* (11), 5164-5170.

167. Jou, J.-H.; Li, C.-J.; Shen, S.-M.; Peng, S.-H.; Chen, Y.-L.; Jou, Y.-C.; Hong, J. H.; Chin, C.-L.; Shyue, J.-J.; Chen, S.-P.; Li, J.-Y.; Wang, P.-H.; Chen, C.-C., Highly efficient green organic light emitting diode with a novel solution processable iridium complex emitter. *Journal of Materials Chemistry C* **2013,** *1* (27), 4201-4208.

168. Buckley, A., *Organic Light-Emitting Diodes (OLEDs): Materials, Devices and Applications*. 2013; p 1-647.

169. So, F.; Kondakov, D., Degradation Mechanisms in Small-Molecule and Polymer Organic Light-Emitting Diodes. **2010,** *22* (34), 3762-3777.

170. Geffroy, B.; le Roy, P.; Prat, C., Organic light-emitting diode (OLED) technology: materials, devices and display technologies. **2006,** *55* (6), 572-582.

171. Aziz, H.; Popovic, Z. D., Degradation Phenomena in Small-Molecule Organic Light-Emitting Devices. *Chemistry of Materials* **2004,** *16* (23), 4522-4532.

172. Burrows, P. E.; Bulovic, V.; Forrest, S. R.; Sapochak, L. S.; McCarty, D. M.; Thompson, M. E., Reliability and degradation of organic light emitting devices. *Applied Physics Letters* **1994,** *65* (23), 2922-2924.

173. McElvain, J.; Antoniadis, H.; Hueschen, M. R.; Miller, J. N.; Roitman, D. M.; Sheats, J. R.; Moon, R. L., Formation and growth of black spots in organic light-emitting diodes. *Journal of Applied Physics* **1996,** *80* (10), 6002-6007.

174. Scholz, S.; Kondakov, D.; Lüssem, B.; Leo, K., Degradation Mechanisms and Reactions in Organic Light-Emitting Devices. *Chemical Reviews* **2015,** *115* (16), 8449-8503.

175. Reineke, S.; Lindner, F.; Schwartz, G.; Seidler, N.; Walzer, K.; Lüssem, B.; Leo, K., White organic light-emitting diodes with fluorescent tube efficiency. *Nature* **2009,** *459* (7244), 234-238.

176. Li, C.; Wang, S.; Chen, W.; Wei, J.; Yang, G.; Ye, K.; Liu, Y.; Wang, Y., High performance full color OLEDs based on a class of molecules with dual carrier transport channels and small singlet–triplet splitting. *Chemical Communications* **2015,** *51* (53), 10632-10635.

177. Li, L.; Liang, J.; Chou, S.-Y.; Zhu, X.; Niu, X.; ZhibinYu; Pei, Q., A Solution Processed Flexible Nanocomposite Electrode with Efficient Light Extraction for Organic Light Emitting Diodes. *Scientific Reports* **2014,** *4* (1), 4307.

178. Tian, M.; Luo, J.; Liu, X., Highly efficient organic light-emitting devices beyond theoretical prediction under high current density. *Opt. Express* **2009,** *17* (24), 21370-21375.

179. Forrest, S. R.; Bradley, D. D. C.; Thompson, M. E., Measuring the Efficiency of Organic Light-Emitting Devices. **2003,** *15* (13), 1043-1048.

180. Jordan, R. H.; Dodabalapur, A.; Slusher, R. E., Efficiency enhancement of microcavity organic light emitting diodes. *Applied Physics Letters* **1996,** *69* (14), 1997-1999.

181. Gu, G.; Garbuzov, D. Z.; Burrows, P. E.; Venkatesh, S.; Forrest, S. R.; Thompson, M. E., High-external-quantum-efficiency organic light-emitting devices. *Opt. Lett.* **1997,** *22* (6), 396-398.

182. Madigan, C. F.; Lu, M.-H.; Sturm, J. C., Improvement of output coupling efficiency of organic light-emitting diodes by backside substrate modification. *Applied Physics Letters* **2000,** *76* (13), 1650-1652.

183. Boroditsky, M.; Krauss, T. F.; Coccioli, R.; Vrijen, R.; Bhat, R.; Yablonovitch, E., Light extraction from optically pumped light-emitting diode by thin-slab photonic crystals. *Applied Physics Letters* **1999,** *75* (8), 1036-1038.

184. Yamasaki, T.; Sumioka, K.; Tsutsui, T., Organic light-emitting device with an ordered monolayer of silica microspheres as a scattering medium. *Applied Physics Letters* **2000,** *76* (10), 1243-1245.

185. Jurow, M. J.; Mayr, C.; Schmidt, T. D.; Lampe, T.; Djurovich, P. I.; Brütting, W.; Thompson, M. E., Understanding and predicting the orientation of heteroleptic phosphors in organic light-emitting materials. *Nature Materials* **2016,** *15* (1), 85-91.

186. Yeh, S.-J.; Wu, M.-F.; Chen, C.-T.; Song, Y.-H.; Chi, Y.; Ho, M.-H.; Hsu, S.-F.; Chen, C. H., New Dopant and Host Materials for Blue-Light-Emitting Phosphorescent Organic Electroluminescent Devices. **2005,** *17* (3), 285-289.

187. Friend, R. H.; Gymer, R.; Holmes, A.; Burroughes, J.; Marks, R.; Taliani, C.; Bradley, D.; Santos, D. D.; Bredas, J.-L.; Lögdlund, M. J. N., Electroluminescence in conjugated polymers. **1999,** *397* (6715), 121-128.

188. Tao, Y.; Yang, C.; Qin, J., Organic host materials for phosphorescent organic light-emitting diodes. *Chemical Society Reviews* **2011,** *40* (5), 2943-2970.

189. Gather, M. C.; Alle, R.; Becker, H.; Meerholz, K., On the Origin of the Color Shift in White-Emitting OLEDs. **2007,** *19* (24), 4460-4465.

190. Sajoto, T.; Djurovich, P. I.; Tamayo, A. B.; Oxgaard, J.; Goddard, W. A., III; Thompson, M. E., Temperature Dependence of Blue Phosphorescent Cyclometalated Ir(III) Complexes. *Journal of the American Chemical Society* **2009,** *131* (28), 9813-9822.

191. Adachi, C.; Baldo, M. A.; Thompson, M. E.; Forrest, S. R., Nearly 100% internal phosphorescence efficiency in an organic light-emitting device. *Journal of Applied Physics* **2001,** *90* (10), 5048-5051.

192. Wang, S.; Lee, C. W.; Lee, J. Y.; Hwang, S.-H., Synthesis and green phosphorescent OLED device performance of cyanofluorene-linked phenylcarbazoles as host material. *New Journal of Chemistry* **2018,** *42* (7), 5059-5065.

193. Kim, S.-Y.; Jeong, W.-I.; Mayr, C.; Park, Y.-S.; Kim, K.-H.; Lee, J.-H.; Moon, C.-K.; Brütting, W.; Kim, J.-J., Organic Light-Emitting Diodes with 30% External Quantum Efficiency Based on a Horizontally Oriented Emitter. **2013,** *23* (31), 3896-3900.

194. Su, Y.-J.; Huang, H.-L.; Li, C.-L.; Chien, C.-H.; Tao, Y.-T.; Chou, P.-T.; Datta, S.; Liu, R.-S., Highly Efficient Red Electrophosphorescent Devices Based on Iridium Isoquinoline Complexes: Remarkable External Quantum Efficiency Over a Wide Range of Current. **2003,** *15* (11), 884-888.

195. Yang, C.-H.; Tai, C.-C.; Sun, I. W., Synthesis of a high-efficiency red phosphorescent emitter for organic light-emitting diodes. *Journal of Materials Chemistry* **2004,** *14* (6), 947-950.

196. Pierloot, K.; Ceulemans, A.; Merchán, M.; Serrano-Andrés, L., Electronic Spectra of the Cyclometalated Complexes M(2-thienylpyridine)2 with M = Pd, Pt: A Theoretical Study. *The Journal of Physical Chemistry A* **2000,** *104* (19), 4374-4382.

197. Lee, J.-H.; Shin, H.; Kim, J.-M.; Kim, K.-H.; Kim, J.-J., Exciplex-Forming Co-Host-Based Red Phosphorescent Organic Light-Emitting Diodes with Long Operational Stability and High Efficiency. *ACS Applied Materials & Interfaces* **2017,** *9* (4), 3277-3281.

198. Su, S.-J.; Sasabe, H.; Takeda, T.; Kido, J., Pyridine-Containing Bipolar Host Materials for Highly Efficient Blue Phosphorescent OLEDs. *Chemistry of Materials* **2008,** *20* (5), 1691-1693.

199. Liu, Y.; Ye, K.; Fan, Y.; Song, W.; Wang, Y.; Hou, Z., Amidinate-ligated iridium(iii) bis(2-pyridyl)phenyl complex as an excellent phosphorescent material for electroluminescence devices. *Chemical Communications* **2009,** (25), 3699-3701.

200. Peng, T.; Li, G.; Ye, K.; Wang, C.; Zhao, S.; Liu, Y.; Hou, Z.; Wang, Y., Highly efficient phosphorescent OLEDs with host-independent and concentration-insensitive properties based on a bipolar iridium complex. *Journal of Materials Chemistry C* **2013,** *1* (16), 2920-2926.

201. Shin, H.; Ha, Y. H.; Kim, H.-G.; Kim, R.; Kwon, S.-K.; Kim, Y.-H.; Kim, J.-J., Controlling Horizontal Dipole Orientation and Emission Spectrum of Ir Complexes by Chemical Design of Ancillary Ligands for Efficient Deep-Blue Organic Light-Emitting Diodes. **2019,** *31* (21), 1808102.

202. Goushi, K.; Yoshida, K.; Sato, K.; Adachi, C., Organic light-emitting diodes employing efficient reverse intersystem crossing for triplet-to-singlet state conversion. *Nature Photonics* **2012,** *6* (4), 253-258.

203. Berberan-Santos, M. N.; Garcia, J. M. M., Unusually Strong Delayed Fluorescence of C70. *Journal of the American Chemical Society* **1996,** *118* (39), 9391-9394.

204. Whittle, V. L.; Williams, J. G. J. I. c., A new class of iridium complexes suitable for stepwise incorporation into linear assemblies: Synthesis, electrochemistry, and luminescence. **2008,** *47* (15), 6596-6607.

205. Neve, F.; Crispini, A.; Campagna, S.; Serroni, S., Synthesis, Structure, Photophysical Properties, and Redox Behavior of Cyclometalated Complexes of Iridium(III) with Functionalized 2,2‘-Bipyridines. *Inorganic Chemistry* **1999,** *38* (10), 2250-2258.

206. Andreiadis, E. S.; Imbert, D.; Pécaut, J.; Calborean, A.; Ciofini, I.; Adamo, C.; Demadrille, R.; Mazzanti, M. J. I. c., Phosphorescent Binuclear Iridium Complexes Based on Terpyridine–Carboxylate: An Experimental and Theoretical Study. **2011,** *50* (17), 8197-8206.

207. M'hamedi, A.; Batsanov, A. S.; Fox, M. A.; Bryce, M. R.; Abdullah, K.; Al-Attar, H. A.; Monkman, A. P. J. J. o. M. C., Dinuclear iridium (III) complexes of cyclometalated fluorenylpyridine ligands as phosphorescent dopants for efficient solution-processed OLEDs. **2012,** *22* (27), 13529-13540.

208. Santoro, A.; Prokhorov, A. M.; Kozhevnikov, V. N.; Whitwood, A. C.; Donnio, B.; Williams, J. G.; Bruce, D. W. J. J. o. t. A. C. S., Emissive metallomesogens based on 2-phenylpyridine complexes of iridium (III). **2011,** *133* (14), 5248-5251.

209. Shin, C. H.; Huh, J. O.; Baek, S. J.; Kim, S. K.; Lee, M. H.; Do, Y., Dinuclear Iridium (III) Complexes Linked by a Bis (β-diketonato) Bridging Ligand: Energy Convergence versus Aggregation-Induced Emission. Wiley Online Library: 2010.

210. Xu, W. J.; Liu, S. J.; Zhao, X.; Zhao, N.; Liu, Z. Q.; Xu, H.; Liang, H.; Zhao, Q.; Yu, X. Q.; Huang, W. J. C. A. E. J., Synthesis, One-and Two-Photon Photophysical and Excited-State Properties, and Sensing Application of a New Phosphorescent Dinuclear Cationic Iridium (III) Complex. **2013,** *19* (2), 621-629.

211. Auffrant, A.; Barbieri, A.; Barigelletti, F.; Lacour, J.; Mobian, P.; Collin, J.-P.; Sauvage, J.-P.; Ventura, B. J. I. c., Bimetallic iridium (III) complexes consisting of Ir (ppy) 2 units (ppy= 2-phenylpyridine) and two laterally connected n∧ n chelates as bridge: synthesis, separation, and photophysical properties. **2007,** *46* (17), 6911-6919.

212. Donato, L.; McCusker, C. E.; Castellano, F. N.; Zysman-Colman, E. J. I. C., Mono-and dinuclear cationic iridium (III) complexes bearing a 2, 5-dipyridylpyrazine (2, 5-dpp) ligand. **2013,** *52* (15), 8495-8504.

213. Lafolet, F.; Welter, S.; Popović, Z.; De Cola, L. J. J. o. M. C., Iridium complexes containing p-phenylene units. The influence of the conjugation on the excited state properties. **2005,** *15* (27-28), 2820-2828.

214. Yuan, X.; Zhang, S.; Ding, Y. J. I. C. C., Isolation, characterization and photophysical properties of a 2-(4, 6-difluorophenyl) pyridyl Iridium (III) methoxide dimeric complex. **2012,** *17*, 26-29.

215. Fernández-Cestau, J.; Giménez, N.; Lalinde, E.; Montaño, P.; Moreno, M. T.; Sánchez, S. J. O., Synthesis, characterization, and properties of doubly alkynyl bridging dinuclear cyclometalated iridium (III) complexes. **2015,** *34* (9), 1766-1778.

216. Chandrasekhar, V.; Hajra, T.; Bera, J. K.; Rahaman, S. W.; Satumtira, N.; Elbjeirami, O.; Omary, M. A. J. I. C., Ligand-bridged dinuclear cyclometalated IrIII complexes: from metallamacrocycles to discrete dimers. **2012,** *51* (3), 1319-1329.

217. Li, G.; Wu, Y.; Shan, G.; Che, W.; Zhu, D.; Song, B.; Yan, L.; Su, Z.; Bryce, M. R. J. C. C., New ionic dinuclear Ir (III) Schiff base complexes with aggregation-induced phosphorescent emission (AIPE). **2014,** *50* (53), 6977-6980.

218. Daniels, R. E.; Culham, S.; Hunter, M.; Durrant, M. C.; Probert, M. R.; Clegg, W.; Williams, J. G.; Kozhevnikov, V. N. J. D. T., When two are better than one: bright phosphorescence from non-stereogenic dinuclear iridium (III) complexes. **2016,** *45* (16), 6949-6962.

219. Congrave, D. G.; Hsu, Y.-t.; Batsanov, A. S.; Beeby, A.; Bryce, M. R. J. O., Synthesis, Diastereomer separation, and optoelectronic and structural properties of dinuclear cyclometalated iridium (III) complexes with bridging diarylhydrazide ligands. **2017,** *36* (5), 981-993.

220. Jiang, Y.; Li, G.; Che, W.; Liu, Y.; Xu, B.; Shan, G.; Zhu, D.; Su, Z.; Bryce, M. R. J. C. C., A neutral dinuclear Ir (III) complex for anti-counterfeiting and data encryption. **2017,** *53* (21), 3022-3025.

221. Li, G.; Guan, W.; Du, S.; Zhu, D.; Shan, G.; Zhu, X.; Yan, L.; Su, Z.; Bryce, M. R.; Monkman, A. P. J. C. c., Anion-specific aggregation induced phosphorescence emission (AIPE) in an ionic iridium complex in aqueous media. **2015,** *51* (95), 16924-16927.

222. Li, G.; Ren, X.; Shan, G.; Che, W.; Zhu, D.; Yan, L.; Su, Z.; Bryce, M. R. J. C. C., New AIE-active dinuclear Ir (III) complexes with reversible piezochromic phosphorescence behaviour. **2015,** *51* (65), 13036-13039.

223. M'hamedi, A.; Fox, M. A.; Batsanov, A. S.; Al-Attar, H. A.; Monkman, A. P.; Bryce, M. R. J. J. o. M. C. C., Bright green PhOLEDs using cyclometalated diiridium (III) complexes with bridging oxamidato ligands as phosphorescent dopants. **2017,** *5* (27), 6777-6789.

224. Yang, X.; Feng, Z.; Zhao, J.; Dang, J.-S.; Liu, B.; Zhang, K.; Zhou, G., Pyrimidine-Based Mononuclear and Dinuclear Iridium(III) Complexes for High Performance Organic Light-Emitting Diodes. *ACS Applied Materials & Interfaces* **2016,** *8* (49), 33874-33887.

225. Yang, X.; Xu, X.; Dang, J.-s.; Zhou, G.; Ho, C.-L.; Wong, W.-Y. J. I. c., From mononuclear to dinuclear iridium (III) complex: effective tuning of the optoelectronic characteristics for organic light-emitting diodes. **2016,** *55* (4), 1720-1727.

226. Zheng, Y.; Batsanov, A. S.; Fox, M. A.; Al-Attar, H. A.; Abdullah, K.; Jankus, V.; Bryce, M. R.; Monkman, A. P. J. A. C. I. E., Bimetallic cyclometalated iridium (III) diastereomers with non-innocent bridging ligands for high-efficiency phosphorescent OLEDs. **2014,** *53* (43), 11616-11619.

227. Graf, M.; Sünkel, K.; Czerwieniec, R.; Böttcher, H.-C. J. J. o. O. C., Luminescent diiridium (III) complex with a bridging biuretato ligand in unprecedented N, N′: O, O′ coordination. **2013,** *745*, 341-346.

228. Chen, Y.; Xu, W.; Zuo, J.; Ji, L.; Chao, H. J. J. o. M. C. B., Dinuclear iridium (III) complexes as phosphorescent trackers to monitor mitochondrial dynamics. **2015,** *3* (16), 3306-3314.

229. Cui, Y.; Wen, L.-L.; Shan, G.-G.; Sun, H.-Z.; Mao, H.-T.; Zhang, M.; Su, Z.-M. J. S.; Chemical, A. B., Di-/trinuclear cationic Ir (III) complexes: Design, synthesis and application for highly sensitive and selective detection of TNP in aqueous solution. **2017,** *244*, 314-322.

230. Lu, L.; Wang, M.; Mao, Z.; Kang, T.-S.; Chen, X.-P.; Lu, J.-J.; Leung, C.-H.; Ma, D.-L., A novel dinuclear iridium(III) complex as a G-quadruplex-selective probe for the luminescent switch-on detection of transcription factor HIF-1α. *Scientific Reports* **2016,** *6* (1), 22458.

231. Chandrasekhar, V.; Mahanti, B.; Bandipalli, P.; Bhanuprakash, K. J. I. c., Cyclometalated iridium (III) complexes containing hydroxide/chloride ligands: isolation of heterobridged dinuclear iridium (III) compounds containing μ-OH and μ-pyrazole ligands. **2012,** *51* (20), 10536-10547.

232. Lanoë, P.-H.; Tong, C. M.; Harrington, R. W.; Probert, M. R.; Clegg, W.; Williams, J. G.; Kozhevnikov, V. N. J. C. C., Ditopic bis-terdentate cyclometallating ligands and their highly luminescent dinuclear iridium (III) complexes. **2014,** *50* (52), 6831-6834.

233. Mao, H.-T.; Cui, Y.; Li, G.-F.; Shan, G.-G.; Zeng, Q.-Y.; Li, F.-S.; Su, Z.-M., Dinuclear Ir(iii) complexes with asymmetrical bridging ligands as highly efficient phosphors for single-layer electroluminescent devices. *Journal of Materials Chemistry C* **2019,** *7* (43), 13461-13467.

234. Shafikov, M. Z.; Zaytsev, A. V.; Kozhevnikov, V. N., Halide-Enhanced Spin–Orbit Coupling and the Phosphorescence Rate in Ir(III) Complexes. *Inorganic Chemistry* **2021,** *60* (2), 642-650.

235. Gao, T.-B.; Zhang, J.-J.; Wen, J.; Yang, X.-X.; Ma, H.-b.; Cao, D.-K.; Jiang, D., Single-Molecule MicroRNA Electrochemiluminescence Detection Using Cyclometalated Dinuclear Ir(III) Complex with Synergistic Effect. *Analytical Chemistry* **2020,** *92* (1), 1268-1275.

236. Congrave, D. G.; Hsu, Y.-t.; Batsanov, A. S.; Beeby, A.; Bryce, M. R., Synthesis, Diastereomer Separation, and Optoelectronic and Structural Properties of Dinuclear Cyclometalated Iridium(III) Complexes with Bridging Diarylhydrazide Ligands. *Organometallics* **2017,** *36* (5), 981-993.

237. Lu, C.; Xu, W.; Shah, H.; Liu, B.; Xu, W.; Sun, L.; Qian, S. Y.; Sun, W., In Vitro Photodynamic Therapy of Mononuclear and Dinuclear Iridium(III) Bis(terpyridine) Complexes. *ACS Applied Bio Materials* **2020,** *3* (10), 6865-6875.

238. Plummer, E. A.; Hofstraat, J. W.; De Cola, L. J. D. T., Mono-and di-nuclear iridium (iii) complexes. Synthesis and photophysics. **2003,** (10), 2080-2084.

239. Costa, R. D.; Fernández, G.; Sánchez, L.; Martín, N.; Ortí, E.; Bolink, H. J., Dumbbell-Shaped Dinuclear Iridium Complexes and Their Application to Light-Emitting Electrochemical Cells. **2010,** *16* (32), 9855-9863.

240. Nasr, G.; Guerlin, A.; Dumur, F.; Beouch, L.; Dumas, E.; Clavier, G.; Miomandre, F.; Goubard, F.; Gigmes, D.; Bertin, D. J. C. C., Iridium (III) soft salts from dinuclear cationic and mononuclear anionic complexes for OLED devices. **2011,** *47* (38), 10698-10700.

241. Li, G.; Congrave, D. G.; Zhu, D.; Su, Z.; Bryce, M. R. J. P., Recent advances in luminescent dinuclear iridium (III) complexes and their application in organic electroluminescent devices. **2018,** *140*, 146-157.

242. Hao, Z.; Jiang, H.; Liu, Y.; Zhang, Y.; Yu, J.; Wang, Y.; Tan, H.; Su, S.; Zhu, W. J. T., Synthesis and optoelectronic properties of dinuclear iridium (III) complexes containing deep blue fluorescence chromophore in the single-emissive-layer WPLEDs. **2016,** *72* (52), 8542-8549.

243. He, K.; Su, N.; Junting, Y.; Liu, Y.; Xiong, W.; Hao, Z.; Ma, D.; Zhu, W. J. T., Dinuclear cyclometalated iridium (III) complex containing functionalized triphenylamine core: synthesis, photophysics and application in the single-emissive-layer WOLEDs. **2016,** *72* (45), 7164-7169.

244. He, K.; Wang, X.; Yu, J.; Jiang, H.; Xie, G.; Tan, H.; Liu, Y.; Ma, D.; Wang, Y.; Zhu, W. J. O. E., Synthesis and optoelectronic properties of novel fluorene-bridged dinuclear cyclometalated iridium (III) complex with A–D–A framework in the single-emissive-layer WOLEDs. **2014,** *15* (11), 2942-2949.

245. Hao, Z.; Li, M.; Liu, Y.; Wang, Y.; Xie, G.; Liu, Y., Near-infrared emission of dinuclear iridium complexes with hole/electron transporting bridging and their monomer in solution-processed organic light-emitting diodes. *Dyes and Pigments* **2018,** *149*, 315-322.

246. Yang, X.; Chen, X.; Dang, J.; Sun, Y.; Feng, Z.; Tian, Z.; Zhou, G.; Wu, Z., Dinuclear Ir(III) complex based on different flanking and bridging cyclometalated ligands: An impressive molecular framework for developing high performance phosphorescent emitters. *Chemical Engineering Journal* **2020,** *391*, 123505.

CHAPTER 2

Exploring a Mitochondria Targeting, Dinuclear Cyclometalated Iridium (III) Complex for Image-Guided Photodynamic Therapy in Triple-negative Breast Cancer Cells

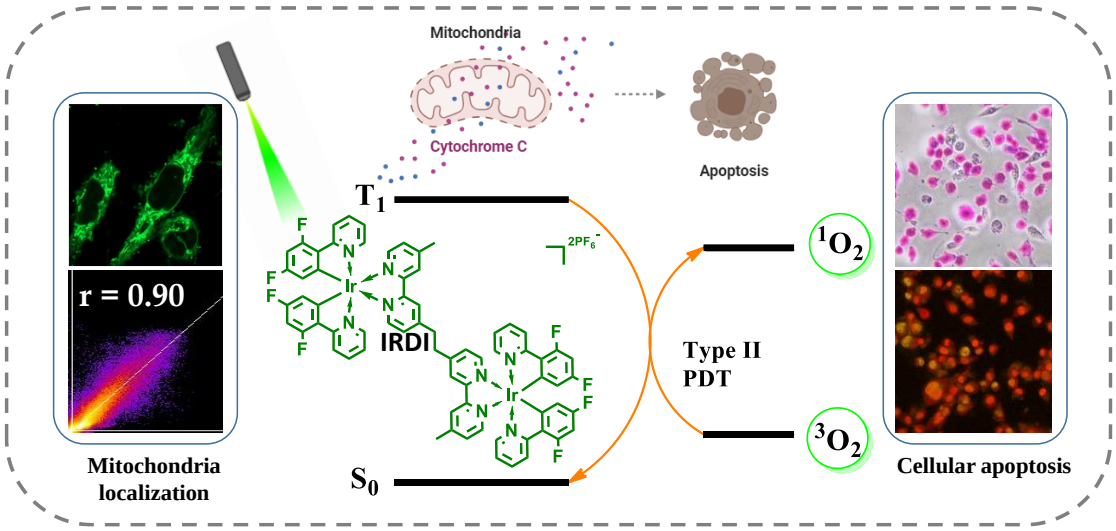

2.1. Abstract

Photodynamic therapy (PDT) has gained recognition as a highly effective, non-invasive cancer treatment that uses laser-activated photosensitizers to selectively target and destroy cancer cells. Among the latest developments in this field, iridium-based photosensitizers stand out due to their dual functionality as both imaging probes and PDT agents, offering precision in diagnosis and treatment. Despite this potential, most iridium(III) photosensitizers developed to date are mononuclear, with only a few dinuclear variants explored. Fully harnessing the capabilities of dinuclear iridium systems for PDT remains a significant challenge. Herein, we introduce a novel dinuclear Ir(III) complex, **IR-DI**, alongside its mononuclear counterpart, **IR-MO**, both containing 2-(2,4-

difluorophenyl)pyridine and 4'-methyl-2,2'-bipyridine ligands. Comparative studies between the two complexes reveal that, while their absorption profiles are similar, the dinuclear **IR-DI** exhibits a notably higher photoluminescence quantum yield (Φ_p = 0.70) compared to the mononuclear **IR-MO** (Φ_p = 0.47). Furthermore, **IR-DI** shows a significantly improved singlet oxygen generation quantum yield (Φ_s = 0.49) over **IR-MO** (Φ_s = 0.28), suggesting that the dinuclear complex holds greater promise for image-guided PDT applications. In vitro experiments demonstrate that **IR-DI** is efficiently absorbed by cells and induces substantial photocytotoxicity in the triple-negative breast cancer cell line MDA-MB-231. Notably, the dinuclear structure's dual positive charge allows for natural mitochondrial targeting without the need for additional targeting groups. Mitochondrial singlet oxygen generation was verified using the singlet oxygen imaging probe Si-DMA, and ROS-mediated PDT-induced cell apoptosis was confirmed through live-dead assays performed with and without the singlet oxygen scavenger NaN_3. The underlying cell death mechanism was further explored using Annexin V-FITC/PI flow cytometry, along with Cytochrome C release assays via western blotting. This study demonstrates that the design of the dinuclear Ir(III) complex, which optimizes spin-orbit coupling while minimizing excitonic interactions, provides a compelling approach for efficient image-guided PDT, expanding the utility of iridium complexes in therapeutic applications.

2.2. Introduction

In recent decades, photodynamic therapy has emerged as a highly promising clinical approach for treating various diseases, particularly cancer and actinic keratosis.[1-5] This non-invasive approach involves a light-activated interaction between a photosensitizer and molecular oxygen, generating cytotoxic reactive oxygen species (ROS) that induce the death of cancer cells.[3] The processes underlying the generation of reactive oxygen species (ROS) are intricate, but they can be broadly divided into two main pathways. Type I process involves a photoinduced electron transfer with biological substrates, resulting in the formation of radical species such as superoxide ($O_2^{\bullet-}$), hydroxyl ($^{\bullet}OH$) and hydrogen peroxide (H_2O_2). While in type II pathway photo reactivity occurs through a direct energy transfer to molecular oxygen ($^3O_2$) resulting in the production of singlet oxygen ($^1O_2$).[6-8]

The effectiveness of photodynamic therapy greatly depends upon the characteristics of photosensitizers, in addition to light dosage and oxygen concentration.[9] For image-guided therapeutic applications, the photosensitizer must possess several key attributes: a long lived excited state capable of generating ROS upon interaction with oxygen, non-toxicity in its non-irradiated form, preferential absorption in a specific range, photochemical stability and prompt clearance from the body to minimize the risk of long term photosensitivity.[10] Although porphyrin, chlorin, and phthalocyanine derivatives have been commonly used as photosensitizers in PDT due to their advantageous light absorption, fluorescence emission, and singlet oxygen production, they often present challenges such as complex synthesis and purification, low water solubility, extended retention in the body, and the risk of hepatotoxicity. Metal complexes have emerged as promising photosensitizers for PDT offering advantages such as long-lived triplet states, high ROS production, photochemical stability and water solubility. Efficient room temperature

photoluminescence of metal complexes offers an additional advantage of cellular imaging, which makes them suitable for image guided PDT compared to conventional photosensitizers.[11] Recently, cyclometalated transition-metal complexes particularly Pt(II) and Ir(III) have gained widespread attention due to their impressive luminescent properties and for their performance as a highly effective class of singlet oxygen photosensitizers.[12-16] Even though the success of cisplatin as an anticancer agent has ignited a pursuit for the development of several inorganic anticancer drugs, they generally induce cell death via the oxygen-independent type III pathway and are referred as photoactivated chemotherapeutic (PACT) agents rather than as PDT agents.[10, 17, 18] Despite numerous reported examples of Pt(II) complexes as efficient singlet oxygen sensitizers, only a few platinum complexes have demonstrated photosensitizing effects via type I or type II mechanism.[10] Subsequently, it was found that iridium(III) complexes act as efficient photosensitizers through type I or type II mechanisms and are suitable for live-cell imaging guided, PDT applications.[10, 19] In addition, iridium complexes show excellent photophysical and photochemical properties, such as a large Stokes shift, ease in colour tuning, high triplet and singlet oxygen quantum yield, long luminescence lifetimes, and high chemical and photochemical stabilities.[20, 21]

Several examples for mononuclear iridium complexes used as photosensitizers for PDT are reported in recent years.[6, 22-28] M. E Thompson *et al*. reported two iridium complexes based on cyclometalating ligand, phenylbenzothiazole with ancillary ligands pyridine and acac respectively, showing singlet oxygen generation efficiencies as high as 100% (**Figure 2.1**).[29] Significant research efforts were also focused on organelle targeted PDT using iridium-based photosensitizers.[23, 24, 26] For example, endoplasmic reticulum targeted phenylquinoline based iridium complexes for efficient ROS generation and rapid cell death were demonstrated by T. H. Kwon *et al*., where the phenylisoquinoline based

iridium enhances ROS generation by tuning the photosensitizer energy level for efficient energy transfer to triplet oxygen.[25] Huang and colleagues developed two Ir(III) complexes, Ir-P(ph)$_3$ and Ir-alkyl, targeting mitochondria and lysosomes, respectively, with a high singlet oxygen ($^1O_2$) quantum yield of 0.21 and strong oxygen sensitivity. The mitochondria targeted Ir-P(ph)$_3$ showed increased luminous intensity, longer lifetime, and exceptional photodynamic therapy (PDT) effectiveness under hypoxic conditions, enhancing its efficacy against hypoxic tumors (**Figure 2.2**).[23] H. Chao *et al.*, reported mitochondria targeting iridium complex for hypoxic tumors.[30] The overall positive charge and lipophilic nature of iridium complexes help them to get localised in the mitochondria of cell even without having any specific targeting group.[30, 31] The subcellular localization plays a crucial role in immunogenic response. As the energetic powerhouse of the cell, mitochondria act as ideal subcellular location for photosensitizer agent.[32-34] Efforts were also made in utilizing the iridium complexes for two-photon based PDT and for extending the absorption of the complexes to the NIR region by substitution and conjugation, to overcome the inherent limitations of low wavelength absorptions for PDT.[35-38]

a)

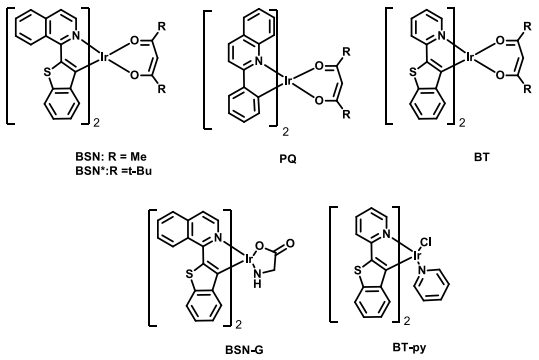

b)

Sensitizer[a]	λ (nm)	ϕ_Δ[b]	$k_{q,sv}$ (10^9 M^{-1} s^{-1})	k_q ($^1O_2$) ($^1O_2$ M^{-1} s^{-1})
BSN	355	0.59±0.07		6.3±0.2
	532	0.89±0.02		
BSN*	355	0.60±0.06	2.9±0.1	4.0±0.3
	532	0.77±0.08		
PQ	355	0.62±0.05	7.2±0.3	1.0±0.2
	532	0.89±0.07		
BT	355	0.86±0.07	5.9±0.6	0.5±0.2
	532	1.00±0.07		
BSN-G	355	0.54±0.02		2.1±0.5
	532	0.81±0.06		
BT-py	355	0.95±0.09		None detected
	532	1.00±0.09		

[a] Measurement were made in C_6H_6 solvent. [b] The refernces for quantum yield measurements were C_{60} (0.76), TPP (0.62), and perinaphthenone (0.95) at 355 nm and TPP (0.62) at 532 nm.

Figure 2.1. (a) The structures of the singlet oxygen sensitizers and (b) Table of singlet oxygen quantum yields (Φ_Δ) with excitation (λ) at 355 or 532 nm, the rate constant of singlet oxygen quenching, calculated by Stern-Volmer Analysis ($k_{q,SV}$), and singlet oxygen quenching rate constant by the Ir (III) Complex sensitizer [$k_q(^1O_2)$]. Adapted from reference 29.

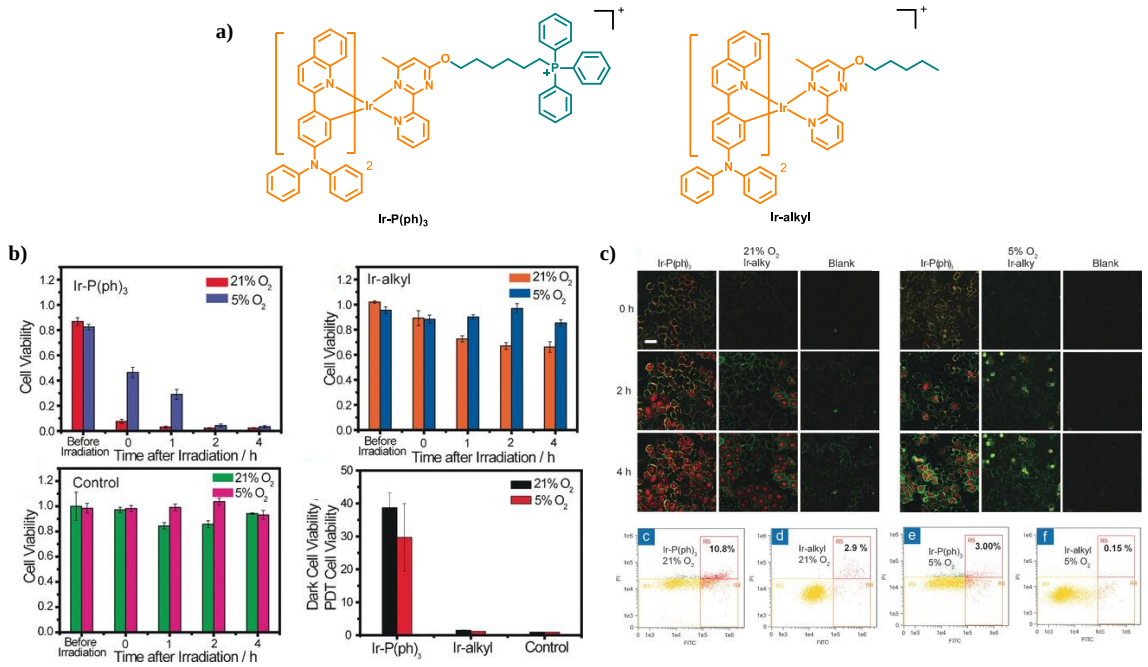

Figure 2.2. (a) The structure of the lysosome and mitochondria targeted iridium complexes; (b) Cell viability evaluation of both the complexes in normoxic and hypoxic situations and (c) Confocal microscopy images and flow cytometry analysis showing the quantification of HeLa cells labelled with Annexin V-FITC and propidium iodide (PI). Adapted from reference 23.

Despite the numerous reports on homoleptic and heteroleptic monomer iridium complexes for PDT applications, study of di/multi-nuclear iridium complexes as photosensitizers remains less explored. Although the synthetic difficulties of dinuclear iridium complexes may be a reason for them being initially overlooked, reports on photophysical and device properties of di/multi-nuclear iridium complexes used for optoelectronic applications have highlighted their advantages over monomers.[39, 40] Typically, multiple metal centres are expected to enhance spin orbit coupling (SOC) in di/multi-nuclear iridium complexes resulting in enhanced luminescence quantum yields and ROS generation.[41-44]

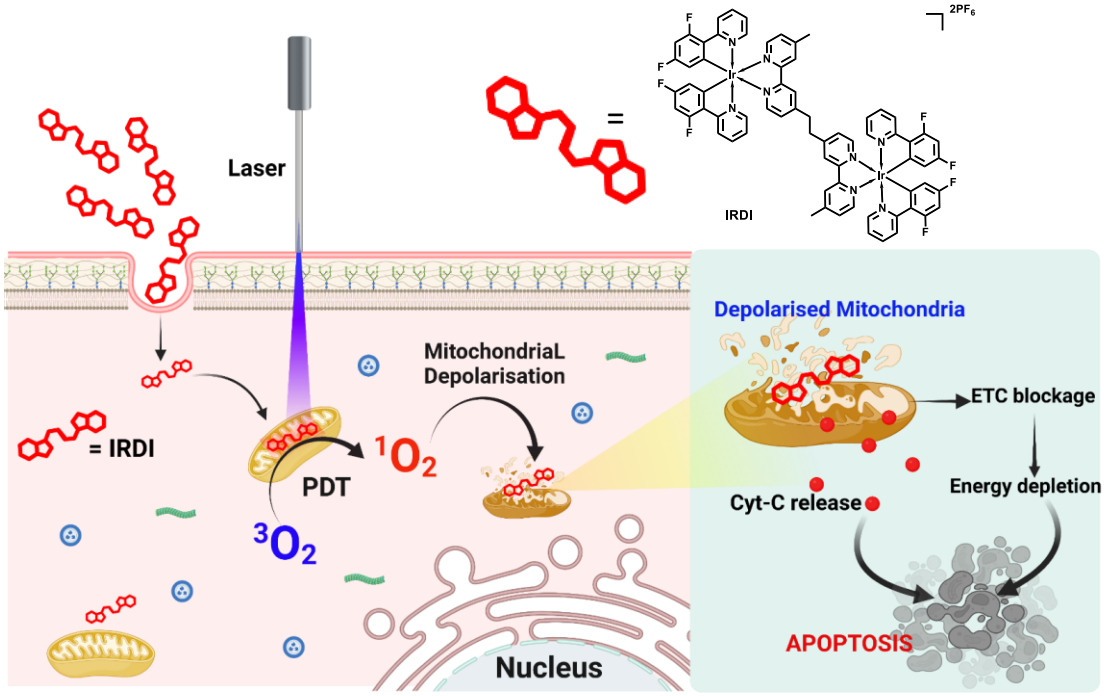

Figure 2.3. Schematic illustration of the action mechanism of **IR-DI** through photodynamic therapy.

Herein, we have designed a mitochondria targeting, dinuclear iridium complex with 2-(2,4-difluorophenyl)pyridine as the cyclometalating ligand, and 4'-methyl-2,2'-bipyridine ancillary ligand joined through a flexible ethyl spacer (**Figure 2.3**) and investigated their photophysical and photocytotoxicity properties in comparison with the corresponding mononuclear iridium complex (**IR-MO**). The flexible ethyl spacer ensures minimum through-bond electronic coupling while ensuring close proximity of the metal centres leading to efficient spin orbital coupling without the quenching of photoluminescence. Consequently, the dinuclear iridium complex show enhanced triplet quantum yield and singlet oxygen generation efficiency compared to the monomer iridium complex. In addition to this, the dual positive charge of dinuclear complex (**IR-DI**) enhance the mitochondria targeting properties. The *in vitro* analysis on the cellular internalization, mitochondrial localization and photocytotoxicity of **IR-DI** was conducted in triple-

negative breast cancer cell line MDA-MB-231. Finally, the investigation on the cell death mechanism deciphered the ROS driven mitochondria mediated apoptotic pathway initiated by **IR-DI** upon photosensitization. Thus, the dinuclear design can unleash the full potential of iridium-based photosensitizers in image-guided cancer photodynamic therapy.

2.3. Results and Discussion

2.3.1. Synthesis of IR-MO and IR-DI Complexes

Herein, we synthesized a dinuclear iridium complex (**IR-DI**) and a structurally similar, mononuclear iridium complex (**IR-MO**) for comparative investigation of the photophysical properties, as shown in **Figure 2.4a**. The cyclometalating ligand, 2-(2,4-difluorophenyl)pyridine (dfppy) was synthesised via a Pd-catalysed Suzuki cross-coupling reaction using 2-bromopyridine and 2,4-difluorophenylboronic acid. Subsequently, the chlorine bridged iridium dinuclear complex $[(dfppy)_2IrCl]_2$ was synthesized by coupling of the cyclometalating ligand with iridium(III) chloride ($IrCl_3.xH_2O$) via a Nonoyama reaction.[45] The synthesis of dinuclear Ir(III) complex**, IR-DI** and the corresponding monomer Ir(III) complex, **IR-MO** were achieved by the final replacement of the bridged chlorine with respective ancillary bipyridine ligands. Finally, the chlorine counter ions in the complexes were exchanged with hexafluorophosphate anions through an anion exchange reaction with ammonium hexafluorophosphate (**Figure 2.4b**). The synthesized monomeric and dinuclear complexes and all the synthetic intermediates were well-characterised using HRMS and NMR spectroscopic methods.

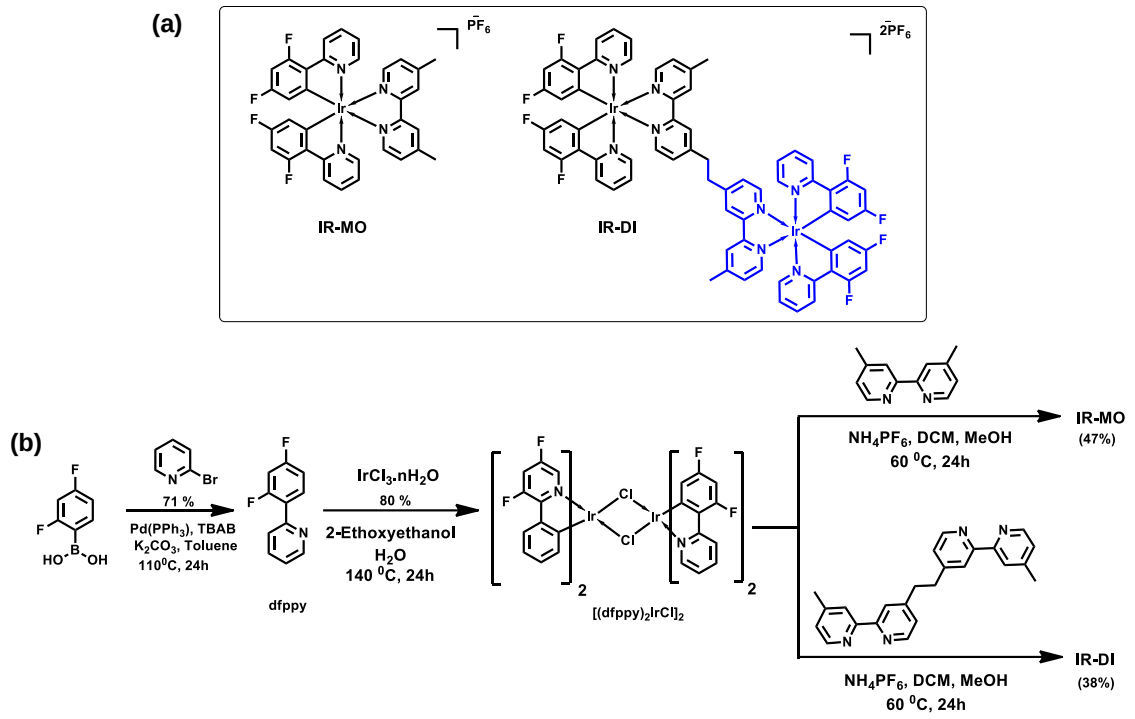

Figure 2.4. (a) Structures of mononuclear iridium complex, **IR-MO** and dinuclear iridium complex, **IR-DI** and (b) Scheme adopted for the synthesis of **IR-DI** and **IR-MO**.

2.3.2. Photophysical Properties

The absorption spectra of the complexes in acetonitrile solution at room temperature are shown in **Figure 2.5a**. The UV-Vis absorption spectra of both **IR-MO** and **IR-DI** exhibited an intense band around 200 nm - 300 nm, which can be assigned to spin allowed $^{1}\pi$-π^* ligand centred transitions in 2-(2,4-difluorophenyl)pyridine and ancillary bipyridine ligands.[46] The less intense absorption bands in the range of 300 nm - 400 nm correspond to spin allowed and spin forbidden, mixed singlet and triplet metal-to-ligand charge transfer (^{1}MLCT and ^{3}MLCT) admixes with the ligand-to-ligand charge-transfer (LLCT) transitions.[46]

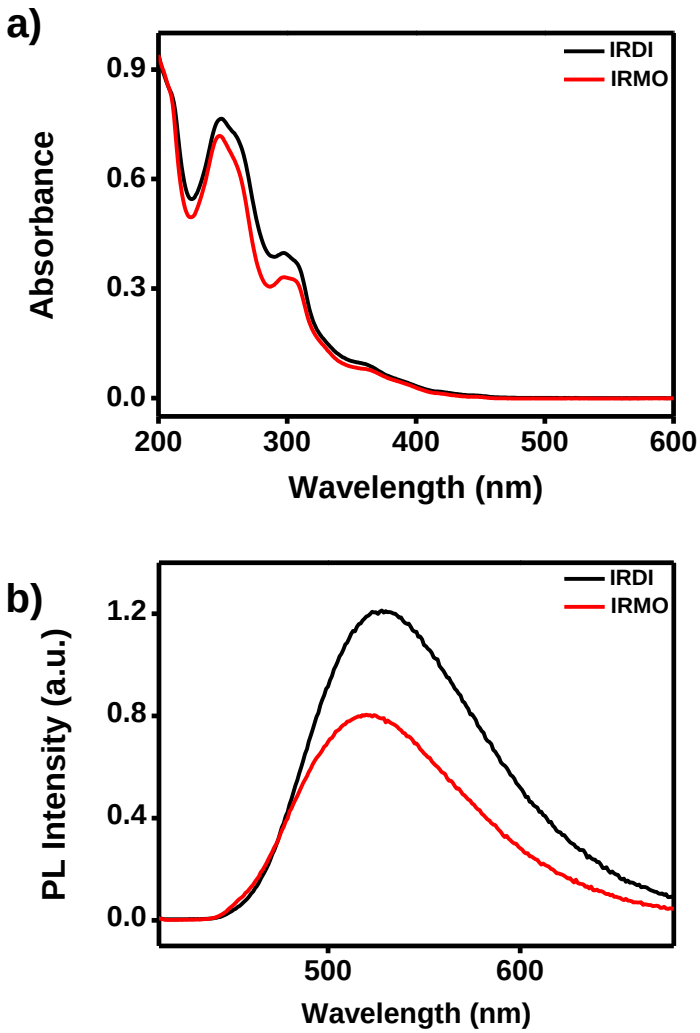

Figure 2.5. (a) UV-Visible absorption spectra of **IR-DI** and **IR-MO** in acetonitrile and (b) Emission characteristics of **IR-DI** and **IR-MO in** acetonitrile at 365 nm excitation.

The emission spectra of **IR-MO** and **IR-DI** in acetonitrile at room temperature under degassed conditions were shown in **Figure 2.5b**. An intense, broad and featureless emission band with a maximum at 525 nm is observed for **IR-DI**, which is slightly red shifted compared to that of the monomer complex **IR-MO** (λ_{em} = 519 nm). The broad and featureless emission bands are mainly attributable to charge-transfer (CT) states, while the structured emission occurs when charge transfer is combined with interactions between the excited state and the ligand's vibrational modes.[47] The emission intensity of the dinuclear Ir(III) complex, **IR-DI** is nearly two-fold compared to that of the mononuclear Ir(III)

complex, **IR-MO** which is also reflected in the calculated photoluminescence quantum yields for **IR-DI** (Φ_p = 0.70) and **IR-MO** (Φ_p = 0.47) in acetonitrile, with reference to standard $Ir(ppy)_3$ in dichloroethane (Φ_p = 0.89).[48] The PL lifetime measurements of **IR-DI** and **IR-MO**, using time resolved single photon counting techniques exhibited lifetimes of 185 ns and 97 ns, respectively (**Figure 2.6a**).

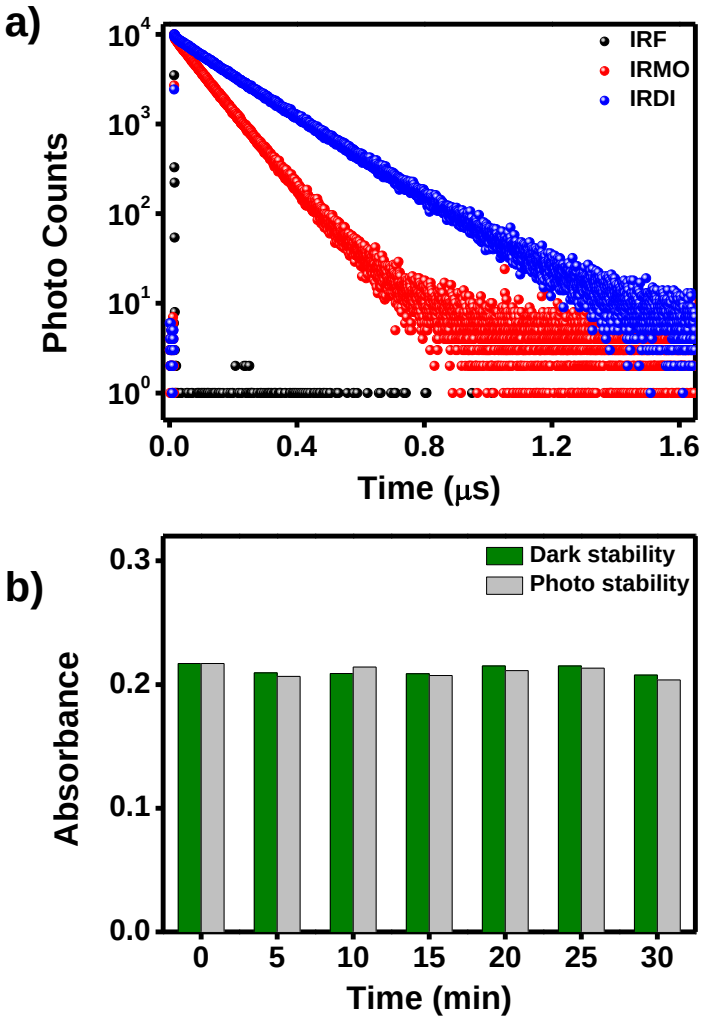

Figure 2.6. (a) Time-correlated single photon counting (TCSPC) measurement of **IR-DI** and **IR-MO** and (d) Photo and dark stability of **IR-DI**.

To investigate the photobleaching effect of the dinuclear Ir(III) complex **IR-DI**, photostability measurements were conducted with and without irradiation using a 200 W Xenon Arc lamp on an Oriel optical bench as shown in **Figure 2.6b**. The **IR-DI** complex

exhibited stable and reproducible absorption profiles in presence and absence of irradiation in a time dependent manner, indicating the excellent photostability of the complex **IR-DI**. The pH sensitive absorption and emission properties of **IR-DI** were studied (**Figure. 2. 7a&b**), as the nature of environment can perturb the electronic and photophysical properties of molecules. The absorption and emission profiles were recorded in PBS buffer by incubating **IR-DI** at different pH (5-9), which exhibited no significant sensitivity. The minimal impact of acidity on photophysical behaviour allows **IR-DI** to be stable under normal and acidic cell conditions.

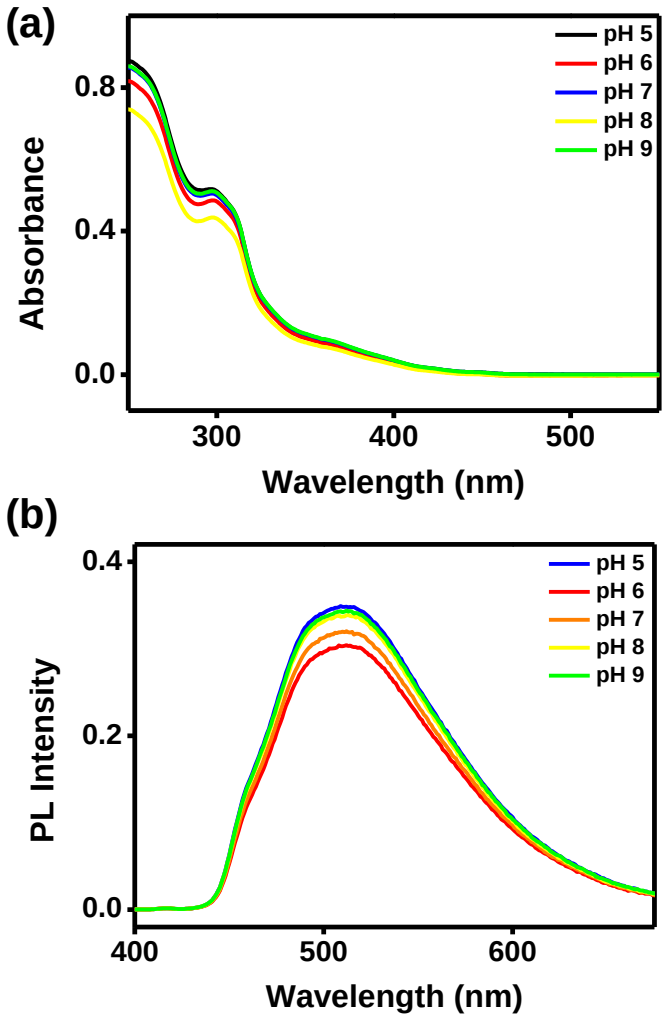

Figure 2.7. (a) pH-dependent graph of **IR-DI** at different pH starting from 5 to 9 (a) absorption spectra and (b) emission spectra (excitation 365 nm).

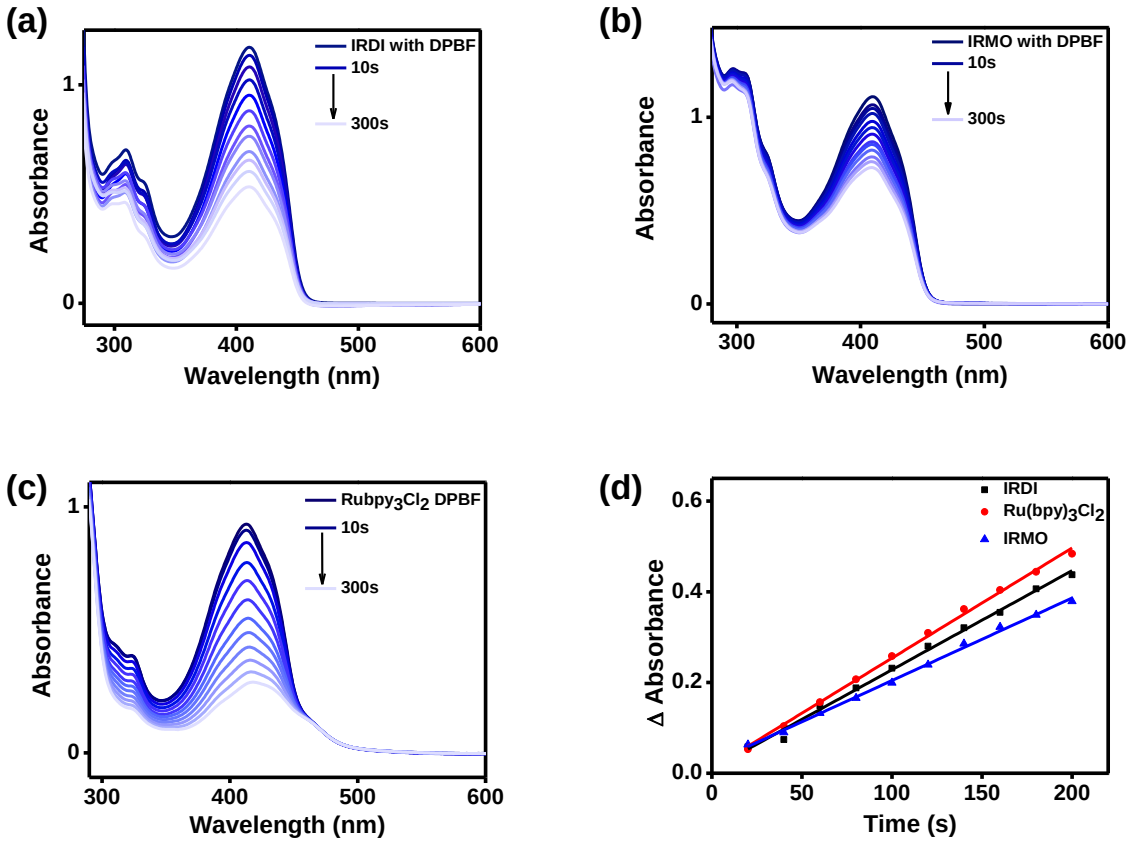

Figure 2.8. Absorption spectra of the complex-DPBF mixture upon irradiation with a 200 W xenon lamp equipped with a 400 nm band-pass filter: (a) **IR-DI**; (b) **IR-MO**; (c) $Ru(bpy)_3]Cl_2$ and (d) Relative plot of decrease in absorption of DPBF at 410 nm in the presence of **IR-DI**, **IR-MO** and reference $[Ru(bpy)_3]Cl_2$ (Φ_s = 0.57 in acetonitrile).

The singlet oxygen generation efficiencies of the **IR-DI** and **IR-MO** complexes were investigated by employing 1,3-diphenylbenzofuran (DPBF) as the singlet oxygen scavenger and $[Ru(bpy)_3]Cl_2$ (Φ_s = 0.57 in acetonitrile) as reference.[12] DPBF acts as a singlet oxygen ($^1O_2$) scavenger by reacting specifically with $^1O_2$ to form an endoperoxide. This reaction results in a measurable decrease in DPBF's absorbance, allowing for the quantification of singlet oxygen production. The decrease in DPBF absorbance at 410 nm of **IR-DI**, **IR-MO** and and $[Ru(bpy)_3]Cl_2$ are depicted in **Figure 2.8a-c**. The reduction in absorbance was substantial upon light irradiation in the presence of **IR-DI** compared to **IR-MO** complex suggesting higher singlet oxygen generation capacity of the dinuclear complex. To calculate and demonstrate the ROS capacity of iridium complexes using DPBF, we documented the linear correlation of change in absorption with time as in **Figure**

2.8d. The singlet oxygen quantum yields of **IR-DI** and **IR-MO** were calculated as 0.49 and 0.28, respectively which suggests that dinuclear complex, **IR-DI** is better photoactivatable ROS generator for PDT compared to **IR-MO**. The singlet oxygen quantum yields obtained for **IR-DI** and **IR-MO** are comparable with earlier literature reports.[25, 49]

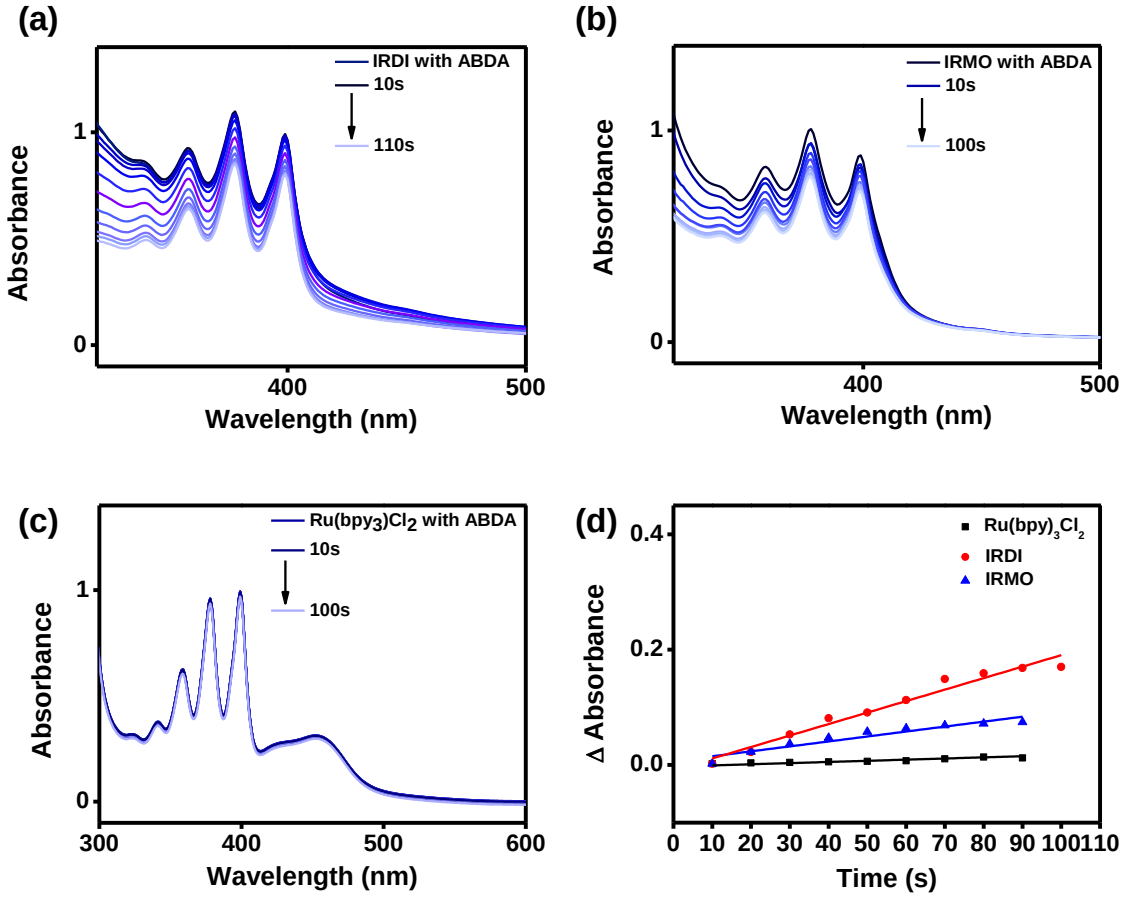

Figure 2.9. Absorption spectra of the complex- ABDA mixture upon irradiation with a 200 W xenon lamp equipped with a 400 nm band-pass filter: (a) **IR-DI**; (b) **IR-MO**; (c) $Ru(bpy)_3]Cl_2$ and (d) Relative plot of decrease in absorption of DPBF at 400 nm in the presence of **IR-DI**, **IR-MO** and reference $[Ru(bpy)_3]Cl_2$ (Φ_s = 0.22 in water).

Further, the singlet oxygen generation capability of **IR-DI** in aqueous media was calculated using water soluble singlet oxygen sensors ABDA (9,10-Anthracenediyl-bis(methylene)dimalonic acid) and Si-DMA (Silicon 2,9,10-Dimethylanthracene). The detection using the ABDA derivative involves a reaction with singlet oxygen ($^1O_2$),

forming an endoperoxide through a [4+2]-cycloaddition. This reaction leads to the disruption of the extended π-electron system, resulting in the loss of its characteristic spectroscopic properties. The decrease in ABDA absorbance of **IR-DI**, **IR-MO** and $[Ru(bpy)_3]Cl_2$ (Φ_s = 0.22 in water) are depicted in **Figure 2.9a-c**. The linear correlation of change in absorption with time plotted as in **Figure 2.9d** and the singlet oxygen quantum yields in water for **IR-DI** and **IR-MO** were obtained as 0.66 and 0.34, respectively.

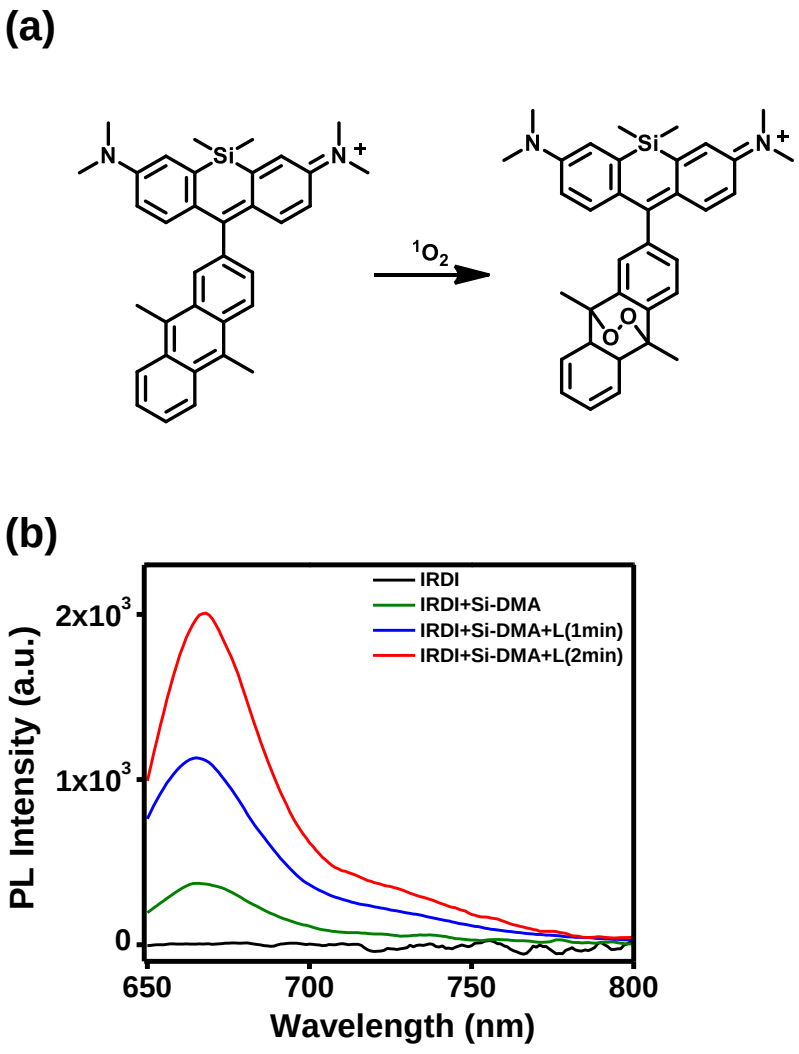

Figure 2.10. (a) Structure and mechanism of singlet oxygen probe Si-DMA and (b) Change in fluorescent intensity of **IR-DI** in presence of Si-DMA with 1 min and 2 min light irradiation.

To further support the claim, we have carried out the singlet oxygen generation study using Si-DMA probe as in **Figure 2.10a&b**. The Si-DMA fluorescence probe composed of silicon-conjugated rhodamine and anthracene moieties act as a chromophore and a $^1O_2$ reactive site. The presence of $^1O_2$ facilitate an endoperoxide formation at the anthracene moiety which enhance the fluorescence emission of Si-DMA to selectively detect the $^1O_2$ species. Here, the **IR-DI** incubated with singlet oxygen sensor Si-DMA is exhibiting an emission in the range of 670 nm. Upon laser irradiation the production of singlet oxygen by **IR-DI** leads to enhancement of emission intensity of Si-DMA. The laser irradiation of 1 min and 2 min exhibited a spike in the emission intensity, which confirms the photoinduced singlet oxygen generation by **IR-DI** in the aqueous media.

Further the cyclic voltammetry curve was obtained for the iridium complexes **IR-DI** and **IR-MO** in acetonitrile using ferrocene as standard.

$$E_{HOMO} = -(E_{ox} - E_{Fc/Fc+} + 4.8) \quad (1)$$

$$E_{LUMO} = -(E_{red} - E_{Fc/Fc+} + 4.8) \quad (2)$$

$$\Delta E_{gap} = E_{LUMO} - E_{HOMO} \quad (3)$$

By using equations 1 and 2, the HOMO and LUMO energy levels (E_{HOMO} and E_{LUMO}) of both the iridium dinuclear complexes were calculated **(Figure 2.11a,b)**.[50] The results of the cyclic voltammetry reveal that the E_{HOMO} values for **IR-DI** and **IR-MO** are -6.12 eV and -6.03 eV, respectively, while the E_{LUMO} values are -3.40 eV for **IR-DI** and -3.11 eV for **IR-MO**. The energy gap (ΔE_{gap}) was calculated using Equation 3, resulting in values of 2.73 eV for **IR-DI** and 2.92 eV for **IR-MO**. A summary of all the photophysical and electrochemical data is presented in **Table 2.1**.

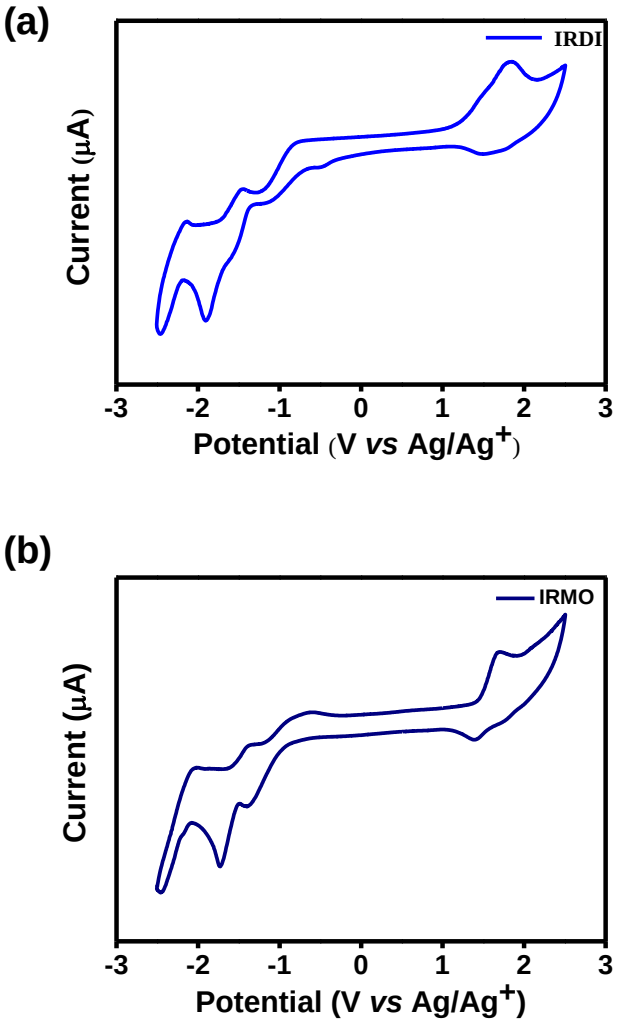

Figure 2.11. Cyclic voltammetry curve in acetonitrile using ferrocene as standard: (a) **IR-DI** and (b) **IR-MO**.

Table 2.1. Photophysical and Electrochemical Properties for Ir(III) complexes.

Complex	**λ_{abs}[a] (nm)**	**λ_{ems}[b] (nm)**	**HOMO[c] (eV)**	**LUMO[d] (eV)**	**E_g[e] (eV)**	**Φ_p[f]**	**Φ_s[g]**	**Φ_s[h]**	**Lifetime[h] (ns)**
IR-DI	365	525	-6.12	-3.40	2.73	0.70	0.49	0.66	185
IR-MO	365	519	-6.03	-3.11	2.92	0.47	0.28	0.34	97

[a]Absorption maxima. [b]Emission maxima. [c,d]HOMO and LUMO determined by cyclic voltammograms in degassed acetonitrile. [e]Eg = (E_{ox} − E_{red}) [eV]. [f]Φ_p refers to the photoluminescence quantum yield, with $Ir(ppy)_3$ in dichloroethane (Φ_p = 0.89) as the reference. [g]Φ_s refers to singlet oxygen quantum yield with $[Ru(bpy)_3]Cl_2$ in acetonitrile (Φ_s = 0.57) as a reference . [h]Φ_s refers to singlet oxygen quantum yield with $[Ru(bpy)_3]Cl_2$ in water (Φ_s = 0.22) as a reference. [h]Lifetime data (excitation wavelength 365 nm).

The presence of two heavy metals in the dinuclear Ir(III) complex, **IR-DI** facilitate enhanced spin-orbit coupling, resulting in effective intersystem crossing (ISC) and high population of triplet excited states. As a result of their long lasting triplet excited states, these iridium complexes can efficiently interact with oxygen, leading to high yields of singlet oxygen generation. The dinuclear **IR-DI** reported in this work is designed to address the emission quenching exhibited by dinuclear systems in general, which marked them as less potential candidates for PDT applications. Here the ethyl spacer in **IR-DI** eliminates the chance of electronic coupling of monomer units via conjugation and the energy transfer by FRET, which happen to be the main reasons for poor PL performance of dinuclear complexes.[41, 43, 49, 51, 52] Further, the extra positive charge also augment the mitochondria targeting ability of the dinuclear complex by utilizing the negative membrane potential.[53-56] As the dinuclear complex, **IR-DI** exhibited better photophysical performance compared to **IR-MO** in all aspects, **IR-DI** was subjected to detailed *in vitro* studies.

2.3.3. In vitro Assessment of Photodynamic Therapy

2.3.3.1. Cytotoxicity, Internalization, and Mitochondrial Targeting of IR-DI in MDA-MB-231 cells

The cytotoxicity of a dinuclear complex, **IR-DI** was evaluated in the triple-negative breast cancer cell line MDA-MB 231. An ideal photosensitizer should exhibit minimal toxicity in the dark and become cytotoxic when exposed to light.[57, 58] To understand the cytotoxicity of **IR-DI**, MTT assay was performed using the triple-negative breast cancer cell line MDA-MB 231 and normal breast epithelial cell line, MCF-10A. The complex **IR-DI** demonstrated a proliferation of cells above 90% at a 10 µM concentration, confirming its non-toxic nature. Subsequent experiments involving varying concentrations of **IR-DI** (ranging from 0 µM to 100 µM) at 24 h incubation revealed minimal dark toxicity up to 20

µM concentrations (**Figure 2.12a**). The IC_{50} value calculated for **IR-DI** with laser is 5.31 µM and without laser is 48.3 µM by concentration dependent cytotoxicity profiling of MDA-MB-231 cells using MTT assay. To assess the non-toxicity of **IR-DI** in normal cells, MTT assay was carried out in a normal breast epithelial cell line, MCF-10A with doxorubicin as the standard. The results showed no significant dark toxicity at 10 µM concentration (**Figure 2.12b**).

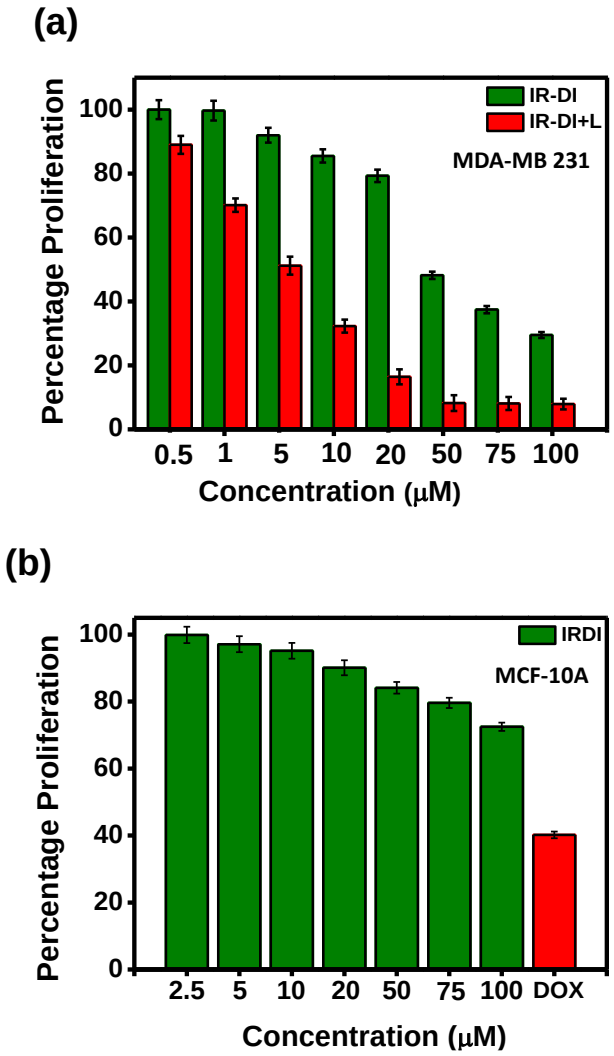

Figure 2.12. (a) *In vitro* cytotoxicity profiling of **IR-DI** in MDA-MB-231 cells at 24 h using MTT assay in presence and absence of light irradiation and (b) *In vitro* cytotoxicity profiling of **IRDI** in MCF-10A cells at 24 h using MTT assay.

To better understand the cellular uptake of **IR-DI** in MDA-MB 231 cells, time and concentration dependent internalization studies were performed. Cells were exposed to 10 µM concentration of **IR-DI** in plain DMEM, and the green fluorescence of **IR-DI** was monitored in a time dependent manner. The intensity of green fluorescence increased from 0 to 3 h, indicating the progress of cellular uptake (**Figure 2.13a,b**). The green fluorescence signals were detectable from 30 min onwards and reached their maximum intensity at 3 h, identifying the optimum internalization time as 3 h. Subsequently, concentration-dependent internalization experiments with various **IR-DI** concentrations ranging from 0 µM to 30 µM exhibited a gradual increase in green fluorescence intensity with rising **IR-DI** concentrations (**Figure 2.13c,d**). Based on these findings and considering the dark toxicity results, a 10 µM concentration of **IR-DI** was selected as an ideal concentration for *in vitro* studies.

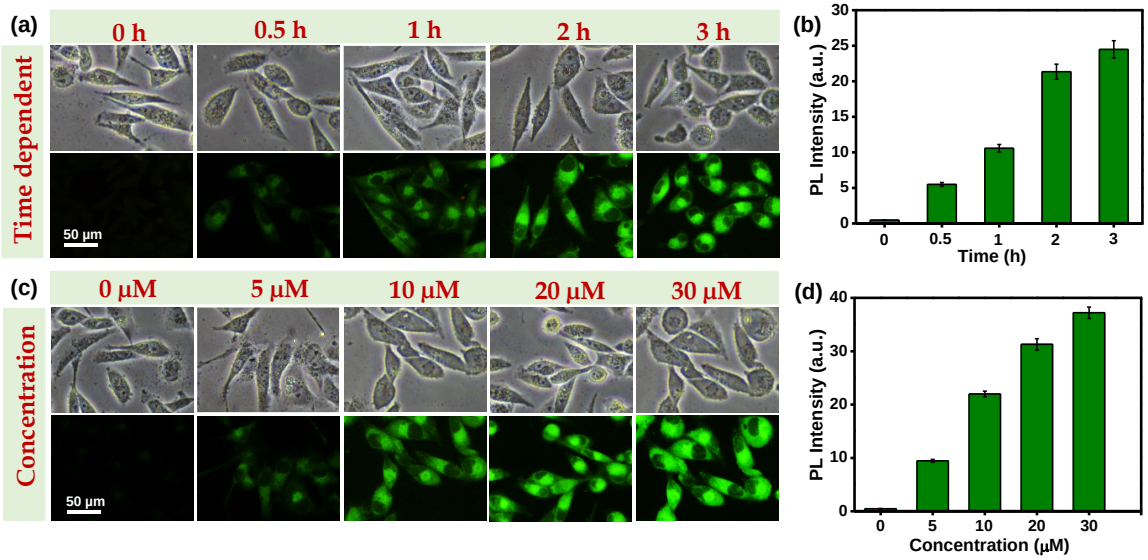

Figure 2.13. (a) Time-dependent fluorescent cell images from 0 h to 3 h incubation; (b) Time-dependent fluorescent intensity quantification of **IR-DI** treated MDA-MB 231 cells; (c) Concentration-dependent internalization of **IR-DI** from 0 µM to 30 µM probed using fluorescence microscopy and (d) Concentration dependent fluorescent intensity quantification of **IR-DI**.

Mitochondria-targeted photodynamic therapy (PDT) is a cutting-edge approach that holds immense promise in the treatment of various diseases, particularly cancer.[23, 59-62] This innovative technique involves using photosensitizing agents specifically designed to accumulate within the mitochondria, the energy powerhouses of cells. The advantage of this targeting lies in its ability to selectively destroy mitochondria within diseased cells while leaving healthy ones unaffected, resulting in a more precise and less harmful treatment. By disrupting the crucial functions of the mitochondria, such as energy production and cellular signalling, this therapy can effectively imposed for cell death in the targeted diseased tissues. **IR-DI** exhibits a unique di-cationic structure that enables its specific accumulation in mitochondria. This phenomenon is attributed to the negative membrane potential found in these organelles, which actively attracts cationic species. Consequently, cationic iridium complexes are more prone to being internalized by the mitochondria.[61, 63] To confirm the mitochondrial targeting properties of **IR-DI** in MDA-MB-231 cells, co-incubation experiments were performed with a mitochondria-specific dye, MitoTracker™ Red (**Figure 2.14a**). Fluorescence images displayed a high congruency with a Pearson's correlation coefficient (PCC) of 0.90, strongly indicating the localization of **IR-DI** in the mitochondria.

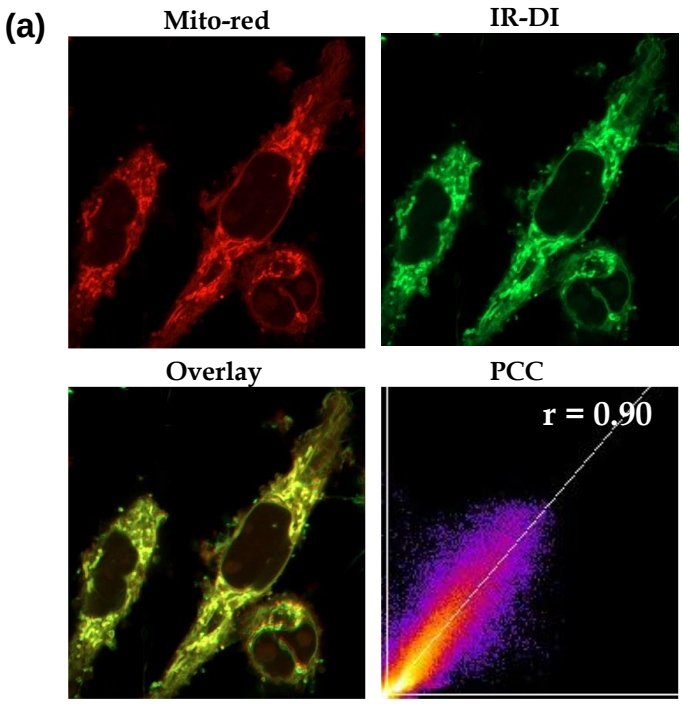

Figure. 2.14. (a) The mitochondrial localization images of **IR-DI** treated cells MitoTracker Red staining assay and corresponding scatter plot.

To further verify the non-nuclear localization of the complex, co-localization studies were conducted with the nuclear-targeted dye Hoechst. Hoechst's blue fluorescence was clearly visible in the nuclear region, while the green fluorescence of **IR-DI** was exclusively observed in the cytoplasm. This non-nuclear localization was confirmed with a Pearson's correlation coefficient (PCC) of 0.33 upon co-localization with Hoechst (**Figure 2.15a**).The subcellular localization of **IR-DI** was confirmed again with the inductively coupled plasma mass spectrometry (ICP-MS) technique. The extraction of subcellular fractions (i.e., mitochondrial, cytosolic, nuclear) after incubation with **IR-DI**, demonstrated 72% of the iridium content in the mitochondrial fraction, confirming mitochondria as the primary target (**Figure 2.15b**).

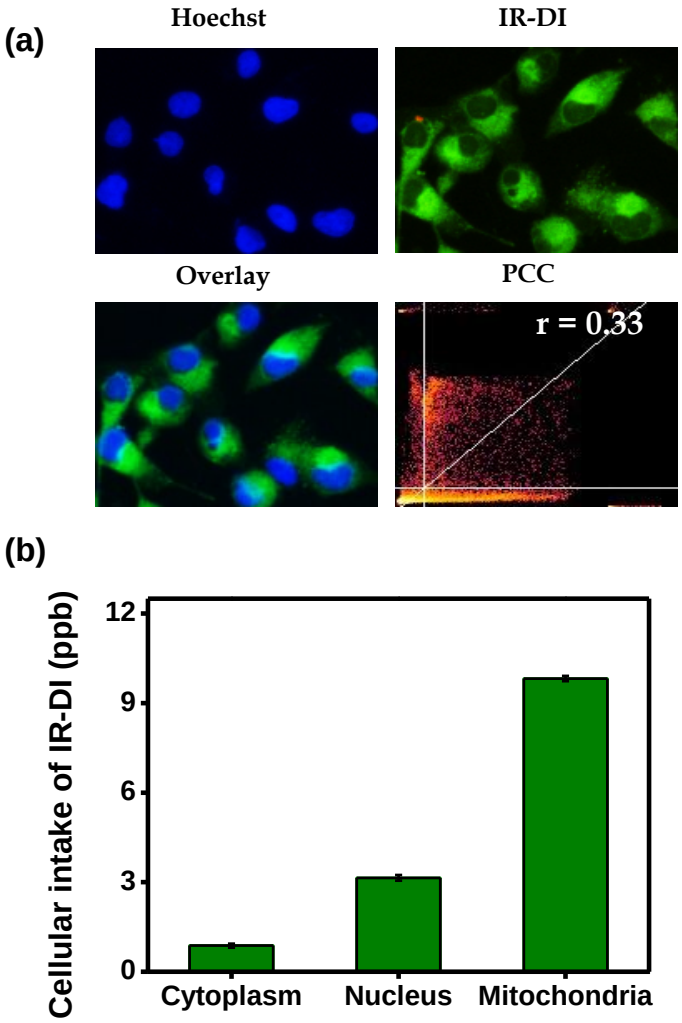

Figure 2.15. (a) The non-nuclear localization images of **IR-DI** treated cells with the nuclear-targeted dye Hoechst and (b) The subcellular distribution of **IR-DI** in the mitochondria, cytoplasm, and nucleus determined by ICP-MS.

2.3.3.2. Photoactivation and PDT studies of IR-DI in MDA-MB 231 cells

The generation of singlet oxygen during the photoexcitation of iridium dimeric complex (**IR-DI**) in MDA-MB 231 cells was verified using a singlet oxygen red probe known as Si-DMA. The experimental procedure entailed the co-administration of **IR-DI** and Si-DMA to the cells, followed by exposure to light irradiation. The detection of a specific red fluorescence signal only in the presence of **IR-DI** upon photoexcitation with a 405 nm laser demonstrated the photochemical capability of **IR-DI** to produce singlet oxygen (**Figure 2.16a**).

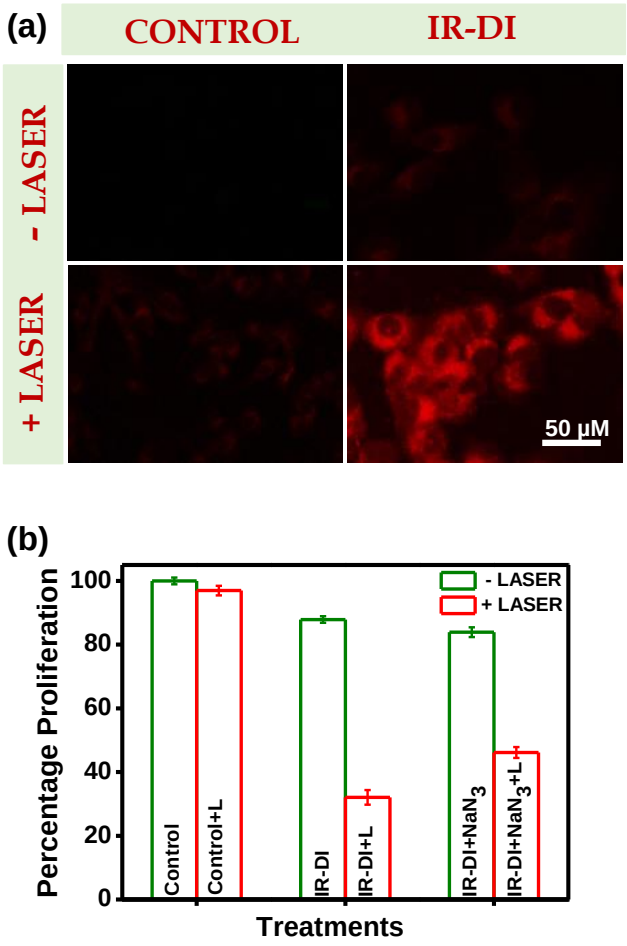

Figure 2.16. (a) The subcellular singlet oxygen generation study of **IR-DI** using Si-DMA in MDA-MB 231 cells and (b) MTT assay showing the photodynamic effect of **IR-DI** treated and laser irradiated cells with and without singlet oxygen scavenger NaN_3; ns $p > 0.05$ and *** $p < 0.001$.

Further to substantiate these findings and establish **IR-DI** as a promising type II photodynamic therapy (PDT) agent, we conducted an in-depth investigation of the photodynamic effect of laser irradiation on **IR-DI**-treated cells in the presence of a singlet oxygen scavenger sodium azide (NaN_3), using the MTT assay (**Figure 2.16b**). Under the influence of the 405 nm laser, cells treated with **IR-DI** (10µM) exhibited a remarkable decrease in viability up to 35%, attributed to the robust generation of singlet oxygen during **IR-DI** photoactivation. Notably, when **IR-DI** was co-incubated with 50 µM of NaN_3, a substantial recovery in cell viability was observed, amounting to an impressive 50% increase. This observation firmly established the potent singlet oxygen-scavenging

properties of NaN_3, leading to a marked enhancement in cell survival. These results provide strong evidence of **IR-DI**'s exceptional capability to induce singlet oxygen production *in vitro,* substantiating its potential as a highly effective type II PDT agent.

2.3.3.3. Cell Death Mechanism of IR-DI in MDA-MB 231 cells

To investigate the mechanism of cell death and the potency of **IR-DI** as a PDT agent, the standard apoptosis assays were performed using MDA-MB-231 cancer cells. The live-dead assays were conducted in the presence of the singlet oxygen scavenger NaN_3 to ascertain the role of singlet oxygen and validate the type II pathway. Membrane changes associated with apoptosis were monitored through trypan blue dye exclusion assay, AO-EB dual fluorescent labelling assay and APOP staining. Trypan blue can differently stain the dead cells only as the healthy cells with intact cell membrane are not permeable to trypan blue and will remain unstained. **Figure 2.17a** showed the results of the trypan blue assay where, only a few number of stained cells with compromised membrane permeability were observed in the control group with **IR-DI** treatment. In contrast, the cells in the laser-irradiated group with **IR-DI** treatment displayed clear apoptotic features and significant trypan blue intake, indicating the efficacy of **IR-DI** as a PDT agent. Furthermore, the acridine orange/ethidium bromide (AO/EB) dual staining assay was utilized to evaluate distinct apoptosis features. AO, a green fluorescent dye, penetrated all viable cells, while the orange-red fluorescence of EB indicated compromised cytoplasmic membrane integrity (**Figure 2.17b**). Cells treated with **IR-DI**, without laser irradiation exhibited green fluorescence whereas cells treated with **IR-DI** after laser irradiation displayed red fluorescence, confirming the presence of apoptotic characteristics.

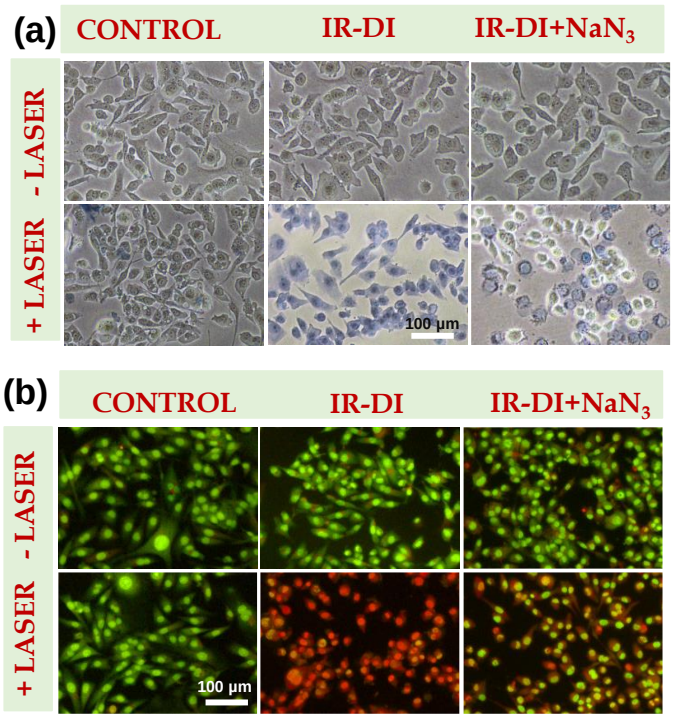

Figure 2.17. The apoptotic evaluation of the **IR-DI** treated cells followed by 405 nm laser excitation. (a) Trypan blue staining assay where apoptotic cells exhibits the blue colour and (b) Acridine orange-ethidium bromide dual staining assay where apoptotic cells stains in orange color.

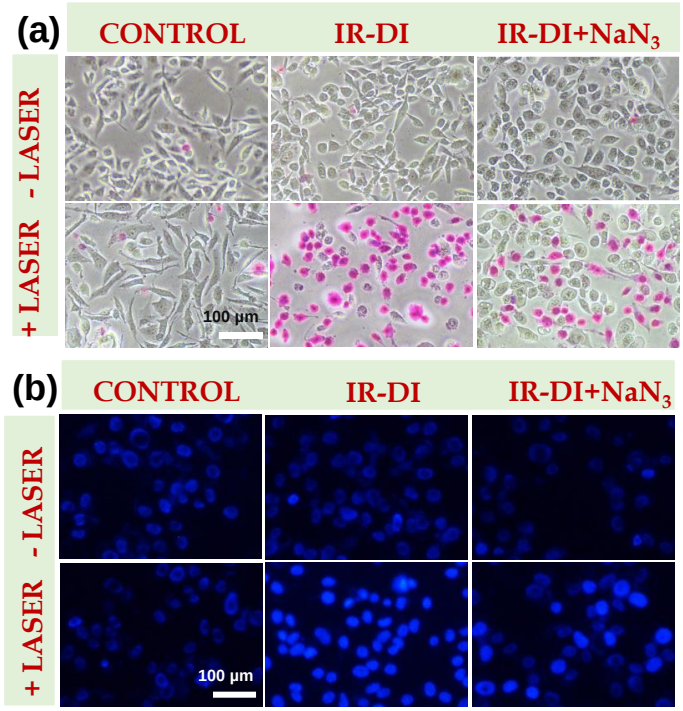

Figure 2.18. The apoptotic evaluation of the **IR-DI** treated cells followed by 405 nm laser excitation. (a) APO Percentage assay showing the dead cells in pink stain and (b) Hoechst staining assay demonstrating the nuclear damage induced by **IR-DI** with enhanced blue emission.

To visualise apoptosis in a non-fluorescent platform, the APO Percentage assay was employed. This assay demonstrated that **IR-DI** and laser treatment induced the uptake of the dye, leading to the appearance of pink-stained dead cells, consistent with expected apoptotic behaviour (**Figure 2.18a**). This observation provides additional evidence of apoptosis occurrence in the experimental context. Additionally, a nuclear staining experiment was also conducted using Hoechst dye, to study the nuclear condensation, yet another hall mark of apoptosis. The results revealed a striking enhancement of blue fluorescence in laser-treated **IR-DI**-incubated cells, indicative of a robust interaction between Hoechst and condensed chromatin, providing strong evidence of DNA damage and apoptosis (**Figure 2.18b**). These findings were consistent with all the live-dead staining assays performed, reinforcing the credibility of the observations. To further confirm the role of singlet oxygen in the apoptotic process triggered by **IR-DI**, cells were pre-treated with NaN_3, leading to a notable reduction in apoptotic features across all assays. This compelling evidence solidifies the classification of **IR-DI** as a type II PDT agent, highlighting its ability to induce apoptosis through the generation of singlet oxygen.

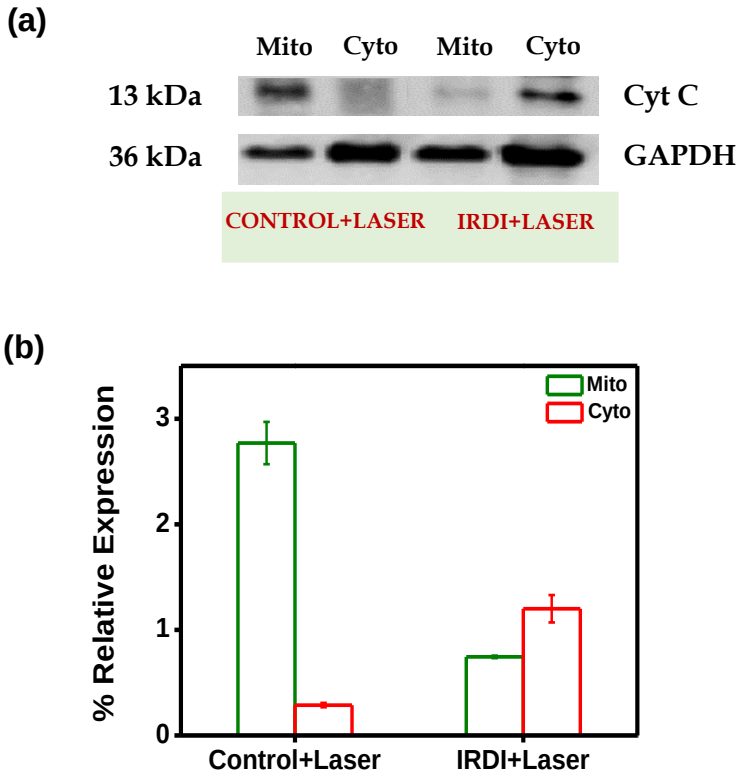

Figure 2.19. (a) Cytochrome C release from mitochondrial membrane to cytosol with **IR-DI**+Laser treatment confirmed with western blot analysis and (b) Corresponding bar diagram representation.

Mitochondria play a critical role in cellular energy production, facilitated by the establishment of a substantial proton gradient across their lipid bilayer, creating a significant membrane potential of approximately 180 mV.[59] However, in the context of photodynamic therapy (PDT), the disruption of mitochondrial membrane potential becomes a pivotal event leading to apoptosis. The administration of **IR-DI** and subsequent light exposure generate singlet oxygen, a highly reactive species that directly targets the mitochondrial membrane. This singlet oxygen interacts with crucial components of the mitochondrial inner membrane, such as cardiolipin, resulting in their peroxidation and subsequent degradation. Consequently, the mitochondrial membrane potential is lost, causing depolarization. Furthermore, the singlet oxygen produced during **IR-DI**

photoactivation triggers lipid peroxidation, interfering with the proper functioning of electron transport chain complexes. This disruption leads to the leakage of electrons and additional ROS production, establishing a self-perpetuating cycle of ROS generation that further damages the mitochondrial membrane and exacerbates depolarization.[64, 65] Cytochrome C (Cyt C) is an inter mitochondrial membrane residing protein which plays a crucial role in apoptosis induction.[66] Several proapoptotic stimuli like ROS can cause the release Cyt C from the mitochondria to the cytoplasm leading to the initiation of apoptotic complex formation. Here, we also have analysed the Cyt C release in to the cytoplasm by checking the levels in mitochondrial and cytosolic fractions. As depicted in **Figure 2.19a,b,** in the **IR-DI** treated laser irradiated cells Cyt C is mostly found in cytosolic fraction and the relative expression of the Cyt C normalized with GAPDH is graphically represented. Whereas the laser exposed untreated cells shows mainly mitochondrial homing of the Cyt C, confirms the mitochondria mediated cell death of **IR-DI**-PDT.

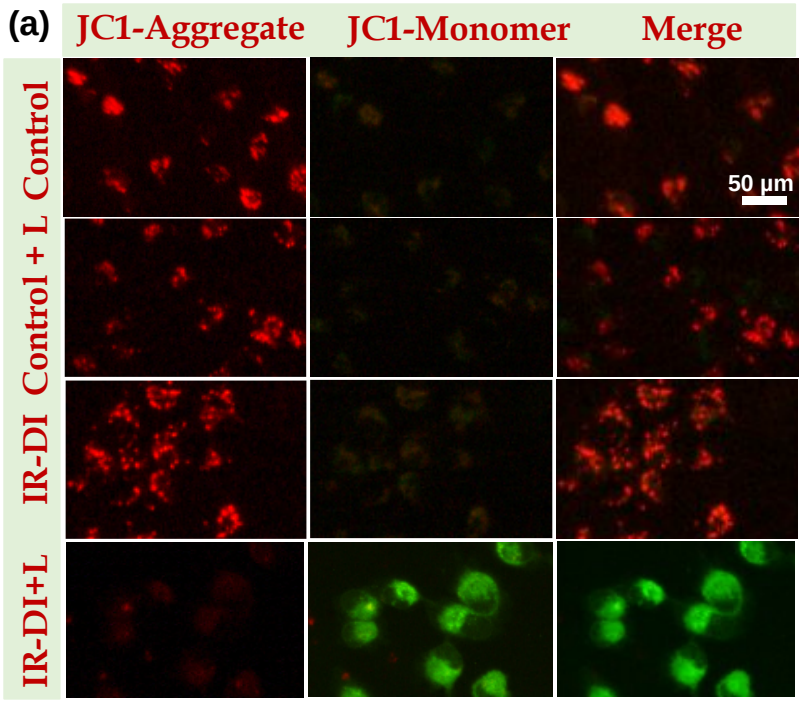

Figure 2.20. (a) Evaluation of mitochondrial membrane potential using JC-1 assay, the elevation of green colour in the green panel indicate the reduction in membrane potential.

To further validate the claim, the widely used JC-1 assay was performed for direct monitoring of mitochondrial membrane potential. JC-1 is a cationic dye that selectively accumulates in mitochondria, where it exhibits potential-dependent fluorescence. In healthy cells, JC-1 forms aggregates that emit red fluorescence, while in cells with low mitochondrial potential, it remains in its monomeric form, emitting green fluorescence. The red-to-green fluorescence ratio provides a reliable measure of mitochondrial health and cell viability. In **IR-DI**-treated MDA-MB-231 cancer cells, mitochondrial membrane depolarization prevents JC-1 dye from accumulating in mitochondria at the required concentration to form red-emissive J-aggregates in the laser-treated groups. Instead, the JC-1 dye predominantly remains in its green-emissive monomeric state, clearly indicating the loss of mitochondrial membrane potential in the **IR-DI**-treated cells subjected to laser irradiation **(Figure 2.20a)**.

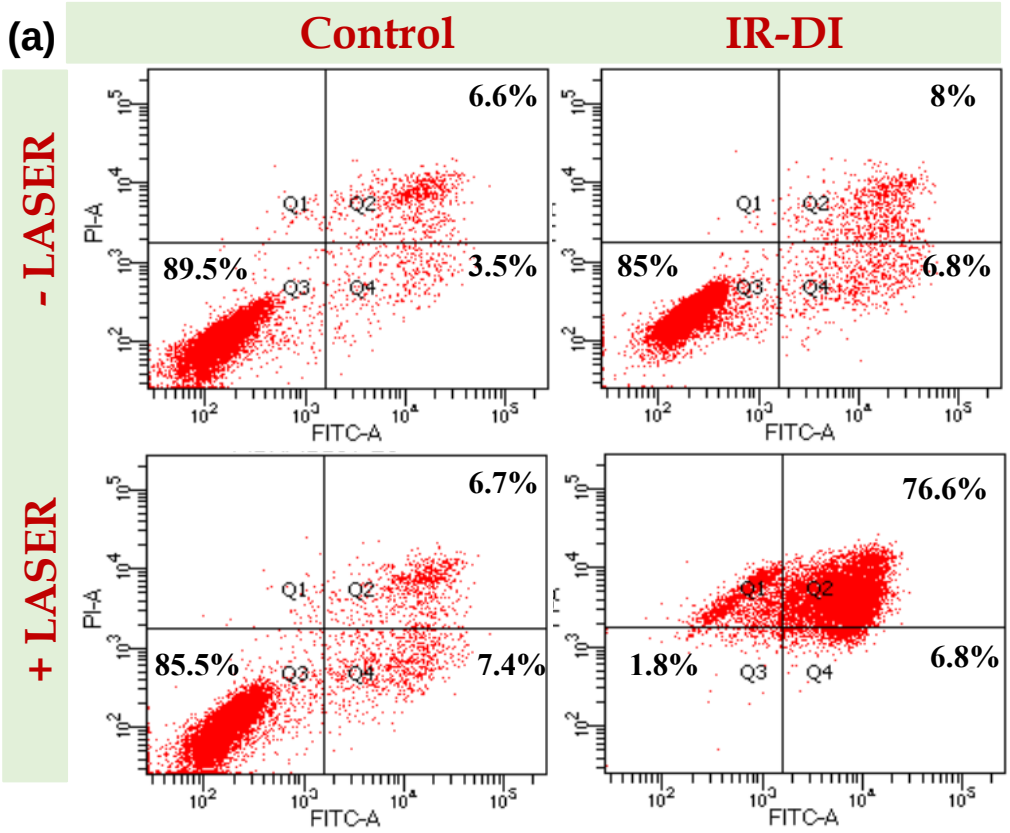

Figure 2.21. (a) The extent of apoptosis was calculated via Annexin V-FITC method using flow cytometry.

Further, we aimed to understand the underlying mechanism of Photodynamic Therapy (PDT) using the **IR-DI** compound, focusing on its impact on cell death in MDA-MB-231 cells. To evaluate this, we employed the Annexin V-FITC/PI flow cytometric assay after subjecting the cells to a 24 h PDT treatment with **IR-DI**, along with laser irradiation. The results depicted in **Figure 2.21a** revealed a remarkable increase in late apoptosis, accounting for approximately 76% of the treated cell population when **IR-DI** was combined with laser activation. In contrast, using **IR-DI** alone without laser exposure resulted in only 8% late apoptosis. Importantly, our study incorporated relevant controls, demonstrating that the activation of **IR-DI** by laser is critical in inducing significant cell death, as cells treated with **IR-DI** without laser exhibited negligible late apoptosis. Furthermore, the control groups (with and without laser) showed minimal apoptosis, reinforcing that the observed effects are specifically attributed to PDT treatment with **IR-DI**. Overall, our findings offer evidence that **IR-DI** predominantly induces apoptosis as the major form of cell death in MDA-MB-231 cells. This discovery holds promising potential for further exploration and potential therapeutic applications of **IR-DI**-based PDT in cancer treatment.

2.4. Conclusion

In conclusion, we report the comparative investigation of the photophysical and biological properties of mononuclear and dinuclear Ir(III) complexes, **IR-MO** and **IR-DI**. The **IR-DI** exhibited a higher singlet oxygen quantum yield of 0.49 compared to that of **IR-MO** (0.28), demonstrating the potential of **IR-DI** as a better PDT agent. The *in vitro* assessment of **IR-DI** was carried out using triple-negative breast cancer cell line MDA-MB-231. The mitochondrial localization of **IR-DI** confirmed using confocal fluorescence imaging with mitochondria-specific dye, MitoTracker red. An efficient laser triggered

apoptotic feature of **IR-DI** on MDA-MB-231 cancer cell line demonstrated via live dead assays such as Trypan, Acridine ethidium bromide, APOP and Hoechst. **IR-DI** mediated PDT was found to trigger Cytochrome C release from mitochondria leading to apoptosome formation. Finally, mitochondrial membrane potential was examined using JC-1 assay and the extent of apoptotic cell death was evaluated by Annexin flowcytometric assay which reinforced **IR-DI** as potential image-guided PDT agent.

2.5. Experimental Section

2.5.1 Materials and General Instruments

The chemicals used in this work, 2-bromopyridine, 2,4-difluorophenylboronic acid, 4,4'-dimethyl-2,2'-bipyridyl, 1,2-bis(4'-methyl-2,2'-bipyridin-4-yl)ethane, potassium carbonate, tetrabutylammonium bromide, $Pd(PPh_3)_4$, $IrCl_3.xH_2O$, NH_4PF_6, and 2-ethoxyethanol were purchased from Sigma Aldrich and TCI Chemicals, used as received without further purification. Moisture and oxygen sensitive reactions were carried out under argon atmosphere in dried solvents purchased from Sigma-Aldrich and Merck chemical suppliers. Thin Layer Chromatography (TLC) analysis was performed using aluminium plates coated with silica gel, purchased from Merck. 100-200 and 230-400 mesh silica gels were used for column chromatography. ^{1}H NMR (500 MHz) and ^{13}C NMR (125 MHz) analysis were achieved using Bruker Avance DPX spectrometer, with TMS as the internal standard ($\delta H = 0$ ppm and $\delta C = 0$ ppm). Acetonitrile-d3 and DMSO-d6 were used as solvents for NMR analysis. High-resolution mass spectra (HRMS) were obtained from Thermo Scientific Q Exactive Hybrid Quadrupole-Orbitrap Electrospray Ionization Mass Spectrometer (ESI-MS).

2.5.2. Photophysical Measurements

The UV/Vis absorption spectra were measured using Shimadzu UV-Vis spectrophotometer (UV-2600) and emission spectra using SPEX Fluorolog spectrofluorimeter. The photostability of the **IR-DI** was studied by recording absorption spectra with freshly prepared 10 µM solution in acetonitrile in presence and absence of light irradiation on an Oriel optical bench model 11200 fitted with 200 W Xenon lamp using a 400 nm band pass filter at regular time intervals. The pH dependent study of **IR-DI** was done by recording the emission spectra of 10 µM solution of **IR-DI** in PBS buffer at different pH range from 5 to 9. Cyclic voltammetric analysis were done using PARSTAT 4000A potentiostat under an argon atmosphere in dry and oxygen-free acetonitrile with 0.1 M tetrabutylammonium hexafluorophosphate (TBAH) as supporting electrolyte. A standard three-electrode configuration utilizing an Ag/AgCl electrode and platinum wire counter electrode was used with the redox potentials referenced to the ferrocene/ferrocenium as standard for the measurement. Singlet oxygen generation quantum yields (Φ_s) were determined using 1,3-diphenylisobenzofuran (DPBF) as the singlet oxygen scavenger for **IR-MO** and **IR-DI**.[12] The DPBF undergoes a [4+2] cycloaddition with $^1O_2$ to form *o*-dibenzoylbenzene, which can be evaluated by a decrease in absorbance of DPBF at 410 nm. The studies were done with a sample concentration ratio 1:10 of Ir(III) complexes and DPBF, irradiated using Oriel lamp fitted with a 400 nm band pass filter at regular time intervals followed by UV-vis measurement. The singlet oxygen quantum yields for **IR-DI** and **IR-MO** in acetonitrile were measured using the reference molecule $[Ru(bpy)_3]Cl_2$ in acetonitrile. ($\Phi_s = 0.57$) using Equation (4)

$$\Phi c = \Phi s \frac{Sc \times Fs}{Ss \times Fc} \qquad \text{Equation (4)}$$

where, S is the slope of a plot of the change in absorbance of DPBF (at 410 nm) with the irradiation time, and F is the absorption correction factor, which is given by $F = 1 - 10^{-OD}$ (OD represents the optical density). The photoluminescence quantum yield of **IR-DI** and **IR-MO** were measured by a relative comparison method using $Ir(ppy)_3$ (Φ_p = 0.89 in dichloroethane) as the standard.[67] The fluorescence lifetime measurements were done using a picosecond single photon counting system (TCSPC) from Horiba (DeltaFlex), and a picosecond photon detection module (PPD-850) as the detector. The fluorescence decay profiles were analysed using EzTime software and fitted with a multi exponential decay model, with a chi-square value 1± 0.2.

2.5.3. *In vitro* studies

MTT assay was performed using MDA-MB-231 breast cancer cell lines (Purchased from ATCC). The cells were seeded in 96 well plate at a density of 12,000 cells/well and maintained for 24 h in DMEM media with 10% FBS. Then, the cells were incubated with **IR-DI** at concentration of 5 µM to 100 µM in different wells for 24 h. After the required incubation MTT assay was performed to get the cell viability. Internalization of **IR-DI** was checked in MDA-MB-231 breast cancer cells. The cells were incubated with **IR-DI** in plain DMEM media at concentration of 5 µM - 30 µM per well. The images were captured from 0 h to 3 h in a time dependent manner (FITC channel).

Mitochondrial colocalization experiments were conducted using commercially available MitoTracker Red (Molecular probes). In these experiments, cells were first incubated with the **IR-DI** molecule for approximately 3 h. After the incubation period, the cells were washed and then treated with a 100 nM concentration of MitoTracker Red. Following a 15-min incubation with MitoTracker Red, the cells were washed twice with PBS. Finally, images were captured using a confocal fluorescent microscope to study the

colocalization of the **IR-DI** molecule and MitoTracker Red within the mitochondria. Again, the mitochondrial localization of the complex **IR-DI** was confirmed using ICP-MS analysis. MDA-MB-231 breast cancer cells were seeded into 16 well plate for 24 h. The medium was removed and replaced with **IR-DI** (10 μM) in plain DMEM. After 3 h incubation, the cells were scraped out, collected in PBS (3 mL) and counted. The cells were pelletized and different subcellular fractions (nuclear, cytosolic and mitochondrial) were collected by repeated centrifugation using the previously reported method.[68] HNO_3 (65%, 1 mL) was added to these fractions and the mixture was incubated at room temperature for 24 h to digest entirely. The solution was then diluted to a final volume of 10 mL with Milli-Q water, and the cellular concentration of iridium was measured using the ICP-MS.

The singlet oxygen generation experiments was performed using Si-DMA(Sigma Aldrich). Cells were incubated with **IR-DI** for 3h prior to the treatment with Si-DMA. After the required incubation, cells were washed two times with PBS and fluorescence images were taken in the inverted fluorescence microscope using TRITC channel.

IR-DI driven cellular cytotoxicity and membrane damages were analysed using various selective staining procedures. For these, MDA-MB-231 cells were seeded in 96 well plate (10000 cells/well), and after 24 h, The cells were incubated with **IR-DI** (10μM) about 3 h, washed with PBS twice and then irradiated with 405 nm laser for 2min (0.5 W laser power). Treatment groups like, **IR-DI** treated/untreated cells with and without laser irradiation were included in all the studies. After 24 h, cells were washed and incubated with corresponding staining agents. Trypan blue dye exclusion study was performed by incubating the **IR-DI** treated laser irradiated cells with 0.2% trypan blue solution in PBS for 5 minutes. Cells were washed and bright field images were captured using inverted microscope. For acridine orange (AO) - ethidium bromide (EB) dual fluorescent staining

assay, the live-dead assay cocktail (5 µg of each in 1 mL PBS), was incubated for 5 minutes with the treated and untreated cells and the images were then captured in green and red fluorescence channels. AO will be taken up by all the cells giving green fluorescence while, orange-red fluorescence of EB indicates membrane compromised dead cells. For APOP assay, the cells were treated as mentioned above, after 24 h, the wells were washed and added the APOP reagent, images were then captured in bright field mode. To examine Hoechst nuclear staining assay, the cell lines were seeded in a 96 well plate for 24 h and incubated with/without **IR-DI** for 3 h followed by the laser irradiation using 405 nm laser. After 24 h washed with PBS and stained with Hoechst dye (10 µg/mL) and images were captured under the DAPI filter of the fluorescence microscope. (UV range excitation, 340-390 nm and emission range, 430-490 nm, green channel images were taken with excitation range, 460-495 nm, emission range, 510-550 nm, whereas, the red channel images MitoTracker with excitation range, 530-550 nm, emission range 575 nm). The Cytochrome C release from mitochondrial membrane to cytoplasm was analysed by protein expression studies using cytosolic and mitochondrial fractions. For this, MDA-MB-231 cells were cultured in 6 well plates at a density of $1.5x10^5$ cells/well and after 24 h cells were treated with and without **IR-DI** for 3 h. Laser irradiation was given as mentioned above and incubated the plates for 8 h. Cells were then washed and scraped out to isolate the mitochondrial and cytosolic fraction as per the reported procedure and western blot analysis was performed for Cytochrome C with GAPDH as loading control.[66] The JC-1 assay was employed to analyse mitochondrial membrane depolarization in this study. Cells were cultured in 48-well plates at a density of 12,000 cells per well and subjected to various treatments as per the experimental requirements. The cells were then incubated for approximately 24 h to allow for cellular responses. After the treatment period, the cells were carefully washed to remove any residual substances and then incubated with JC-1 dye

at a concentration of 2 μM for 15 min. Following the incubation with JC-1 dye, the cells were washed again with phosphate-buffered saline (PBS) to remove excess dye. Finally, images of the cells were captured using a fluorescent microscope, with separate channels for green and red fluorescence. The intensity of green and red fluorescence in the images indicates the extent of mitochondrial membrane depolarization, providing valuable insights into the mitochondrial health and function of the treated cells. Further, Annexin binding assay was carried out to confirm the cellular apoptosis. For this, cells were seeded in 6 well plates (1.5×10^5 cells/well) and treated with or without **IR-DI**. Laser irradiation was carried out for the required treatment groups. After 24 h of laser treatment, cell were harvested by trypsinization and performed the Annexin V-FITC-PI staining as per the manufacturer's instructions provided in the Apoptosis Detection Kit (BD Pharmingen) and flow cytometric analysis carried out using FACS Aria (BD, USA).

2.5.4. Synthesis and Characterization of the molceules

2.5.4a.Synthesis of **dfppy** ligand

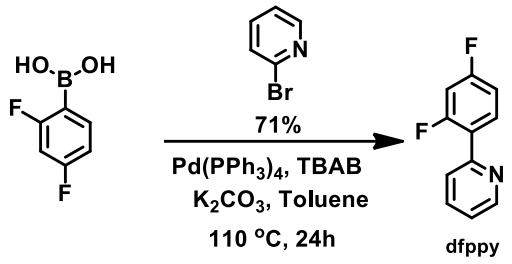

Scheme 2.1

To a mixture of 2-bromopyridine (500 mg, 3.1 mmol) and 2,4-difluorophenylboronic acid (496 mg, 3.1 mmol) in 25 mL toluene, 2M K_2CO_3 (7 g in 25 mL distilled water) and TBAB (3.2 g, 8.42 mmol) was added. Then tetrakis(triphenylphosphine) palladium (0) was charged in to it after 30 minutes of stirring under argon atmosphere, followed by continuous stirring and refluxing for 24 h. After being cooled, the mixture was extracted with

dichloromethane (DCM) and water. The crude product was then purified by silica column chromatography with 50% DCM and n-hexane as the eluent to give colourless liquid product in 71 % yield. ^{1}H NMR (500 MHz, DMSO-d_6): δ 8.70 (d, 1H), δ 8.01 (m, 1H), δ 7.73 (s, 2H), δ 7.23 (m, 1H), δ 7.01 (m, 1H), δ 6.90 (m, 1H). HRMS: Calculated for $C_{11}H_7F_2N$ with m/z 191.05, where z =1, found: 192.06.

2.5.4b.Synthesis of **$[(dfppy)_2IrCl]_2$**

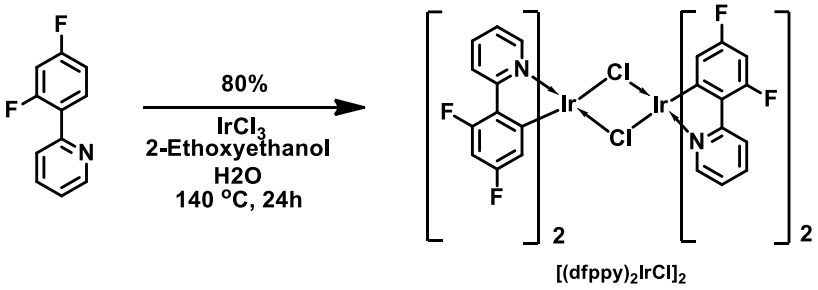

Scheme 2.2

A solution of $IrCl_3.nH_2O$ (300 mg, 0.85 mmol) and dfppy (406 mg, 2.1 mmol) in 2-ethoxyethanol (12 mL) / water (4 mL) mixture was refluxed for 24 h. After the solution was cooled, the addition of distilled water gave a pale yellow precipitate that was filtered and washed with hexane and diethyl ether. The yellow crude product in 80% yield was used for the next reaction without further purification. HRMS: Calculated for $C_{11}H_7F_2N$ with m/z 1216.05, where z =1, found: 513.05.

2.5.4c. Synthesis of **IR-MO**

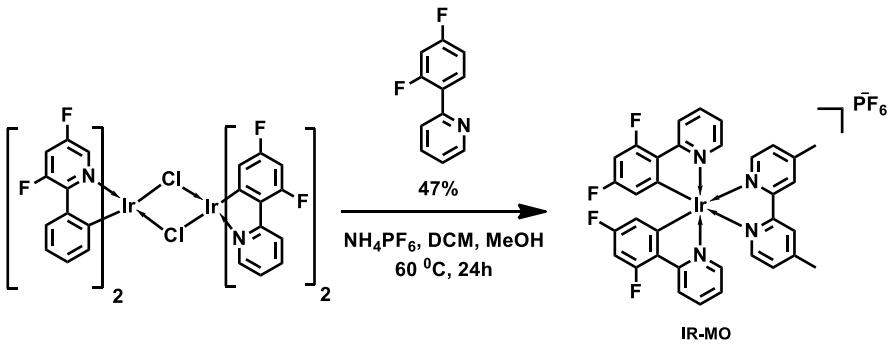

Scheme 2.3

A mixture of $[(dfppy)_2IrCl]_2$ (100 mg, 0.08 mmol) and 4,4'-dimethyl-2,2'-dipyridyl (bpy) (45 mg, 0.24 mmol) were refluxed for 12 h in CH_2Cl_2/CH_3OH (1:1) solution under argon atmosphere. After being cooled, the solvent was removed under reduced pressure. Then purified by silica column chromatography with DCM and methanol as the eluent followed by precipitation with saturated NH_4PF_6 solution to yield. yellow coloured powder (47%). ^{1}H NMR (500 MHz, DMSO-d_6, TMS): δ 8.76 (s, 2H), δ 8.30 (d, 2H), δ 8.05 (m, 2H), δ 7.74 (d, 2H), δ 7.69 (d, 2H), δ 7.54 (d, 2H), δ 7.25 (m, 2H), δ 6.96 (m, 2H), δ 5.63 (d, 2H), δ 2.54 (d, 6H). ^{13}C NMR (125 MHz, DMSO-d_6): δ 164.2, 163.3, 162.2, 160.1, 155.3, 155.2, 152.5, 149.9, 140.4, 130.0, 128.0, 126.2, 123.8, 123.7, 113.7, 99.3, 21.43. HRMS: Calculated for $C_{34}H_{24}F_4IrN_4^+$ with m/z 757.16, where z =1, found: 757.15.

2.5.4d.Synthesis of **IR-DI**

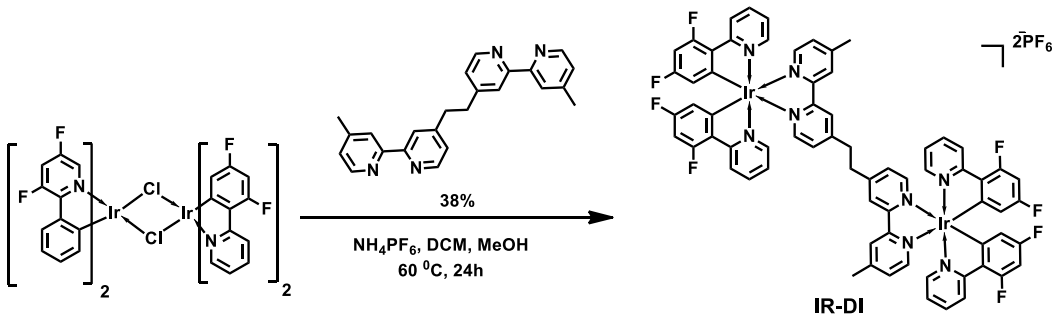

Scheme 2.4

A mixture of $[(dfppy)_2IrCl]_2$ (100 mg, 0.08 mmol) and 1,2-bis(4'-methyl-2,2'-bipyridin-4-yl) ethane (bpye) (30 mg, 0.08 mmol) were refluxed for 48 h in CH_2Cl_2/CH_3OH (1:1) solution under argon atmosphere. After being cooled, the solvent was removed under reduced pressure. Then purified by silica column chromatography with DCM and methanol as the eluent followed by precipitation with saturated NH_4PF_6 solution to yield yellow coloured powder (38%). ^{1}H NMR (500 MHz, Acetonitrile-d_3, TMS): δ 8.78 (s, 2H), δ 8.74 (s, 2H), δ 8.36(d, 2H), δ 8.31 (d, 2H), δ 7.88 (d, 2H), δ 7.82 (t, 4H), δ 7.73 (m, 4H), δ 7.55 (d, 2H), δ 7.43 (d, 2H), δ 7.24 (d, 2H), δ 7.14 (t, 2H), δ 7.03 (t, 2H), δ 6.57 (m, 4H), δ 5.67 (m, 4H), δ 3.24 (m, 4H), δ 2.66 (s, 6H). ^{13}C NMR (125 MHz, DMSO-d_6): δ 164.3, 163.2, 162.2, 155.6, 155.1, 154.8, 152.6, 150.0, 149.4, 140.5, 130.1, 129.3, 128.0, 126.3, 125.6, 124.9, 113.7, 99.5, 34.9, 21.4. HRMS: Calculated for $C_{68}H_{46}F_8Ir_2N_8^{2+}$ with m/z 756.15, where z =2, found 756.15.

2.5.5. NMR and Mass spectrum

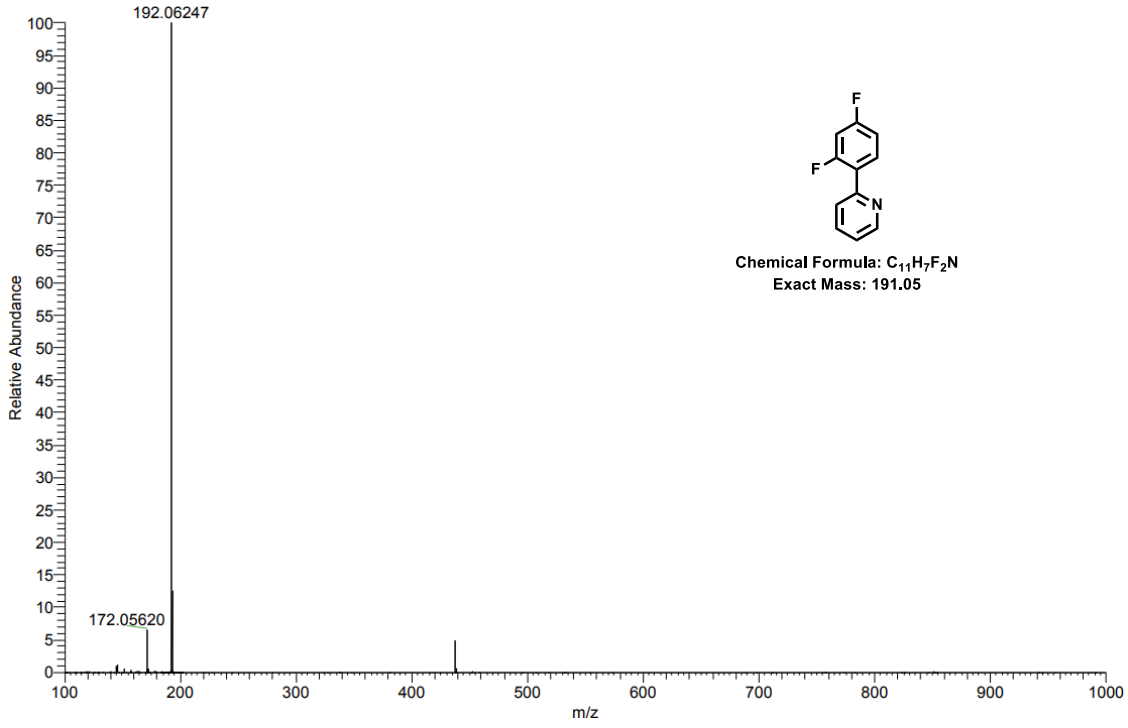

Figure 2.22. HRMS spectra of dfppy

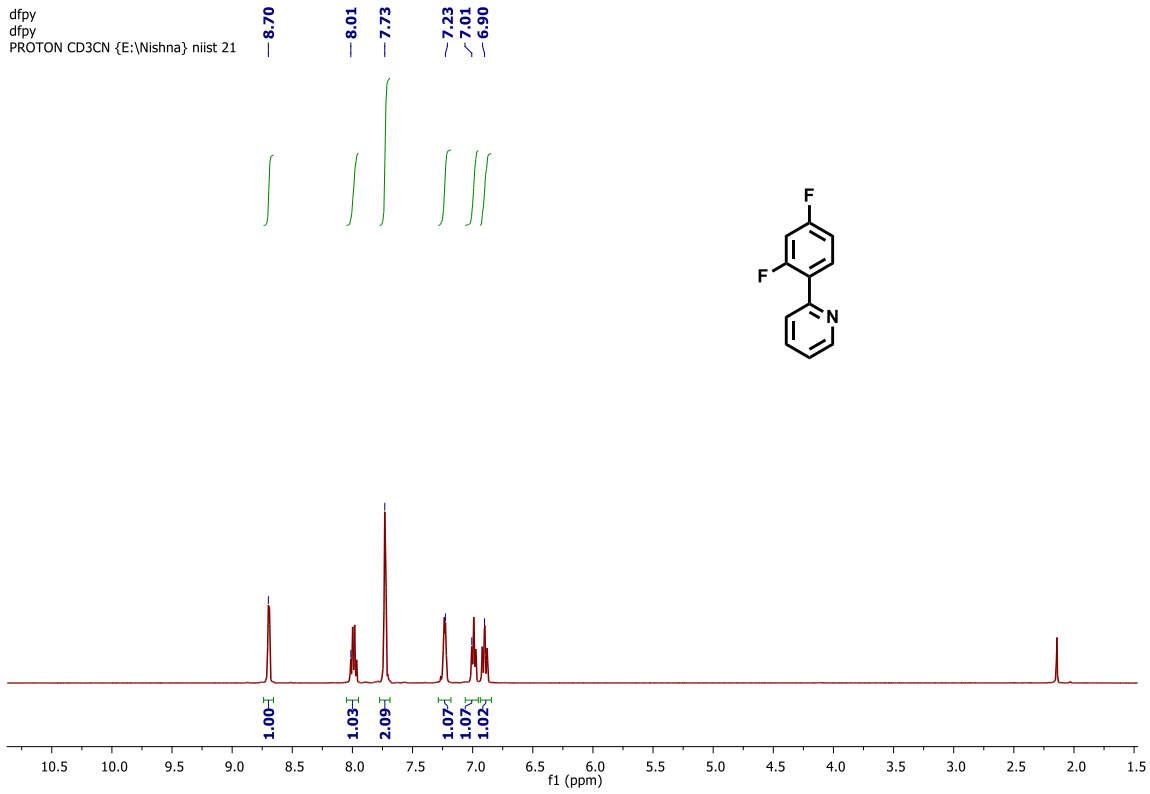

Figure 2.23. ^{1}H NMR spectra of dfppy

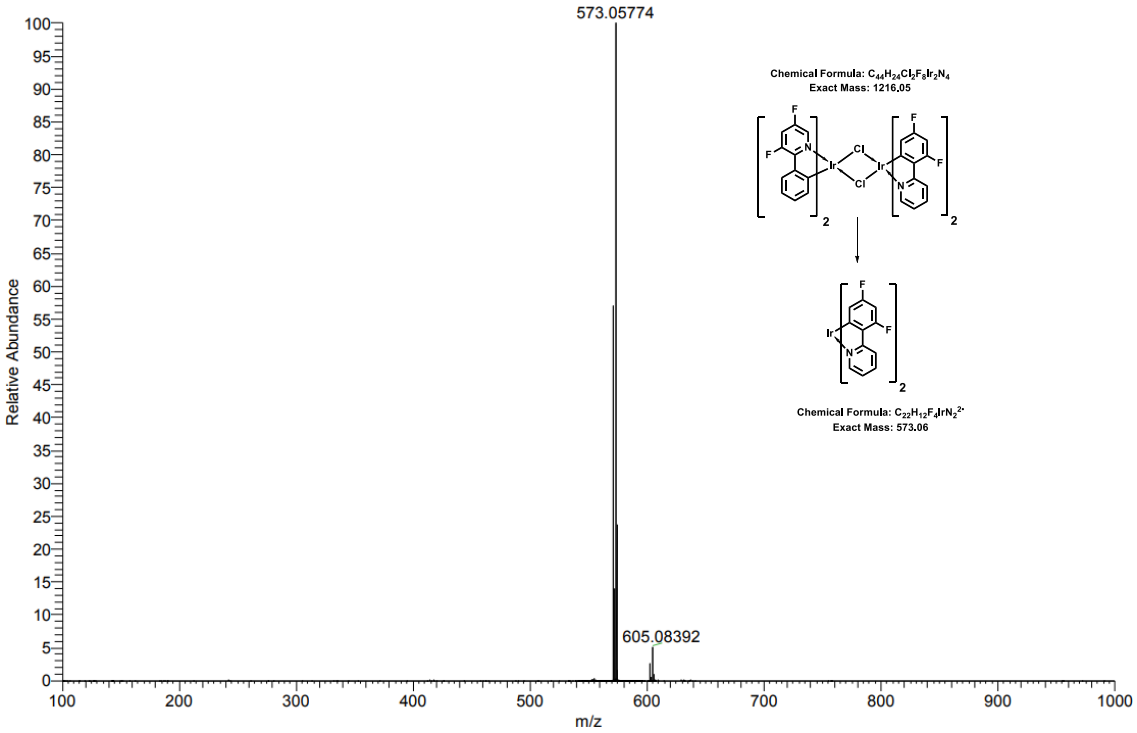

Figure 2.24. HRMS spectra of $[(dfppy)_2IrCl]_2$

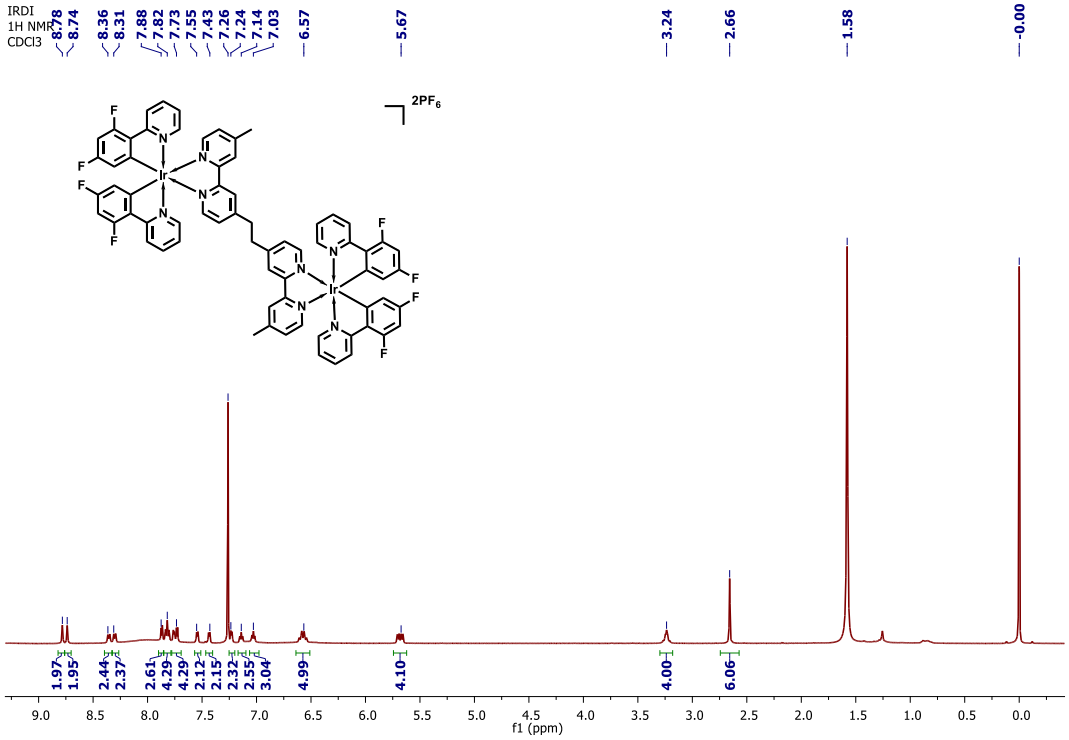

Figure 2.25. ^{1}H NMR spectra of **IR-DI**

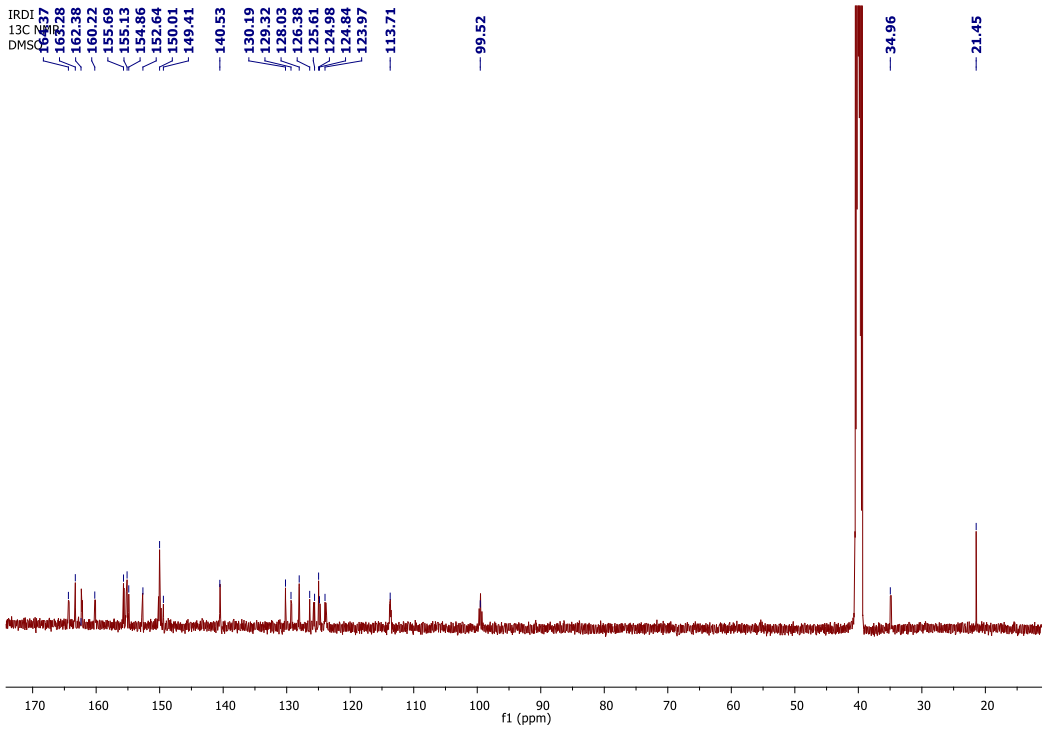

Figure 2.26. ^{13}C NMR spectra of **IR-DI**

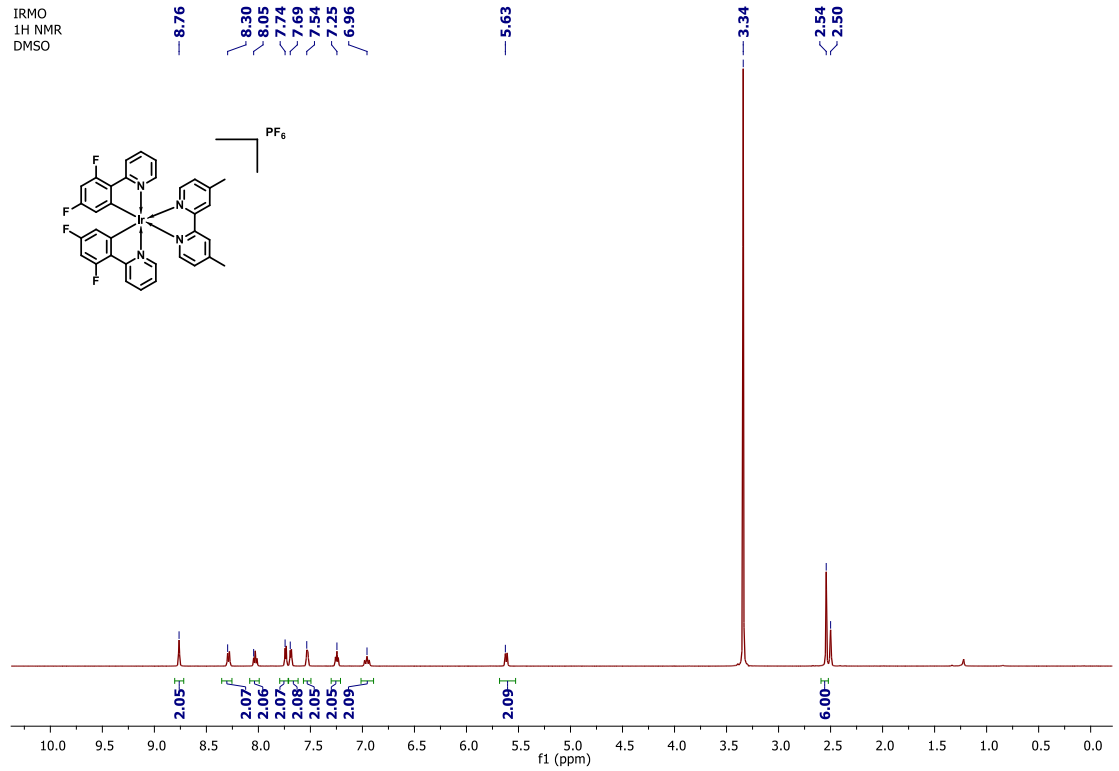

Figure 2.27. ^{1}H NMR specra of **IR-MO**

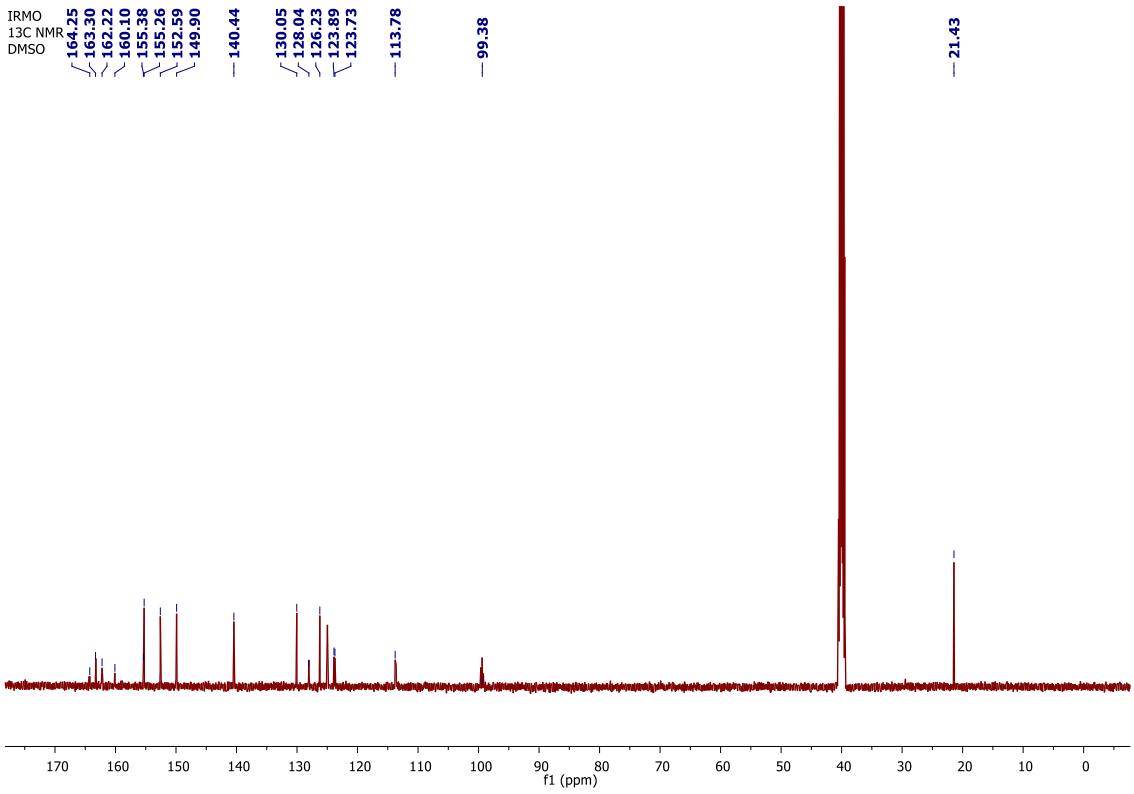

Figure 2.28. ^{13}C NMR spectra of **IR-MO**

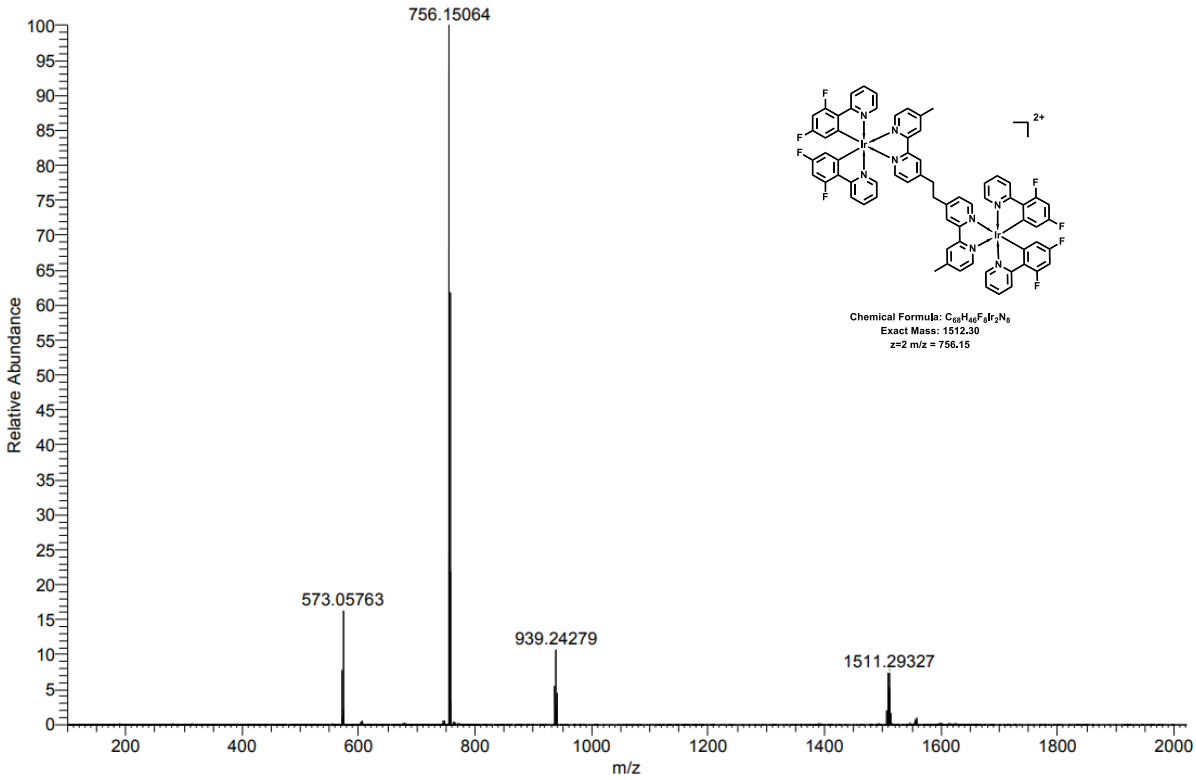

Figure 2.29. HRMS spectra of **IR-DI**

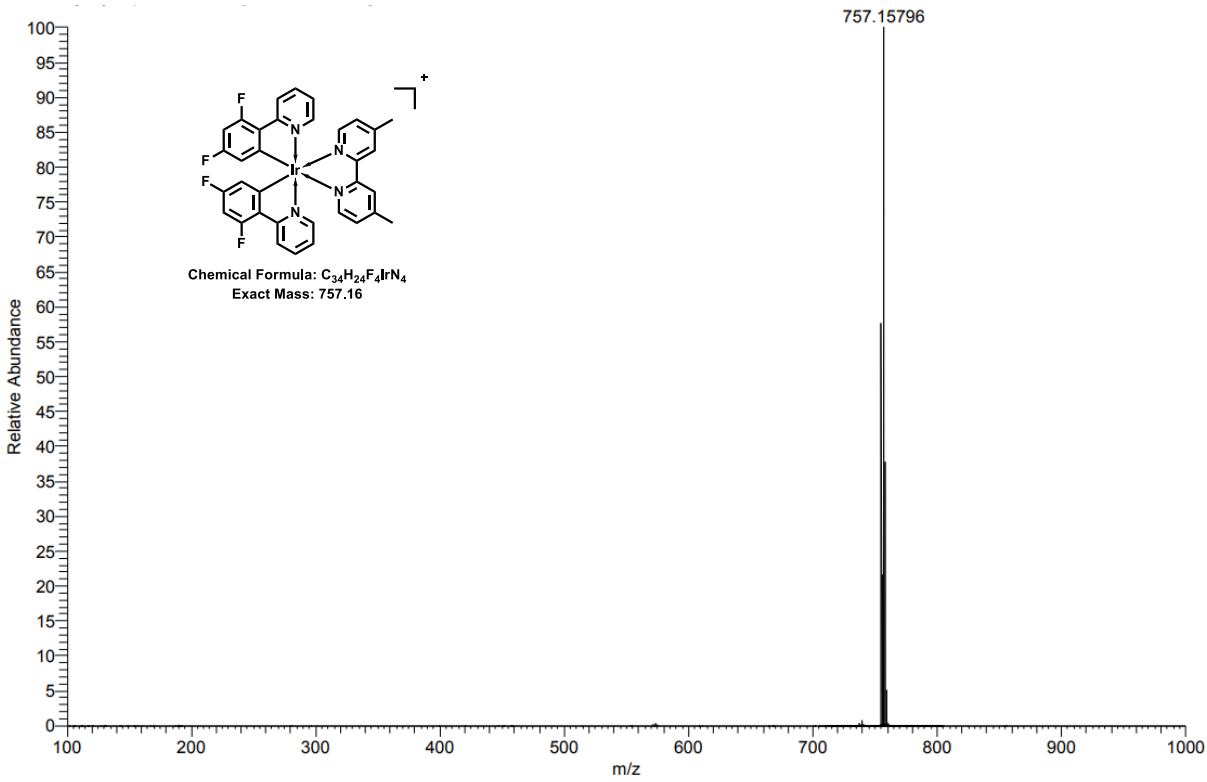

Figure 2.30. HRMS spectra of **IR-MO**

2.6. References

1. Stritt, A.; Merk, H. F.; Braathen, L. R.; Von Felbert, V., Photodynamic Therapy in the Treatment of Actinic Keratosis†. **2008,** *84* (2), 388-398.

2. Smits, T.; Moor, A. C. E., New aspects in photodynamic therapy of actinic keratoses. *Journal of Photochemistry and Photobiology B: Biology* **2009,** *96* (3), 159-169.

3. Jiang, X.; Zhu, N.; Zhao, D.; Ma, Y., New cyclometalated transition-metal based photosensitizers for singlet oxygen generation and photodynamic therapy. *Science China Chemistry* **2016,** *59* (1), 40-52.

4. Li, W.; Yang, J.; Luo, L.; Jiang, M.; Qin, B.; Yin, H.; Zhu, C.; Yuan, X.; Zhang, J.; Luo, Z.; Du, Y.; Li, Q.; Lou, Y.; Qiu, Y.; You, J., Targeting photodynamic and photothermal therapy to the endoplasmic reticulum enhances immunogenic cancer cell death. *Nature Communications* **2019,** *10* (1), 3349.

5. Stritt, A.; Merk, H. F.; Braathen, L. R.; von Felbert, V., Photodynamic therapy in the treatment of actinic keratosis. *Photochemistry and photobiology* **2008,** *84* (2), 388-98.

6. Bevernaegie, R.; Doix, B.; Bastien, E.; Diman, A.; Decottignies, A.; Feron, O.; Elias, B., Exploring the Phototoxicity of Hypoxic Active Iridium(III)-Based Sensitizers in 3D Tumor Spheroids. *Journal of the American Chemical Society* **2019,** *141* (46), 18486-18491.

7. Tavakkoli Yaraki, M.; Liu, B.; Tan, Y. N., Emerging Strategies in Enhancing Singlet Oxygen Generation of Nano-Photosensitizers Toward Advanced Phototherapy. *Nano-Micro Letters* **2022,** *14* (1), 123.

8. Yu, H.; Chen, B.; Huang, H.; He, Z.; Sun, J.; Wang, G.; Gu, X.; Tang, B. Z., AIE-Active Photosensitizers: Manipulation of Reactive Oxygen Species Generation and Applications in Photodynamic Therapy. **2022,** *12* (5), 348.

9. Sarbadhikary, P.; George, B. P.; Abrahamse, H., Recent Advances in Photosensitizers as Multifunctional Theranostic Agents for Imaging-Guided Photodynamic Therapy of Cancer. *Theranostics* **2021,** *11* (18), 9054-9088.

10. McKenzie, L. K.; Bryant, H. E.; Weinstein, J. A., Transition metal complexes as photosensitisers in one- and two-photon photodynamic therapy. *Coordination Chemistry Reviews* **2019,** *379*, 2-29.

11. Pham, T. C.; Nguyen, V.-N.; Choi, Y.; Lee, S.; Yoon, J., Recent Strategies to Develop Innovative Photosensitizers for Enhanced Photodynamic Therapy. *Chemical Reviews* **2021,** *121* (21), 13454-13619.

12. Shamjith, S.; Joseph, M. M.; Murali, V. P.; Remya, G. S.; Nair, J. B.; Suresh, C. H.; Maiti, K. K., NADH-depletion triggered energy shutting with cyclometalated iridium (III) complex enabled bimodal Luminescence-SERS sensing and photodynamic therapy. *Biosensors and Bioelectronics* **2022,** *204*, 114087.

13. Zheng, X.; Tang, H.; Xie, C.; Zhang, J.; Wu, W.; Jiang, X., Tracking Cancer Metastasis In Vivo by Using an Iridium-Based Hypoxia-Activated Optical Oxygen Nanosensor. **2015,** *54* (28), 8094-8099.

14. Li, J.; Chen, T., Transition metal complexes as photosensitizers for integrated cancer theranostic applications. *Coordination Chemistry Reviews* **2020,** *418*, 213355.

15. Huang, T.; Yu, Q.; Liu, S.; Huang, W.; Zhao, Q., Phosphorescent iridium(iii) complexes: a versatile tool for biosensing and photodynamic therapy. *Dalton Transactions* **2018,** *47* (23), 7628-7633.

16. Lee, L. C.-C.; Lo, K. K.-W., Luminescent and Photofunctional Transition Metal Complexes: From Molecular Design to Diagnostic and Therapeutic Applications. *Journal of the American Chemical Society* **2022,** *144* (32), 14420-14440.

17. Kelland, L., The resurgence of platinum-based cancer chemotherapy. *Nature Reviews Cancer* **2007,** *7* (8), 573-584.

18. Su, S.; Chen, Y.; Zhang, P.; Ma, R.; Zhang, W.; Liu, J.; Li, T.; Niu, H.; Cao, Y.; Hu, B.; Gao, J.; Sun, H.; Fang, D.; Wang, J.; Wang, P. G.; Xie, S.; Wang, C.; Ma, J., The role of Platinum(IV)-based antitumor drugs and the anticancer immune response in medicinal inorganic chemistry. A systematic review from 2017 to 2022. *European Journal of Medicinal Chemistry* **2022,** *243*, 114680.

19. Wang, F.-X.; Chen, M.-H.; Lin, Y.-N.; Zhang, H.; Tan, C.-P.; Ji, L.-N.; Mao, Z.-W., Dual Functions of Cyclometalated Iridium(III) Complexes: Anti-Metastasis and Lysosome-Damaged Photodynamic Therapy. *ACS Applied Materials & Interfaces* **2017,** *9* (49), 42471-42481.

20. Guan, R.; Xie, L.; Ji, L.; Chao, H., Phosphorescent Iridium(III) Complexes for Anticancer Applications. **2020,** *2020* (42), 3978-3986.

21. Lo, K. K.-W.; Zhang, K. Y., Iridium(iii) complexes as therapeutic and bioimaging reagents for cellular applications. *RSC Advances* **2012,** *2* (32), 12069-12083.

22. Huang, C.; Liang, C.; Sadhukhan, T.; Banerjee, S.; Fan, Z.; Li, T.; Zhu, Z.; Zhang, P.; Raghavachari, K.; Huang, H., In-vitro and In-vivo Photocatalytic Cancer Therapy with Biocompatible Iridium(III) Photocatalysts. **2021,** *60* (17), 9474-9479.

23. Lv, W.; Zhang, Z.; Zhang, K. Y.; Yang, H.; Liu, S.; Xu, A.; Guo, S.; Zhao, Q.; Huang, W., A Mitochondria-Targeted Photosensitizer Showing Improved Photodynamic Therapy Effects Under Hypoxia. **2016,** *55* (34), 9947-9951.

24. Zamora, A.; Vigueras, G.; Rodríguez, V.; Santana, M. D.; Ruiz, J., Cyclometalated iridium(III) luminescent complexes in therapy and phototherapy. *Coordination Chemistry Reviews* **2018,** *360*, 34-76.

25. Nam, J. S.; Kang, M.-G.; Kang, J.; Park, S.-Y.; Lee, S. J. C.; Kim, H.-T.; Seo, J. K.; Kwon, O.-H.; Lim, M. H.; Rhee, H.-W.; Kwon, T.-H., Endoplasmic Reticulum-Localized

Iridium(III) Complexes as Efficient Photodynamic Therapy Agents via Protein Modifications. *Journal of the American Chemical Society* **2016,** *138* (34), 10968-10977.

26. Huang, H.; Banerjee, S.; Sadler, P. J., Recent Advances in the Design of Targeted Iridium(III) Photosensitizers for Photodynamic Therapy. **2018,** *19* (15), 1574-1589.

27. Manav, N.; Kesavan, P. E.; Ishida, M.; Mori, S.; Yasutake, Y.; Fukatsu, S.; Furuta, H.; Gupta, I., Phosphorescent rhenium-dipyrrinates: efficient photosensitizers for singlet oxygen generation. *Dalton Transactions* **2019,** *48* (7), 2467-2478.

28. Prieto-Castañeda, A.; Lérida-Viso, A.; Avellanal-Zaballa, E.; Sola-Llano, R.; Bañuelos, J.; Agarrabeitia, A. R.; Martínez-Máñez, R.; Ortiz, M. J., Phosphorogenic dipyrrinato-iridium(III) complexes as photosensitizers for photodynamic therapy. *Dyes and Pigments* **2022,** *197*, 109886.

29. Gao, R.; Ho, D. G.; Hernandez, B.; Selke, M.; Murphy, D.; Djurovich, P. I.; Thompson, M. E., Bis-cyclometalated Ir(III) Complexes as Efficient Singlet Oxygen Sensitizers. *Journal of the American Chemical Society* **2002,** *124* (50), 14828-14829.

30. Kuang, S.; Wei, F.; Karges, J.; Ke, L.; Xiong, K.; Liao, X.; Gasser, G.; Ji, L.; Chao, H., Photodecaging of a Mitochondria-Localized Iridium(III) Endoperoxide Complex for Two-Photon Photoactivated Therapy under Hypoxia. *Journal of the American Chemical Society* **2022,** *144* (9), 4091-4101.

31. Kuang, S.; Sun, L.; Zhang, X.; Liao, X.; Rees, T. W.; Zeng, L.; Chen, Y.; Zhang, X.; Ji, L.; Chao, H., A Mitochondrion-Localized Two-Photon Photosensitizer Generating Carbon Radicals Against Hypoxic Tumors. **2020,** *59* (46), 20697-20703.

32. Wang, L.; Karges, J.; Wei, F.; Xie, L.; Chen, Z.; Gasser, G.; Ji, L.; Chao, H., A mitochondria-localized iridium(iii) photosensitizer for two-photon photodynamic immunotherapy against melanoma. *Chemical science* **2023,** *14* (6), 1461-1471.

33. Wang, D.; Huang, H.; Zhou, M.; Lu, H.; Chen, J.; Chang, Y.-T.; Gao, J.; Chai, Z.; Hu, Y., A thermoresponsive nanocarrier for mitochondria-targeted drug delivery. *Chemical Communications* **2019,** *55* (28), 4051-4054.

34. Yuan, L.; Wang, L.; Agrawalla, B. K.; Park, S.-J.; Zhu, H.; Sivaraman, B.; Peng, J.; Xu, Q.-H.; Chang, Y.-T., Development of Targetable Two-Photon Fluorescent Probes to Image Hypochlorous Acid in Mitochondria and Lysosome in Live Cell and Inflamed Mouse Model. *Journal of the American Chemical Society* **2015,** *137* (18), 5930-5938.

35. Tian, X.; Zhu, Y.; Zhang, M.; Luo, L.; Wu, J.; Zhou, H.; Guan, L.; Battaglia, G.; Tian, Y., Localization matters: a nuclear targeting two-photon absorption iridium complex in photodynamic therapy. *Chemical Communications* **2017,** *53* (23), 3303-3306.

36. Bolze, F.; Jenni, S.; Sour, A.; Heitz, V., Molecular photosensitisers for two-photon photodynamic therapy. *Chemical Communications* **2017,** *53* (96), 12857-12877.

37. Bi, X.-D.; Yang, R.; Zhou, Y.-C.; Chen, D.; Li, G.-K.; Guo, Y.-X.; Wang, M.-F.; Liu, D.; Gao, F., Cyclometalated Iridium(III) Complexes as High-Sensitivity Two-Photon Excited

Mitochondria Dyes and Near-Infrared Photodynamic Therapy Agents. *Inorganic Chemistry* **2020,** *59* (20), 14920-14931.

38. Wang, L.; Yin, H.; Cui, P.; Hetu, M.; Wang, C.; Monro, S.; Schaller, R. D.; Cameron, C. G.; Liu, B.; Kilina, S.; McFarland, S. A.; Sun, W., Near-infrared-emitting heteroleptic cationic iridium complexes derived from 2,3-diphenylbenzo[g]quinoxaline as in vitro theranostic photodynamic therapy agents. *Dalton Transactions* **2017,** *46* (25), 8091-8103.

39. Yang, X.; Xu, X.; Dang, J.-s.; Zhou, G.; Ho, C.-L.; Wong, W.-Y., From Mononuclear to Dinuclear Iridium(III) Complex: Effective Tuning of the Optoelectronic Characteristics for Organic Light-Emitting Diodes. *Inorganic Chemistry* **2016,** *55* (4), 1720-1727.

40. Zheng, Y.; Batsanov, A. S.; Fox, M. A.; Al-Attar, H. A.; Abdullah, K.; Jankus, V.; Bryce, M. R.; Monkman, A. P., Bimetallic Cyclometalated Iridium(III) Diastereomers with Non-Innocent Bridging Ligands for High-Efficiency Phosphorescent OLEDs. **2014,** *53* (43), 11616-11619.

41. Shafikov, M. Z.; Zaytsev, A. V.; Kozhevnikov, V. N., Halide-Enhanced Spin–Orbit Coupling and the Phosphorescence Rate in Ir(III) Complexes. *Inorganic Chemistry* **2021,** *60* (2), 642-650.

42. Gao, T.-B.; Zhang, J.-J.; Wen, J.; Yang, X.-X.; Ma, H.-b.; Cao, D.-K.; Jiang, D., Single-Molecule MicroRNA Electrochemiluminescence Detection Using Cyclometalated Dinuclear Ir(III) Complex with Synergistic Effect. *Analytical Chemistry* **2020,** *92* (1), 1268-1275.

43. Congrave, D. G.; Hsu, Y.-t.; Batsanov, A. S.; Beeby, A.; Bryce, M. R., Synthesis, Diastereomer Separation, and Optoelectronic and Structural Properties of Dinuclear Cyclometalated Iridium(III) Complexes with Bridging Diarylhydrazide Ligands. *Organometallics* **2017,** *36* (5), 981-993.

44. Lu, C.; Xu, W.; Shah, H.; Liu, B.; Xu, W.; Sun, L.; Qian, S. Y.; Sun, W., In Vitro Photodynamic Therapy of Mononuclear and Dinuclear Iridium(III) Bis(terpyridine) Complexes. *ACS Appl Bio Mater* **2020,** *3* (10), 6865-6875.

45. Matsuo, N., Benzo[h]quinolin-10-yl-N Iridium(III) Complexes. **1974,** *47* (3), 767-768.

46. Chen, Y.; Liu, C.; Wang, L., Effects of fluorine substituent on properties of cyclometalated iridium(III) complexes with a 2,2′-bipyridine ancillary ligand. *Tetrahedron* **2019,** *75* (47), 130686.

47. Zhao, Q.; Yu, M.; Shi, L.; Liu, S.; Li, C.; Shi, M.; Zhou, Z.; Huang, C.; Li, F., Cationic Iridium(III) Complexes with Tunable Emission Color as Phosphorescent Dyes for Live Cell Imaging. *Organometallics* **2010,** *29* (5), 1085-1091.

48. Brouwer, A., Standards for photoluminescence quantum yield measurements in solution (IUPAC Technical Report)*. *Pure and Applied Chemistry* **2011,** *83*, 2213-2228.

49. Liu, B.; Monro, S.; Lystrom, L.; Cameron, C. G.; Colón, K.; Yin, H.; Kilina, S.; McFarland, S. A.; Sun, W., Photophysical and Photobiological Properties of Dinuclear Iridium(III) Bis-tridentate Complexes. *Inorganic Chemistry* **2018,** *57* (16), 9859-9872.

50. Lu, G.; Yao, J.; Chen, Z.; Ma, D.; Yang, C., Saturated red iridium(iii) complexes containing a unique four-membered Ir–S–C–N backbone: mild synthesis and application in OLEDs. *Journal of Materials Chemistry C* **2020,** *8* (4), 1391-1397.

51. Soliman, A. M.; Fortin, D.; Harvey, P. D.; Zysman-Colman, E., Intimate electronic coupling in cationic homodimeric iridium(iii) complexes. *Dalton Transactions* **2012,** *41* (31), 9382-9393.

52. Li, G.; Zhu, D.; Wang, X.; Su, Z.; Bryce, M. R., Dinuclear metal complexes: multifunctional properties and applications. *Chemical Society Reviews* **2020,** *49* (3), 765-838.

53. Davis, S.; Weiss, M. J.; Wong, J. R.; Lampidis, T. J.; Chen, L. B., Mitochondrial and plasma membrane potentials cause unusual accumulation and retention of rhodamine 123 by human breast adenocarcinoma-derived MCF-7 cells. *Journal of Biological Chemistry* **1985,** *260* (25), 13844-13850.

54. Chen, L. B., Mitochondrial Membrane Potential in Living Cells. **1988,** *4* (1), 155-181.

55. Murphy, M. P., Selective targeting of bioactive compounds to mitochondria. *Trends in Biotechnology* **1997,** *15* (8), 326-330.

56. Zhang, Q.; Cao, R.; Fei, H.; Zhou, M., Mitochondria-targeting phosphorescent iridium(iii) complexes for living cell imaging. *Dalton Transactions* **2014,** *43* (44), 16872-16879.

57. Detty, M. R.; Gibson, S. L.; Wagner, S. J., Current Clinical and Preclinical Photosensitizers for Use in Photodynamic Therapy. *Journal of Medicinal Chemistry* **2004,** *47* (16), 3897-3915.

58. Juarranz, Á.; Jaén, P.; Sanz-Rodríguez, F.; Cuevas, J.; González, S., Photodynamic therapy of cancer. Basic principles and applications. *Clinical and Translational Oncology* **2008,** *10* (3), 148-154.

59. Arya, J. S.; Joseph, M. M.; Sherin, D. R.; Nair, J. B.; Manojkumar, T. K.; Maiti, K. K., Exploring Mitochondria-Mediated Intrinsic Apoptosis by New Phytochemical Entities: An Explicit Observation of Cytochrome c Dynamics on Lung and Melanoma Cancer Cells. *Journal of Medicinal Chemistry* **2019,** *62* (17), 8311-8329.

60. Nair, J. B.; Joseph, M. M.; Arya, J. S.; Sreedevi, P.; Sujai, P. T.; Maiti, K. K., Elucidating a Thermoresponsive Multimodal Photo-Chemotherapeutic Nanodelivery Vehicle to Overcome the Barriers of Doxorubicin Therapy. *ACS Applied Materials & Interfaces* **2020,** *12* (39), 43365-43379.

61. Pathania, D.; Millard, M.; Neamati, N., Opportunities in discovery and delivery of anticancer drugs targeting mitochondria and cancer cell metabolism. *Advanced Drug Delivery Reviews* **2009,** *61* (14), 1250-1275.

62. Singh, H.; Sareen, D.; George, J. M.; Bhardwaj, V.; Rha, S.; Lee, S. J.; Sharma, S.; Sharma, A.; Kim, J. S., Mitochondria targeted fluorogenic theranostic agents for cancer therapy. *Coordination Chemistry Reviews* **2022,** *452*, 214283.

63. Yoshihara, T.; Murayama, S.; Masuda, T.; Kikuchi, T.; Yoshida, K.; Hosaka, M.; Tobita, S., Mitochondria-targeted oxygen probes based on cationic iridium complexes with a 5-amino-1, 10-phenanthroline ligand. *Journal of Photochemistry and Photobiology A: Chemistry* **2015,** *299*, 172-182.

64. Lee, C.; Nam, J. S.; Lee, C. G.; Park, M.; Yoo, C.-M.; Rhee, H.-W.; Seo, J. K.; Kwon, T.-H., Analysing the mechanism of mitochondrial oxidation-induced cell death using a multifunctional iridium(III) photosensitiser. *Nature Communications* **2021,** *12* (1), 26.

65. Zafon, E.; Echevarría, I.; Barrabés, S.; Manzano, B. R.; Jalón, F. A.; Rodríguez, A. M.; Massaguer, A.; Espino, G., Photodynamic therapy with mitochondria-targeted biscyclometallated Ir(iii) complexes. Multi-action mechanism and strong influence of the cyclometallating ligand. *Dalton Transactions* **2022,** *51* (1), 111-128.

66. Garrido, C.; Galluzzi, L.; Brunet, M.; Puig, P. E.; Didelot, C.; Kroemer, G., Mechanisms of cytochrome c release from mitochondria. *Cell Death & Differentiation* **2006,** *13* (9), 1423-1433.

67. Brouwer, A. M., Standards for photoluminescence quantum yield measurements in solution (IUPAC Technical Report). **2011,** *83* (12), 2213-2228.

68. Dimauro, I.; Pearson, T.; Caporossi, D.; Jackson, M. J., A simple protocol for the subcellular fractionation of skeletal muscle cells and tissue. *BMC Research Notes* **2012,** *5* (1), 513.

CHAPTER 3

Mitochondria-Targeted Dinuclear Iridium(III) Photosensitizer with Intrinsic Viscosity Sensing for Activatable Photodynamic Therapy

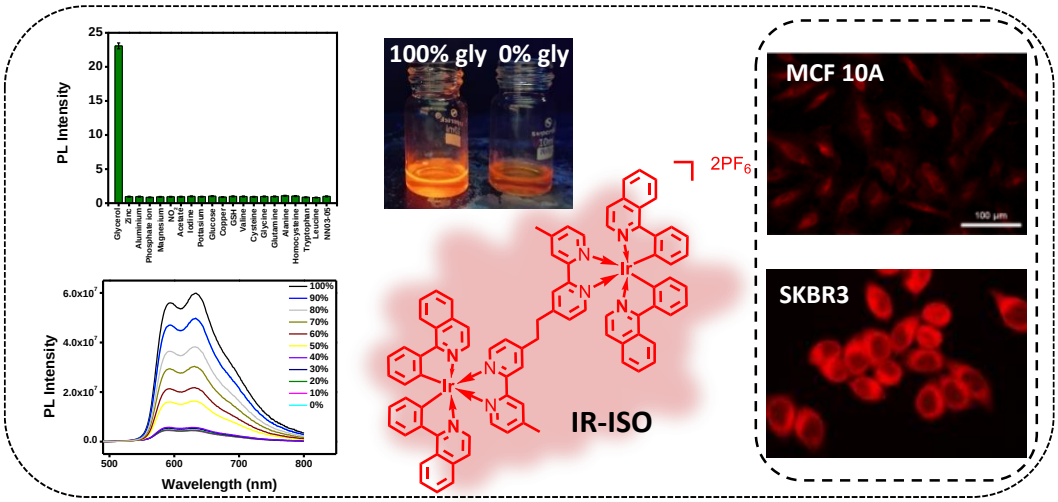

3.1. Abstract

Intracellular viscosity is considered as an important factor and biomarker for diseases like diabetes, atherosclerosis, and cancer, as these disease conditions can alter the interactions between proteins in cell membranes. It is imperative to develop a rapid and non-destructive viscosity-sensing probe for cellular imaging and therapeutic applications. Herein, we report a viscosity-sensitive dinuclear iridium complex (**IR-ISO**) consisting of two monomeric units with 1-phenylisoquinoline as the cyclometalating ligands and 4,4′-methyl-2,2′-bipyridine as the bridging ligand joined via a flexible ethyl spacer. This flexible C-C bond rotates freely and hence the molecule exhibits weak luminescence in low-viscosity environments. However, in highly viscous media, it displays significantly enhanced luminescence due to restricted intermolecular rotation (RIR). The iridium based

viscosity probe **IR-ISO**, exhibited a higher photoluminescence (PLQY) and singlet oxygen generation quantum yield (SOQY) of 0.67 and 0.90, respectively. *In vitro* evaluations demonstrate efficient cellular uptake of **IR-ISO** and enhanced photoluminescence intensity during cellular imaging in the viscous SK-BR-3 breast cancer cell line, while it exhibits diminished luminescence in the less viscous MCF-10A normal cell line. This viscosity-sensitive, molecular rotor design of **IR-ISO** allows distinguishing cancer cells from normal cell lines. Further, the mitochondria-targeting ability of **IR-ISO** was confirmed by confocal fluorescence imaging. The potential of **IR-ISO** as a photosensitizer for PDT application was confirmed through various live-dead assays such as Trypan blue, Hochest, and AO-EB assay. The cell death mechanism was further investigated by an Annexin V-FITC/PI flow cytometric assay and cell cycle analysis. This work offers a potential design strategy of dinuclear iridium-based probes for viscosity-sensitive, mitochondria targeting photosensitizers for PDT applications.

3.2. Introduction

Intracellular viscosity is an essential factor for regulating diffusion-mediated cellular processes, bio-molecular interactions, and cellular transport of substances and signals. The abnormal changes in cellular viscosity are linked to various diseases, including atherosclerosis, diabetes, Alzheimer's disease, and cancer, due to their impact on protein-protein interactions within cellular membranes.[1] Therefore, monitoring the alterations in cellular viscosity holds significant importance, especially in cancer diagnosis. Viscosity-activated luminescent probes, particularly molecular rotors, offer a promising approach for this purpose. Small organic molecular rotors have traditionally been used as viscosity-sensing probes.[2-12] However, these probes are currently less preferred due to challenges such as small Stokes shifts, self-quenching, short fluorescence lifetimes, and susceptibility to biological auto-fluorescence background.[13] Subsequently, it was found that transition metal complexes, particularly iridium complexes, are highly efficient as luminescent probes as well as photodynamic therapy (PDT) agents.[14-23] This efficacy arises from their advantageous characteristics such as: (i) high photo-stability, which allows for continuous irradiation and real-time monitoring of intracellular changes such as viscosity and polarity; (ii) long-lived triplet states that result in extended luminescence lifetimes; (iii) high triplet and singlet oxygen quantum yields and (iv) large Stokes shifts that reduce the risk of self-quenching even at high concentrations.[13, 24-27] For example, Aoki *et al.*, reported a series of iridium complexes featuring its ability of color tuning, high photoluminescence, and excellent stability for pH sensing applications (**Figure 3.1**).[28]

However, the combined utilization of iridium metal complexes as viscosity-sensitive probes and photodynamic therapy agents in cancer cell lines remains unexplored. Photodynamic therapy is a promising clinical approach for treating various diseases,

mainly cancer and actinic keratosis. This non-invasive method relies on a light-activated reaction between a photosensitizer and molecular oxygen to produce cytotoxic reactive oxygen species (ROS), promoting cancer cell death. The ROS generation in photodynamic therapy occurs through two pathways. In the type I process, photoinduced electron transfer with biological molecules generates radicals like superoxide ($O2^{\bullet-}$), hydroxyl ($^{\bullet}OH$), and hydrogen peroxide (H_2O_2). Iridium complexes predominantly promote the type II process, where energy is directly transferred to molecular oxygen ($^3O_2$), leading to the generation of singlet oxygen ($^1O_2$) that induces cellular apoptosis.[29-31]

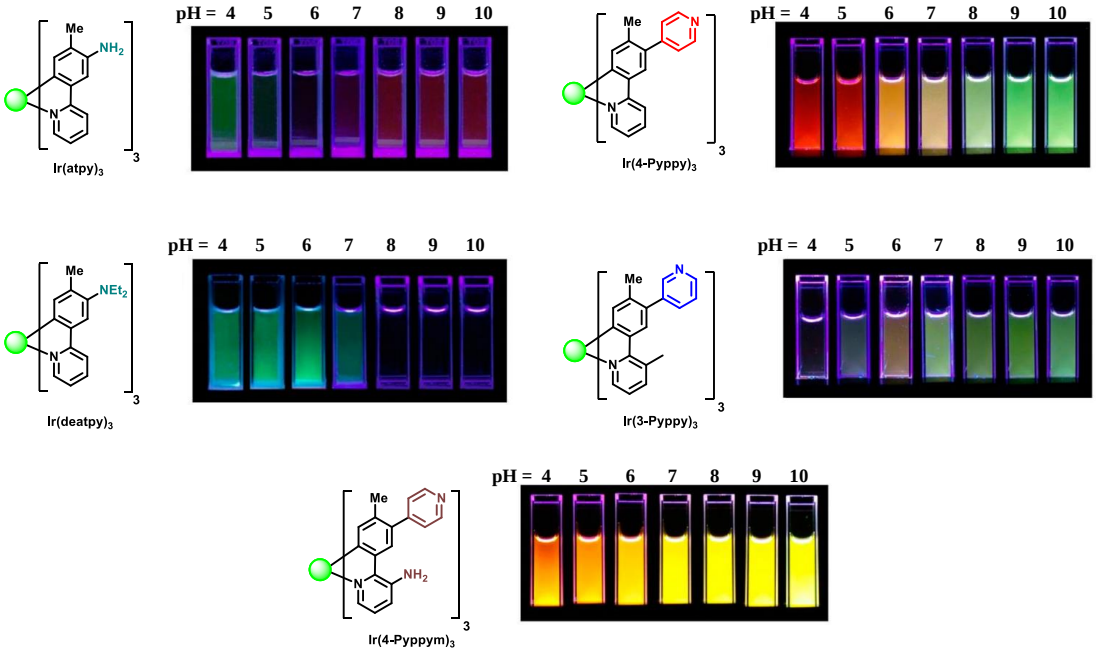

Figure 3.1. A series of cyclometalated iridium complexes for pH sensing. Figure adapted from reference 28.

He *et al.*, reported the synthesis and characterization of two iridium(III) based photosensitizers, **IrL1** and **MitoIrL2**, for application in photodynamic therapy (PDT).[32] Their study demonstrated that the mitochondria-targeting iridium probe significantly enhances apoptosis (**Figure 3.2**). Sun *et al.*, reported a dinuclear and mononuclear iridium complex for viscosity sensing in cancer cell lines MCF-7.[13] The dinuclear iridium probe

C10 was designed with a flexible, long carbon chain linker to enhance its responsiveness to viscosity. C10 shows exceptional sensitivity and selectivity toward viscosity changes. Furthermore, it can permeate cells, enabling it to differentiate cancer cells from normal cells and monitor viscosity fluctuations during apoptosis in MCF-7 cells (**Figure 3.3**).

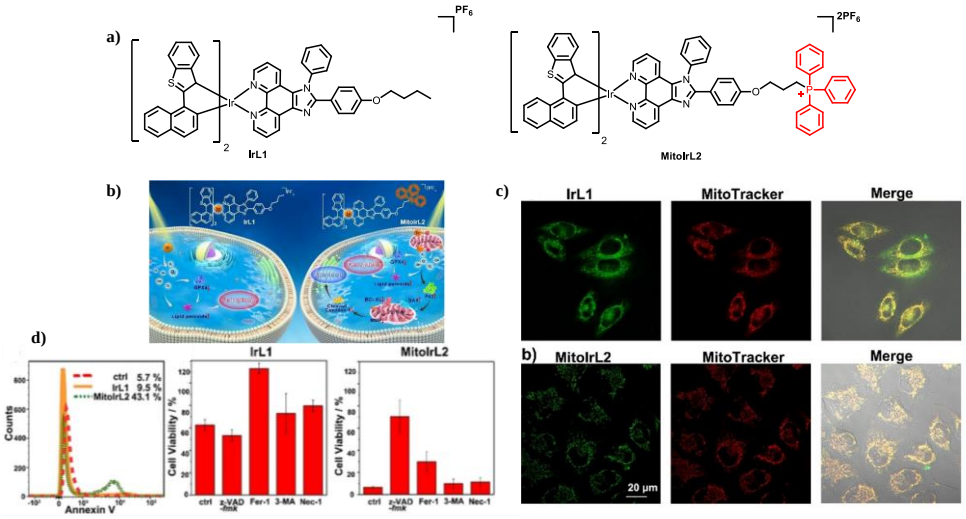

Figure 3.2. (a) Structure of iridium complex **IrL1** and **MitoIrL2**; (b) Schematic illustration of mechanism of **IrL1** and **MitoIrL1** complexes; (c) The intracellular co-localization of **IrL1** and **MitoIrL1** complexes and (d) Assessment of apoptosis induced by **IrL1** and **MitoIrL1** using Annexin assays and cell viability tests. Figure adapted from reference 32.

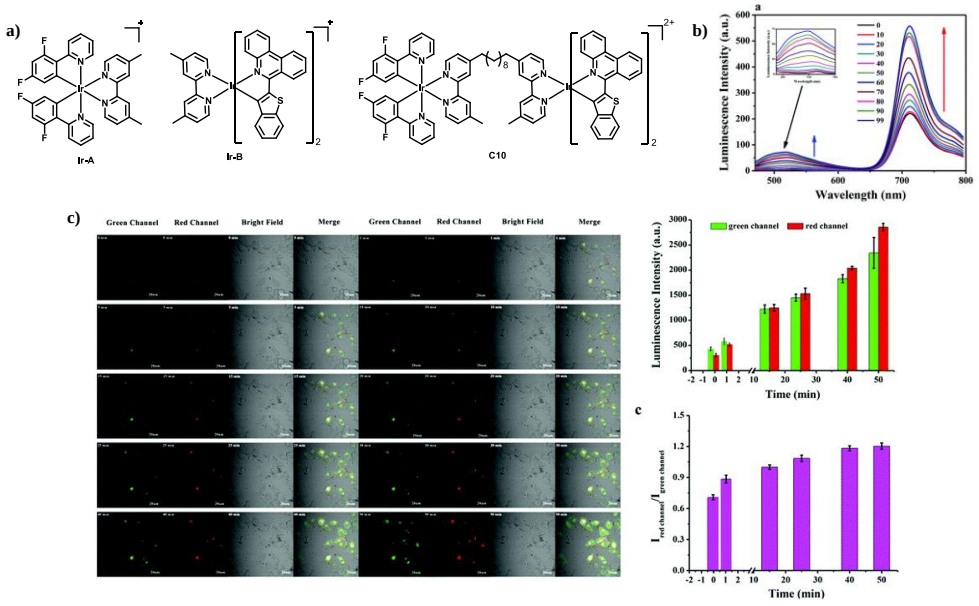

Figure 3.3. (a) Structure of iridium probe **C10** and the corresponding mononuclear iridium complex for viscosity sensing in cancer cell line MCF-7; (b) Emission spectra of **C10** in various percentages of glycerol-water solvents and (d) Tracking viscosity variations of probe **C10** during etoposide-induced cell apoptosis, along with the quantification of **C10**'s emission intensity. Figure adapted from reference 13.

To measure intracellular viscosity, sensors with dual fluorescent components are traditionally used, incorporating a flexible linker, an energy donor, and an energy acceptor. However, the relative orientation of these two fluorophores may shift depending on the medium, dye concentration, and various experimental or instrumental conditions, potentially resulting in ambiguous viscosity measurements.[1] Therefore, designing a dinuclear iridium complex with similar monomer units separated by an ethyl spacer would be ideal. This design minimizes electronic coupling and provides molecular rotors that are primarily sensitive to viscosity changes. Additionally, the high singlet oxygen generation efficiencies and inherent mitochondrial targeting capabilities of the iridium complexes would result in a mitochondrial-targeted viscosity sensor with photodynamic therapeutic potential.

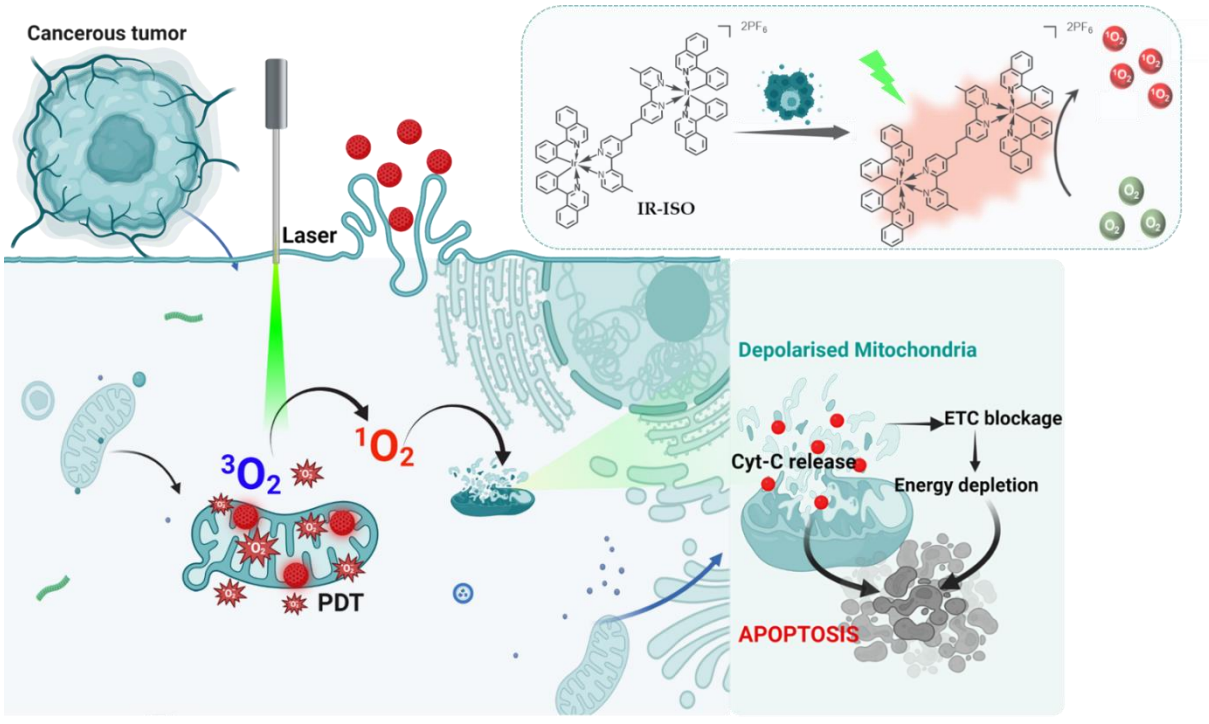

Figure 3.4. Schematic illustration of the mechanism of **IR-ISO** through photodynamic therapy.

In this context, we developed a dinuclear iridium-based viscosity-sensitive probe (**IR-ISO**) with 1-phenylisoquinoline as the cyclometalating ligand and 4,4′-dimethyl-2,2′-

bipyridine ancillary ligand joined through a flexible ethyl spacer (**Figure 3.4**). The rotation of the C−C bond in the ethyl spacer can occur freely in low-viscosity environments, leading to efficient fluorescence quenching. The fluorescence is enhanced in a highly viscous medium due to the restricted rotations. This design strategy ensures that **IR-ISO** is selectively responsive to cancer cell lines, which typically exhibit higher cellular viscosity compared to normal cell lines.[33-36] Additionally, the photophysical and photocytotoxic properties of **IR-ISO** were compared with the mononuclear iridium complex, **IR-IMO**. The dinuclear iridium complex **IR-ISO** demonstrates higher triplet quantum yield and greater efficiency in generating singlet oxygen compared to its mononuclear counterpart. The **IR-ISO** also exhibited improved triplet quantum yield and singlet oxygen quantum yield in a high viscous medium. The *in vitro* analysis of the cellular internalization, mitochondrial localization, and photocytotoxicity of **IR-ISO** was conducted in the SK-BR-3 breast cancer cell line. The investigation of the cell death mechanism deciphered the ROS-driven mitochondria-mediated apoptotic pathway initiated by **IR-ISO** upon photosensitization. Thus the viscosity-sensitive iridium probe showed the potential to enable accurate photodynamic therapy (PDT) in breast cancer cell lines. This offers a valuable direction in developing probes that target mitochondria and are sensitive to viscosity, potentially benefiting both diagnostic and therapeutic applications in cancer treatment.

3.3. Results and Discussion

3.3.1. Design and Synthesis of IR-ISO and IR-IMO Complexes

Herein, we have designed and developed a dinuclear iridium complex (**IR-ISO**) and a structurally similar mononuclear iridium complex (**IR-IMO**) for a comparative analysis of the photophysical properties as shown in **Figure 3.5a**. The reaction intermediate, chlorine-bridged iridium dinuclear complex, $[(pisq)_2IrCl]_2$ was synthesized by coupling the cyclometalating ligand with iridium(III) chloride ($IrCl_3 \cdot xH_2O$) through a Nonoyama reaction.[37] The final complexes, **IR-ISO**, and **IR-IMO**, were obtained by replacing the bridged chlorine with an ancillary bipyridine ligand **(Figure 3.5b)**. Finally, the chlorine counter-ion in the complexes was replaced with PF_6 ion via an anion exchange reaction with ammonium hexafluorophosphate. The synthesized complexes and intermediates were well-characterized using HRMS and NMR spectroscopic methods.

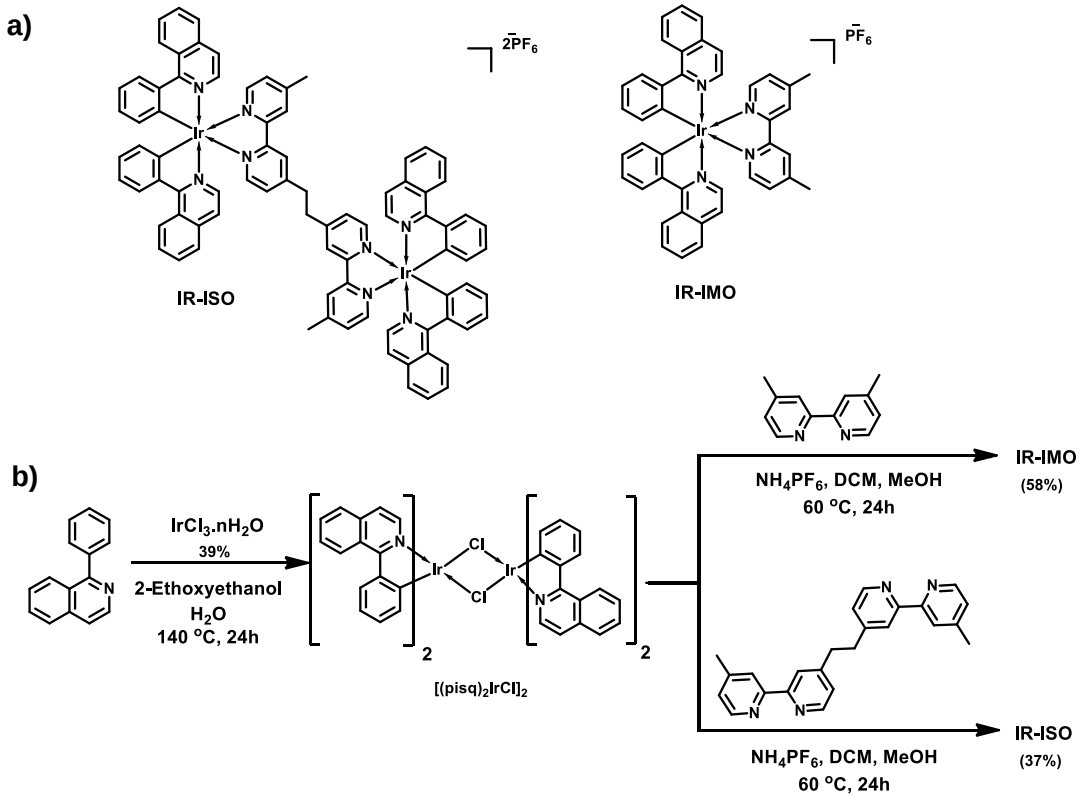

Figure 3.5. (a)Structures of the mononuclear iridium complex, **IR-IMO**, and dinuclear iridium complex, **IR-ISO** and (b) Scheme adopted for the synthesis of both complexes.

3.3.2. Photophysical properties

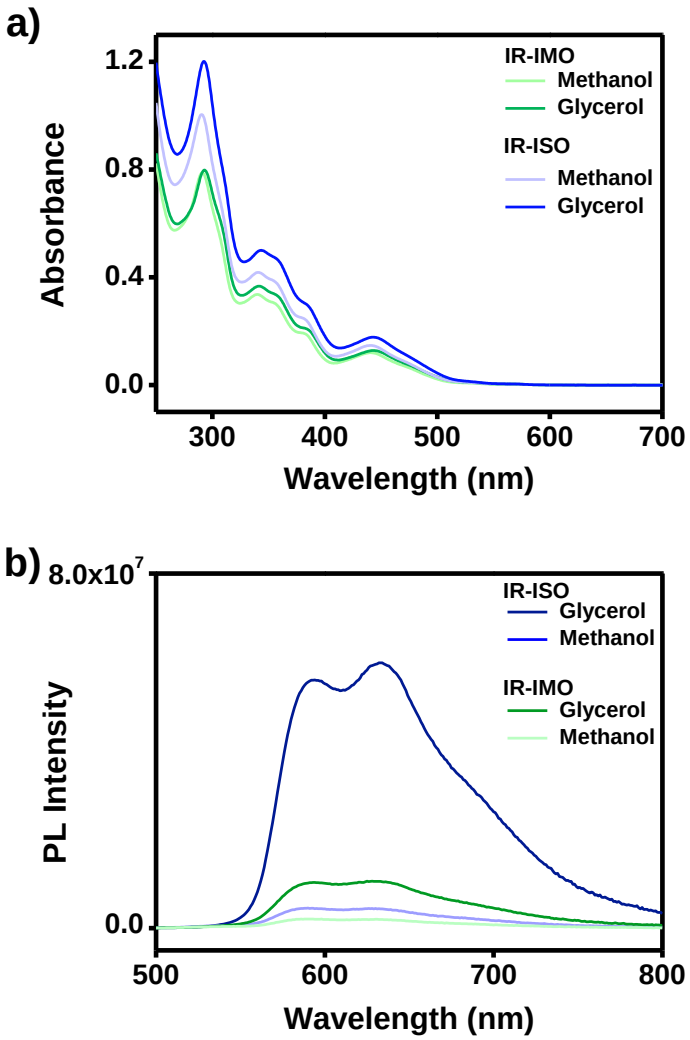

Figure 3.6. (a) UV-visible absorption spectra of **IR-ISO** and **IR-IMO**; (b) Emission spectra of **IR-ISO** (excitation wavelength, 440 nm) and **IR-IMO** (excitation wavelength, 440 nm) in glycerol and methanol.

The UV-visible absorption spectra of **IR-IMO** and **IR-ISO** were recorded in methanol and glycerol at room temperature (**Figure 3.6a**). Both complexes displayed a strong absorption band between 200-400 nm, attributed to spin-allowed $^1\pi$–π^* ligand-centered transitions involving the 1-phenylisoquinoline and ancillary bipyridine ligands.[37] Weaker absorption bands in the 400-500 nm range are associated with spin-allowed and spin-forbidden transitions, representing a mix of singlet and triplet metal-to-ligand charge

transfer (^{1}MLCT and ^{3}MLCT) combined with ligand-to-ligand charge transfer (LLCT).[37] The emission spectra of **IR-ISO** and **IR-IMO** in methanol and glycerol at room temperature are shown in **Figure 3.6b**. **IR-ISO** exhibits a strong, broad, and structured emission band with a maximum at 632 nm, while **IR-IMO** shows emission maxima at 629 nm. The vibrational structure suggests that the lowest excited states involve the ^{3}LC excited state, along with contributions from LLCT and MLCT excited states.[38] The dinuclear Ir(III) complex **IR-ISO** demonstrates higher emission intensity than the mononuclear **IR-IMO**, which is reflected in their calculated photoluminescence quantum yields in methanol: Φ_p = 0.09 for **IR-ISO** and Φ_p = 0.04 for **IR-IMO**, compared to the standard $Ru(bpy)_3^{2+}$ in acetonitrile (Φ_p = 0.06).[39]

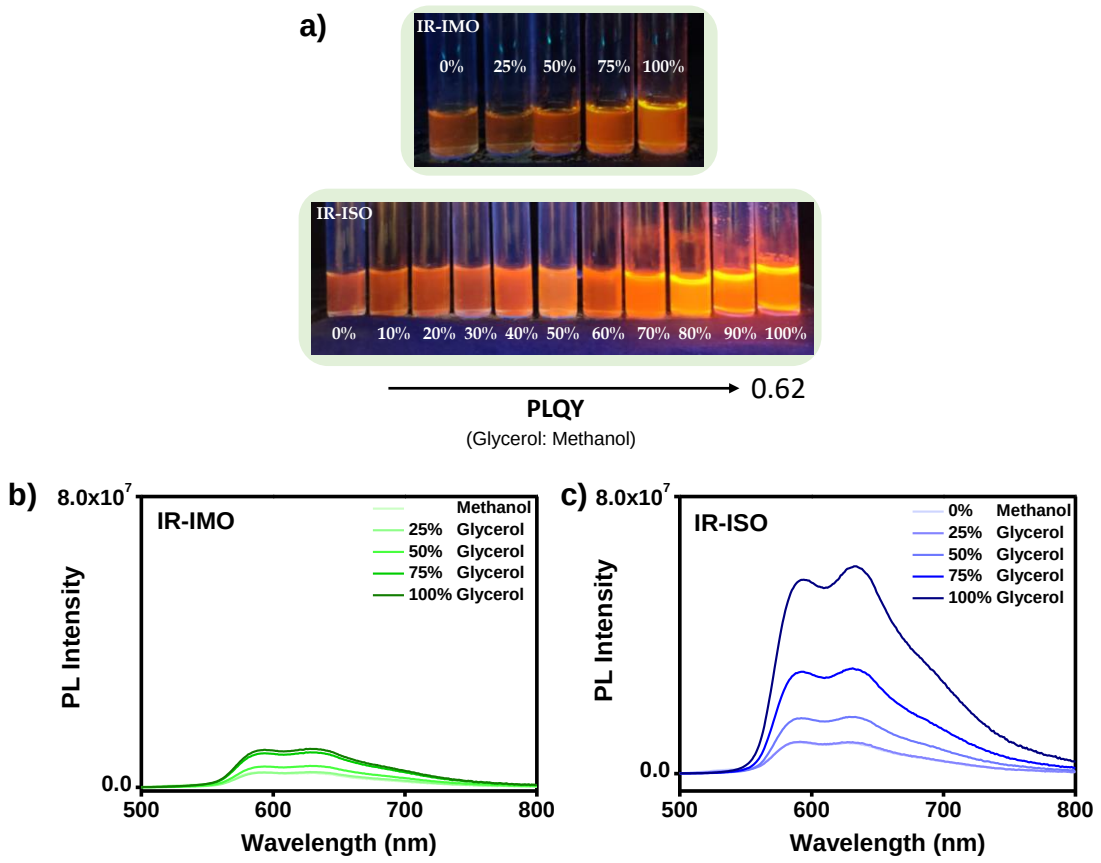

Figure 3.7. (a) The image of **IR-IMO** and **IR-ISO** in various methanol: glycerol percentages, under UV light; (b) Emission spectra of **IR-IMO** in various methanol:glycerol percentages and (c) Emission spectra of **IR-ISO** in various methanol: glycerol percentages.

To investigate the influence of viscosity on fluorescence properties of **IR-ISO** and **IR-IMO,** the emission spectra were recorded using viscosity gradient mixtures of glycerol and methanol at room temperature.[40] **Figure 3.7a** illustrates the increase in luminescence for **IR-ISO** as the glycerol percentage in the glycerol-methanol mixture rises. **IR-ISO** displayed a marked enhancement in luminescence, whereas **IR-IMO** showed only minimal improvement. As the viscosity increased from 4.5 cP to 510 cP (methanol:glycerol), the photoluminescence intensity of **IR-ISO** experienced a 13-fold increase, while **IR-IMO** showed little to no change (**Figure 3.7b,c**).[1] Photoluminescence quantum yields (PLQY) for both compounds were measured at varying viscosities: **IR-ISO** exhibited a PLQY of $\Phi_p = 0.09$ in methanol, which increased to 0.62 in glycerol. This fluorescence enhancement is attributed to viscosity-dependent inhibition of C–C bond rotation between the two iridium centers, which reduces non-radiative energy loss and enhances emission.

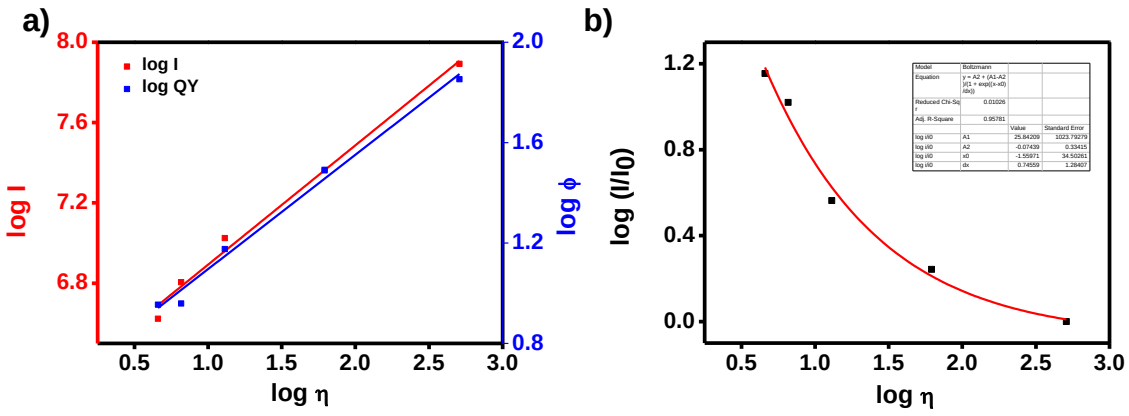

Figure 3.8. (a) Plot of log I/I_0 to log η and (b) Linear relationship of log I, log.η and log ϕ.

A logarithmic plot of **IR-ISO** emission intensity at 632 nm (I_{632} nm) versus the logarithm of viscosity exhibited a strong linear correlation, with an R^2 value of 0.987 (**Figure 3.8a**). Moreover, the logarithm of the ratiometric emission intensity (I/I_0) showed a good nonlinear fitting relationship ($R^2 = 0.982$) with the logarithm of viscosity using

sigmoidal fitting (**Figure 3.8b**)**.** This demonstrated that **IR-ISO** can be effectively used for ratiometric detection of changes in solution viscosity.

The singlet oxygen generation efficiencies of the **IR-ISO** and **IR-IMO** complexes in various glycerol:methanol percentages were investigated by employing 1,3-diphenylbenzofuran (DPBF) as the singlet oxygen scavenger (**Figure 3.9a-f** and **Figure 3.10a-f**). The **IR-ISO** caused a significant decrease in the absorbance of DPBF at 410 nm upon light irradiation in 100% glycerol compared to 100% methanol. Along with the increasing percentage of glycerol from 0 to 100%, the singlet oxygen quantum yield of **IR-ISO** increased from 0.67 to 0.90. The singlet oxygen quantum yield of **IR-IMO** also exhibited a rise from 0.34 to 0.68, as the percentage of glycerol increased due to the restricted rotation of the free methyl units in highly viscous medium. The SOQY and PLQY of **IR-ISO** and **IR-IMO** are summarized in **Table 3.1**.

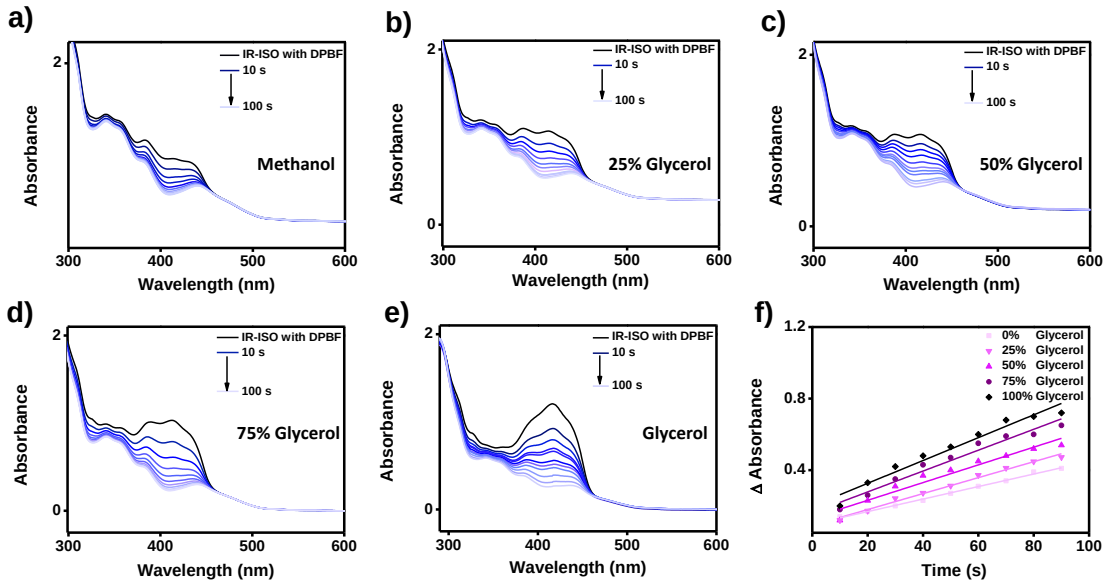

Figure 3.9. Singlet oxygen generation study of **IR-ISO** using the absorbance change of DPBF at 410 nm from 0 to 100 s (the photosensitizer to dye ratio maintained as 1:3, 385 nm laser, 0.5 W/cm^2 power, spectra were taken in 10 s time intervals) in various methanol: glycerol percentages with $[Ru(bpy)_3]Cl_2$ ($\Phi s = 0.57$ in acetonitrile) as reference: (a) 100% methanol; (b) 25% glycerol and 75% methanol; (c) 50% glycerol and 50% methanol; (d) 75% glycerol and 25% methanol; (e) 100% glycerol and (f) Relative plot of decrease in absorption of DPBF at 410 nm in the presence of **IR-ISO** and reference $[Ru(bpy)_3]Cl_2$.

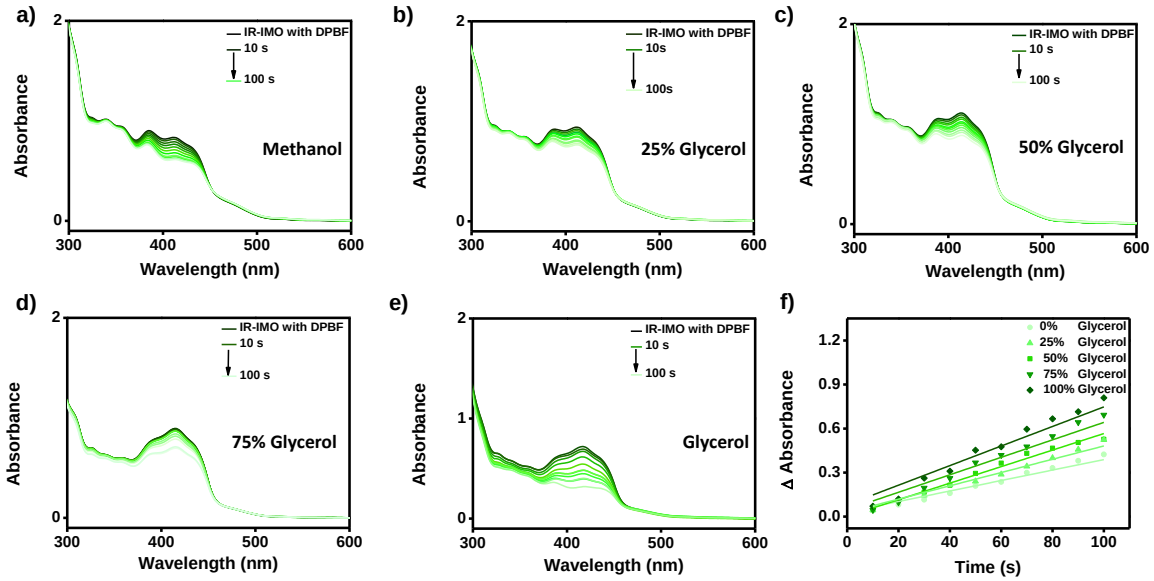

Figure 3.10. Singlet oxygen generation study of **IR-IMO** using the absorbance change of DPBF at 410 nm from 0 to 100s (the photosensitizer to dye ratio maintained as 1:3, 385 nm laser, 0.5W/cm^2 power each spectrum were taken in a time interval of 10 s) in various methanol: glycerol percentages with $[Ru(bpy)_3]Cl_2$ ($\Phi s = 0.57$ in acetonitrile) as reference: (a) 100% methanol; (b) 25% glycerol and 75% methanol; (c) 50% glycerol and 50% methanol; (d) 75% glycerol and 25% methanol; (e) 100% glycerol and (f) Relative plot of decrease in absorption of DPBF at 410 nm in the presence of **IR-IMO** and reference $[Ru(bpy)_3]Cl_2$.

Table 3.1: Summarized PLQY and SOQY data of **IR-ISO** and **IR-IMO** in various methanol:glycerol percentages.

% of Glycerol	IR-ISO PLQY	IR-ISO SOQY	IR-IMO PLQY	IR-IMO SOQY	Viscosity (cP) measured
Methanol	0.09	0.67	0.04	0.34	4.56
25%	0.09	0.76	0.04	0.43	6.56
50%	0.15	0.80	0.05	0.50	13.00
75%	0.31	0.85	0.09	0.57	62.08
Glycerol	0.62	0.90	0.10	0.68	510.48

Further recorded the emission of **IR-ISO** in glycerol systems at different temperatures to monitor the viscosity change induced by temperature. As shown in **Figure 3.11a**, the absorption intensity of **IR-ISO** remains constant to the viscosity changes at temperatures ranging from 30 ^oC to 100 ^oC. The emission intensity of **IR-ISO** in glycerol

decreased with increasing temperature **(Figure 3.11b)**, from 30 °C to 100 °C, due to the reduction in viscosity at higher temperatures, consistent with previous literature reports.[27, 41]

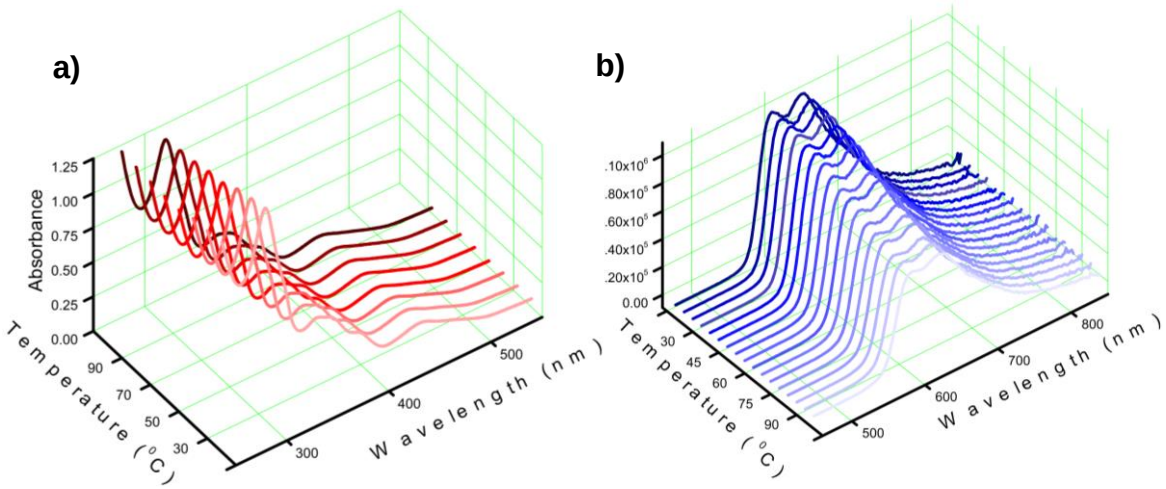

Figure 3.11. (a) The absorption profile of **IR-ISO** in the methanol:glycerol system at various temperatures and (b) The emission profile of **IR-ISO** in the methanol:glycerol system at various temperatures.

The selectivity study of **IR-ISO**, along with various analytes, is exhibited in **Figure 3.12a,b**. The fluorescence spectrum of **IR-ISO** was sensitive only to viscosity, not to any other cellular analytes. The pH-sensitive absorption and emission properties of **IR-ISO** were studied **(Figure 3.12c)**, as the nature of the environment can perturb the electronic and photophysical properties of molecules. The emission spectra were recorded in PBS buffer for **IR-ISO** across different pH levels (5-9), revealing minimal sensitivity to pH changes. This suggests that **IR-ISO** remains stable under both normal and acidic cellular conditions. To assess the photobleaching effect of the dinuclear Ir(III) complex **IR-ISO**, photostability tests were performed with and without irradiation using a 200 W xenon Arc lamp on an Oriel optical bench, as illustrated in **Figure 3.12d**. The **IR-ISO** complex exhibited stable and reproducible absorption profiles in the presence and absence of irradiation in a time-dependent manner, indicating the excellent photostability of the

complex, **IR-ISO**. All these results demonstrated that **IR-ISO** could be employed as a viscosity-sensitive imaging probe and photosensitizer for PDT application.

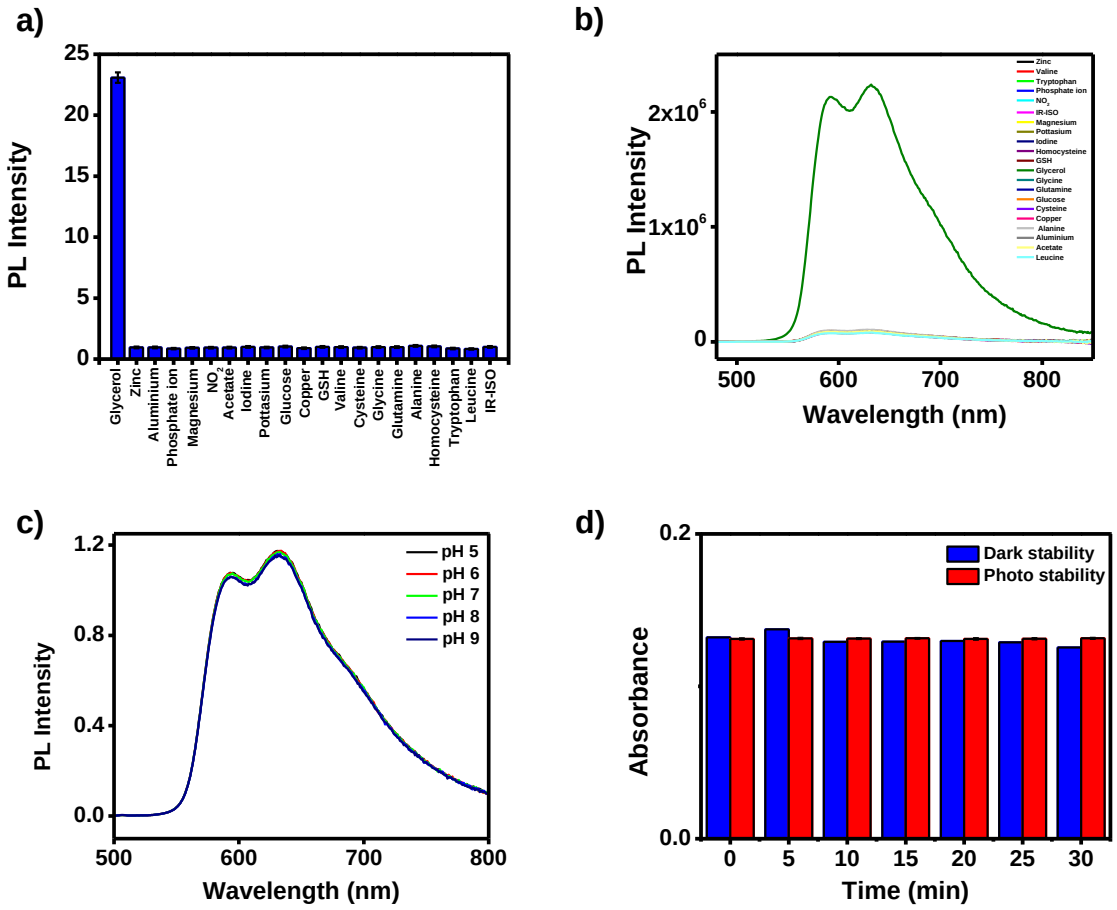

Figure 3.12. (a) The bar diagram representation of the selectivity analysis of **IR-ISO** with different cellular analytes; (b) The fluorescence spectra of viscosity sensitive **IR-ISO** along with various analytes; (c) pH-dependent emission spectral changes of **IR-ISO** at different pH values starting from 5 to 9 (excitation 440 nm) and (d) The photo and dark stability of **IR-ISO**.

3.3.3. In vitro Studies

3.3.3.1. Internalisation and Cytotoxicity of IR-ISO in SK-BR-3 and MCF-10A

The cytotoxicity of **IR-ISO** was assessed in the breast cancer cell line SK-BR-3 and the normal cell line MCF-10A. The MTT assay revealed cell proliferation exceeding 90%, even at a concentration of 20 µM, in both SK-BR-3 and MCF-10A, indicating the non-toxicity of the **IR-ISO** complex **(Figure 3.13a,b)**.

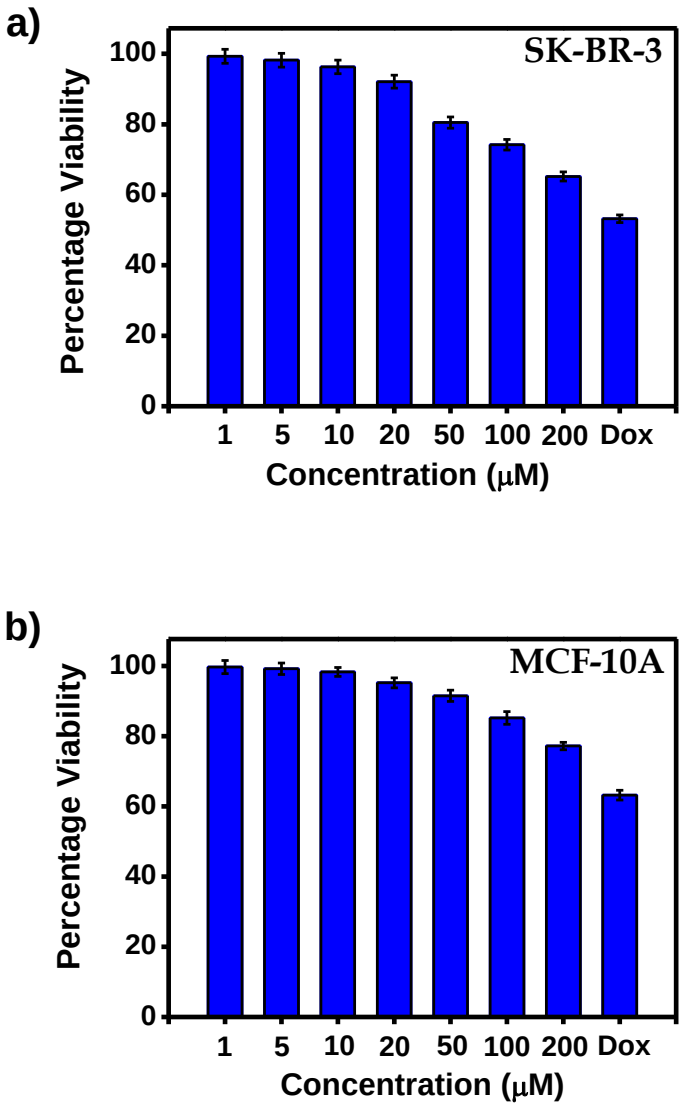

Figure 3.13. (a) *In vitro* cytotoxicity profiling of **IR-ISO** in SK-BR-3 cells at 24 h using MTT assay, commercially available drug doxorubicin was used as the positive control and (b) *In vitro* cytotoxicity profiling of **IR-ISO** in MCF-10A cells at 24 h using MTT assay, commercially available drug doxorubicin was used as the positive control.

To understand the cellular uptake of **IR-ISO** in the normal cell line MCF-10A and the more viscous cancer cell line SK-BR-3, a time- and concentration-dependent internalization experiment was conducted. The cells were incubated with 10 μM of **IR-ISO** in plain DMEM, and the cellular uptake was monitored over time using the red fluorescence of **IR-ISO**. As in **Figure 3.14a,b**, in the low-viscous normal cell line MCF-10A, the red fluorescence signals were not well detectable even after 2 hours, confirming

that **IR-ISO** is not selective to normal cell lines. In SK-BR-3 cell lines, the red fluorescence intensity increased from 0 to 2 hours, indicating efficient cellular uptake **(Figure 3.14c,d)**. The red fluorescence signals were detectable from 30 minutes onward, reaching maximum intensity at 2 hours, confirming 2 hours as the ideal internalization time. Concentration-dependent internalization experiments with **IR-ISO** concentrations ranging from 0 to 20 µM showed a gradual increase in red fluorescence intensity **(Figure 3.14e,f)**. Concentration-dependent internalization experiments and cytotoxicity studies confirmed 10 µM concentration of **IR-ISO** as an ideal concentration for *in vitro* studies.

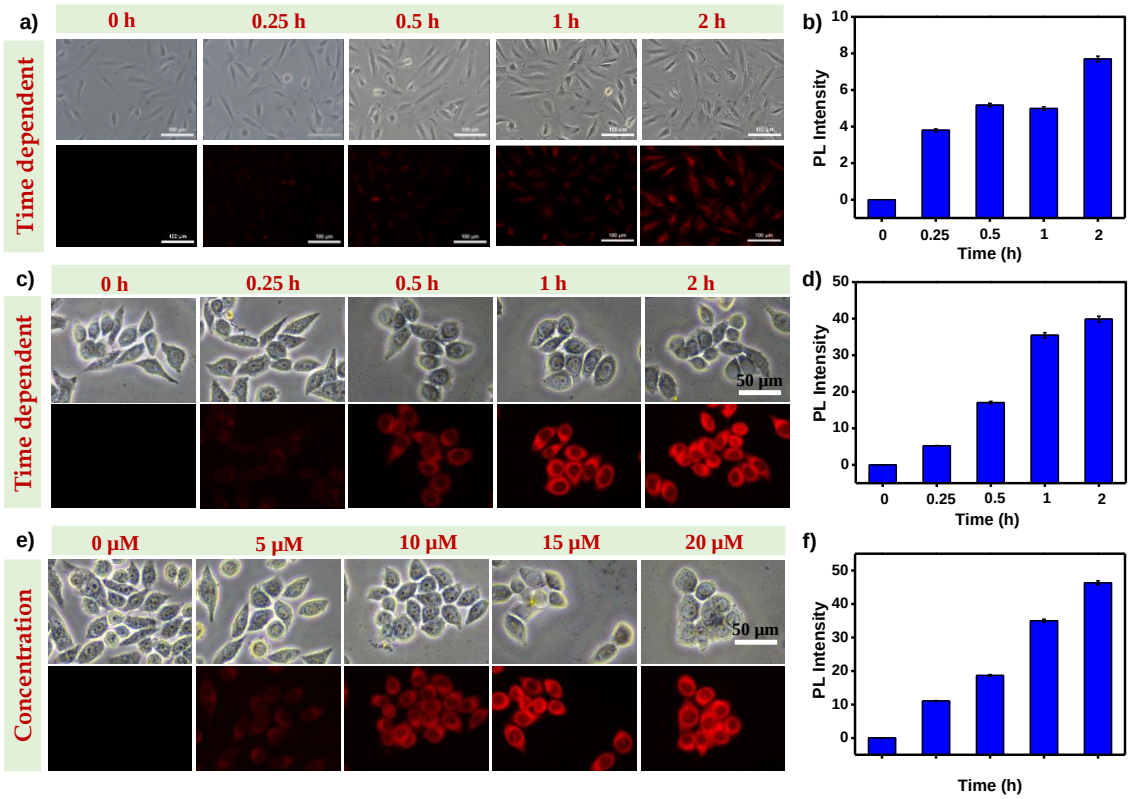

Figure 3.14. (a) Time-dependent internalization of **IR-ISO** in MCF-10A cell line through fluorescence microscopy; (b) corresponding intensity quantification from cells; (c) Time-dependent internalization of **IR-ISO** from 0 to 2 h in SK-BR-3 cancer cell line through fluorescence microscopy; d) corresponding intensity quantification from cells; (e) Concentration-dependent internalization of **IR-ISO** from 0 to 20 µM in SK-BR-3 cancer cell line and (f) corresponding intensity quantification from cells.

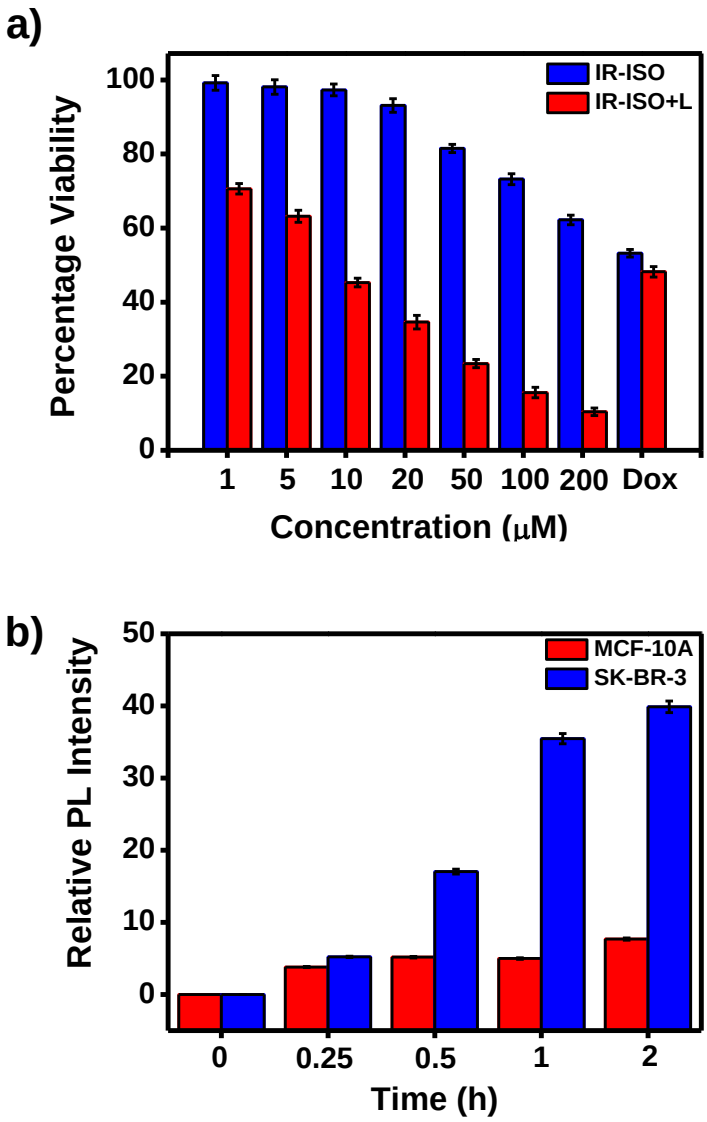

Figure 3.15. (a) MTT assay showing the IC_{50} value of **IR-ISO** in SK-BR-3 cancer cell lines and (b) The relative PL intensity plot of **IR-ISO** in SK-BR-3 and MCF-10A.

The IC_{50} value, calculated as the concentration of a drug required to inhibit 50% of target cells when exposed to light, is a key measure in PDT. It indicates the efficiency of a photosensitizer at a specific concentration when activated by light. A lower IC_{50} signifies higher efficacy, meaning the drug can kill target cells in smaller amounts. This value is essential for assessing the potency of photosensitizers and optimizing treatment dosages to achieve the best therapeutic outcomes while minimizing side effects. For the iridium complex **IR-ISO**, the IC_{50} was calculated to be 7.84 μM with laser treatment, and greater

than 200 μM without laser treatment (**Figure 3.15a**). This highlights **IR-ISO**'s efficiency as a photosensitizer, requiring a minimal dose when activated by laser. The selectivity of **IR-ISO** toward the viscous cancer cell line SK-BR-3 was further confirmed by comparing its relative photoluminescence (PL) intensity in SK-BR-3 and the normal cell line MCF-10A. The SK-BR-3 cancer cells showed a 40% increase in relative PL intensity, while the normal MCF-10A cells exhibited only a 5% increase, as shown in **Figure 3.15b**.

3.3.3.2. Mitochondria Targeting, Photoactivation, and PDT Studies of IR-ISO in SK-BR-3 Cells.

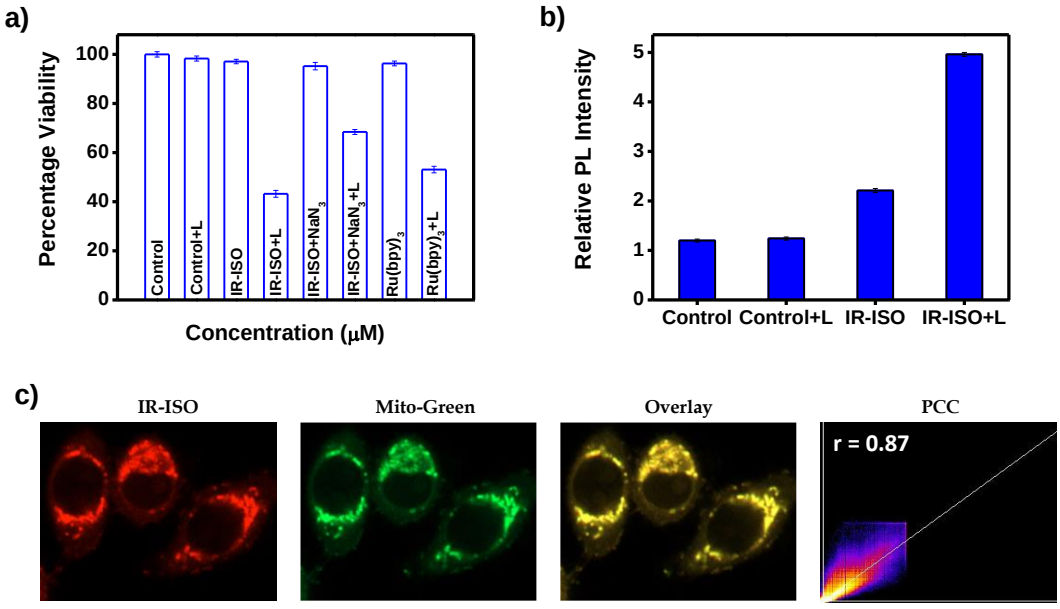

Figure 3.16. (a) MTT assay showing the photodynamic effect of **IR-ISO**-treated and laser-irradiated cells with and without the singlet oxygen scavenger NaN_3; (b) The subcellular singlet oxygen generation study of **IR-ISO** using SOSG in SK-BR-3 cells and (c) The mitochondrial localization images of **IR-ISO** treated cells with Mito Green and the corresponding scatter plot.

The laser-activated generation of singlet oxygen by **IR-ISO** in SK-BR-3 cancer cells was confirmed through an MTT assay, performed both in the presence and absence of the singlet oxygen scavenger NaN_3, with $Ru(bpy)_3Cl_2$ serving as a control (**Figure 3.16a**). In the presence of NaN_3, **IR-ISO** (10μM) showed 70% cellular viability, while in

the absence of NaN_3, viability dropped to 40%, indicating singlet oxygen-mediated cell death. To further validate this, singlet oxygen production in SK-BR-3 cells was assessed using the singlet oxygen sensor green (SOSG) probe. Cells were co-treated with **IR-ISO** and SOSG, followed by light exposure. The observed increase in relative PL intensity of **IR-ISO** upon laser irradiation demonstrated its photochemical ability to generate singlet oxygen (**Figure 3.16b**).

Mitochondria-targeted photodynamic therapy (PDT) is an advanced approach with significant potential for treating diseases like cancer. This technique uses photosensitizing agents designed to accumulate specifically in mitochondria, the powerhouse of the cell. Its key advantage lies in selectively targeting and destroying diseased cell mitochondria resulting in more precise and less harmful treatment. PDT effectively induces cell death in targeted tissues by disrupting essential mitochondrial functions such as energy production and cellular signalling. The **IR-ISO** with its unique dicationic structure, accumulates specifically in mitochondria due to their negative membrane potential, which attracts cationic species and enhances internalization of cationic iridium complexes. To substantiate **IR-ISO**'s mitochondrial targeting properties in SK-BR-3 cells, co-incubation experiments were conducted with a mitochondria-specific dye, Mito Green **(Figure 3.16c)**. Fluorescence images showed a significant overlap with Pearson's correlation coefficient (PCC) of 0.87, indicating the localization of **IR-ISO** within the mitochondria.

Further, the ability of **IR-ISO** to record the mitochondrial viscosity variation was evaluated using the known ionophore nystatin which is reported to increase the mitochondrial viscosity and swelling of mitochondria (**Figure 3.17**).[1, 42] The study indicated that the nystatin pre-treatment led to increase the PL intensity of the **IR-ISO** treated cells by 4 folds. Nystatin induced cell swelling and morphological changes as early

as 10 minutes of incubation. The maximum fluorescence of **IR-ISO** was observed in cells treated with Nystatin for 20 minutes, followed by those treated for 10 minutes and 0 minutes, demonstrating **IR-ISO**'s capability to monitor cellular viscosity variations.

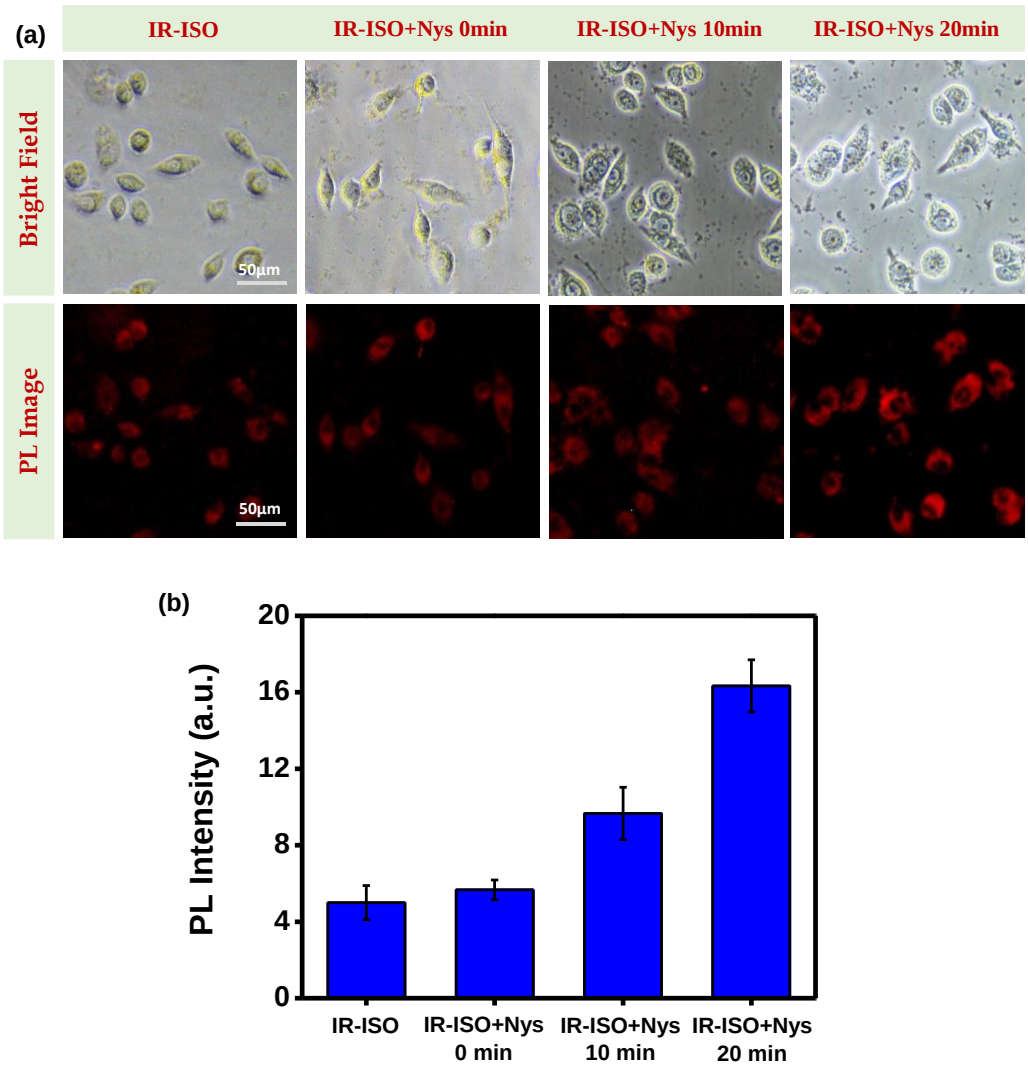

Figure 3.17. (a) PL images of **IR-ISO** treated SK-BR-3 cell lines incubated with and without nystatin and (b) corresponding intensity quantification from cells.

3.3.3.3. Cell Death mechanism of IR-ISO in SK-BR-3 Cells.

To support these findings and confirm **IR-ISO** as a potential agent for photodynamic therapy (PDT), a series of apoptosis assays were conducted. An acridine orange/ethidium bromide dual staining procedure was employed to assess apoptotic

characteristics. Acridine orange (AO), which fluoresces green, entered all viable cells, while ethidium bromide (EB) emitted an orange-red fluorescence in cells with damaged cytoplasmic membranes. Cells exposed to **IR-ISO** alone showed green staining for cellular viability, whereas **IR-ISO** treatment followed by 532 nm laser irradiation resulted in orange-red staining, indicating apoptotic characteristics (**Figure 3.18a**).

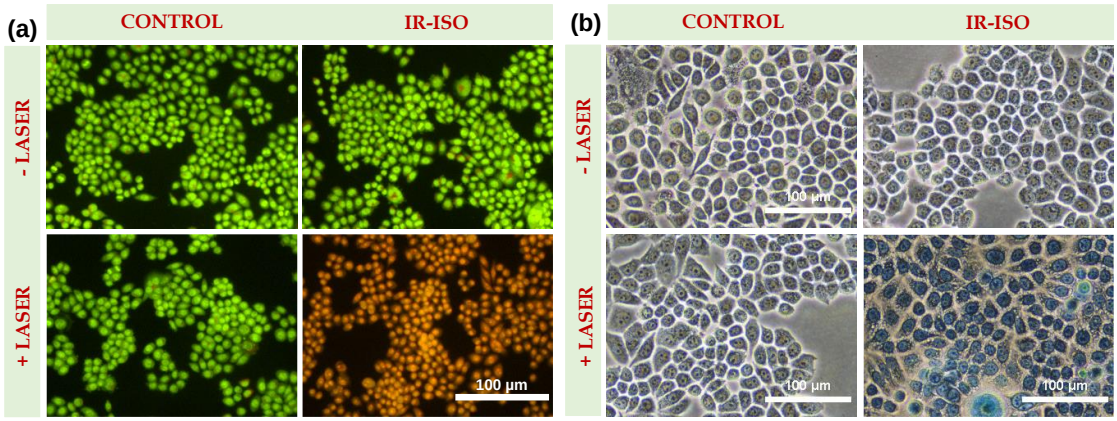

Figure 3.18. Apoptotic assessment of the **IR-ISO** treated cells followed by 532 nm laser excitation: (a) AO-EB dual staining assay where apoptotic cells stain in orange color and (b) Trypan blue staining assay where apoptotic cells stain in blue color.

Trypan blue selectively stains dead cells because healthy cells with intact membranes are impermeable to it and remain unstained. In **Figure 3.18b**, the trypan blue assay results show only a few stained cells with compromised membrane permeability in the control group treated with **IR-ISO**. The cells in the laser-irradiated group treated with **IR-ISO** exhibited significant uptake of trypan blue, indicating cellular apoptosis. Additionally, nuclear staining with Hoechst dye was conducted to assess nuclear condensation, which is a critical marker of apoptosis. The results showed a significant increase in blue fluorescence in cells treated with laser and **IR-ISO**, indicating a strong interaction between Hoechst dye and condensed chromatin, which strongly suggests DNA damage and apoptosis **(Figure 3.19a)**. These findings were consistent across all live-dead staining assays conducted, thereby confirming the reliability of the observations.

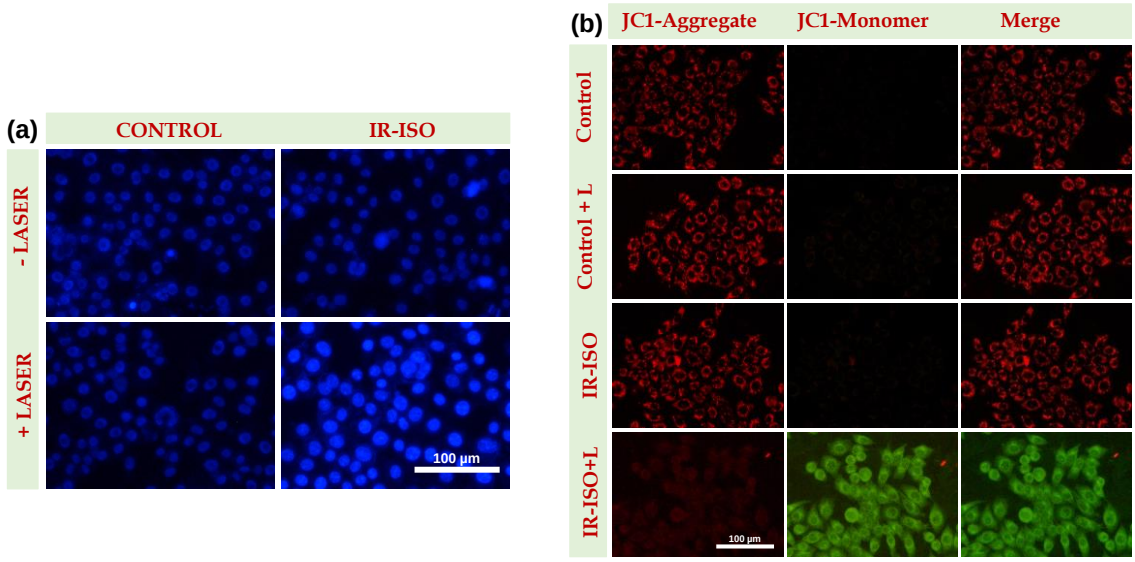

Figure 3.19. (a) Hoechst staining assay exhibiting the nuclear damage induced by **IR-ISO** with enhanced blue emission and (b) Evaluation of the mitochondrial membrane potential using the JC-1 assay. The elevation of the green color in the green panel indicates the reduction in membrane potential.

The JC-1 assay is a widely used fluorescence-based technique for assessing mitochondrial membrane potential, which is an important indicator of mitochondrial health and function. In this assay, the cell-permeable JC-1 dye accumulates in the mitochondria of healthy cells, where it forms aggregates that emit a red fluorescence. Conversely, in cells with depolarized or compromised mitochondria, JC-1 remains in its monomeric form, emitting green fluorescence. This shift from red to green fluorescence serves as a quantitative measure of mitochondria membrane potential. The assay is particularly valuable in studies of apoptosis, as changes in mitochondria membrane potential can signal the onset of cell death or dysfunction. As in **Figure 3.19b**, the laser-treated **IR-ISO** cells exhibited the green-emissive monomeric state clearly indicates the loss of mitochondrial membrane potential and cellular apoptosis.

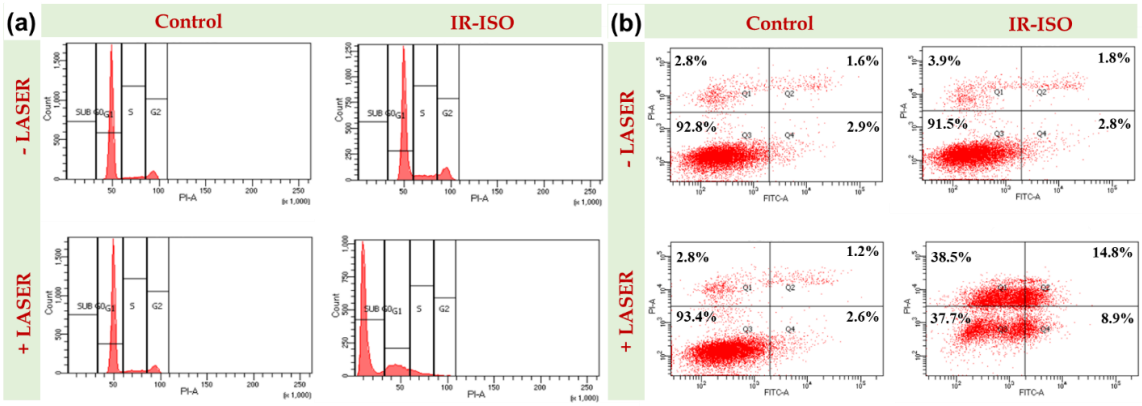

Figure 3.20. (a) Evaluation of apoptosis by cell cycle of the **IR-ISO**-treated SK-BR-3 cancer cell lines followed by 532 nm laser excitation and (b) The extent of apoptosis was calculated via the Annexin V-FITC method using flow cytometry.

To investigate the mechanism of photodynamic therapy (PDT) using the **IR-ISO** complex, its effect on cell death in SK-BR-3 cells was examined. The cell cycle cytometric assay was performed to assess the effects of **IR-ISO** treatment on SK-BR-3 cell proliferation and cell cycle progression and the result indicated that the **IR-ISO** + Laser treated group having the maximum SubG0 population (70 %) indicating the apoptotic cells (**Figure 3.20a**). Further, the Annexin V-FITC/PI flow cytometric assay was conducted following a 24 hour PDT treatment with a laser-irradiated **IR-ISO** batch. The results, shown in **Figure 3.20b**, demonstrated a significant increase in late apoptosis in the cell population treated with both **IR-ISO** and laser activation. These results indicate that **IR-ISO** primarily triggers apoptosis as the main mode of cell death in SK-BR-3 cells.

3.4. Conclusion

In conclusion, a dinuclear iridium based molecular rotor probe has been employed to differentiate cancer cells by detecting changes in intracellular viscosity. We also reported a comparative photophysical investigation of structurally similar mononuclear and dinuclear Ir(III) complexes **IR-ISO** and **IR-ISO** in various glycerol: methanol percentages. The **IR-ISO** exhibited a higher photoluminescence quantum yield and singlet oxygen quantum yield of 0.62 and 0.90 in glycerol respectively. The *in vitro* assessment of **IR-ISO**

was conducted using the SK-BR-3 breast cancer cell line. This demonstrated its mitochondrial colocalization through confocal fluorescence imaging with MitoTracker Green. **IR-ISO** showed effective laser-triggered apoptotic effects on SK-BR-3 cells in various live-dead assays, including trypan blue, acridine ethidium bromide, and Hoechst staining. Further, the JC-1 assay was used to assess mitochondrial membrane potential. The cell cycle and Annexin flow cytometric assay also indicated **IR-ISO**'s potential as a promising agent for image-guided photodynamic therapy.

3.5. Experimental Section

3.5.1. Materials and General Instruments

The chemicals used in this work, 1-phenylisoquinoline, 4,4′-dimethyl-2,2′-bipyridyl, 1,2-bis(4′-methyl-2,2′-bipyridin-4-yl)ethane, potassium carbonate, tetrabutylammonium bromide, $Pd(PPh_3)_4$, $IrCl_3.xH_2O$, NH_4PF_6, and 2-ethoxyethanol, were purchased from Sigma-Aldrich and TCI Chemicals and used as received without further purification. Reactions sensitive to moisture and oxygen were conducted under an argon atmosphere using dried solvents obtained from Sigma Aldrich and Merck. Thin layer chromatography (TLC) was performed on aluminum plates coated with silica gel, sourced from Merck. For column chromatography, silica gels with mesh sizes of 100 - 200 and 230 - 400 were employed. ^1H NMR (500 MHz) and ^{13}C NMR (125 MHz) analyses were done using a Bruker Avance DPX spectrometer, with TMS as the internal standard. DMSO-d_6 was used as solvents for NMR analysis. High-resolution mass spectra (HRMS) were obtained from a Thermo Scientific Q Exactive Hybrid Quadrupole-Orbitrap Electrospray Ionization Mass Spectrometer (ESI-MS).

3.5.2. Photophysical Measurements

UV/vis absorption spectra were obtained using a Shimadzu UV−vis spectrophotometer (UV-2600), and emission spectra were captured with a SPEX Fluorolog

spectrofluorimeter. Singlet oxygen generation quantum yields (Φ_s) were determined using 1,3-diphenylisobenzofuran (DPBF) as the singlet oxygen scavenger for **IR-IMO** and **IR-ISO**.[31] The DPBF reacts with singlet oxygen ($^1O_2$) through a [4 + 2] cycloaddition to produce *o*-dibenzoylbenzene. This reaction can be monitored by a reduction in DPBF absorbance at 410 nm and experiments were conducted with a 1:10 concentration ratio of Ir(III) complexes to DPBF, irradiated with an Oriel lamp equipped with a 445 nm band-pass filter at regular intervals, followed by UV−vis spectroscopy analysis. The singlet oxygen quantum yields for **IR-ISO** and **IR-IMO** in different concentrations of methanol and glycerol were determined using $[Ru(bpy)_3]Cl_2$ in acetonitrile as a reference standard ($\Phi_s = 0.57$) using Equation 1.

$$\Phi c = \Phi s \frac{Sc \times Fs}{Ss \times Fc} \qquad (1)$$

where S is the slope of a plot of the change in absorbance of DPBF (at 410 nm) with the irradiation time and F is the absorption correction factor, which is given by $F = 1-10^{-OD}$ (OD represents the optical density). The photoluminescence quantum yields of **IR-ISO** and **IR-IMO** were measured by a relative comparison method using $Ru(bpy)_3^{2+}$ ($\Phi_p = 0.06$ in acetonitrile) as the standard.[39] The fluorescence lifetime measurements were carried out using a picosecond single photon counting system (TCSPC) from Horiba (DeltaFlex), and a picosecond photon detection module (PPD-850) detector. The fluorescence decay profiles were analyzed using the EzTime software and fitted with a multiexponential decay model, with a chi-square value 1 ± 0.2. The photostability of **IR-ISO** was investigated by measuring the absorption spectra of a freshly prepared 10 μM solution in methanol, both with and without light irradiation. This was performed using an Oriel optical bench model 11200 equipped with a 200 W xenon lamp and a 445 nm band-pass filter at regular time

intervals. Additionally, to study the pH dependence of **IR-ISO**, emission spectra were recorded for a 10 μM solution of **IR-ISO** in PBS buffer across a pH range of 5 to 9.

3.5.3. In Vitro Studies

The MTT assay was conducted using the SK-BR-3 breast cancer cell line, which was obtained from ATCC. The cells were plated in a 96-well plate at a density of 12,000 cells per well and incubated for 24 hours in DMEM supplemented with 10% FBS. Following this, the cells were exposed to **IR-ISO** at concentrations ranging from 5 to 100 μM for an additional 24 hours. Cell viability was then assessed using the MTT assay. To evaluate the internalization of **IR-ISO**, SK-BR-3 cells were incubated with the compound in plain DMEM at concentrations of 5 to 20 μM per well. Images were taken from 0 to 2 hours at regular intervals using the FITC channel. For mitochondrial colocalization studies, cells were first treated with **IR-ISO** for approximately 2 hours. After washing, the cells were exposed to 100 nM MitoTracker Green for 15 minutes and then washed twice with PBS. Colocalization of **IR-ISO** with MitoTracker Green was visualized using a confocal fluorescent microscope. Singlet oxygen generation was assessed using SOSG (Sigma-Aldrich). Cells were first incubated with **IR-ISO** for 2 hours, then treated with SOSG. After incubation, the cells were washed twice with PBS, and fluorescence images were acquired using an inverted fluorescence microscope with the TRITC channel.

Cellular cytotoxicity and membrane damage induced by **IR-ISO** were evaluated using various selective staining methods. SK-BR-3 cells were plated in a 96-well plate at a density of 10,000 cells per well and incubated for 24 hours. The cells were then treated with **IR-ISO** (10 μM) for 2 hours, washed twice with PBS, and irradiated with a 532 nm laser for 2 minutes at 0.5 W power. The study included treatment groups such as **IR-ISO**-treated and untreated cells, both with and without laser irradiation. After 24 hours, the cells were washed and incubated with the appropriate staining reagents. A trypan blue dye

exclusion assay was conducted by treating the **IR-ISO** treated and laser-irradiated cells with 0.2% trypan blue solution in PBS for 5 minutes. After staining, the cells were washed, and bright field images were captured using an inverted microscope. For the acridine orange (AO)−ethidium bromide (EB) dual fluorescent staining assay, a live-dead assay cocktail (5 μg of each dye in 1 mL PBS) was incubated with both treated and untreated cells for 5 minutes, and images were captured in the green and red fluorescence channels. AO was taken up by all cells, emitting green fluorescence, while the orange-red fluorescence of EB indicated membrane-compromised dead cells. To assess nuclear staining with Hoechst, the cell lines were seeded in a 96-well plate for 24 hours, then incubated with **IR-ISO** for 2 hours before being irradiated with a 532 nm laser. After 24 hours, the cells were washed with PBS and stained with Hoechst dye (10 μg/mL). Images were captured using a fluorescence microscope, with DAPI filter settings (UV excitation range of 340−390 nm and emission range of 430−490 nm), green channel images were taken with an excitation range of 460−495 nm and emission range of 510−550 nm, and red channel images (MitoTracker) taken with an excitation range of 530−550 nm and emission at 575 nm.

The JC-1 assay was utilized to assess mitochondrial membrane depolarization in this study. Cells were seeded in 48-well plates at a density of 12,000 cells per well and subjected to various treatments according to the experimental protocol. The cells were incubated for approximately 24 hours to allow for cellular responses. Following the treatment period, the cells were carefully washed to remove any residual substances and then incubated with JC-1 dye at a concentration of 2 μM for 15 minutes. After incubation, the cells were washed once more with phosphate-buffered saline (PBS) to eliminate excess dye. Images of the cells were then captured using a fluorescence microscope, with separate channels for green and red fluorescence. The intensity of green and red fluorescence in the

images reflects the degree of mitochondrial membrane depolarization, offering valuable insights into the mitochondrial health and functionality of the treated cells.

Cell cycle analysis was conducted using the BD CycletestTM plus DNA reagent kit as per the manufactures instructions. For this, SK-BR-3 cells were seeded in six-well plates at a density of 1.5×10^5 cells per well and treated with or without **IR-ISO** and laser treatment was given to the respective groups after 24 h. Cell were tryspsinized and added the PI reagent of the kit and performed the flowcytometric analysis using BD FACS Aria II instrument. Additionally, an annexin-binding assay was conducted to verify cellular apoptosis. Cells were seeded in six-well plates at a density of 1.5×10^5 cells per well and treated with or without **IR-ISO**. Laser irradiation was applied to the designated treatment groups. After 24 hours of laser treatment, the cells were collected through trypsinization. Annexin V-FITC-PI staining was performed according to the manufacturer's instructions outlined in the Apoptosis Detection Kit (BD Pharmingen), and flow cytometric analysis was conducted using a FACS Aria system (BD, USA).

3.5.4. Synthesis and Characterization of Molecules

3.5.4a) Synthesis of **$[(pisq)_2IrCl]_2$**

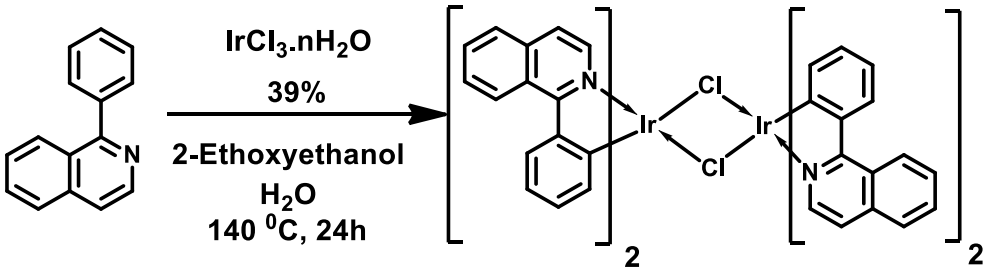

Scheme 3.1

A solution of $IrCl_3.nH_2O$ (300 mg, 0.85 mmol) and 1-phenylisoquinoline (430 mg, 2.1 mmol) in 2-ethoxyethanol (12 mL) / water (4 mL) mixture was refluxed for 24 h. After the

solution was cooled, the addition of distilled water gave a pale yellow precipitate that was filtered and washed with hexane and diethyl ether. The yellow crude product in 39% yield was used for the next reaction without further purification. HRMS: Calculated for $C_{60}H_{40}Cl_2Ir_2N_4$ with m/z 1272.19, where z =1, found 601.12.

3.5.4b) Synthesis of **IR-IMO**

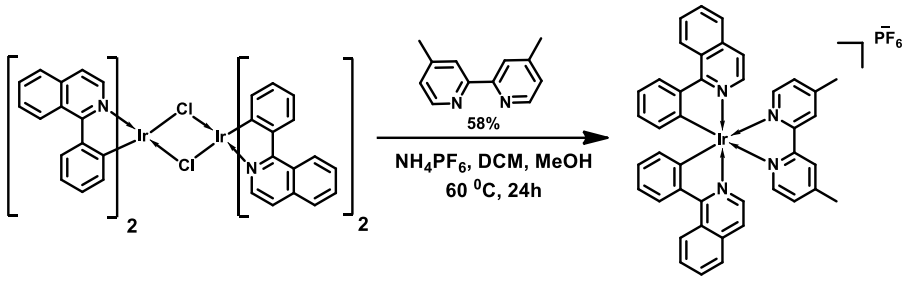

Scheme 3.2

A mixture of $[(pisq)_2IrCl]_2$ (100 mg, 0.07 mmol) and 4,4'-dimethyl-2,2'-dipyridyl (bpy) (25 mg, 0.14 mmol) were refluxed for 12 h in CH_2Cl_2/CH_3OH (1:1) solution under argon atmosphere. After being cooled, the solvent was removed under reduced pressure. Then purified by silica column chromatography with DCM and methanol as the eluent followed by precipitation with saturated NH_4PF_6 solution to yield orange-red coloured powder (58%). ^{1}H NMR (500 MHz, DMSO-d_6, TMS) δ 8.94 (d, 2H), δ 8.71 (s, 2H), δ 8.30 (d, 2H), δ 8.01 (d, 2H), δ 7.82 (d, 4H), δ 7.49 (m, 6H), δ 7.01 (m, 4H), δ 6.83 (t, 2H), δ 6.16 (d, 2H), δ 3.23 (s, 6H). ^{13}C NMR (125 MHz, $CDCl_3$) δ 168.20, 155.40, 154.65, 152.10, 149.37, 145.57, 140.86, 136.93, 132.54, 132.03, 131.07, 130.95, 129.90, 129.69, 128.19, 126.87, 126.06, 125.99, 122.70, 122.63, 21.50. HRMS: Calculated for $C_{42}H_{32}IrN_4^+$ with m/z 785.23, where z =1, found: 785.22.

3.5.4c) Synthesis of **IR-ISO**

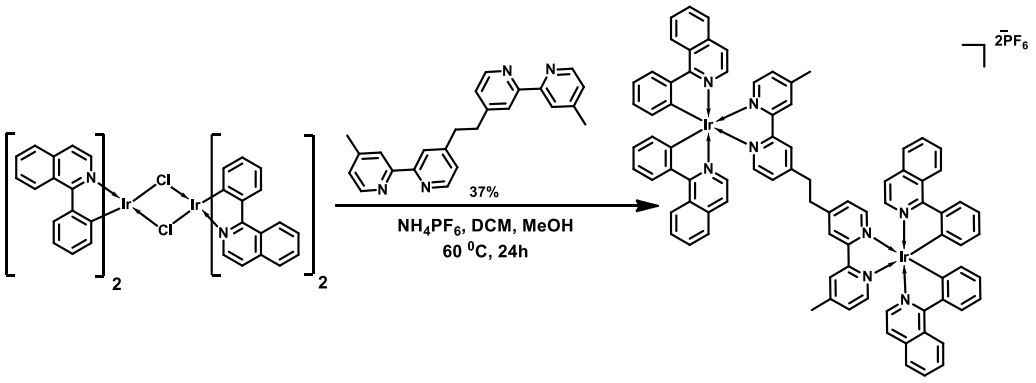

Scheme 3.3

A mixture of $[(pisq)_2IrCl]_2$ (100 mg, 0.07 mmol) and 1,2-bis(4'-methyl-2,2'-bipyridin-4-yl) ethane (bpye) (25 mg, 0.07 mmol) were refluxed for 48 h in CH_2Cl_2/CH_3OH (1:1) solution under argon atmosphere. After being cooled, the solvent was removed under reduced pressure. Then purified by silica column chromatography with DCM and methanol as the eluent, followed by precipitation with saturated NH_4PF_6 solution to yield orange-red colored powder (37%). ^{1}H NMR (500 MHz, DMSO-d_6, TMS) δ 8.92 (m, 4H), δ 8.69 (m, 4H), δ 8.29 (d, 4H), δ 7.99 (d, 4H), δ 7.82 (s, 6H), δ 7.75 (d, 4H), δ 7.50 (m, 12H), δ 7.34 (s, 2H), δ 7.18 (d, 2H), δ 6.84 (m, 6H), δ 6.12 (d, 4H), δ 3.14 (d, 4H), δ 2.44 (d, 6H). ^{13}C NMR (125 MHz, DMSO-d_6) δ 168.97, 156.00, 152.52, 149.06, 145.06, 136.98, 132.20, 131.67, 130.96, 130.45, 128.56, 127.64, 127.23, 125.76, 122.51, 121.90, 29.71, 21.22. HRMS: Calculated for $C_{84}H_{62}Ir_2N_8^{2+}$ with m/z 1568.44, where z =2, found 784.22.

3.5.5. NMR and ESI-HRMS Spectra

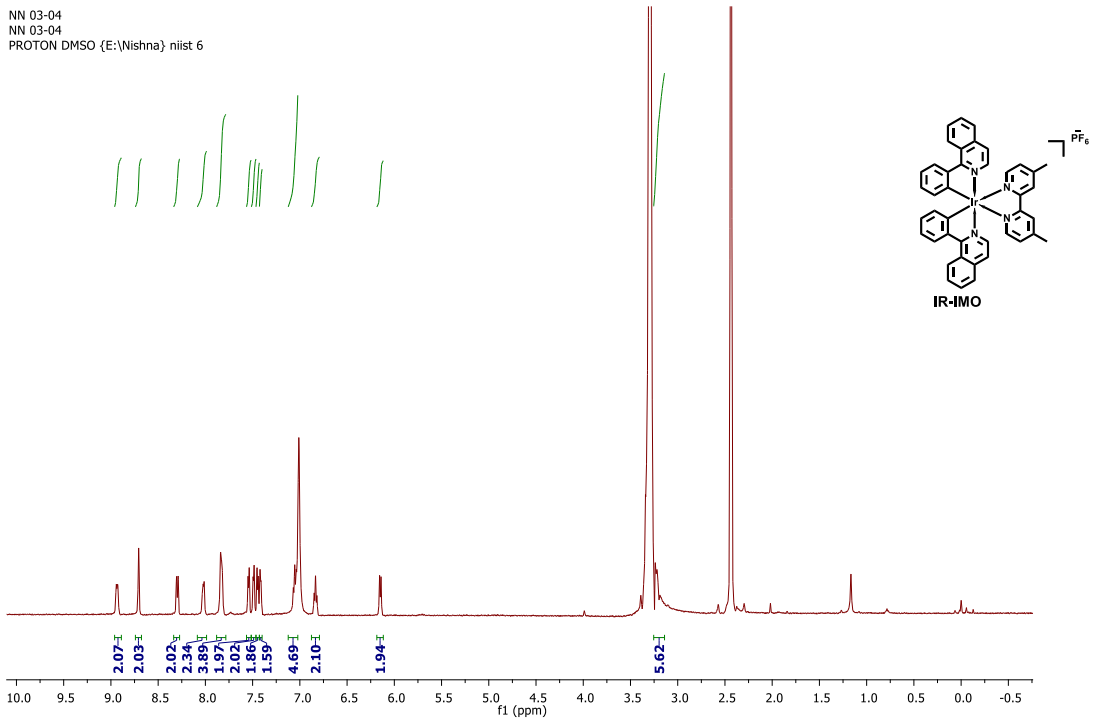

Figure 3.21. ^{1}H NMR of **IR-IMO** in dmso-d_6

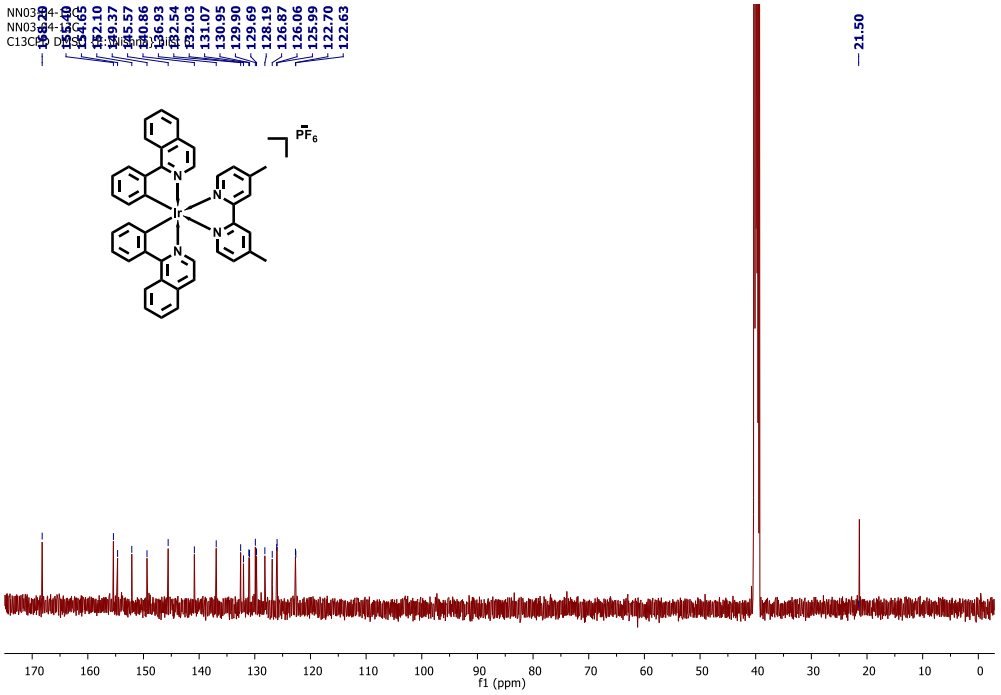

Figure 3.22. ^{13}C NMR of **IR-IMO** in dmso-d_6

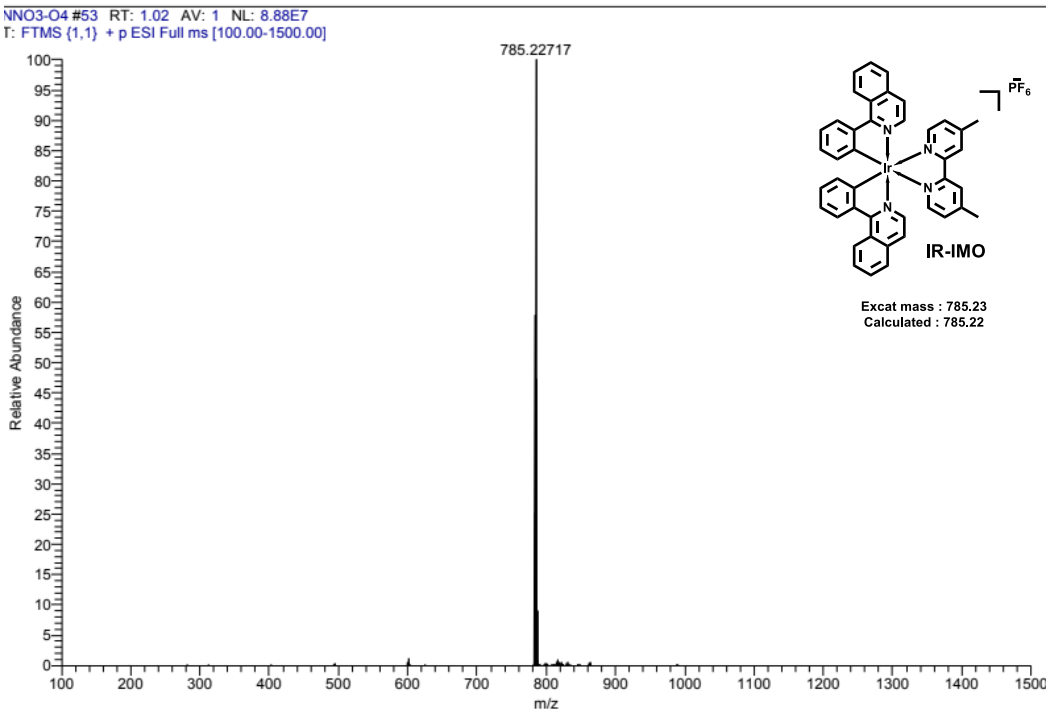

Figure 3.23. HRMS of **IR-IMO**

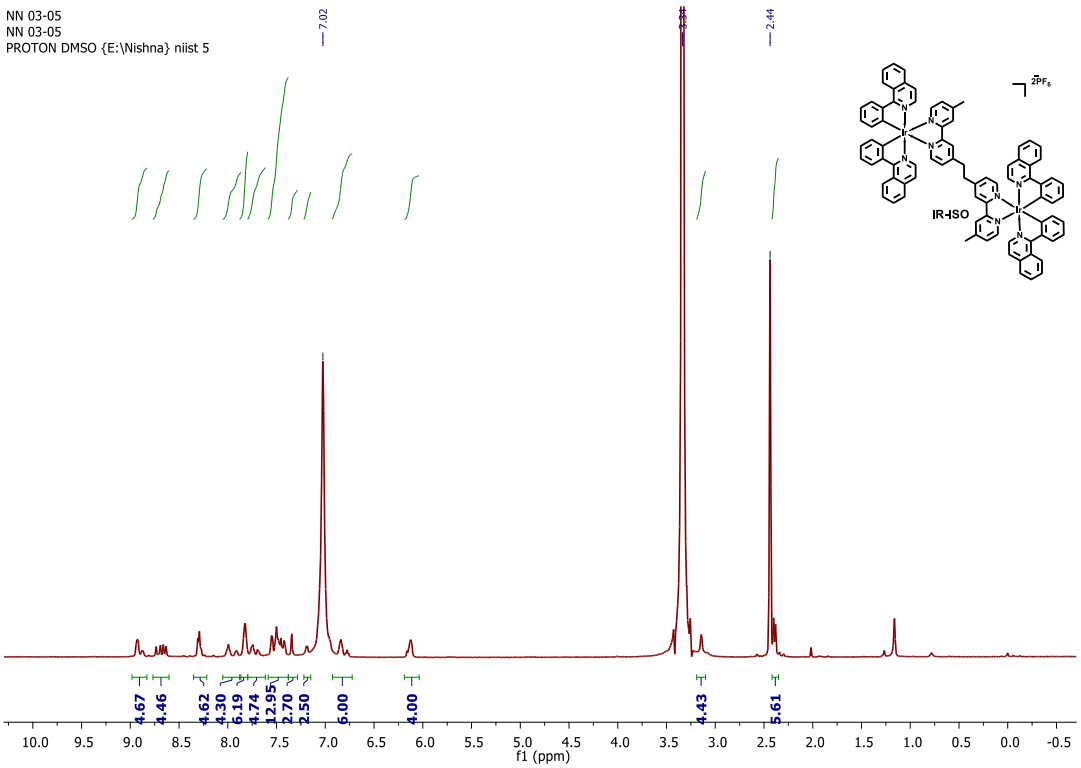

Figure 3.24. ^{1}H NMR of **IR-ISO** in dmso-d_6

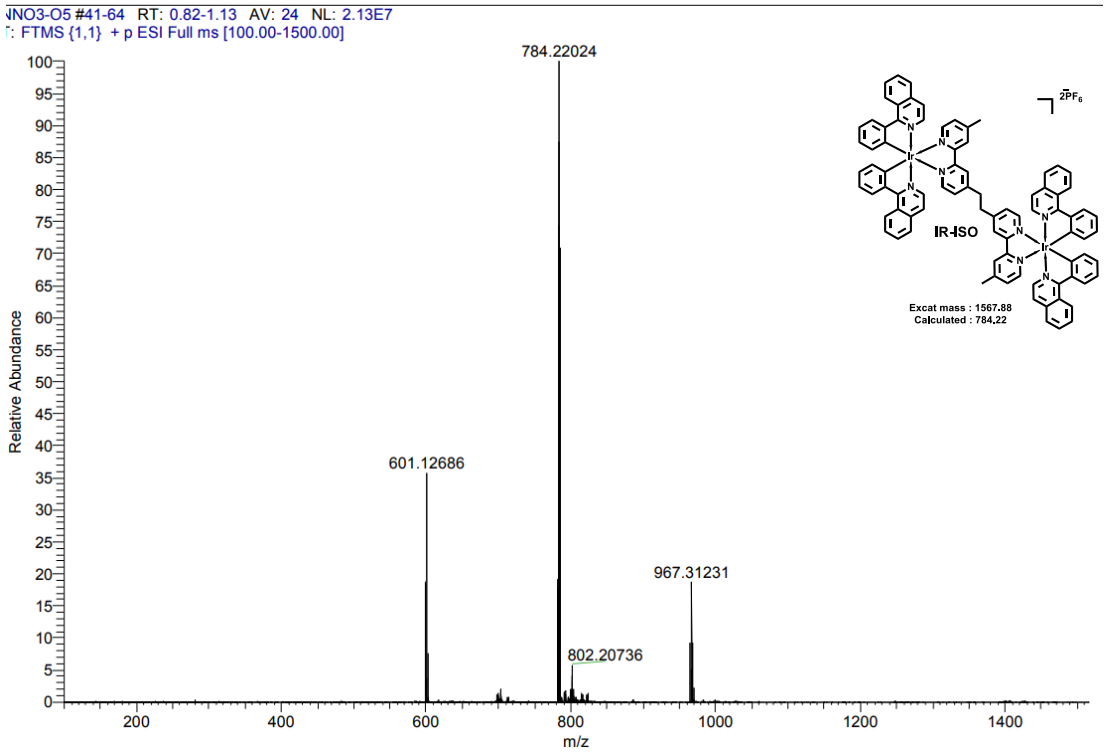

Figure 3.25. HRMS of **IR-ISO**

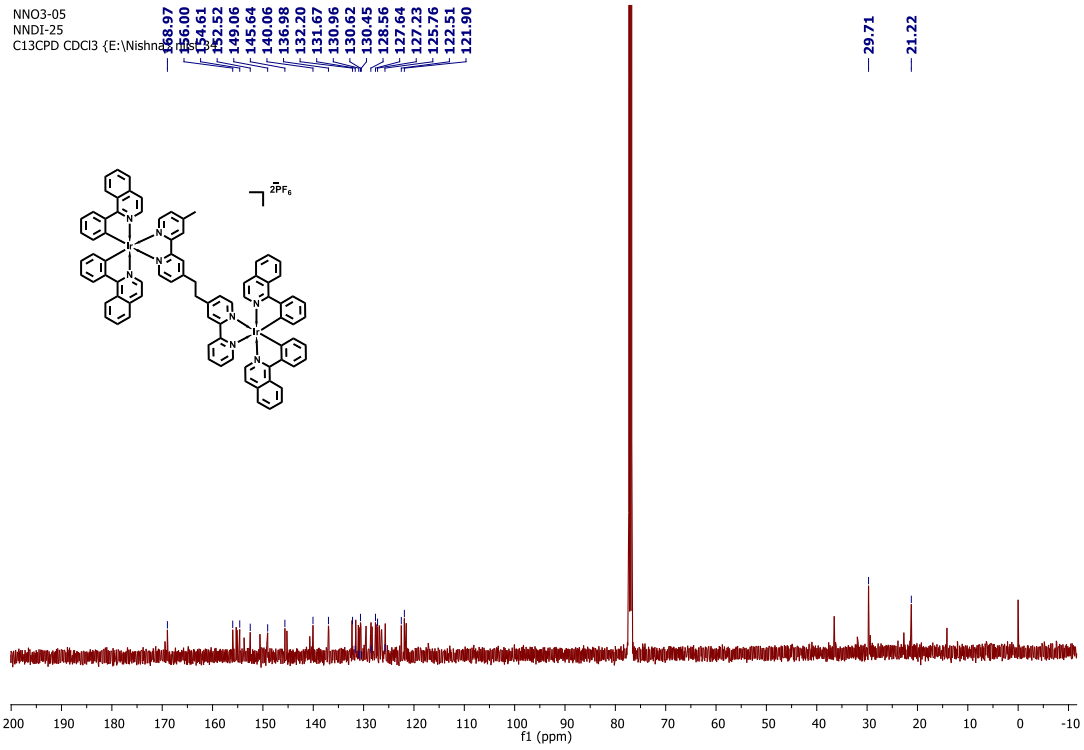

Figure 3.26. ^{13}C NMR of **IR-ISO** in $CDCl_3$

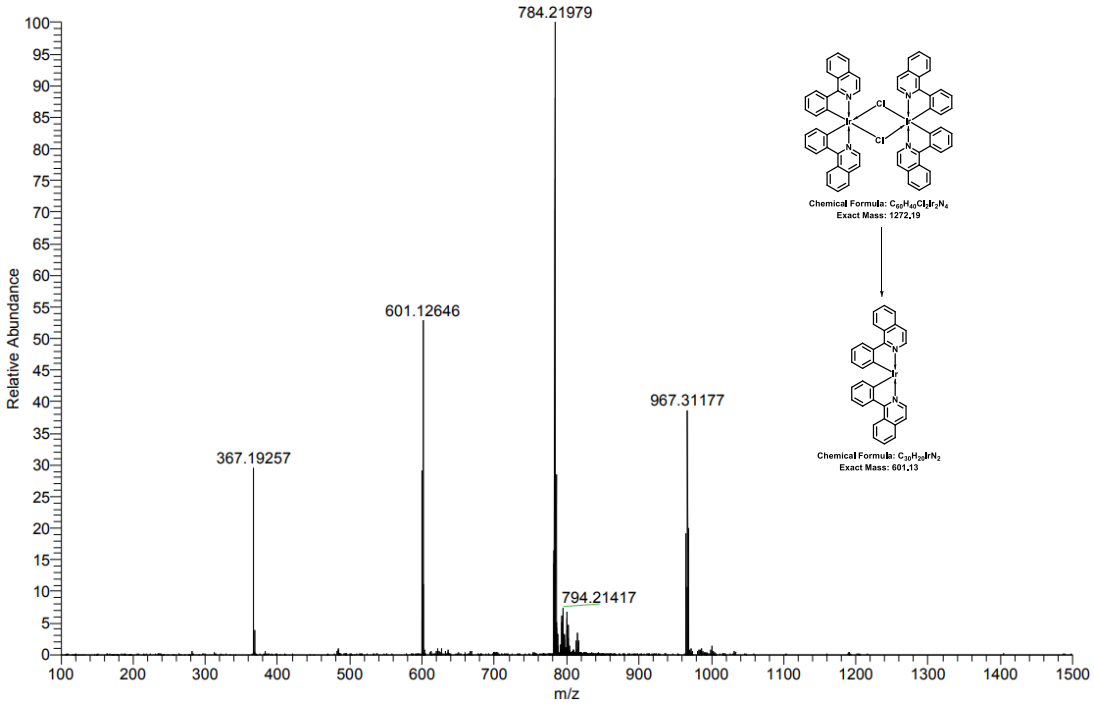

Figure 3.27. HRMS of **[(pisq)$_2$IrCl]$_2$**

3.6. References

1. Yang, Z.; He, Y.; Lee, J.-H.; Park, N.; Suh, M.; Chae, W.-S.; Cao, J.; Peng, X.; Jung, H.; Kang, C.; Kim, J. S., A Self-Calibrating Bipartite Viscosity Sensor for Mitochondria. *Journal of the American Chemical Society* **2013,** *135* (24), 9181-9185.

2. Fischer, D.; Theodorakis, E. A.; Haidekker, M. A., Synthesis and use of an in-solution ratiometric fluorescent viscosity sensor. *Nature Protocols* **2007,** *2* (1), 227-236.

3. Peng, C.; Ma, X.; Lin, D.; Feng, X.; Yu, H.; Li, Y., A novel near-infrared viscosity probe based on synergistic effect of AIE property and molecular rotors for mitophagy imaging during liver injury. *Analytica Chimica Acta* **2021,** *1187*, 339146.

4. Nipper, M. E.; Dakanali, M.; Theodorakis, E.; Haidekker, M. A., Detection of liposome membrane viscosity perturbations with ratiometric molecular rotors. *Biochimie* **2011,** *93* (6), 988-994.

5. Xu, L.; Zhao, J.; Xiong, F.; Huang, Y.; Sui, Y., Activatable molecular rotor based on bithiophene quinolinium toward viscosity detection in liquids. *Analytical Methods* **2022,** *14* (22), 2204-2211.

6. Chakraborty, N.; Silswal, A.; Koner, A. L., Julolidine-based fluorescent molecular rotor: a versatile tool for sensing and diagnosis. *Sensors & Diagnostics* **2024,** *3* (4), 585-598.

7. Xu, L.; Wu, K.; Han, R.; Sui, Y.; Huang, C.; Huang, W.; Liu, L., Visual detection of viscosity through activatable molecular rotor with aggregation-induced emission. *Spectrochimica Acta Part A: Molecular and Biomolecular Spectroscopy* **2021,** *261*, 120016.

8. Haidekker, M. A.; Theodorakis, E. A., Environment-sensitive behavior of fluorescent molecular rotors. *Journal of Biological Engineering* **2010,** *4* (1), 11.

9. Toliautas, S.; Dodonova, J.; Žvirblis, A.; Čiplys, I.; Polita, A.; Devižis, A.; Tumkevičius, S.; Šulskus, J.; Vyšniauskas, A., Enhancing the Viscosity-Sensitive Range of a BODIPY Molecular Rotor by Two Orders of Magnitude. **2019,** *25* (44), 10342-10349.

10. Kuimova, M. K., Mapping viscosity in cells using molecular rotors. *Physical Chemistry Chemical Physics* **2012,** *14* (37), 12671-12686.

11. Vyšniauskas, A.; Cornell, B.; Sherin, P. S.; Maleckaitė, K.; Kubánková, M.; Izquierdo, M. A.; Vu, T. T.; Volkova, Y. A.; Budynina, E. M.; Molteni, C.; Kuimova, M. K., Cyclopropyl Substituents Transform the Viscosity-Sensitive BODIPY Molecular Rotor into a Temperature Sensor. *ACS Sensors* **2021,** *6* (6), 2158-2167.

12. Zhou, F.; Shao, J.; Yang, Y.; Zhao, J.; Guo, H.; Li, X.; Ji, S.; Zhang, Z., Molecular Rotors as Fluorescent Viscosity Sensors: Molecular Design, Polarity Sensitivity, Dipole Moments Changes, Screening Solvents, and Deactivation Channel of the Excited States. **2011,** *2011* (25), 4773-4787.

13. Liu, F.; Wen, J.; Chen, S.-S.; Sun, S., A luminescent bimetallic iridium(iii) complex for ratiometric tracking intracellular viscosity. *Chemical Communications* **2018,** *54* (11), 1371-1374.

14. Wang, X.; Zhang, C.; Madji, R.; Voros, C.; Mazères, S.; Bijani, C.; Deraeve, C.; Cuvillier, O.; Gornitzka, H.; Maddelein, M.-L.; Hemmert, C., N-Heterocyclic Carbene-Iridium Complexes as Photosensitizers for In Vitro Photodynamic Therapy to Trigger Non-Apoptotic Cell Death in Cancer Cells. **2023,** *28* (2), 691.

15. Yokoi, K.; Yasuda, Y.; Kanbe, A.; Imura, T.; Aoki, S., Development of Wireless Power-Transmission-Based Photodynamic Therapy for the Induction of Cell Death in Cancer Cells by Cyclometalated Iridium(III) Complexes. **2023,** *28* (3), 1433.

16. Hohlfeld, B. F.; Gitter, B.; Kingsbury, C. J.; Flanagan, K. J.; Steen, D.; Wieland, G. D.; Kulak, N.; Senge, M. O.; Wiehe, A., Dipyrrinato-Iridium(III) Complexes for Application in Photodynamic Therapy and Antimicrobial Photodynamic Inactivation. **2021,** *27* (21), 6440-6459.

17. Cai, X.; Wang, K.-N.; Ma, W.; Yang, Y.; Chen, G.; Fu, H.; Cui, C.; Yu, Z.; Wang, X., Multifunctional AIE iridium (III) photosensitizer nanoparticles for two-photon-activated imaging and mitochondria targeting photodynamic therapy. *Journal of Nanobiotechnology* **2021,** *19* (1), 254.

18. Shi, H.; Carter, O. W. L.; Ponte, F.; Imberti, C.; Gomez-Gonzalez, M. A.; Cacho-Nerin, F.; Quinn, P. D.; Parker, J. E.; Sicilia, E.; Huang, H.; Sadler, P. J., A Photodynamic and Photochemotherapeutic Platinum-Iridium Charge-Transfer Conjugate for Anticancer Therapy. **2024,** *63* (23), e202400476.

19. He, X.; Wei, L.; Chen, J.; Ge, S.; Kandawa-Shultz, M.; Shao, G.; Wang, Y., Folate-targeted iridium complexes amplify photodynamic therapy efficacy through ferroptosis. *Inorganic Chemistry Frontiers* **2023,** *10* (16), 4780-4788.

20. Prieto-Castañeda, A.; Lérida-Viso, A.; Avellanal-Zaballa, E.; Sola-Llano, R.; Bañuelos, J.; Agarrabeitia, A. R.; Martínez-Máñez, R.; Ortiz, M. J., Phosphorogenic dipyrrinato-iridium(III) complexes as photosensitizers for photodynamic therapy. *Dyes and Pigments* **2022,** *197*, 109886.

21. Tan, Z.; Lin, M.; Liu, J.; Wu, H.; Chao, H., Cyclometalated iridium(iii) tetrazine complexes for mitochondria-targeted two-photon photodynamic therapy. *Dalton Transactions* **2024,** *53* (31), 12917-12926.

22. Huang, H.; Banerjee, S.; Sadler, P. J., Recent Advances in the Design of Targeted Iridium(III) Photosensitizers for Photodynamic Therapy. *Chembiochem* **2018,** *19* (15), 1574-1589.

23. Li, X.-L.; Zeng, L.-Z.; Yang, R.; Bi, X.-D.; Zhang, Y.; Cui, R.-B.; Wu, X.-X.; Gao, F., Iridium(III)-Based Infrared Two-Photon Photosensitizers: Systematic Regulation of Their Photodynamic Therapy Efficacy. *Inorganic Chemistry* **2023,** *62* (39), 16122-16130.

24. Lamansky, S.; Djurovich, P.; Murphy, D.; Abdel-Razzaq, F.; Lee, H.-E.; Adachi, C.; Burrows, P. E.; Forrest, S. R.; Thompson, M. E., Highly Phosphorescent Bis-Cyclometalated Iridium Complexes: Synthesis, Photophysical Characterization, and Use in Organic Light Emitting Diodes. *Journal of the American Chemical Society* **2001,** *123* (18), 4304-4312.

25. Li, G.; Chen, Y.; Wang, J.; Lin, Q.; Zhao, J.; Ji, L.; Chao, H., A dinuclear iridium(iii) complex as a visual specific phosphorescent probe for endogenous sulphite and bisulphite in living cells. *Chemical Science* **2013,** *4* (12), 4426-4433.

26. Zhao, Q.; Li, F.; Huang, C., Phosphorescent chemosensors based on heavy-metal complexes. *Chemical Society Reviews* **2010,** *39* (8), 3007-3030.

27. Zhang, P.; Chen, H.; Huang, H.; Qiu, K.; Zhang, C.; Chao, H.; Zhang, Q., A viscosity-sensitive iridium(iii) probe for lysosomal microviscosity quantification and blood viscosity detection in diabetic mice. *Dalton Transactions* **2019,** *48* (12), 3990-3997.

28. Nakagawa, A.; Hisamatsu, Y.; Moromizato, S.; Kohno, M.; Aoki, S., Synthesis and photochemical properties of pH responsive tris-cyclometalated iridium(III) complexes that contain a pyridine ring on the 2-phenylpyridine ligand. *Inorg Chem* **2014,** *53* (1), 409-22.

29. Neelambaran, N.; Shamjith, S.; Murali, V. P.; Maiti, K. K.; Joseph, J., Exploring a Mitochondria Targeting, Dinuclear Cyclometalated Iridium (III) Complex for Image-Guided Photodynamic Therapy in Triple-Negative Breast Cancer Cells. *ACS Applied Bio Materials* **2023,** *6* (12), 5776-5788.

30. Shamjith, S.; Murali, V. P.; Joesph, M. M.; T S, F.; Chandana, R.; Jayarajan, R. O.; Maiti, K. K., Hydrogen Sulfide-Induced Activatable Photodynamic Therapy Adjunct to Disruption of Subcellular Glycolysis in Cancer Cells by a Fluorescence-SERS Bimodal Iridium Metal–Organic Hybrid. *ACS Applied Materials & Interfaces* **2024,** *16* (21), 27114-27126.

31. Shamjith, S.; Joseph, M. M.; Murali, V. P.; Remya, G. S.; Nair, J. B.; Suresh, C. H.; Maiti, K. K., NADH-depletion triggered energy shutting with cyclometalated iridium (III) complex enabled bimodal Luminescence-SERS sensing and photodynamic therapy. *Biosensors and Bioelectronics* **2022,** *204*, 114087.

32. Yuan, H.; Han, Z.; Chen, Y.; Qi, F.; Fang, H.; Guo, Z.; Zhang, S.; He, W., Ferroptosis Photoinduced by New Cyclometalated Iridium(III) Complexes and Its Synergism with Apoptosis in Tumor Cell Inhibition. *Angewandte Chemie (International ed. in English)* **2021,** *60* (15), 8174-8181.

33. Samanta, S. K.; Maiti, K.; Halder, S.; Guria, U. N.; Mandal, D.; Jana, K.; Mahapatra, A. K., A 'double locked' ratiometric fluorescent probe for detection of cysteine in a viscous system and its application in cancer cells. *Organic & Biomolecular Chemistry* **2023,** *21* (3), 575-584.

34. Song, Y.; Zhang, H.; Wang, X.; Geng, X.; Sun, Y.; Liu, J.; Li, Z., One Stone, Three Birds: pH Triggered Transformation of Aminopyronine and Iminopyronine Based Lysosome Targeting Viscosity Probe for Cancer Visualization. *Analytical Chemistry* **2021,** *93* (3), 1786-1791.

35. Li, Q.; Zhu, W.; Gong, S.; Jiang, S.; Feng, G., Selective Visualization of Tumor Cell Membranes and Tumors with a Viscosity-Sensitive Plasma Membrane Probe. *Analytical Chemistry* **2023,** *95* (18), 7254-7261.

36. Tian, M.; Wu, R.; Xiang, C.; Niu, G.; Guan, W., Recent Advances in Fluorescent Probes for Cancer Biomarker Detection. **2024,** *29* (5), 1168.

37. Nonoyama, M., Benzo[h]quinolin-10-yl-N Iridium(III) Complexes. *Bulletin of the Chemical Society of Japan* **2006,** *47* (3), 767-768.

38. Kuramochi, Y.; Ishitani, O., Iridium(III) 1-Phenylisoquinoline Complexes as a Photosensitizer for Photocatalytic CO2 Reduction: A Mixed System with a Re(I) Catalyst and a Supramolecular Photocatalyst. *Inorganic Chemistry* **2016,** *55* (11), 5702-5709.

39. Brouwer, A. M., Standards for photoluminescence quantum yield measurements in solution (IUPAC Technical Report). **2011,** *83* (12), 2213-2228.

40. Ma, D.-L.; Wang, M.; Liu, C.; Miao, X.; Kang, T.-S.; Leung, C.-H. J. C. c. r., Metal complexes for the detection of disease-related protein biomarkers. **2016,** *324*, 90-105.

41. Vyšniauskas, A.; Qurashi, M.; Gallop, N.; Balaz, M.; Anderson, H. L.; Kuimova, M. K., Unravelling the effect of temperature on viscosity-sensitive fluorescent molecular rotors. *Chemical Science* **2015,** *6* (10), 5773-5778.

42. Yang, L.; Chen, Q.; Wan, Y.; Gan, S.; Li, S.; Lee, C.-S.; Jiang, Y.; Zhang, H.; Sun, H., A NIR molecular rotor photosensitizer for efficient PDT and synchronous mitochondrial viscosity imaging. *Chemical Communications* **2022,** *58* (67), 9425-9428.

CHAPTER 4

Development of Dinuclear Cyclometalated Iridium(III) Complexes with Non-innocent Bridging Ligand for OLED Applications

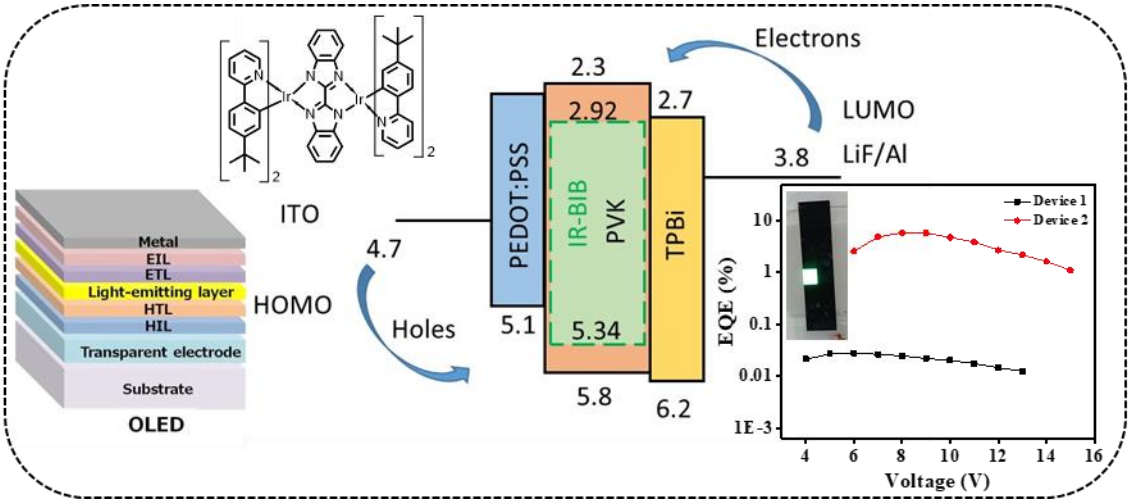

4.1. Abstract

The iridium complexes are widely regarded as the most commonly used class of emitters due to their efficient spin-orbit coupling, which relaxes the spin selection rule. The strong photoluminescence observed in Ir(III) complexes is primarily due to the triplet metal-to-ligand charge transfer (^{3}MLCT). However, the majority of studies on Ir(III)-based photosensitizers have focused on mononuclear complexes, with only limited research on dinuclear systems. Thoroughly exploring the potential of iridium-based dinuclear systems for OLED applications still poses substantial challenges. Herein, we report the synthesis and optoelectronic applications of two iridium dinuclear complexes with 2-(4-tert-butylphenyl)pyridine as the cyclometalating ligands and bibenzimidazole (**IR-BIB**) or diketopyrrolopyrrole (**IR-DPP**) as the bridging ligand. These molecules are designed to

offer high photoluminescence quantum yields and short excited state lifetimes. The prolonged lifetime of excited triplet states enhances the chances of exciton-exciton interactions, resulting in triplet-triplet annihilation and, consequently, efficiency roll-off. [1, 2] The **IR-BIB** and **IR-DPP** complexes exhibited PLQYs of 0.75 and 0.27 and an excited state lifetime of 70 ns and 101 ns, respectively. The OLED devices were fabricated using the high-PLQY derivative **IR-BIB**, and their performance was evaluated for several parameters, including current efficiency, power efficiency, luminescence intensity, and EQE. Optimized devices of **IR-BIB** alone and **IR-BIB** doped in PVK showed a luminescence maximum of 150 cd/m^2 and 6,300 cd/m^2, respectively The OLED device incorporating **IR-BIB** and PVK demonstrated a higher EQE of 5.85%, while the **IR-BIB** alone device exhibited an EQE of 0.028%. This chapter highlights the application of the dinuclear iridium complexes as excellent emitting layers in OLED and demonstrates the potential of these materials for optoelectronic applications.

4.2. Introduction

Organic light-emitting diodes (OLEDs) have achieved widespread popularity in the display and lighting industries due to their remarkable properties, including wide view angles, high contrast ratios, and the ability to produce flexible and lightweight displays.[3-6] OLEDs operate through the electroluminescence of organic compounds, wherein organic layers emit light when an electric current is applied. These devices are categorized into three generations based on their emissive materials: fluorescent, phosphorescent, and thermally activated delayed fluorescence (TADF) OLEDs. When an electric current flows through the organic material, it generates excitons, which are electron-hole pairs that can exist in either singlet (25%) or triplet (75%) spin states, as determined by quantum spin statistics. In traditional fluorescent emitters, the energy from the 75% triplet excitons is lost via non-radiative transitions, limiting the internal quantum efficiency (IQE) to a theoretical maximum of 25%.[2, 6, 7] However, by incorporating heavy metals like iridium or platinum into the emitter, the transition from the lowest triplet excited state (T_1) to the ground state (S_0) is enhanced, allowing for efficient phosphorescence in phosphorescent based OLEDs. This strong spin-orbit coupling effect enables both singlet and triplet excitons to be harnessed for light emission, pushing the IQE close to 100% IQE.[6-8] In TADF OLEDs, triplet excitons are thermally activated into singlet excitons, enabling the recovery of triplet energy and improving efficiency without the need for heavy metals.[9-11]

Iridium complexes are the most widely used emitters among heavy metals due to their efficient spin-orbit coupling, which relaxes the spin selection rule. These complexes exhibit high photoluminescence quantum yields (Φ_P), short excited state lifetimes (τ), and the ability to fine-tune emission colors through ligand modifications.[6, 12] While there has been considerable research on homoleptic and heteroleptic mononuclear iridium

complexes for OLEDs, the exploration of multi-metal iridium complexes has been relatively limited.[13-17] Despite initial synthetic challenges, recent studies highlight their superior photophysical properties and device performance in optoelectronic applications. Multiple metal-centered iridium complexes are expected to enhance luminescence quantum yields by boosting spin-orbit coupling through multiple metal centers.[18-21] Kozhevnikov *et al.,* reported dinuclear iridium(III) complexes using ditopic bis-terdentate cyclometalating ligands, achieving high PLQY values of up to 0.65. Similarly, Bryce *et al.,* developed a highly efficient green-emitting phosphorescent dinuclear iridium(III) complex for OLED application with impressive external quantum efficiency (η_{ext}) of 11%, luminance efficiency (η_L) of 37 cdA^{-1}, and power efficiency (η_P) of 14 lmW^{-1}. These advancements highlight the potential of dinuclear iridium(III) complexes to outperform the mononuclear complexes. OLED technology has made significant strides across its three generations, but challenges remain, particularly in terms of material stability and efficiency. The incorporation of dinuclear iridium(III) complexes offers a promising strategy, leveraging their unique optoelectronic properties and the ability to fine-tune emission characteristics through ligand modifications. Phosphorescent materials are expected to play a pivotal role in making organic light-emitting diode (OLED) displays and lighting more widely available. These materials often rely on heavy metal complexes, with iridium(III) based complexes being particularly effective. Iridium(III) complexes emit light primarily from states with considerable metal-to-ligand charge transfer (MLCT) character, offering a key advantage over fluorescent materials by utilizing both singlet and triplet excitons for light emission. This ability to harvest nearly all excitons enhances their efficiency significantly. Therefore, organic ligands have a significant impact on the photophysical properties of iridium(III) complexes, and numerous organic ligands have been designed to modify their emission color and charge-injection/transport properties.

However, the importance of the metal center is often overlooked, as most iridium(III) complexes discussed in the literature are mononuclear iridium complexes. The exploration of dinuclear iridium(III) complexes has been relatively rare, resulting in the development of only a few new compounds in this area. This has been done either by coupling two mononuclear iridium(III) complexes through active sites or by reacting the iridium(III) chloro-bridged dimer with specially prepared bridge ligands. Despite the complex and laborious synthesis processes, these methods generally yield dinuclear iridium(III) complexes with weak or no luminescence at room temperature, making them unsuitable for high-performance OLED applications.

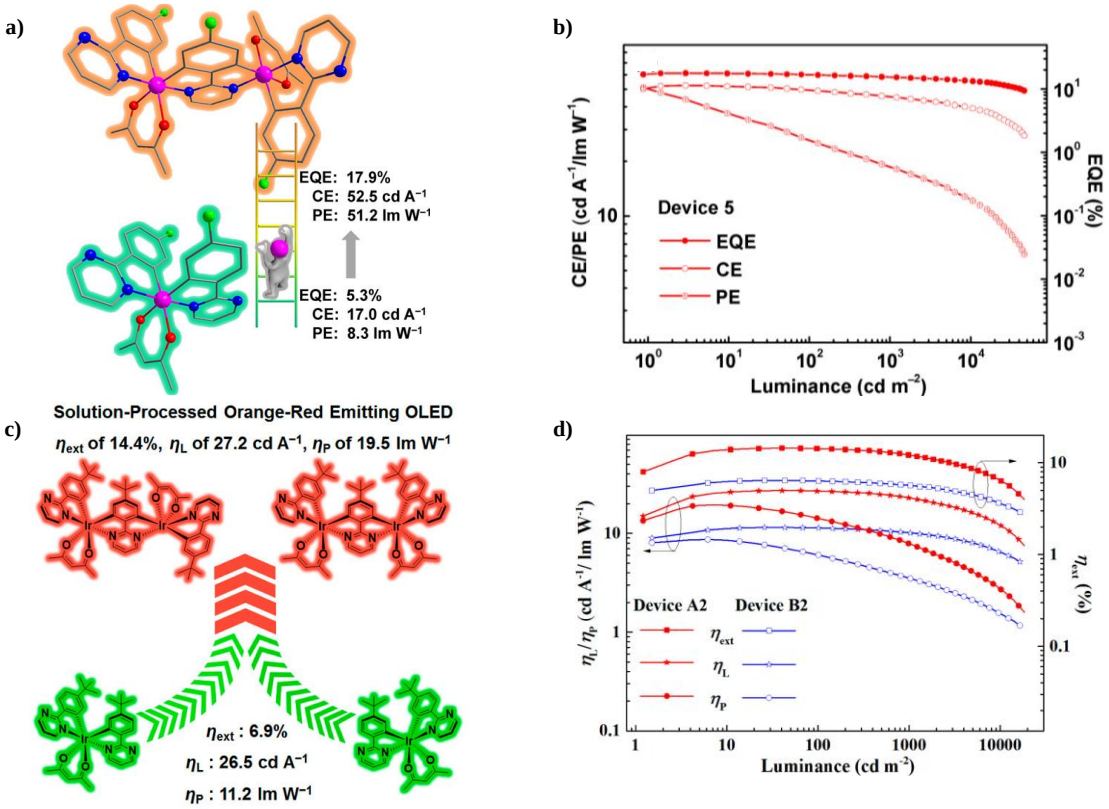

Figure 4.1. Examples of dinuclear iridium complex for OLED device applications: (a) The structure of dinuclear **(FDIr1)** and mononuclear iridium complex **(FIr1)**; (b) Efficiency versus luminance curve of device based on **FDIr1**; (c) The structure of dinuclear complexes **(D1**, **D2)** and mononuclear iridium complex (**M1**) and (d) Efficiency versus luminance curve of devices A2 **(D1)** and B2 **(D2)**. Figure adapted from references 22 and 23, respectively.

As shown in **Figure 4.1a,b**, Zhou and colleagues introduced pyrimidine-based mononuclear **(FIr1)** and dinuclear **(FDIr1)** iridium complexes, with **FDIr1** demonstrating a high photoluminescence quantum yield of 0.68. Solution-processed OLEDs were fabricated using both mononuclear and dinuclear iridium complexes. The mononuclear complex **(FIr1)** achieved an external quantum efficiency (EQE) of 5.3%, along with a current efficiency (CE) of 17.0 cd/A and a power efficiency (PE) of 8.3 lm/W. In contrast, the solution-processed OLED based on the dinuclear Ir(III) complex **(FDIr1)** delivered an impressive EQE of 17.9%, with a CE of 52.5 cd/A and a PE of 51.2 lm/W.[22]

Wong *et al.*, reported a green-emitting mononuclear iridium complex **(M1**) based on 2-phenylpyrimidine, along with two red-emitting isomers of dinuclear iridium(III) complexes **(D1** and **D2)**. The solution-processed OLED using the mononuclear complex **(M1)** showed an external quantum efficiency (η_{ext}) of 6.9%, with a luminance efficiency (η_L) of 26.5 cd/A and a power efficiency (η_P) of 11.2 lm/W. The dinuclear isomers, **D1** and **D2**, achieved higher external quantum efficiencies (η_{ext}) of 14.4% and 6.4%, respectively. **D1** had a luminance efficiency of 27.2 cd/A and a power efficiency of 19.5 lm/W, while **D2** exhibited a luminance efficiency of 11.5 cd/A and a power efficiency of 8.7 lm/W (**Figure 4.1c,d**).[23] Despite these advances, developing dinuclear iridium(III) complexes with desired properties for high-performance OLEDs remains a significant challenge.

Herein, we report a couple of dinuclear cyclometalated iridium(III) complexes synthesized using microwave reaction conditions. These complexes are synthesized using iridium chlorine bridge derivate with bibenzimidazole (**IR-BIB**) and diketopyrrolopyrrole (**IR-DPP**) bridging ligands. The synthesis and characterization of the complexes, along with their photophysical and electrochemical properties, are reported. The iridium(III) bibenzimidazole complex (**IR-BIB**) exhibited a high photoluminescence quantum yield

(Φ_P) compared to the DPP derivative (**IR-DPP**). Further, a solution-processed OLED using the dinuclear iridium(III) benzimidazole complex (**IR-BIB**) as the emitter exhibited an EQE (η_{ext}), luminance efficiency (η_L), and power efficiency (η_J) of 5.85%, 6300 cdm^{-2}, and 155 $mAcm^{-2}$, respectively.

4.3. Results and Discussion

4.3.1. Design and Synthesis of IR-BIB and IR-DPP Complexes

Herein, we synthesized two dinuclear iridium complexes as illustrated in **Figure 4.2** and investigated their photophysical properties. The cyclometalating ligand, 2-(4-tert-butylphenyl)pyridine (tbppy), was synthesized via a Pd-catalyzed Suzuki cross-coupling reaction between 2-bromopyridine and 4-tert-butylphenylboronic acid. The chlorine-bridged iridium dinuclear complex, $[(tbppy)_2IrCl]_2$, was synthesized by coupling the cyclometalating ligand with iridium(III) chloride ($IrCl_3.xH_2O$) via a Nonoyama reaction.[24] The dinuclear Ir(III) complex, **IR-BIB**, was synthesized through a microwave reaction of the chlorine-bridged iridium dinuclear complex $[(tbppy)_2IrCl]_2$ with a bibenzimidazole ligand. Similarly, the iridium dinuclear complex, **IR-DPP**, was produced via a microwave reaction using the same chlorine-bridged iridium dinuclear complex $[(tbppy)_2IrCl]_2$ and the ancillary ligand diketopyrrolopyrrole The synthesized dinuclear complexes, as well as all the synthetic intermediates, were well-characterized using HRMS and NMR spectroscopic methods.

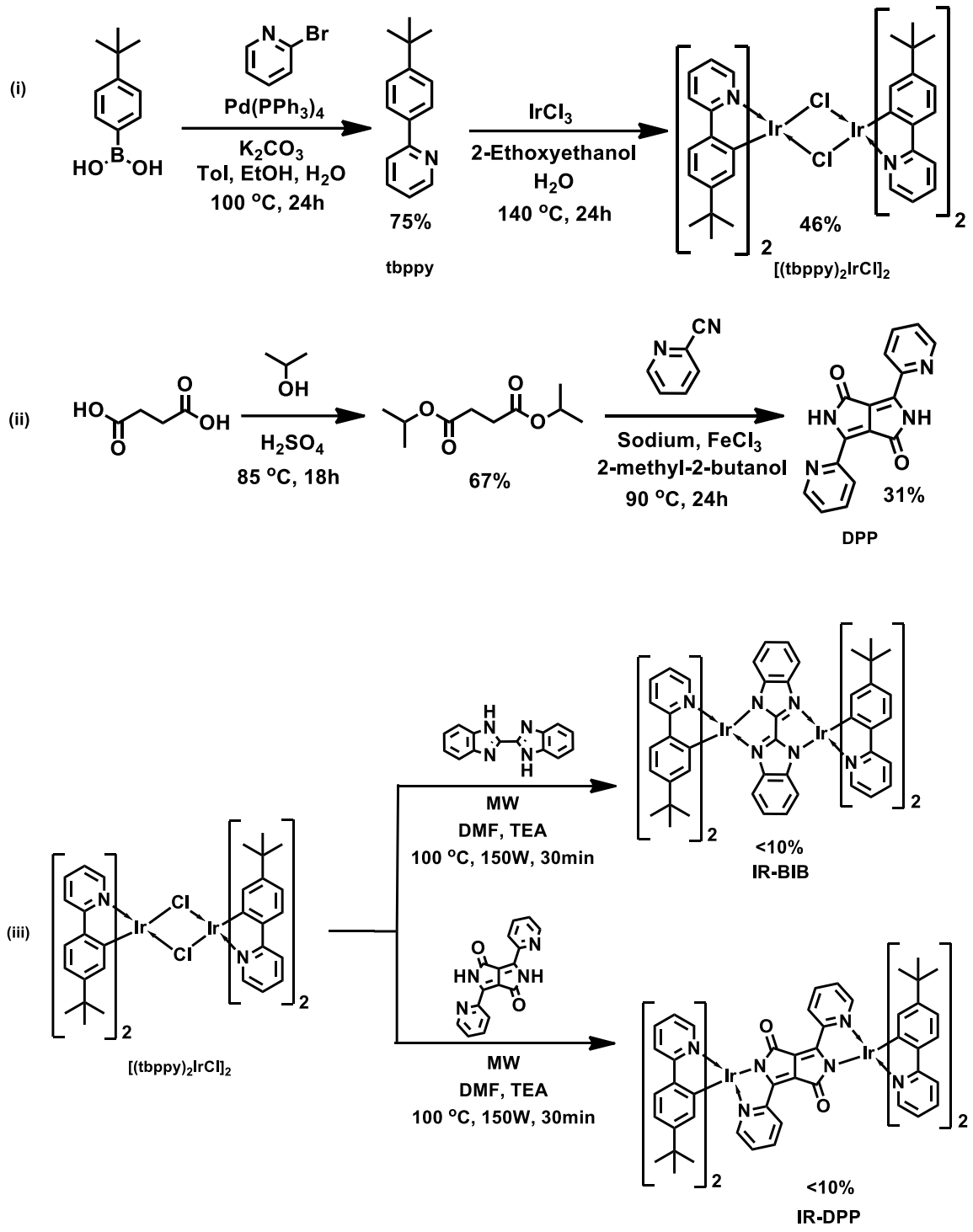

Figure 4.2. Structure and scheme adopted for the synthesis of iridium complexes, **IR-DPP** and **IR-BIB**.

4.3.2. Photophysical and Electrochemical Properties

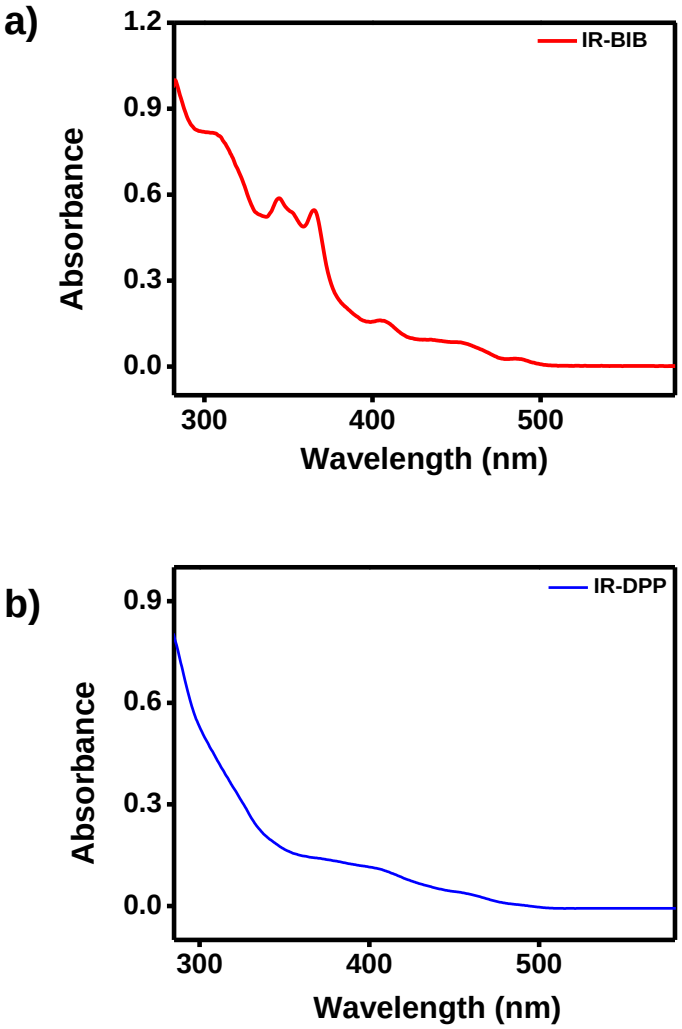

Figure 4.3. (a) UV−visible absorption spectra of **IR-BIB** in toluene and (b) UV−visible absorption spectra of **IR-DPP** in toluene.

The absorption spectra of the dinuclear complexes were recorded in toluene at room temperature, as shown in **Figure 4.3a,b**. The UV-vis absorption spectra of both **IR-BIB** and **IR-DPP** exhibited an intense band around 200 nm - 300 nm, which can be assigned to allowed π-π* ligand-centered transitions in 2-(4-tert-butylphenyl)pyridine (tbppy) and ancillary ligands. The less intense absorption bands in the range of 300 nm - 500 nm correspond to spin allowed and spin forbidden, mixed singlet and triplet metal-to-ligand charge transfer (^{1}MLCT and ^{3}MLCT) admix with the ligand-to-ligand charge-transfer

(LLCT) transitions.[25] The emission spectra of **IR-BIB** and **IR-DPP** in toluene at room temperature under degassed conditions were documented in **Figure 4.4a,b**. An intense, structured emission band with a maximum at 498 nm and a shoulder peak around 532 nm was observed for **IR-BIB**, while **IR-DPP** showed a broad emission band with an emission maximum of 516 nm. The broad and featureless emission bands are mainly attributable to charge-transfer (CT) states, while the structured emission occurs when charge transfer is combined with interactions between the excited state and the ligand's vibrational modes.[8, 26-29]

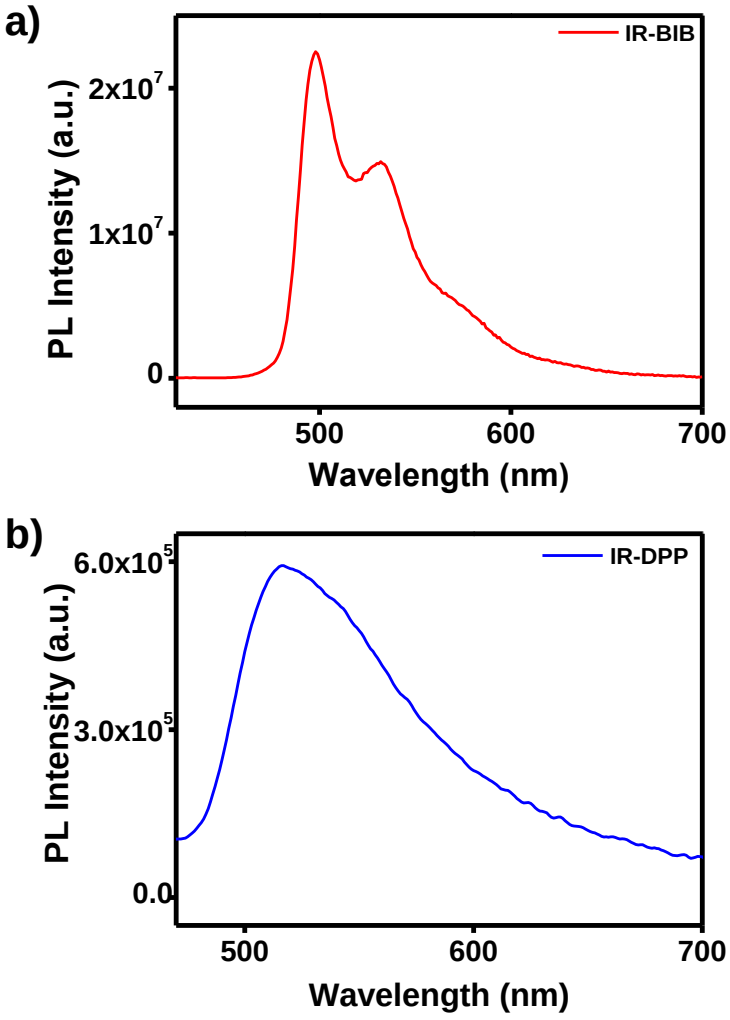

Figure 4.4. (a) Emission characteristics of **IR-BIB** at 365 nm excitation and (b) Emission characteristics of **IR-DPP** at 365 nm excitation.

The photoluminescence quantum yields (PLQYs) of both the dinuclear complexes were examined in degassed toluene solutions at room temperature. **IR-BIB** showed a PLQY of 0.75 while **IR-DPP** had a PLQY of 0.27, measured using $Ir(ppy)_3$ in dichloroethane (ϕ_P = 0.89 in dichloroethane) as the reference.[30] Notably, the PLQY of 0.75 for **IR-BIB** is exceptional for a dinuclear iridium complex.

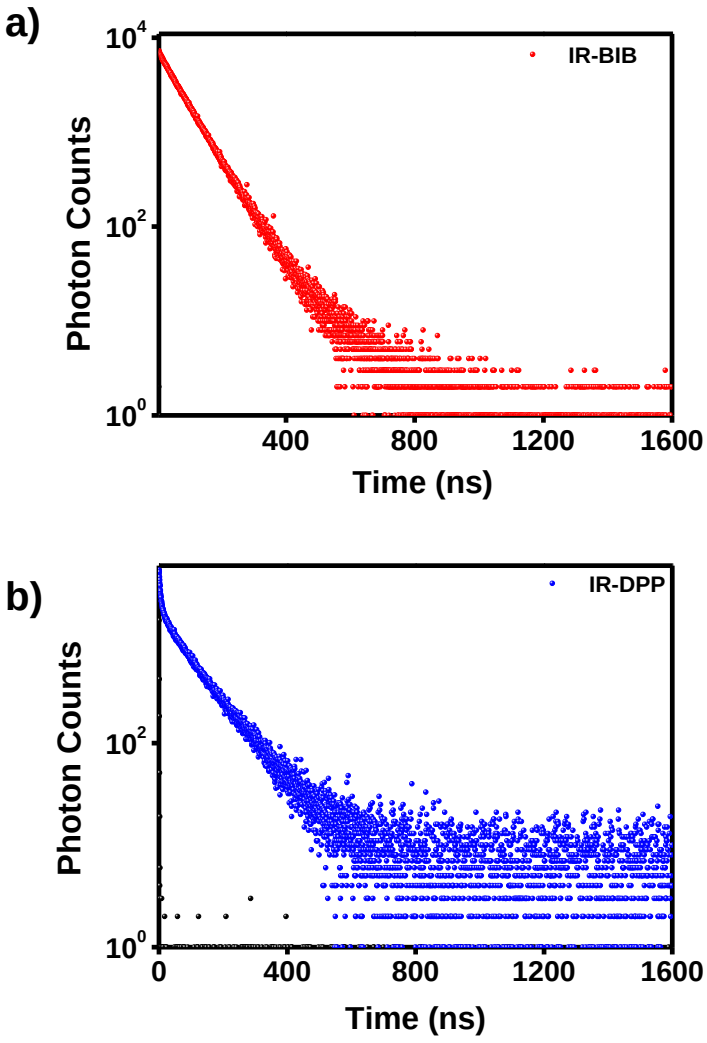

Figure 4.5. Excited state life time measured by Time-Correlated Single Photon Counting (TCSPC): (a) **IR-BIB** and (b) **IR-DPP**.

Further, we recorded the excited state lifetimes (τ) of the dinuclear iridium complexes in toluene at room temperature (**Figure 4.5a,b**). The measured TCPSC lifetime

of **IR-BIB** was 70 ns, while for **IR-DPP** the lifetime was around 101 ns. The **IR-BIB** exhibited a slightly short lifetime compared to **IR-DPP**. To gain further insight into the details, radiative (k_r) and non-radiative (k_{nr}) decay rates of **IR-BIB** and **IR-DPP** were calculated.[31] By integrating Equations 1 and 2 below and utilizing the measured PLQY and lifetime data at room temperature, the radiative (k_r) and non-radiative (k_{nr}) decay rates can be calculated, as detailed in **Table 4.1**.[32]

$$\text{PLQY} = \frac{k_r}{(k_r + k_{nr})} \quad (1)$$

$$\frac{1}{\tau} = k_r + k_{nr} \quad (2)$$

The radiative decay rate of **IR-BIB** was determined to be $k_r = 1.0 \times 10^7$ s^{-1}, while **IR-DPP** showed a radiative decay rate of $k_r = 2.6 \times 10^6$ s^{-1}. The non-radiative decay rate for **IR-BIB** was calculated as $k_{nr} = 3.3 \times 10^6$ s^{-1}, whereas for **IR-DPP** it was $k_{nr} = 7.3 \times 10^6$ s^{-1}.

To examine their electrochemical properties and determine the energy levels of the highest occupied molecular orbital (HOMO) and the lowest unoccupied molecular orbital (LUMO), the electrochemical properties of dinuclear Ir(III) complexes were assessed using cyclic voltammetry in acetonitrile at room temperature. These measurements were conducted relative to an internal ferrocenium/ferrocene reference (Fc^+/Fc) (**Figure 4.6a,b**).

$$E_{HOMO} = -(E_{ox} - E_{Fc/Fc+} + 4.8) \quad (3)$$

$$E_{LUMO} = -(E_{red} - E_{Fc/Fc+} + 4.8) \quad (4)$$

$$\Delta E_{gap} = E_{LUMO} - E_{HOMO} \quad (5)$$

$$\Delta E_{gap} = 1240/\lambda_{abs\text{-}onset} \quad (6)$$

By using Equations 3 and 4, the HOMO and LUMO energy levels (E_{HOMO} and E_{LUMO}) of both the iridium dinuclear complexes were obtained.[13] The cyclic voltammetry results indicate the E_{HOMO} values of **IR-BIB** and **IR-DPP** are both -5.34 eV, while the E_{LUMO} values are -2.92 eV for **IR-BIB** and -3.44 eV for **IR-DPP**. The energy gap (ΔE_{gap}) was calculated using Equation 5, yielding values of 2.42 eV for **IR-BIB** and 1.90 eV for **IR-DPP**.[33] The E_{LUMO} and ΔE_{gap} of the dinuclear iridium complexes were reconfirmed using Equation 6.[33, 34] All the photophyscial and electrochemical data are summarized in **Table 4.1**.

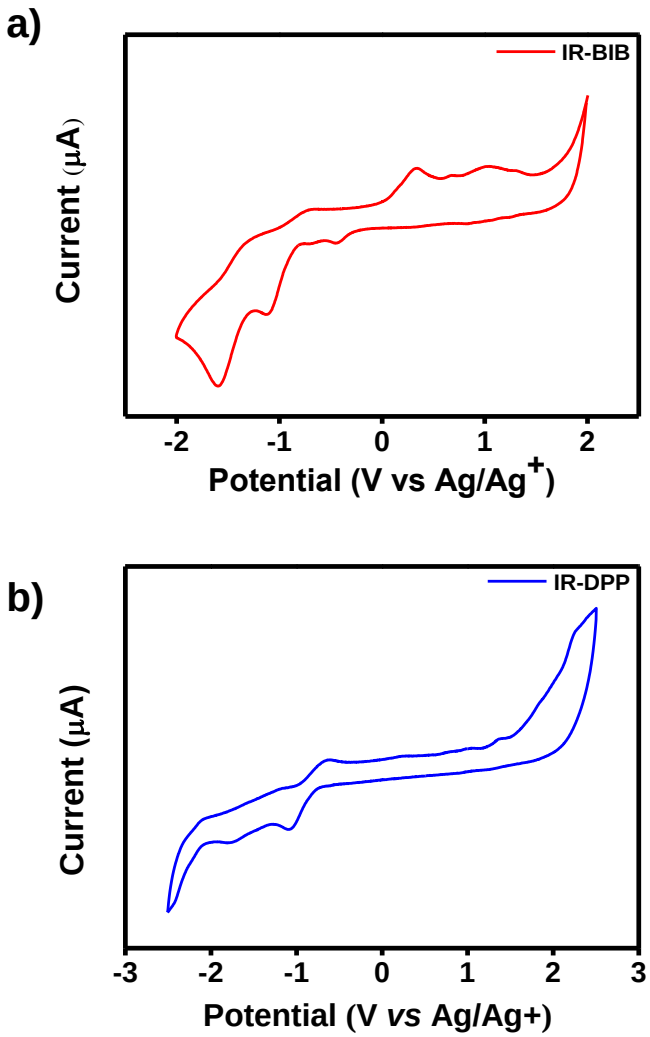

Figure 4.6. Cyclic voltammetry curve in acetonitrile using ferrocene as standard: (a) **IR-BIB** and (b) **IR-DPP**.

Table 4.1. Photophysical and electrochemical properties of Ir(III) complexes.

Compound	[a]λ_{em} (nm)	[b]PLQY	[c]HOMO	[d]LUMO	[e]ΔE(eV)	[f]τ (ns)	[g]$k_r(s^{-1})$	[h]$k_{nr}(s^{-1})$
IR-BIB	498, 532	0.75± .02	-5.34 eV	-2.92 eV	2.42	70	1.07×10^7	3.3×10^6
IR-DPP	516	0.27± .02	-5.34 eV	-3.44 eV	1.90	101	2.6×10^6	7.3×10^6

[a]Emission maxima; [b]PLQY refers to the photoluminescence quantum yield in toluene, with $Ir(ppy)_3$ (Φ_P:0.89) in dichloroethane as the reference; [c]HOMO determined by cyclic voltammograms in degassed acetonitrile; [d]LUMO determined by cyclic voltammograms in degassed acetonitrile; [e]Energy gap = E_{LUMO}-E_{HOMO}; [f]Lifetime (excitation wavelength 365 nm); [g]Radiative decay rate and [h]Non-radiative decay rate.

4.3.3. Electroluminescent (EL) Properties of IR-BIB

We selected the dinuclear iridium complex **IR-BIB** for further investigation of the electroluminescence properties due to its high PLQY and low emission lifetime. Two solution-processed OLED devices were fabricated: one using **IR-BIB** alone as the emitting layer and another with **IR-BIB** doped in PVK. **Device 1**, consisting of **IR-BIB** alone as the emitting layer, was fabricated with a multilayered architecture: Indium tin oxide (ITO)/ PEDOT: PSS (40 nm)/ **IR-BIB** (30 nm)/ TPBi (40 nm)/ LiF (1 nm)/ Al (100 nm). **Device 2**, consisting of **IR-BIB** doped in PVK as the emitting layer, was fabricated with the architecture: ITO/ PEDOT: PSS (40 nm)/ PVK: **IR-BIB** (2w%, 30 nm)/ TPBi (40 nm)/ LiF (1 nm)/ Al (100 nm).

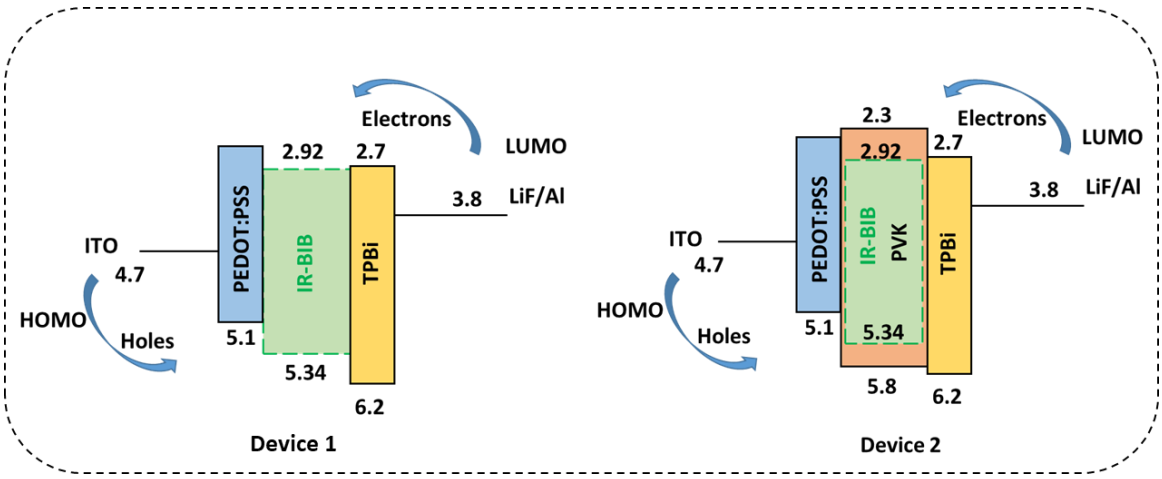

Figure 4.7. Schematic representation of the device architecture of **Device 1** and **Device 2**.

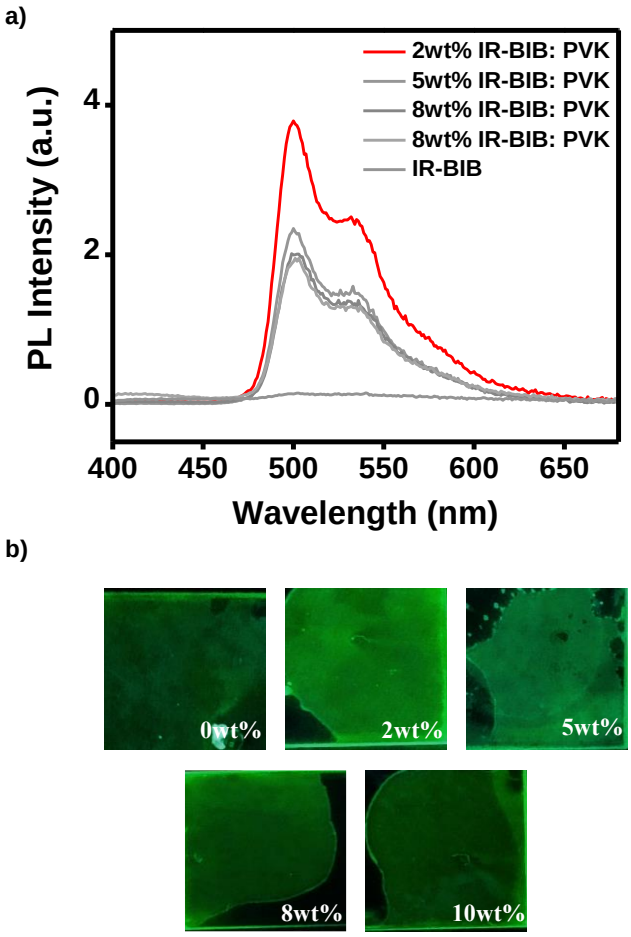

Figure 4.8. (a) Solid state photoluminescence of thin films of **IR-BIB** doped in PVK at various weight percentages and (b) Images of **IR-BIB** doped in PVK at various weight percentages under UV light illumination.

As shown in **Figure 4.7**, PEDOT:PSS [poly(3,4-ethylenedioxythiophene):polystyrene sulfonate] is the hole-transporting material (HTL), TPBi [1,3,5-tris(N-phenylbenzimidazole-2-yl)benzene] is the electron transporting material (ETL) and LiF [Lithium Fluoride] serve as electron injecting layer. PVK [poly(9-vinylcarbazole)] was utilized as a host material due to its suitable HOMO and LUMO energy levels. The **IR-BIB complex**, fully embedded within the PVK matrix, demonstrated effective energy transfer from the host material to the **IR-BIB** emitting layer (EML).[35] To optimize the dopant concentration, the emission profiles of thin films with **IR-BIB** doped in PVK were recorded. The doping ratios used for thin films were 2 wt%, 5 wt%, 8 wt%,

and 10 wt% (**Figure 4.8a,b**). The maximum emission intensity was achieved for 2 wt% of **IR-BIB**, which was selected for device fabrication. The electroluminescence (EL) spectra, current density (J)-voltage (V)-luminance (L) curves, and external quantum efficiency (EQE) characteristics of devices, **Device 1** and **Device 2**, are depicted in **Figure 4.9** - **Figure 4.12**, with key EL data summarized in **Table 4.2**.

Table 4.2. Electroluminescence parameters for Device 1 and Device 2.

	[a]EL_{max}	[b]L_{max}	[c]J_{max}	[d]CIE	[e]CE	[f]PE	[g]EQE
Device 1	504	150cd/m^2	400 A/cm^2	(0.26,0.55)	0.07cd/A	0.04lm/W	0.028%
Device 2	504	6300cd/m^2	155mA/cm^2	(0.22,0.61)	18.39cd/A	7.15lm/W	5.85%

[a]Electroluminescence spectra; [b]Luminescence maximum; [c]Current density maximum; [d]CIE 1931 chromaticity coordinates; [e]Current Efficiency; [f]Power Efficiency and [g]External Quantum Efficiency.

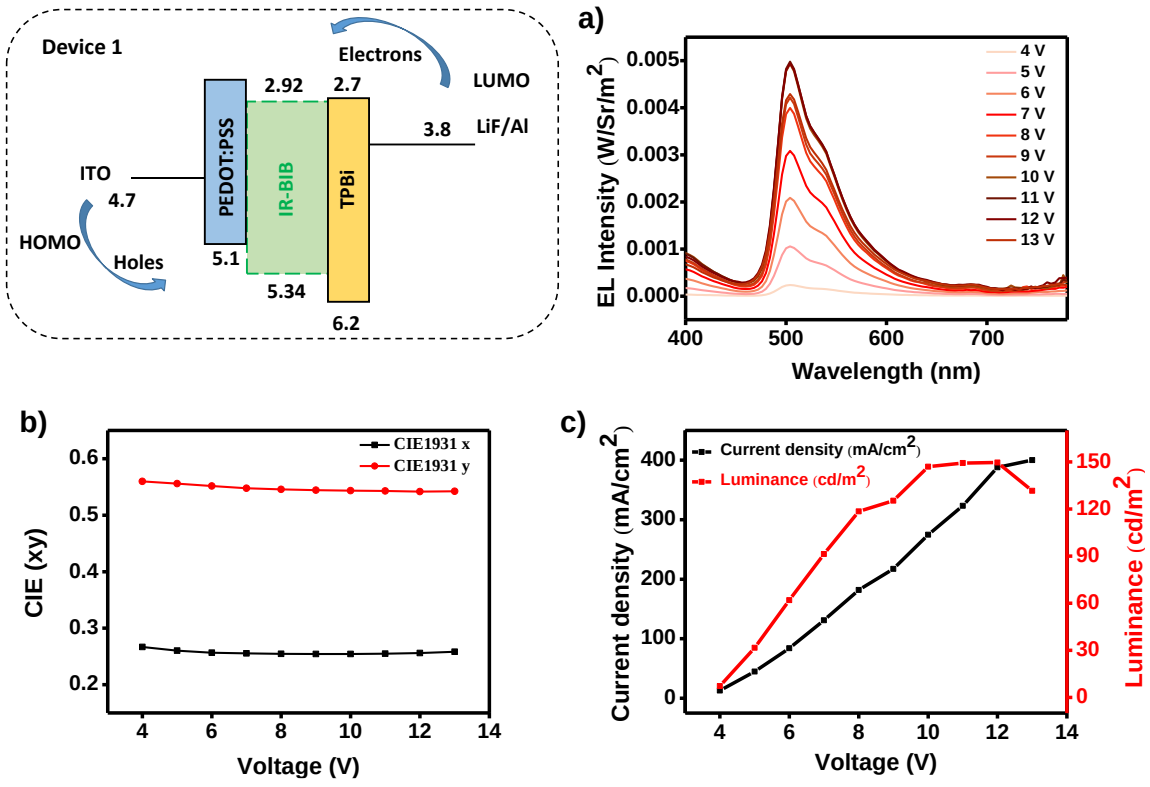

Figure 4.9. EL performance of **Device 1** (**IR-BIB** alone) OLED: (a) EL spectra at various operating voltages; (b) CIE 1931 chromaticity coordinates versus voltage plot and (c) Current density versus voltage and luminance versus voltage curves.

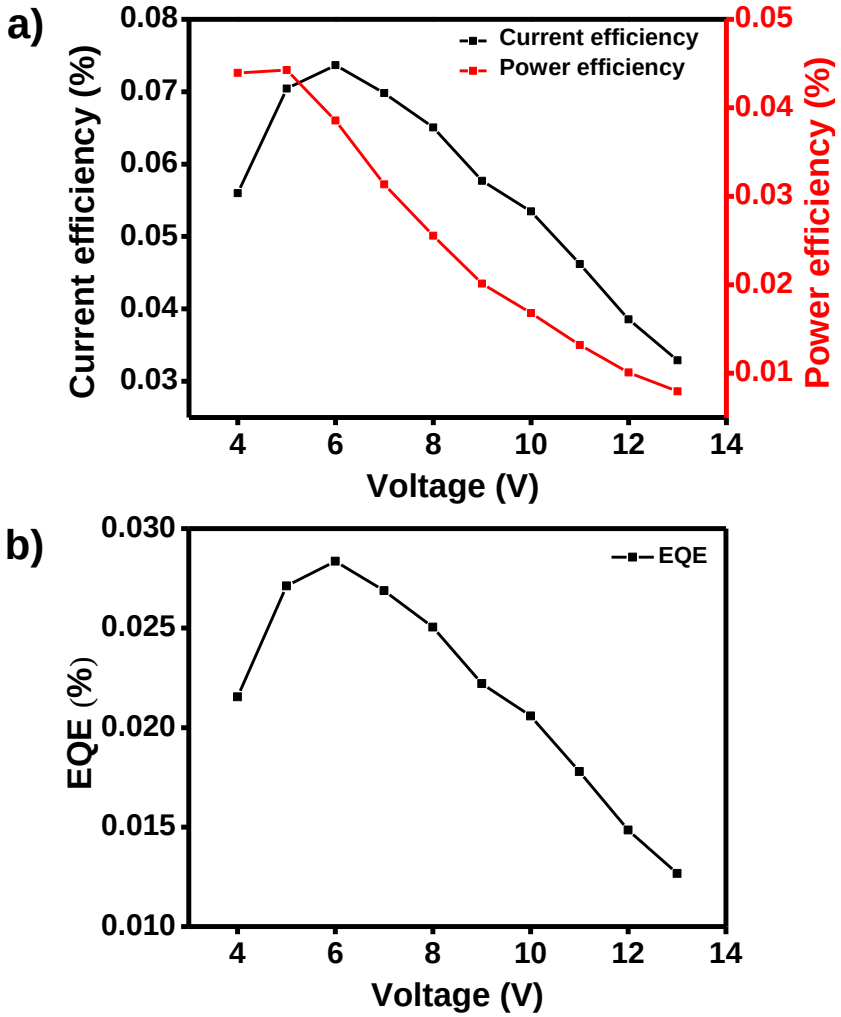

Figure 4.10. EL performance of **Device 1** (**IR-BIB** alone) OLED: (a) Current efficiency versus voltage and power efficiency versus voltage curves and (b) EQE- voltage plot.

The EL emission peaks at 504 nm for both **Device 1** and **Device 2** closely align with PL emission observed in toluene solution and doped films **(Figure 4.9a** and **Figure 4.11a)**, indicating that the EL and PL emission originates from the same (triplet) states of the emitters.[13] As shown in **Figure 4.9b,c** and **Figure 4.10a,b**, **Device 1** exhibited weak green emission with a peak maximum at 504 nm and CIE 1931 chromaticity coordinates of (0.26, 0.55). **Device 1** achieved a turn-on voltage of 4 V, a maximum current density of 400 mA/cm^2, and a maximum luminescence of 150 cd/m^2. Moreover, **Device 1** exhibited

a current efficiency of 0.07 cd/A, a power efficiency of 0.04 lm/W, and a maximum EQE of 0.028%.

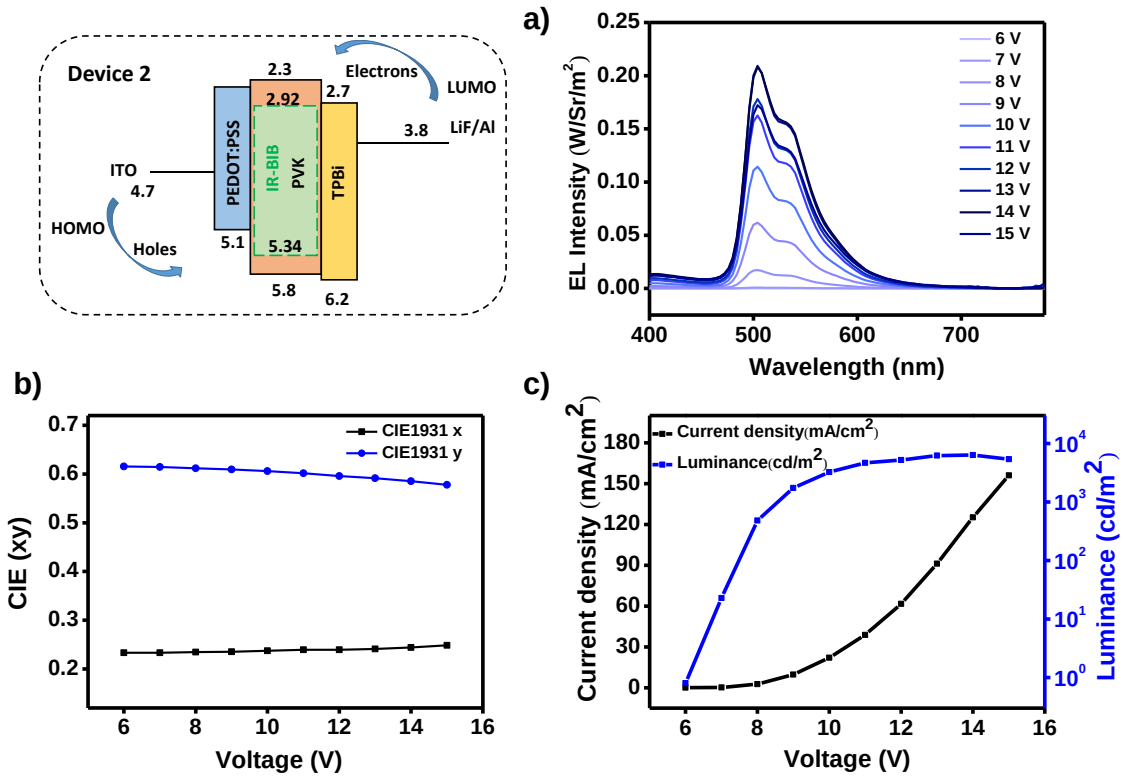

Figure 4.11. EL performance of **Device 2** (PVK:**IR-BIB**) OLED: (a) EL spectra at various operating voltages; (b) CIE 1931 chromaticity coordinates versus voltage and (c) Current density versus voltage and luminance versus voltage curves.

Device D2 employing PVK: **IR-BIB** as the emitter shows EL performances with a turn-on voltage of 6 V and bright green emission with CIE 1931 chromaticity coordinates of (0.22, 0.61) (**Figure 4.11b**). As shown in **Figure 4.11c** and **Figure 4.12a,b**, the **Device 2** achieved excellent characteristics with a maximum luminance (L_{max}) of 6300 cd/m^2, and peak current density (J_{max}) of 155 mA/cm^2. Moreover, **Device 2** exhibited a higher current efficiency of 18.39 cd/A, power efficiency of 7.15 lm/W, and maximum external quantum efficiency (EQE_{max}) of 5.85%, respectively.

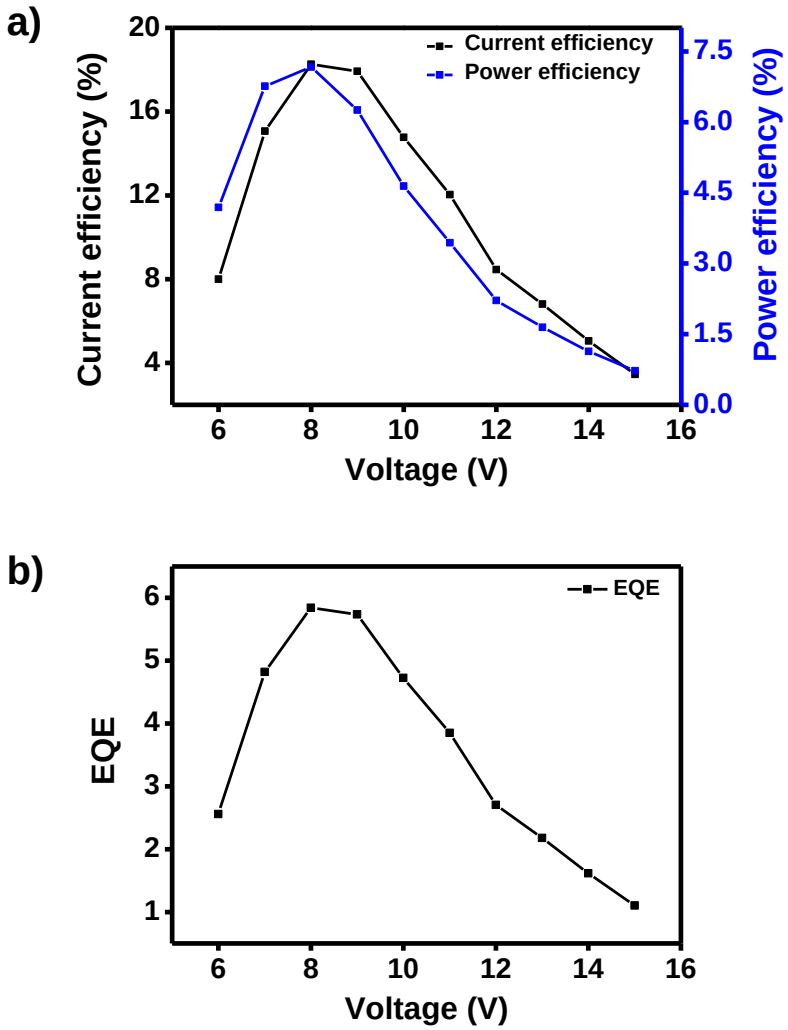

Figure 4.12. EL performance of **Device 2** (PVK:**IR-BIB**) OLED: (a) Current efficiency versus voltage and power efficiency versus voltage curve and (b) EQE-voltage plot.

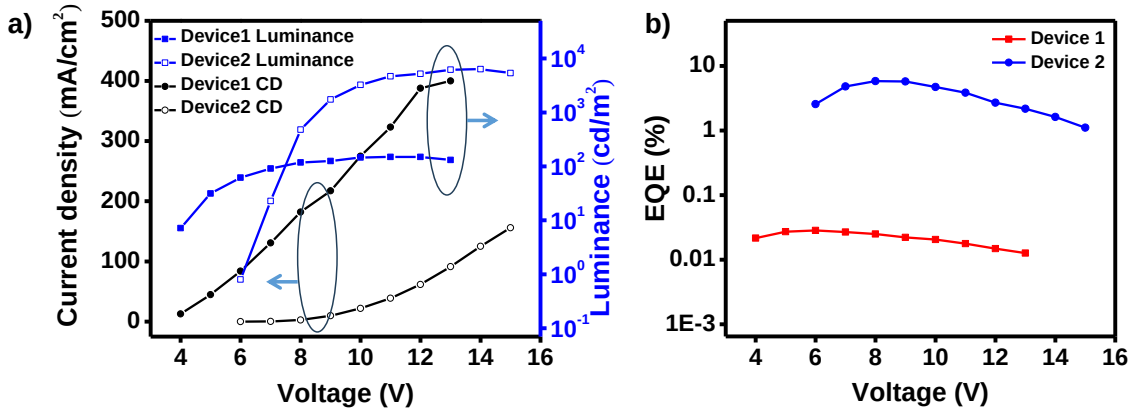

Figure 4.13. (a) Current density versus voltage and luminescence versus voltage plot **(Device 1** and **Device 2)** and (b) EQE-voltage characteristics of **Device 1** and **Device 2**.

As shown in **Figure 4.13a,b**, **Device 2** outperforms **Device 1** primarily due to enhanced and balanced charge injection and transport properties facilitated by the use of PVK as the host material.[13, 35] The findings underscore the promising potential of dinuclear iridium(III) complexes for developing highly efficient solution-processed OLEDs. This chapter discusses the synthesis of neutral dinuclear cyclometalated iridium(III) complexes, successfully optimizing their phosphorescent properties to obtain high photoluminescence quantum yields (PLQY) and short lifetime values. This advancement holds promise for the development of solution-processed OLEDs and opens avenues for designing and synthesizing a wide range of highly phosphorescent dinuclear iridium(III) complexes for various potential applications.

4.4. Conclusion

In summary, we report the synthesis, photophysical, and electrochemical properties of two iridium dinuclear complexes, **IR-BIB** and **IR-DPP**. These complexes feature 2-(4-tert-butylphenyl)pyridine as the cyclometalating ligands, with bibenzimidazole (**IR-BIB**) or diketopyrrolopyrrole (**IR-DPP**) as the bridging ligand. The **IR-BIB** and **IR-DPP** complexes exhibited photoluminescence quantum yields of 0.75 and 0.27, and excited state lifetimes of 70 ns and 101 ns, respectively. To evaluate the electroluminescent (EL) properties of the dinuclear iridium system, **IR-BIB** was chosen as the emitter for OLED device fabrication due to its higher PLQY and shorter emission lifetime. Further, two solution-processed OLED devices were fabricated: one with **IR-BIB** as the sole emitting layer and another with **IR-BIB** doped in PVK. The optimized devices with **IR-BIB** alone and **IR-BIB** doped in PVK achieved maximum luminescence of 150 cd/m² and 6,300 cd/m², respectively. The OLED device incorporating **IR-BIB** doped in PVK exhibited a higher EQE of 5.85%, compared to the 0.028% EQE of the **IR-BIB** alone device. This

work underscores the potential of dinuclear iridium complexes as effective emitting layers in OLEDs, demonstrating their promise for optoelectronic applications.

4.5. Experimental Section

4.5.1. Materials and General Instruments

The chemicals utilized in this study, including 2-bromopyridine, 4-tert-butylphenylboronic, K_2CO_3, $PdCl_2(PPh_3)_2$, $IrCl_3 \cdot xH_2O$, NH_4PF_6, 2-ethoxyethanol, succinic acid, H_2SO_4, isopropanol, sodium bicarbonate, magnesium sulphate, sodium, $FeCl_3$, tert-amyl alcohol, 2-cyanopyridine, 2-methyl-2-butanol, CaH_2 (calcium hydride) were obtained from Alfa Aesar, Sigma-Aldrich and TCI Chemicals and used without further purification. Reactions sensitive to moisture and oxygen were carried out under an argon atmosphere using dried solvents obtained from Sigma-Aldrich and Merck. Thin layer chromatography (TLC) was performed using aluminum plates coated with silica gel from Merck. Silica gels (100−200 and 230−400 mesh) were employed for column chromatography. ^{1}H NMR (500 MHz) and ^{13}C NMR (125 MHz) analyses were conducted on a Bruker Avance DPX spectrometer, with TMS as the internal standard. Chloroform-d was used as a solvent for NMR analysis. High-resolution mass spectra (HRMS) were acquired using a Thermo Scientific Q Exactive Hybrid Quadrupole-Orbitrap Electrospray Ionization Mass Spectrometer (ESI-MS).

4.5.2. Photophysical and Electrochemical Measurements

UV/Vis absorption spectra were recorded with a Shimadzu UV-2600 spectrophotometer, while emission spectra were obtained using a SPEX Fluorolog spectrofluorimeter. Cyclic voltammetry was performed with a PARSTAT 4000A potentiostat in an argon atmosphere, using dry, oxygen-free acetonitrile with 0.1 M tetrabutylammonium hexafluorophosphate (TBAH) as the supporting electrolyte. The

measurements were conducted with a standard three-electrode configuration, which included an Ag/AgCl reference electrode and a platinum wire counter electrode, with redox potentials referenced to the ferrocene/ferrocenium couple. Photoluminescence quantum yields for **IR-BIB** and **IR-DPP** were determined by relative comparison to $Ir(ppy)_3$ (Φ_p = 0.89 in dichloroethane) as the standard.[30] Fluorescence lifetime measurements were carried out using a Horiba DeltaFlex picosecond single-photon counting system, equipped with a picosecond photon detection module (PPD-850). The fluorescence decay profiles were analyzed with EzTime software and fitted using a multi-exponential decay model, yielding a chi-square value of 1 ± 0.2.

4.5.3. OLED Fabrication and Measurements

Patterned ITO-coated substrates (sheet resistance 10Ω per square) were brushed with soap solution and cleaned in an ultrasonic bath with 2-propanol and deionized water. The device structure in this study was ITO (150 nm) / PEDOT: PSS (40 nm) / Emissive layer (30 nm) / TPBi (35 nm) / LiF (1 nm) /Al (100 nm). Devices were fabricated by sequential spin coating of PEDOT: PSS and the emissive layer (**IR-BIB** and PVK at 2wt% **IR-BIB**) under a nitrogen atmosphere and all other layers were thermally evaporated in an evaporation chamber under high vacuum conditions (~10^{-8} Torr). Emissive layer solutions were prepared in chlorobenzene and coated at 3000 rpm rate for one minute. Aluminum, used as a cathode, was thermally evaporated without breaking the vacuum. Devices were encapsulated with a cover glass using epoxy resin in a nitrogen atmosphere before measurements were done in ambient conditions, with the measured device area 25 mm^2. Electroluminescence spectra and other device parameters of the devices were measured using a spectroradiometer (Photoresearch PR-655) attached to an integrating sphere and a Keithley 2400 Source Meter.

4.5.4. Synthesis and Characterization of Molecules

4.5.4a. Synthesis of 2-(4-tert-butylphenyl)pyridine **(tbppy)**

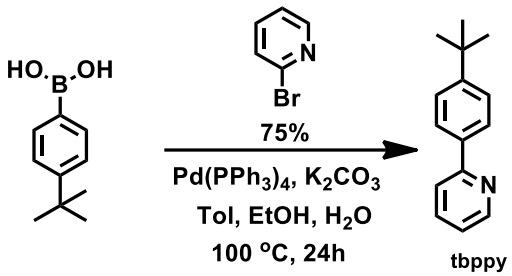

Scheme 4.1

A solution of 2-bromopyridine (295 mg, 1.8 mmol), 4-tert-butylphenylboronic acid (400 mg, 2.2 mmol), and potassium carbonate (K_2CO_3) (1.29 g, 9.3 mmol) was prepared in a mixture of toluene (4.4 mL), ethanol (1.6 mL), and water (0.8 mL). The resulting reaction mixture was degassed for 20 minutes. Under an argon atmosphere, $PdCl_2(PPh_3)_2$ (0.1 mmol) was introduced, and the mixture was stirred continuously while refluxing for 24 hours. Upon cooling to room temperature, the mixture was extracted with dichloromethane (DCM) and water. The crude product was purified via silica gel column chromatography using a DCM/n-hexane eluent, yielding a colorless liquid product with a 75% yield. ^{1}H NMR (500 MHz, $CDCl_3$): δ 8.70 (d, 1H), δ 7.97 (m, 2H), δ 7.74 (m, 2H), δ 7.51 (d, 2H), δ 7.21 (m, 1H), δ 1.39 (s, 9H).

4.5.4b. Synthesis of **$[(tbppy)_2IrCl]_2$**

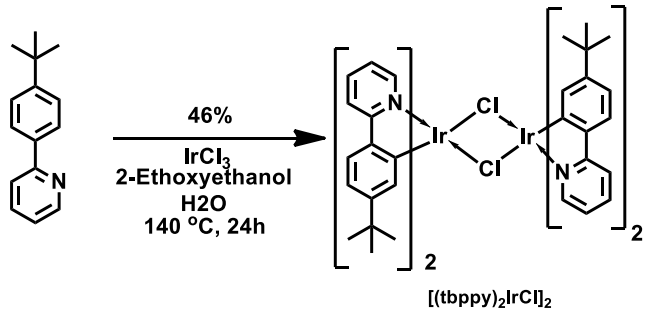

Scheme 4.2

A mixture of $IrCl_3.nH_2O$ (100 mg, 0.33 mmol) and tbppy (141 mg, 0.66 mmol) in 2-ethoxyethanol (6 mL) and water (2 mL) were refluxed for 24 hours. After cooling, distilled water was added, resulting in the formation of a yellow precipitate. The precipitate was collected by filtration, then washed with hexane and diethyl ether. The crude yellow product, obtained in a 46% yield, was used in the subsequent reaction without further purification. HRMS: Calculated for $C_{60}H_{64}Cl_2Ir_2N_4$ with m/z 1296.38, where z =1, found: 613.22.

4.5.4c. Synthesis of **di-isopropyl succinate**

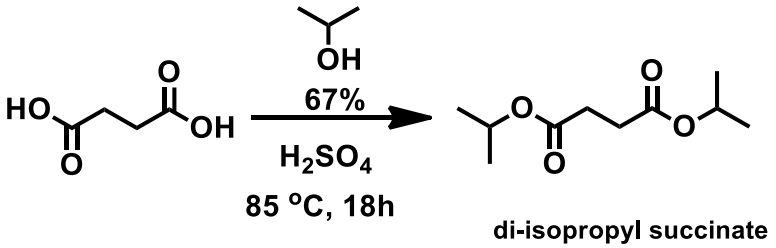

Scheme 4.3

A mixture of succinic acid (3 g, 25.4 mmol) and a catalytic amount of H_2SO_4 (~500 μL) in isopropanol (39.6 mL) was refluxed at 85 °C for 18 hours. After cooling, the reaction mixture was quenched and neutralized with a saturated sodium bicarbonate solution. The organic phase was extracted with diethyl ether, and the combined extracts were washed successively with saturated sodium bicarbonate solution, water, and brine. The solution was then dried over anhydrous magnesium sulfate, filtered, and the solvent removed under reduced pressure to afford the product as a clear oil in 67% yield. ^{1}H NMR (500 MHz, $CDCl_3$): δ 5.04 (m, 2H), δ 2.60 (s, 4H), δ 1.25 (d, 12H).

4.5.4d. Synthesis of diketopyrrolopyrrole, **DPP**

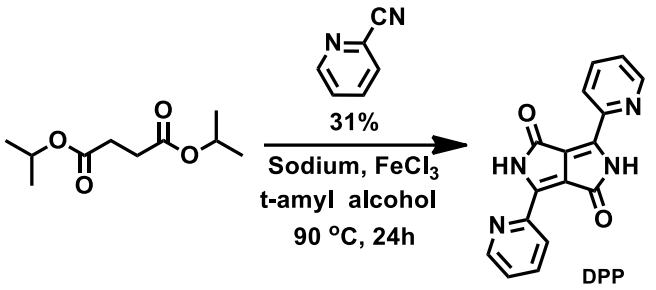

Scheme 4.4

Sodium (200 mg, 8.6 mmol) and $FeCl_3$ (13 mg, 0.08 mmol) were dissolved in dry 2-methyl-2-butanol (6 mL) by heating at 90 °C under an argon atmosphere. Once the sodium had fully dissolved, the solution was cooled to approximately 50 °C, and 2-cyanopyridine (625 mg, 6 mmol) was added. A solution of diisopropyl succinate (553 mg, 2.7 mmol) in dry 2-methyl-2-butanol (2.5 mL) was then added dropwise over 1 hour at 90 °C. The 2-methyl-2-butanol was pre-dried by stirring over CaH_2 overnight and fractionally distilled before use. After stirring the reaction mixture for 24 hours, acetic acid (2.5 mL) was added, and the mixture was heated to 120 °C for 1 hour. The resulting precipitate was filtered and washed thoroughly with water, methanol, and dichloromethane under vacuum, yielding a red solid in 31% yield.

4.5.4e. Synthesis of **IR-DPP**

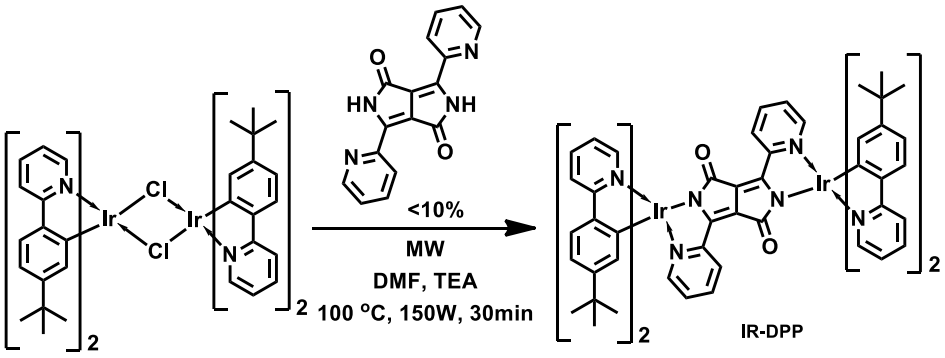

Scheme 4.5

A microwave tube was charged with $[(tbppy)_2IrCl]_2$ (28 mg, 0.021 mmol) and DPP (5.6 mg, 0.019 mmol). To this dry DMF (2 mL) and TEA (1 mL) were added. The mixture was degassed for 15 minutes and heated in a microwave at 100 °C for 30 minutes (150 W, 3 bar pressure). Further, the solution was extracted with dichloromethane (DCM) and water, yielding a blue powder. Purification was achieved through multiple-column chromatographies using ethyl acetate and hexane, followed by a mixture of DCM, methanol, and hexane. The pure product was obtained in dark green color with a yield of less than 10%. ^{1}H NMR (500 MHz, $CDCl_3$): δ 9.18 (d, 2H), δ 8.78 (m, 2H), δ 7.81 (m, 4H), δ 7.69 (m, 4H), δ 7.58 (m, 4H), δ 7.50 (m, 4H), δ 6.94 (m, 12H), δ 6.37 (d, 2H), δ 6.26 (d, 2H), δ 1.07 (d, 36H). ^{13}C NMR (125 MHz, $CDCl_3$): δ 168.65, 157.05, 153.84, 151.33, 148.16, 140.55, 137.21, 136.30, 135.80, 128.29, 126.36, 124.72, 123.60, 123.24, 121.89, 120.93, 118.31, 117.28, 34.31, 21.81. Mass Spectrum: Calculated for $C_{76}H_{72}Ir_2N_8O_2$ with m/z 1514.50, where z =1, found: 1514.50.

4.5.4f. Synthesis of **IR-BIB**

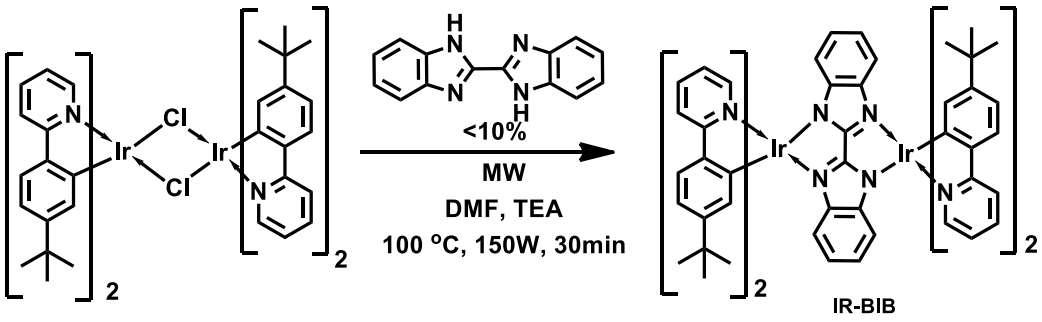

Scheme 4.6

A mixture of $[(tbppy)_2IrCl]_2$ (28 mg, 0.021 mmol) and bibenzimidazole (4.6 mg, 0.019 mmol) in 2 mL of dry DMF and 1 mL of TEA was degassed under argon for 15 minutes. The reaction mixture was then treated in a microwave reactor for 30 minutes at 100 °C, with a power setting of 150 W and a pressure of 3 bar. Further, the product was extracted

with water and DCM. The DCM layer was dried over magnesium sulfate, and the solvent was removed under reduced pressure. Purification was achieved by column chromatography using DCM, methanol, and hexane, as well as chromatotron, yielding less than 10%. ^{1}H NMR (500 MHz, $CDCl_3$): δ 7.86 (d, 4H), δ 7.72 (d, 4H), δ 7.63 (m,8H), δ 7.04 (m, 4H), δ 6.71 (d, 4H), δ 6.67 (m, 4H), δ 6.62 (m, 4H), δ 6.01 (m, 4H), δ 1.12 (s, 36H). ^{13}C NMR (125 MHz, $CDCl_3$): δ 169.17, 159.79, 151.65, 150.21, 149.78, 148.95, 144.28, 142.77, 135.84, 129.65, 123.38, 121.04, 120.88, 120.01, 118.33, 118.05, 117.85, 115.99, 34.46, 31.21. Mass Spectrum: Calculated for $C_{74}H_{72}Ir_2N_8$ with m/z 1458.51, where z =1, found: 1458.51.

4.5.5. NMR and Mass Spectrum

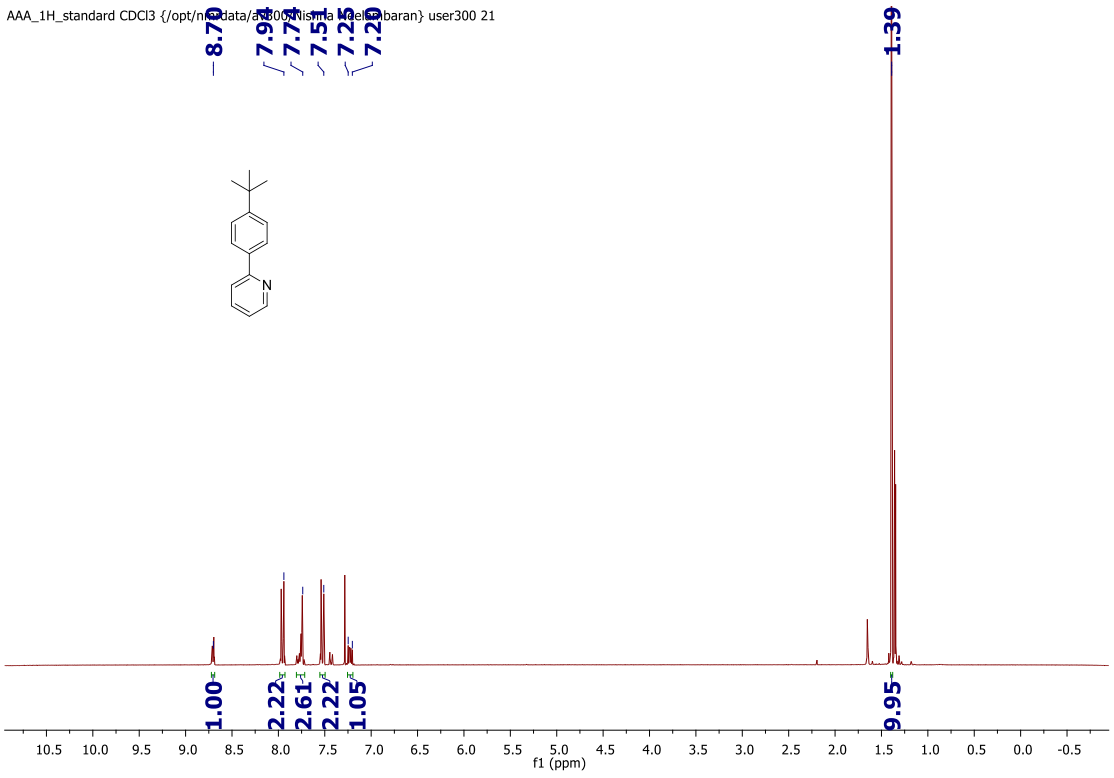

Figure 4.14. ^{1}H NMR of tbppy in $CDCl_3$

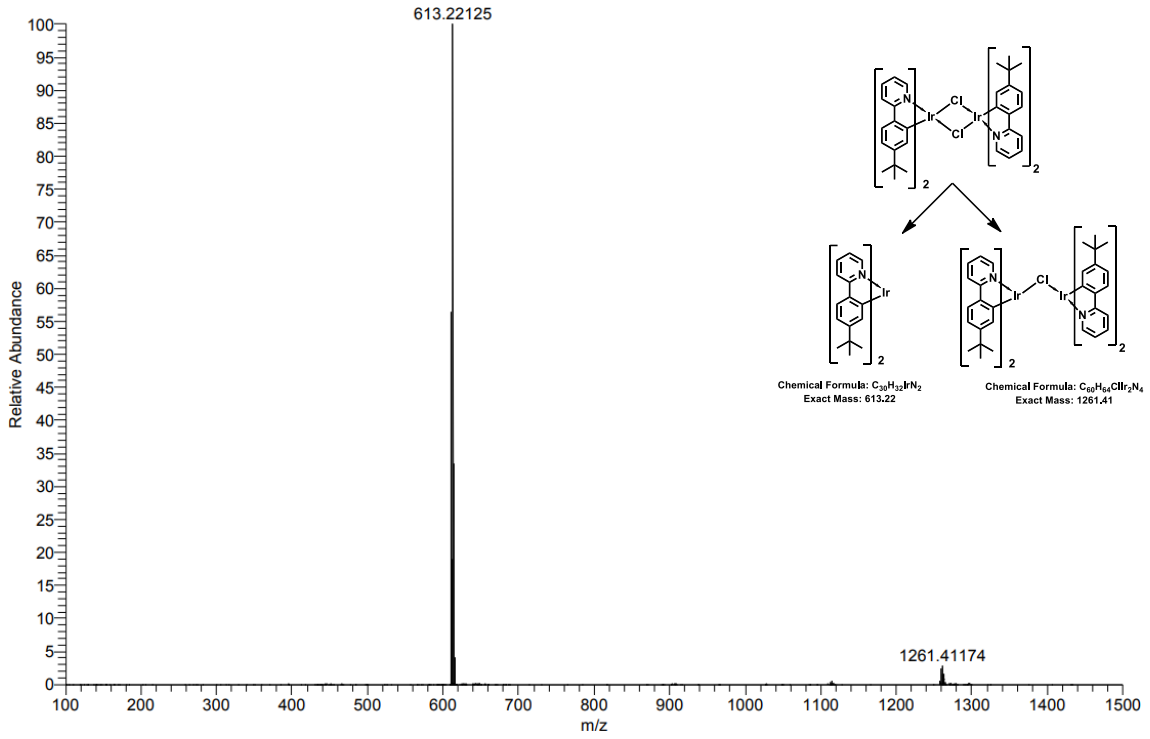

Figure 4.15. HRMS of $[(tbppy)_2IrCl]_2$

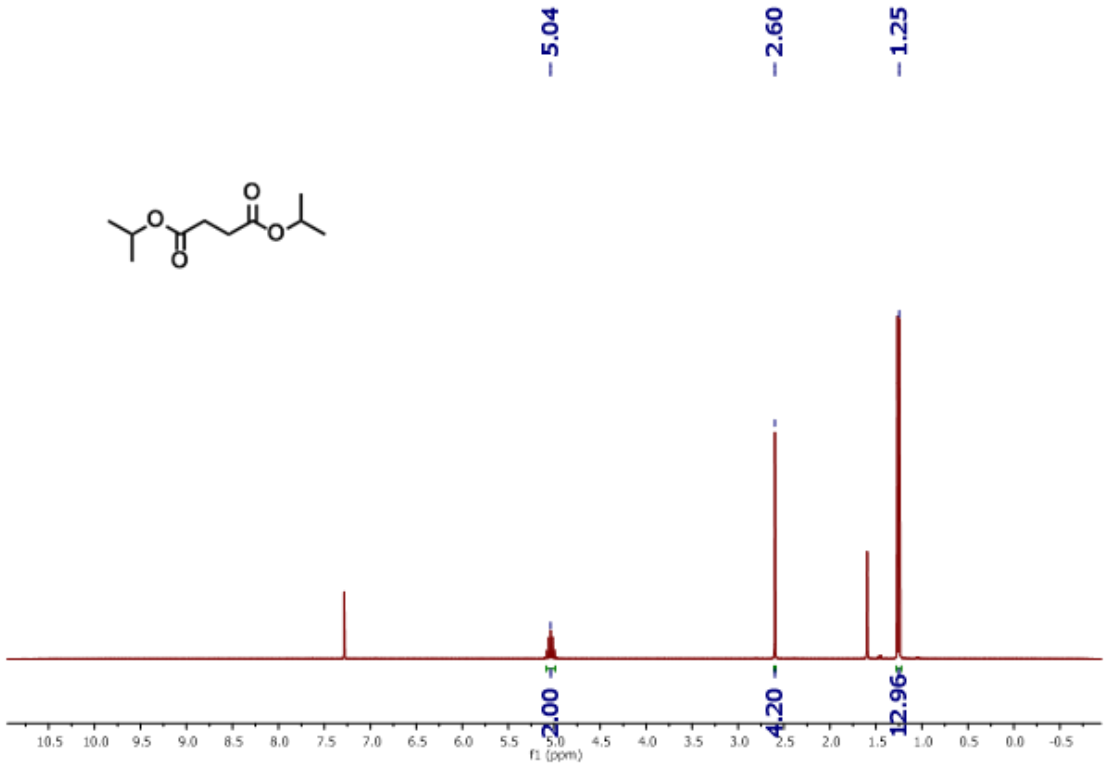

Figure 4.16.^{1}H NMR of di-isopropyl succinate in $CDCl_3$

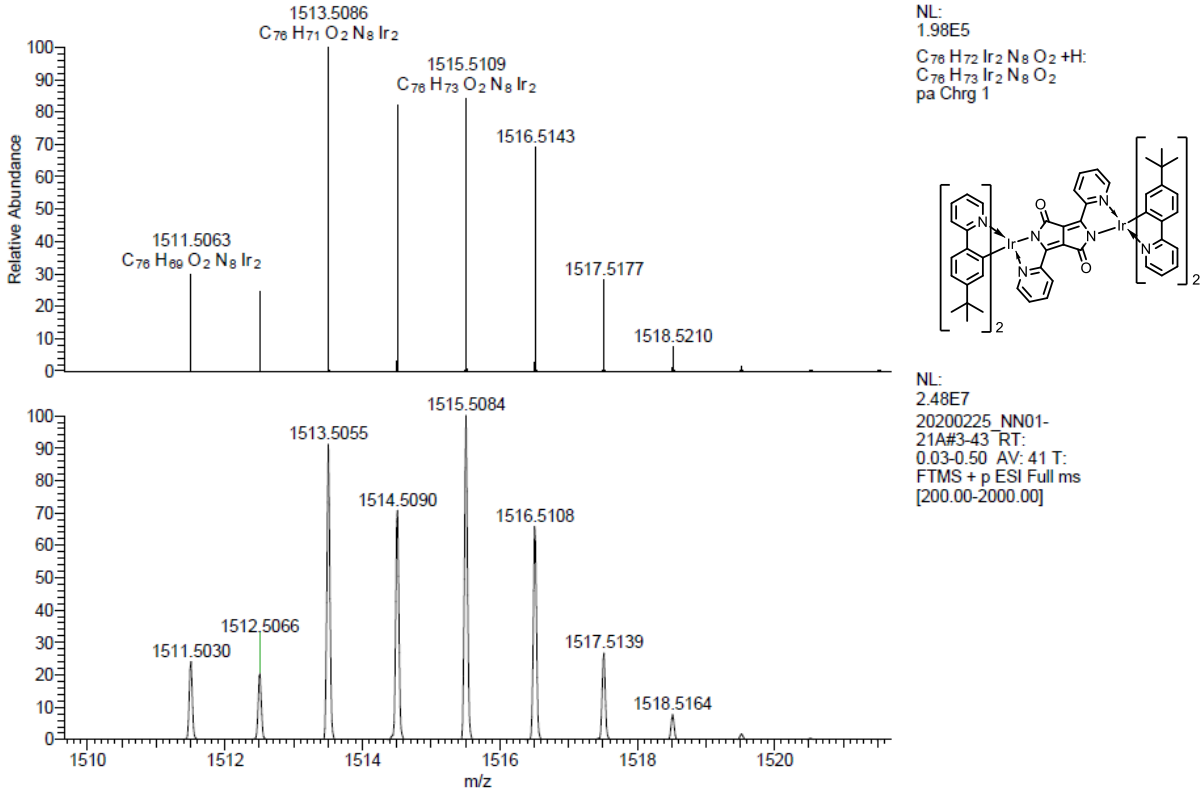

Figure 4.17. Mass spectrum of **IR-DPP**

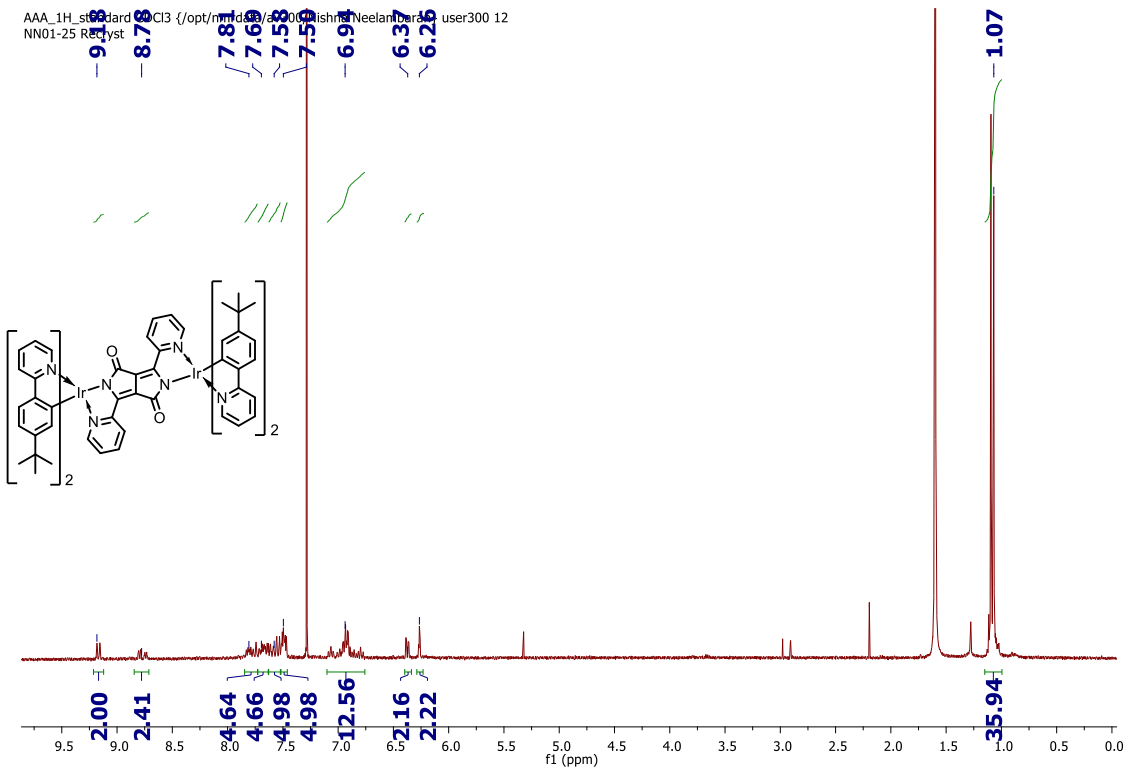

Figure 4.18.^{1}H NMR of **IR-DPP** in $CDCl_3$

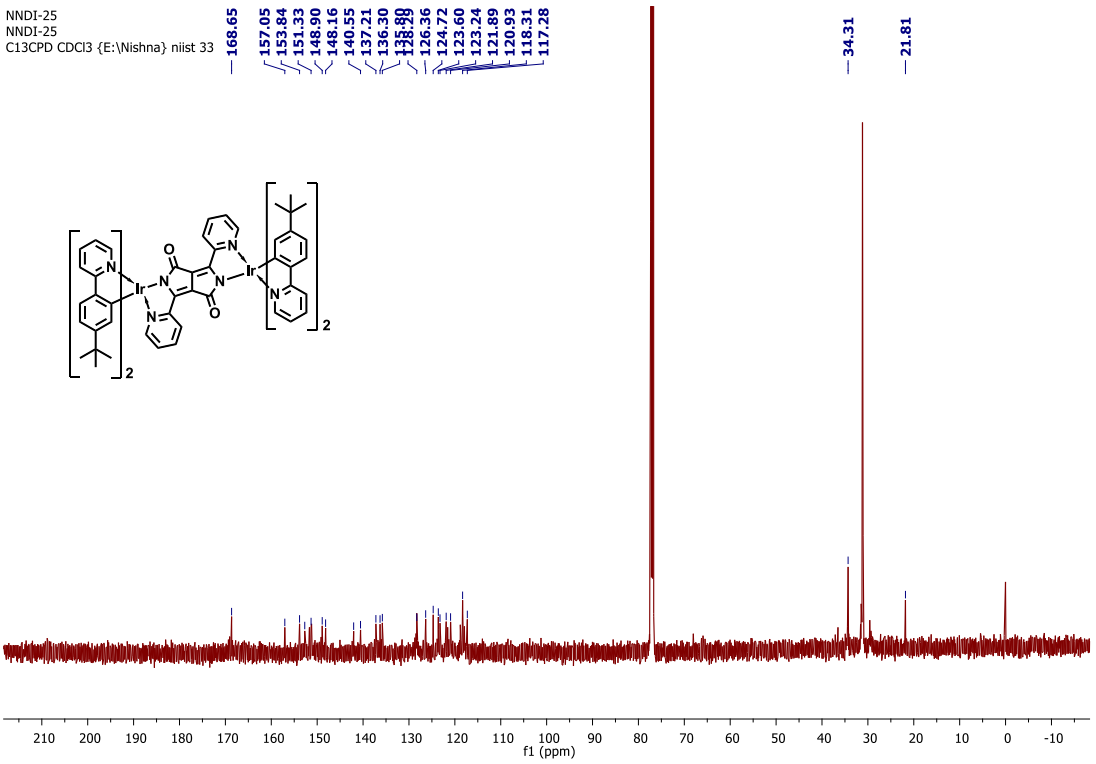

Figure 4.19.^{13}C NMR of **IR-DPP** in $CDCl_3$

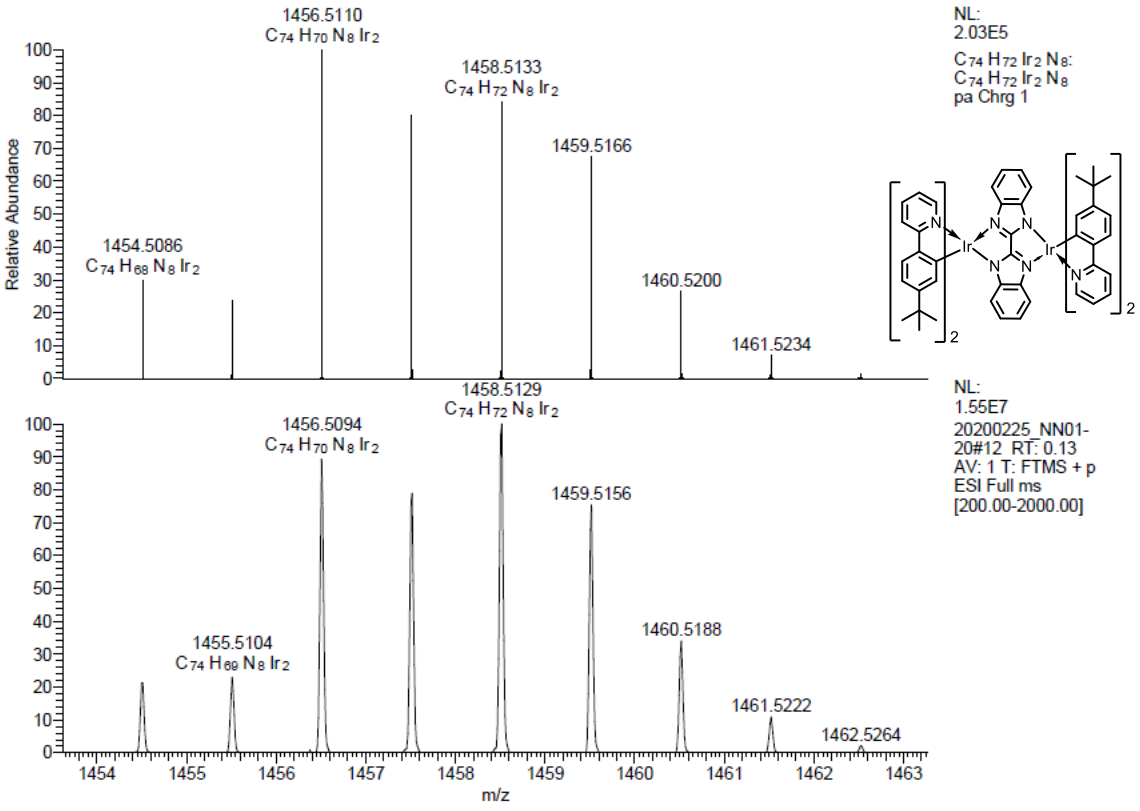

Figure 4.20. Mass spectrum of **IR-BIB**

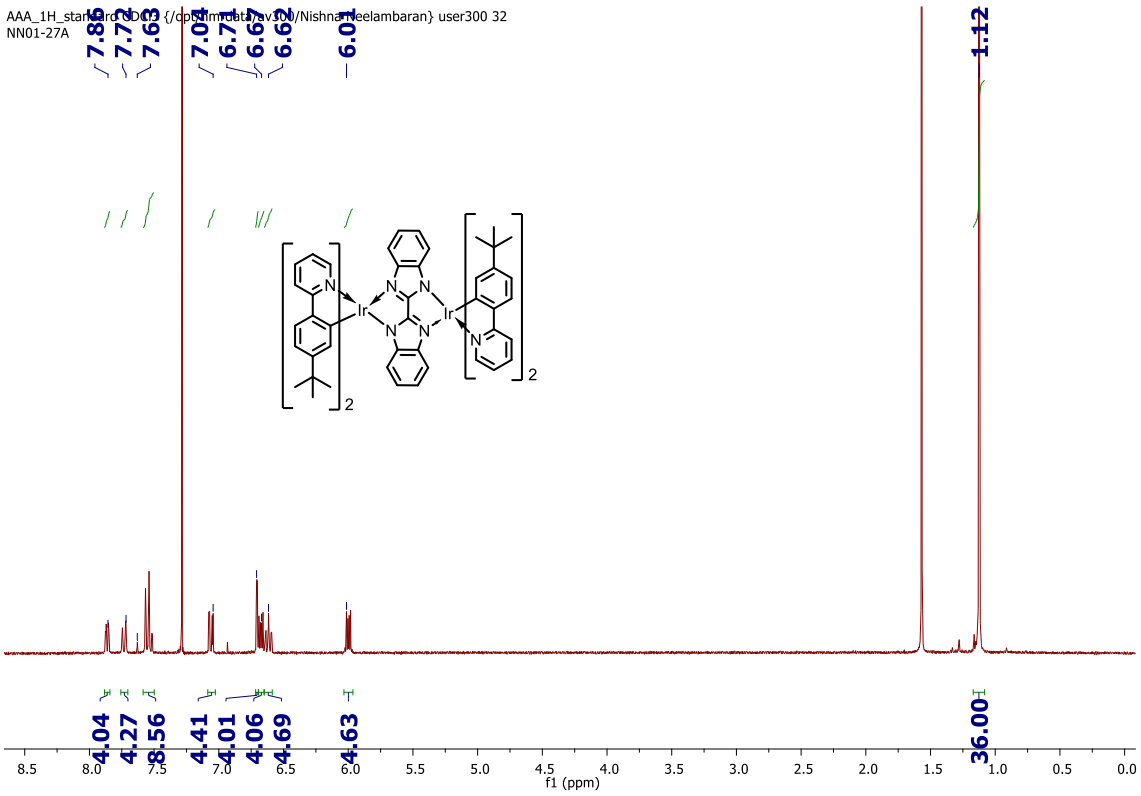

Figure 4.21.^{1}H NMR of **IR-BIB** in $CDCl_3$

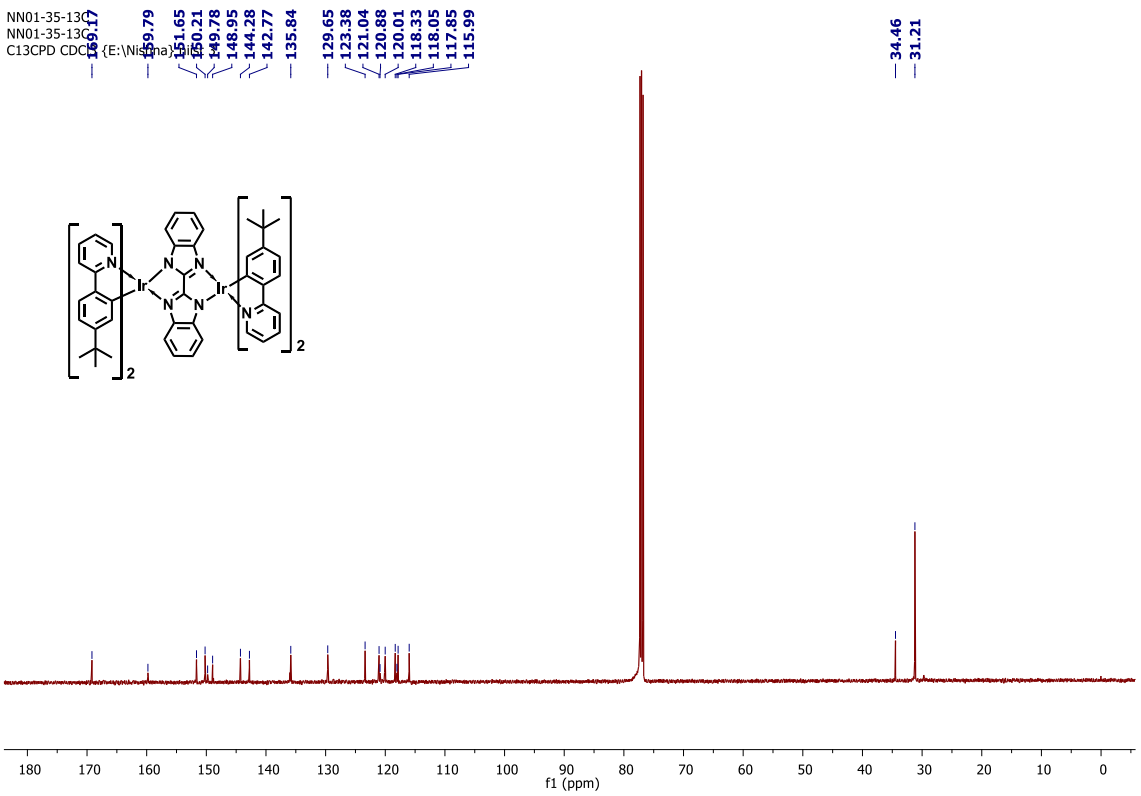

Figure 4.22.^{13}C NMR of **IR-BIB** in $CDCl_3$

4.6. References

1.Murawski, C.; Leo, K.; Gather, M. C., Efficiency Roll-Off in Organic Light-Emitting Diodes. **2013,** *25* (47), 6801-6827.

2.Ibrahim-Ouali, M.; Dumur, F., Recent Advances on Metal-Based Near-Infrared and Infrared Emitting OLEDs. **2019,** *24* (7), 1412.

3.Tang, C. W.; VanSlyke, S. A., Organic electroluminescent diodes. *Applied Physics Letters* **1987,** *51* (12), 913-915.

4.Baldo, M. A.; O'Brien, D. F.; You, Y.; Shoustikov, A.; Sibley, S.; Thompson, M. E.; Forrest, S. R., Highly efficient phosphorescent emission from organic electroluminescent devices. *Nature* **1998,** *395* (6698), 151-154.

5.Fleetham, T.; Li, G.; Li, J., Phosphorescent Pt(II) and Pd(II) Complexes for Efficient, High-Color-Quality, and Stable OLEDs. **2017,** *29* (5), 1601861.

6.Mao, H.-T.; Li, G.-F.; Shan, G.-G.; Wang, X.-L.; Su, Z.-M., Recent progress in phosphorescent Ir(III) complexes for nondoped organic light-emitting diodes. *Coordination Chemistry Reviews* **2020,** *413*, 213283.

7.Li, G.; Congrave, D. G.; Zhu, D.; Su, Z.; Bryce, M. R., Recent advances in luminescent dinuclear iridium(III) complexes and their application in organic electroluminescent devices. *Polyhedron* **2018,** *140*, 146-157.

8.Li, G.; Zhu, D.; Wang, X.; Su, Z.; Bryce, M. R., Dinuclear metal complexes: multifunctional properties and applications. *Chemical Society Reviews* **2020,** *49* (3), 765-838.

9.dos Santos, P. L.; Ward, J. S.; Bryce, M. R.; Monkman, A. P., Using Guest–Host Interactions To Optimize the Efficiency of TADF OLEDs. *The Journal of Physical Chemistry Letters* **2016,** *7* (17), 3341-3346.

10.Chen, X.-K.; Kim, D.; Brédas, J.-L., Thermally Activated Delayed Fluorescence (TADF) Path toward Efficient Electroluminescence in Purely Organic Materials: Molecular Level Insight. *Accounts of Chemical Research* **2018,** *51* (9), 2215-2224.

11.Teng, J.-M.; Wang, Y.-F.; Chen, C.-F., Recent progress of narrowband TADF emitters and their applications in OLEDs. *Journal of Materials Chemistry C* **2020,** *8* (33), 11340-11353.

12.Bin Mohd Yusoff, A. R.; Huckaba, A. J.; Nazeeruddin, M. K., Phosphorescent Neutral Iridium (III) Complexes for Organic Light-Emitting Diodes. *Topics in Current Chemistry* **2017,** *375* (2), 39.

13.Lu, G.; Yao, J.; Chen, Z.; Ma, D.; Yang, C., Saturated red iridium(iii) complexes containing a unique four-membered Ir–S–C–N backbone: mild synthesis and application in OLEDs. *Journal of Materials Chemistry C* **2020,** *8* (4), 1391-1397.

14.Altinolcek, N.; Battal, A.; Tavasli, M.; Cameron, J.; Peveler, W. J.; Yu, H. A.; Skabara, P. J.; Fairbairn, N. J.; Hedley, G. J., A red-orange carbazole-based iridium(III) complex: Synthesis, thermal, optical and electrochemical properties and OLED application. *Journal of Organometallic Chemistry* **2021,** *951*, 122004.

15.Zanoni, K. P. S.; Kariyazaki, B. K.; Ito, A.; Brennaman, M. K.; Meyer, T. J.; Murakami Iha, N. Y., Blue-Green Iridium(III) Emitter and Comprehensive Photophysical Elucidation of Heteroleptic Cyclometalated Iridium(III) Complexes. *Inorganic Chemistry* **2014,** *53* (8), 4089-4099.

16.Zhang, Y.; Li, Q.; Cai, M.; Xue, J.; Qiao, J., An 850 nm pure near-infrared emitting iridium complex for solution-processed organic light-emitting diodes. *Journal of Materials Chemistry C* **2020,** *8* (25), 8484-8492.

17.Liu, J.; Li, M.; Lu, Z.; Huang, Y.; Pu, X.; Zhou, L., Color tuning of iridium(III) complexes containing 2-phenylbenzothiazole-based cyclometalated ligands for application in highly efficient organic light-emitting diodes. *Dyes and Pigments* **2020,** *175*, 108145.

18.Shafikov, M. Z.; Zaytsev, A. V.; Kozhevnikov, V. N., Halide-Enhanced Spin-Orbit Coupling and the Phosphorescence Rate in Ir(III) Complexes. *Inorg Chem* **2021,** *60* (2), 642-650.

19.Gao, T.-B.; Zhang, J.-J.; Wen, J.; Yang, X.-X.; Ma, H.-b.; Cao, D.-K.; Jiang, D., Single-Molecule MicroRNA Electrochemiluminescence Detection Using Cyclometalated Dinuclear Ir(III) Complex with Synergistic Effect. *Analytical Chemistry* **2020,** *92* (1), 1268-1275.

20.Congrave, D. G.; Hsu, Y.-t.; Batsanov, A. S.; Beeby, A.; Bryce, M. R., Synthesis, Diastereomer Separation, and Optoelectronic and Structural Properties of Dinuclear Cyclometalated Iridium(III) Complexes with Bridging Diarylhydrazide Ligands. *Organometallics* **2017,** *36* (5), 981-993.

21.Lu, C.; Xu, W.; Shah, H.; Liu, B.; Xu, W.; Sun, L.; Qian, S. Y.; Sun, W., In Vitro Photodynamic Therapy of Mononuclear and Dinuclear Iridium(III) Bis(terpyridine) Complexes. *ACS Appl Bio Mater* **2020,** *3* (10), 6865-6875.

22.Yang, X.; Feng, Z.; Zhao, J.; Dang, J.-S.; Liu, B.; Zhang, K.; Zhou, G., Pyrimidine-Based Mononuclear and Dinuclear Iridium(III) Complexes for High Performance Organic Light-Emitting Diodes. *ACS Applied Materials & Interfaces* **2016,** *8* (49), 33874-33887.

23.Xue, F.; Shi, M.; Yan, Y.; Yang, H.; Zhou, Z.; Yang, S., Iridium complex loaded polypyrrole nanoparticles for NIR laser induced photothermal effect and generation of singlet oxygen. *RSC Advances* **2016,** *6* (19), 15509-15512.

24.Nonoyama, M., Benzo[h]quinolin-10-yl-N Iridium(III) Complexes. *Bulletin of the Chemical Society of Japan* **2006,** *47* (3), 767-768.

25.Chen, Y.; Liu, C.; Wang, L., Effects of fluorine substituent on properties of cyclometalated iridium(III) complexes with a 2,2′-bipyridine ancillary ligand. *Tetrahedron* **2019,** *75* (47), 130686.

26.Neelambaran, N.; Shamjith, S.; Murali, V. P.; Maiti, K. K.; Joseph, J., Exploring a Mitochondria Targeting, Dinuclear Cyclometalated Iridium (III) Complex for Image-Guided

Photodynamic Therapy in Triple-Negative Breast Cancer Cells. *ACS Applied Bio Materials* **2023,** *6* (12), 5776-5788.

27.Kanti Seth, S.; Gupta, P.; Purkayastha, P., Efficiency of photoinduced electron transfer in mono- and di-nuclear iridium complexes: a comparative study. *New Journal of Chemistry* **2017,** *41* (14), 6540-6545.

28.Wu, S.-H.; Ling, J.-W.; Lai, S.-H.; Huang, M.-J.; Cheng, C. H.; Chen, I. C., Dynamics of the Excited States of [Ir(ppy)2bpy]+ with Triple Phosphorescence. *The Journal of Physical Chemistry A* **2010,** *114* (38), 10339-10344.

29.Zhao, Q.; Liu, S.; Shi, M.; Wang, C.; Yu, M.; Li, L.; Li, F.; Yi, T.; Huang, C., Series of New Cationic Iridium(III) Complexes with Tunable Emission Wavelength and Excited State Properties: Structures, Theoretical Calculations, and Photophysical and Electrochemical Properties. *Inorganic Chemistry* **2006,** *45* (16), 6152-6160.

30.Brouwer, A. M., Standards for photoluminescence quantum yield measurements in solution (IUPAC Technical Report). **2011,** *83* (12), 2213-2228.

31.Hao, Z.; Zhang, K.; Chen, K.; Lu, Z.; Wang, P.; Zhu, W.; Liu, Y., An Effective Approach to Obtain Near-Infrared Emission from Binuclear Platinum(II) Complexes Involving Thiophenpyridine-Isoquinoline Bridging Ligand in Solution-Processed OLEDs. *Chemistry - An Asian Journal* **2020,** *15*.

32.Lo, S.-C.; Shipley, C. P.; Bera, R. N.; Harding, R. E.; Cowley, A. R.; Burn, P. L.; Samuel, I. D. W., Blue Phosphorescence from Iridium(III) Complexes at Room Temperature. *Chemistry of Materials* **2006,** *18* (21), 5119-5129.

33.Su, N.; Li, F.-L.; Zheng, Y.-X., Four-membered red iridium(iii) complexes with Ir–S–C–S structures for efficient organic light-emitting diodes. *Journal of Materials Chemistry C* **2020,** *8* (22), 7411-7416.

34.Fan, C.; Zhu, L.; Jiang, B.; Zhong, C.; Ma, D.; Qin, J.; Yang, C., Efficient blue and bluish-green iridium phosphors: Fine-tuning emissions of FIrpic by halogen substitution on pyridine-containing ligands. *Organic Electronics* **2013,** *14* (12), 3163-3171.

35.Das, D.; Gopikrishna, P.; Barman, D.; Yathirajula, R. B.; Iyer, P. K., Substantial efficiency enhancement in solution processed phosphorescent light emitting diode with polymer host: Efficient optimization of charge balance and processing conditions. *Journal of Physics and Chemistry of Solids* **2022,** *163*, 110577.

ABSTRACT

Name of the Student: **Ms. Nishna N.** Registration No.: 10CC18J39004
Faculty of Study: Chemical Sciences Year of Submission: 2024
AcSIR academic centre/CSIR Lab: CSIR-National Institute for Interdisciplinary Science and Technology (CSIR-NIIST) Name of the Supervisor: Dr. Joshy Joseph

Title of the thesis: **Design and Development of Iridium based Dinuclear Complexes for Photodynamic Therapy and Optoelectronic Applications**

Cyclometalated iridium(III) complexes find extensive applications in diverse fields such as cellular imaging, photodynamic therapy (PDT), organic light-emitting diodes (OLEDs), catalysis, photochemical sensors, and as biomarkers. These complexes are highly valued for their distinct photophysical properties, including high photoluminescence quantum yields, tunable emission wavelengths, strong photostability, large Stokes shifts, and long luminescence lifetimes. These characteristics are primarily attributed to the effective spin-orbit coupling (SOC) provided by the iridium center, which facilitates efficient inter-system crossing from singlet to triplet states. In therapeutic applications, especially in PDT, iridium complexes have emerged as potent photosensitizers. PDT is a non-invasive treatment method that relies on the light-induced activation of a photosensitizer (PS), which reacts with molecular oxygen to generate reactive oxygen species (ROS). These cytotoxic ROS promote cancer cell death, making PDT a promising clinical approach for treating various conditions. While mononuclear iridium(III) complexes have been widely studied and used the potential of di- and multinuclear iridium complexes remains underexplored. Beyond their biomedical applications, iridium complexes are also integral to optoelectronic devices such as OLEDs. OLEDs consist of an emitting layer, sandwiched between two electrodes. When voltage is applied, electrons and holes combine in the emissive layer to form excitons, whose radiative decay results in light emission. Given the significance of iridium complexes in both bioimaging and optoelectronics, the design and development of new, efficient photosensitizers and emissive materials is crucial. This thesis focuses on the synthesis, characterization, and exploration of dinuclear iridium(III) complexes, which have been less studied compared to their mononuclear counterparts. The work aims to understand the structure-property relationships of these complexes and investigates their potential applications in both therapeutic fields, particularly PDT, and optoelectronics, such as OLEDs. **Chapter 1** provides an overview of iridium complexes, highlighting their applications as photosensitizers in photodynamic therapy (PDT) and as emissive materials in OLEDs. It delves into recent advancements and developments in these fields.

In **Chapter 2**, we developed a dinuclear iridium complex (**IR-DI**) for imaging and PDT. Compared to its mononuclear counterpart (**IR-MO**), **IR-DI** shows superior photoluminescence quantum yield (Φ_p = 0.70) and singlet oxygen generation quantum yield (Φ_s = 0.49). The complex exhibits efficient cellular uptake, mitochondria targeting, and significant photocytotoxicity in triple-negative breast cancer cells. Mechanisms of cell death are explored through live-dead assays and flow cytometry analysis.

Chapter 3 introduces a viscosity-sensitive iridium complex (**IR-ISO**) for viscosity-activated PDT and carried a comparative photophysical investigation along with the monomer counterpart **IR-IMO**. The complex **IR-ISO** displays enhanced luminescence in viscous environments, with selective activity in cancer cells over normal cells. This chapter highlights the potential of viscosity-assisted PDT for selective cancer treatment.

Finally, **Chapter 4** focuses on the synthesis and optoelectronic applications of two dinuclear iridium complexes (**IR-BIB** and **IR-DPP**) designed for use in OLEDs. The **IR-BIB** complex, with a high photoluminescence quantum yield, performed exceptionally well in OLED devices, achieving a luminescence of 6,300 cd/m^2 and an external quantum efficiency (EQE) of 5.85%, demonstrating its promise for solid-state lighting applications.

List of Publications Emanating from the Thesis

1. **Nishna Neelambaran,** Shanmughan Shamjith, Vishnu Priya Murali, Kaustabh Kumar Maiti* and Joshy Joseph*, Exploring a Mitochondria Targeting, Dinuclear Cyclometalated Iridium (III) Complex for Image-Guided Photodynamic Therapy in Triple-Negative Breast Cancer Cells, https://doi.org/10.1021/acsabm.3c00883, *ACS Appl. Bio Mater. 2023.*
2. **Nishna Neelambaran,** Shanmughan Shamjith, Vishnu Priya Murali, Kaustabh Kumar Maiti* and Joshy Joseph*, Mitochondria-Targeted Dinuclear Iridium (III) Photosensitizer with Intrinsic Viscosity Sensing for Precision in Photodynamic Therapeutic Application (*Manuscript under preparation*).
3. **Nishna Neelambaran,** Vibhu Darshan, Sarah KM McGregor, Shih-Chun Lo*, Ebinazar Namdas*, K. N. Narayanan Unni* and Joshy Joseph*, Development of Dinuclear Cyclometalated Iridium Complexes with Non-innocent Bridging Ligand for OLED Application (*Manuscript under preparation*).

List of Papers/Posters Presented in Conferences

1. *Development of Bimetallic Cyclometalated Iridium(III) Complexes with Non-innocent Bridging Ligand for OLED Application*, **Nishna N.** and Joshy Joseph*, International Conference on Chemistry and Applications of Soft Materials, CASM 2022 at CSIR-National Institute for Interdisciplinary Science and Technology (NIIST), Thiruvananthapuram, 25-27 July 2022 (Poster Presentation).

2. *Development of Mitochondria Targeting Dinuclear Cyclometalated Iridium (III) Complexes for Image-Guided Photodynamic Therapy*, **Nishna N.**, Shanmughan Shamjith, Vishnu Priya Murali, Kaustabh Kumar Maiti* and Joshy Joseph*, National Seminar on Materials for a Sustainable Future 2023 at St. Paul's College, Kalamassery, 12-13 October 2023 (**Best Paper Presentation Award**).

3. *Development of Mitochondria Targeting Dinuclear Cyclometalated Iridium (III) Complexes for Image-Guided Photodynamic Therapy*, **Nishna N.**, Shanmughan Shamjith, Vishnu Priya Murali, Kaustabh Kumar Maiti* and Joshy Joseph*, National Conference on Emerging Trends in Healthcare Biotechnology: Innovations, Challenges and Future Prospects (ETHB 2023) at Regional Cancer Centre (RCC), Thiruvananthapuram, 30 November – 02 December 2023 (Oral Presentation).

4. *Development of Mitochondria Targeting Dinuclear Cyclometalated Iridium (III) Complexes for Image-Guided Photodynamic Therapy*, **Nishna N.**, Shanmughan Shamjith, Vishnu Priya Murali, Kaustabh Kumar Maiti* and Joshy Joseph*, One Week One Theme National Conclave and Research Scholar Symposium on "Specialty Chemicals & Sustainable Packaging" at CSIR-National Institute for Interdisciplinary Science and Technology (NIIST), Thiruvananthapuram, 19 July 2024 (**Best Paper Presentation Award**).

Abstracts for Conference Presentations

1. *International Conference on Chemistry and Applications of Soft Materials, CASM 2022 at CSIR-National Institute for Interdisciplinary Science and Technology (NIIST), Thiruvananthapuram, 25-27 July 2022.*

Development of Bimetallic Cyclometalated Iridium (III) Complexes with Non-innocent Bridging Ligand for OLED Application

Nishna N[1,2], Joshy Joseph[1,2]*

[1]*CSIR-National Institute for Interdisciplinary Science and Technology (NIIST), Thiruvananthapuram 695 019, India*
[2]*Academy of Scientific and Innovative Research (AcSIR), Ghaziabad 201 002, India.*
Email: joshy@niist.res.in

Highly phosphorescent cyclometalated Iridium(III) complexes have been widely employed to fabricate organic light-emitting diodes (OLEDs) because of their unique optoelectronic properties.[1] Phosphorescent dinuclear iridium(III) complexes that can show high luminescent efficiencies and good electroluminescent abilities are very rare. Herein, we demonstrating highly phosphorescent 2-(4-tert-butylphenyl)pyridine based dinuclear Iridium(III) complexes with two different non innocent bridging ligand for OLED application. The introduction of second metal centre in the complex helps us to achieve some superior properties with respect to the common monmer complexes. The molar absobivity of the complex generally hike as more metal centres are present and, more imperative feature we observed for these complexes were the notable drop in the lifetime which could benefit on device to control the efficiency roll off.[2] One of the new dinuclear iridium(III) complex (1) achieves a PLQY of 75%, which is the highest PLQY for dinuclear iridium(III) systems so far. The photophysical characterization of the novel dinuclear systems proved them as potential candidate for OLED application.

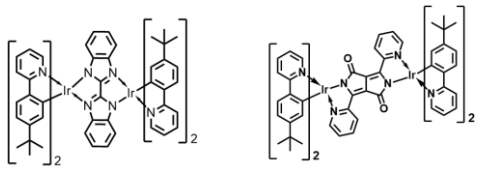

(1) (2)

a) Chemical structure of the new Iridium (III) dimer complexes.

References

[1] Wong, W. Y; Ho, L. C; Zhou, G; Dang, J; Xu, X; Yang, X. Inorg. Chem. 2016, 55, 1720 –1727.
[2] Gather, C. M; Leo, K; Murawski, C. Adv. Mater. 2013, 25, 6801−6827.

2. *National Seminar on Materials for a Sustainable Future 2023 at St. Paul's College, Kalamassery, 12-13 October 2023.*

Development of Mitochondria Targeting Dinuclear Cyclometalated Iridium (III) Complexes for Image-Guided Photodynamic Therapy

Nishna N [a,b], Shanmughan Shamjith [a,b], Vishnu Priya Murali [a,b] Kaustabh Kumar Maiti* [a,b], and Joshy Joseph* [a,b]

[a]*Chemical Sciences & Technology Division (CSTD), CSIR-National Institute for Interdisciplinary Science & Technology (CSIR-NIIST), Thiruvananthapuram, Kerala - 695019, India*

[b]*Academy of Scientific and Innovative Research (AcSIR), Ghaziabad - 201002, India*

*E-mail address: joshy@niist.res.in (JJ); kkmaiti@niist.res.in (KKM)

Photodynamic therapy (PDT) is a highly effective and minimally invasive treatment strategy that employs laser-triggered photosensitizers to combat cancer.[1] This prevalent method relies on a light-activated interaction between a photosensitizer and molecular oxygen, generating cytotoxic reactive oxygen species (ROS) that induce cancer cell death.[2] In rapidly advancing field of PDT, iridium-based photosensitizers stand out due to their dual functionality as both imaging probes and PDT agents, offering potential for precise and targeted therapeutic interventions. Despite the numerous reported classes of mononuclear iridium(III) based photosensitizers, there are limited examples of dinuclear systems. The synthetic difficulties of dinuclear systems may have led to them being initially overlooked, but reports in optoelectronic applications have highlighted their advantages over monomers.[3, 4] The multiple metal centers aid enhanced spin orbit coupling in dinuclear systems result in a wider absorption range and increased production of triplet excitons, offering impressive advantages. The focus here was exploring the full potential of iridium-based dinuclear systems for PDT applications remains a challenge.

Herein, we demonstrating a dinuclear Ir(III) complex, designated as **IRDI**, alongside its structurally analogous monomer complex, **IRMO**. Both complexes feature 2-(2,4-difluorophenyl)pyridine and 4'-methyl-2,2'-bipyridine ligands. Our comparative analysis of the mononuclear and dinuclear Ir(III) complexes revealed a higher photoluminescence quantum yield (Φ_p) of 0.70 for **IRDI** in comparison to **IRMO** (Φ_p = 0.47). And **IRDI** also exhibited a higher singlet oxygen generation quantum yield (Φ_s) of 0.49 compared to **IRMO** (Φ_s = 0.28) which is a vital criteria for a photosensitizer in photodynamic therapy.[5] The in vitro assessments confirmed the efficient cellular uptake and the inherent mitochondria-targeting ability of **IRDI** without the need of a specific targeting group. The light-triggered cellular apoptosis via reactive oxygen species (ROS)-mediated photodynamic therapy (PDT) was confirmed through diverse live-dead assays conducted both in the presence and absence of the singlet oxygen scavenger NaN_3. Further, the mechanism of cell death was elucidated through the Annexin V-FITC/PI flow cytometric assay. Thus, proving the dinuclear complex **IRDI** as a potential candidate for image-guided PDT application.

1. Nam, J. S.; Kang, M.-G.; Kang, J.; Park, S.-Y.; Lee, S. J. C.; Kim, H.-T.; Seo, J. K.; Kwon, O.-H.; Lim, M. H.; Rhee, H.-W.; Kwon, T.-H., Endoplasmic Reticulum-Localized Iridium(III) Complexes as Efficient Photodynamic Therapy Agents via Protein Modifications. Journal of the American Chemical Society 2016, 138 (34), 10968-10977.
2. Xiang, H.; Chen, H.; Tham, H. P.; Phua, S. Z. F.; Liu, J.-G.; Zhao, Y., Cyclometalated Iridium(III)-Complex-Based Micelles for Glutathione-Responsive Targeted Chemotherapy and Photodynamic Therapy. ACS Applied Materials & Interfaces 2017, 9 (33), 27553-27562.
3. Yang, X.; Xu, X.; Dang, J.-s.; Zhou, G.; Ho, C.-L.; Wong, W.-Y., From Mononuclear to Dinuclear Iridium(III) Complex: Effective Tuning of the Optoelectronic Characteristics for Organic Light-Emitting Diodes. Inorganic Chemistry 2016, 55 (4), 1720-1727.
4. Zheng, Y.; Batsanov, A. S.; Fox, M. A.; Al-Attar, H. A.; Abdullah, K.; Jankus, V.; Bryce, M. R.; Monkman, A. P., Bimetallic Cyclometalated Iridium(III) Diastereomers with Non-Innocent Bridging Ligands for High-Efficiency Phosphorescent OLEDs. 2014, 53 (43), 11616-11619.
5. Wang, L.; Karges, J.; Wei, F.; Xie, L.; Chen, Z.; Gasser, G.; Ji, L.; Chao, H., A mitochondria-localized iridium(iii) photosensitizer for two-photon photodynamic immunotherapy against melanoma. Chemical Science 2023, 14 (6), 1461-1471.

3. *National Conference on Emerging Trends in Healthcare Biotechnology: Innovations, Challenges and Future Prospects (ETHB 2023) at Regional Cancer Centre (RCC), Thiruvananthapuram, 30 November – 02 December 2023.*

Development of Mitochondria Targeting Dinuclear Cyclometalated Iridium (III) Complexes for Image-Guided Photodynamic Therapy

Nishna N [a,b], Shanmughan Shamjith [a,b], Vishnu Priya Murali [a,b] Kaustabh Kumar Maiti* [a,b], and Joshy Joseph* [a,b]

[a]*Chemical Sciences & Technology Division (CSTD), CSIR-National Institute for Interdisciplinary Science & Technology (CSIR-NIIST), Thiruvananthapuram, Kerala - 695019, India*

[b]*Academy of Scientific and Innovative Research (AcSIR), Ghaziabad - 201002, India*

*E-mail address: joshy@niist.res.in (JJ); kkmaiti@niist.res.in (KKM)

Introduction: Photodynamic therapy is an effective and non-invasive treatment strategy that employs laser-triggered photosensitizers to combat cancer. This prevalent method relies on a light-activated interaction between a photosensitizer and molecular oxygen, generating cytotoxic ROS species that induce cancer cell death. The iridium-based photosensitizers stand out due to their dual functionality as both imaging probes and PDT agents, offering potential for precise and targeted therapeutic interventions. Despite the numerous reports of mononuclear iridium(III) based photosensitizers, there are limited examples of dinuclear systems.

Aim of study: The multiple metal centers aid enhanced spin-orbit coupling in dinuclear systems result in a wider absorption range and increased production of triplet excitons, offering impressive advantages. So, the aim of study here was exploring the full potential of iridium-based dinuclear systems for PDT applications. Herein, we exploring a dinuclear Ir(III) complex, designated as **IRDI**, alongside its structurally analogous monomer complex, **IRMO**.

Materials and Methods: Chemicals, NMR, Photophysical experiment workstation, Various cellular assay kits

Results: Our comparative analysis of the mononuclear and dinuclear Ir(III) complexes revealed a higher PLQY (Φ_p) of 0.70 for **IRDI** in comparison to **IRMO** (Φ_p = 0.47). And **IRDI** also exhibited a higher singlet oxygen quantum yield (Φ_s) of 0.49 compared to IRMO (Φ_s = 0.28) which is a vital criteria for a photosensitizer in photodynamic therapy. The in-vitro assessments confirmed the efficient cellular-uptake and the inherent mitochondria-targeting ability of **IRDI** without any specific targeting group. The light-triggered cellular apoptosis via ROS-mediated PDT was confirmed through diverse live-dead assays conducted with and without singlet oxygen scavenger NaN_3. Further, the mechanism of cell death was elucidated through the Annexin V-FITC/PI flow cytometric assay. Conclusion: The **IRDI** act as better photosensitizer in all the experiments compared to **IRMO**. So, it confirms efficient employment of dinuclaer systems instead of monomuclear can unleash the full potential of iridium based PDT.

Keywords: Dinuclear Iridium complex, Reactive Oxygen Species (ROS), Photosensitizers (PS), Photodynamic Therapy (PDT), Targeted therapy, Apoptosis

4. *CSIR-National Institute for Interdisciplinary Science and Technology (NIIST), Thiruvananthapuram, 19 July 2024.*

Development of Mitochondria Targeting Dinuclear Cyclometalated Iridium (III) Complexes for Image-Guided Photodynamic Therapy

Nishna N [a,b], Shanmughan Shamjith [a,b], Vishnu Priya Murali [a,b] Kaustabh Kumar Maiti* [a,b], and Joshy Joseph* [a,b]

[a]*Chemical Sciences & Technology Division (CSTD), CSIR-National Institute for Interdisciplinary Science & Technology (CSIR-NIIST), Thiruvananthapuram, Kerala - 695019, India*

[b]*Academy of Scientific and Innovative Research (AcSIR), Ghaziabad - 201002, India*

*E-mail address: joshy@niist.res.in (JJ); kkmaiti@niist.res.in (KKM)

Photodynamic therapy (PDT) is a highly effective and minimally invasive treatment strategy that employs laser-triggered photosensitizers to combat cancer.1 This prevalent method relies on a light-activated interaction between a photosensitizer and molecular oxygen, generating cytotoxic reactive oxygen species (ROS) that induce cancer cell death.2 In rapidly advancing field of PDT, numerous mononuclear Ir(III) based photosensitizers are reported while there are limited examples of dinuclear systems. The synthetic difficulties of dinuclear systems may have led to them being initially overlooked, but reports in optoelectronic applications have highlighted their advantages over monomers.3 The multiple metal centers aid enhanced spin orbit coupling in dinuclear systems result in a wider absorption range and increased production of triplet excitons, offering impressive advantages. Herein, we demonstrate a dinuclear Ir(III) complex, designated as **IRDI**, with a structurally similar monomer complex, **IRMO**. Both complexes feature 2-(2,4-difluorophenyl)pyridine and 4'-methyl-2,2'-bipyridine ligands. Our comparative analysis of the mononuclear and dinuclear Ir(III) complexes revealed a higher PLQY (Φ_p) of 0.70 for **IRDI** in comparison to **IRMO** (Φ_p = 0.47). And **IRDI** also exhibited a higher singlet oxygen generation quantum yield (Φ_s) of 0.49 compared to **IRMO** (Φ_s = 0.28). The in vitro assessments confirmed the efficient cellular uptake and the inherent mitochondria-targeting ability of **IRDI** without any specific targeting group. The light-triggered cellular apoptosis via ROS-mediated PDT was confirmed through diverse live-dead assays conducted. Further, the mechanism of cell death was elucidated through the Annexin V-FITC/PI flow cytometric assay. Thus, proving the dinuclear complex **IRDI** as a potential candidate for image-guided PDT application.

Keywords: Photodynamic therapy, Iridium complexes, Reactive Oxygen species (ROS)

1. *Nam, J. S.; Kang, M.-G.; Kang, J.; Park, S.-Y.; Lee, S. J. C.; Kim, H.-T.; Seo, J. K.; Kwon, O.-H.; Lim, M. H.; Rhee, H.-W.; Kwon, T.-H., Endoplasmic Reticulum-Localized Iridium(III) Complexes as Efficient Photodynamic Therapy Agents via Protein Modifications. Journal of the American Chemical Society 2016, 138 (34), 10968-10977.*

2. Xiang, H.; Chen, H.; Tham, H. P.; Phua, S. Z. F.; Liu, J.-G.; Zhao, Y., Cyclometalated Iridium(III)-Complex-Based Micelles for Glutathione-Responsive Targeted Chemotherapy and Photodynamic Therapy. ACS Applied Materials & Interfaces 2017, 9 (33), 27553-27562.

3. Yang, X.; Xu, X.; Dang, J.-s.; Zhou, G.; Ho, C.-L.; Wong, W.-Y., From Mononuclear to Dinuclear Iridium(III) Complex: Effective Tuning of the Optoelectronic Characteristics for Organic Light-Emitting Diodes. Inorganic Chemistry 2016, 55 (4), 1720-1727.

ACS APPLIED BIO MATERIALS

www.acsabm.org

Article

Exploring a Mitochondria Targeting, Dinuclear Cyclometalated Iridium (III) Complex for Image-Guided Photodynamic Therapy in Triple-Negative Breast Cancer Cells

Nishna Neelambaran, Shanmughan Shamjith, Vishnu Priya Murali, Kaustabh Kumar Maiti,* and Joshy Joseph*

Cite This: *ACS Appl. Bio Mater.* 2023, 6, 5776−5788

Read Online

ACCESS | Metrics & More | Article Recommendations | Supporting Information

ABSTRACT: Photodynamic therapy (PDT) has emerged as an efficient and noninvasive treatment approach utilizing laser-triggered photosensitizers for combating cancer. Within this rapidly advancing field, iridium-based photosensitizers with their dual functionality as both imaging probes and PDT agents exhibit a potential for precise and targeted therapeutic interventions. However, most reported classes of Ir(III)-based photosensitizers comprise mononuclear iridium(III), with very few examples of dinuclear systems. Exploring the full potential of iridium-based dinuclear systems for PDT applications remains a challenge. Herein, we report a dinuclear Ir(III) complex (**IRDI**) along with a structurally similar monomer complex (**IRMO**) having 2-(2,4-difluorophenyl)pyridine and 4′-methyl-2,2′-bipyridine ligands. The comparative investigation of the mononuclear and dinuclear Ir(III) complexes showed similar absorption profiles, but the dinuclear derivative **IRDI** exhibited a higher photoluminescence quantum yield (Φ_p) of 0.70 compared to that of **IRMO** (Φ_p = 0.47). Further, **IRDI** showed a higher singlet oxygen generation quantum yield (Φ_s) of 0.49 compared to **IRMO** (Φ_s = 0.28), signifying the enhanced potential of the dinuclear derivative for image-guided photodynamic therapy. *In vitro* assessments indicate that **IRDI** shows efficient cellular uptake and significant photocytotoxicity in the triple-negative breast cancer cell line MDA-MB-231. In addition, the presence of a dual positive charge on the dinuclear system facilitates the inherent mitochondria-targeting ability without the need for a specific targeting group. Subcellular singlet oxygen generation by **IRDI** was confirmed using Si-DMA, and light-activated cellular apoptosis via ROS-mediated PDT was verified through various live−dead assays performed in the presence and absence of the singlet oxygen scavenger NaN_3. Further, the mechanism of cell death was elucidated by an annexin V-FITC/PI flow cytometric assay and by investigating the cytochrome *c* release from mitochondria using Western blot analysis. Thus, the dinuclear complex designed to enhance spin−orbit coupling with minimal excitonic coupling represents a promising strategy for efficient image-guided PDT using iridium complexes.

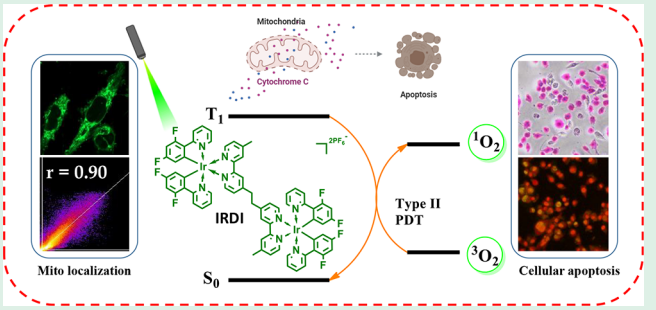

KEYWORDS: *dinuclear iridium complex, reactive oxygen species (ROS), photosensitizers (PSs), photodynamic therapy (PDT), targeted therapy, apoptosis*

1. INTRODUCTION

Over the past few decades, photodynamic therapy has established itself as a highly promising clinical modality for treating a variety of diseases, particularly cancer and actinic keratosis.[1−5] It is a noninvasive method utilizing a light-activated reaction between a photosensitizer and molecular oxygen to generate cytotoxic reactive oxygen species (ROS) facilitating cancer cell death.[3] The processes underlying the generation of reactive oxygen species (ROS) are intricate, but they can be broadly divided into two main pathways. The type I process involves a photoinduced electron transfer with biological substrates, resulting in the formation of radical species such as superoxide ($O_2^{\bullet-}$), hydroxyl ($^{\bullet}OH$), and hydrogen peroxide (H_2O_2). Meanwhile, in the type II pathway, photoreactivity occurs through a direct energy transfer to molecular oxygen ($^3O_2$) resulting in the production of singlet oxygen ($^1O_2$).[6−8]

The effectiveness of photodynamic therapy greatly depends upon the characteristics of the photosensitizers, in addition to light dosage and oxygen concentration.[9] For image-guided therapeutic applications, the photosensitizer must possess several key attributes: a long-lived excited state capable of

Received: September 29, 2023
Revised: November 23, 2023
Accepted: November 23, 2023
Published: December 7, 2023

https://doi.org/10.1021/acsabm.3c00883
ACS Appl. Bio Mater. 2023, 6, 5776−5788

Scheme 1. Schematic Illustration of the Action Mechanism of IRDI through Photodynamic Therapy

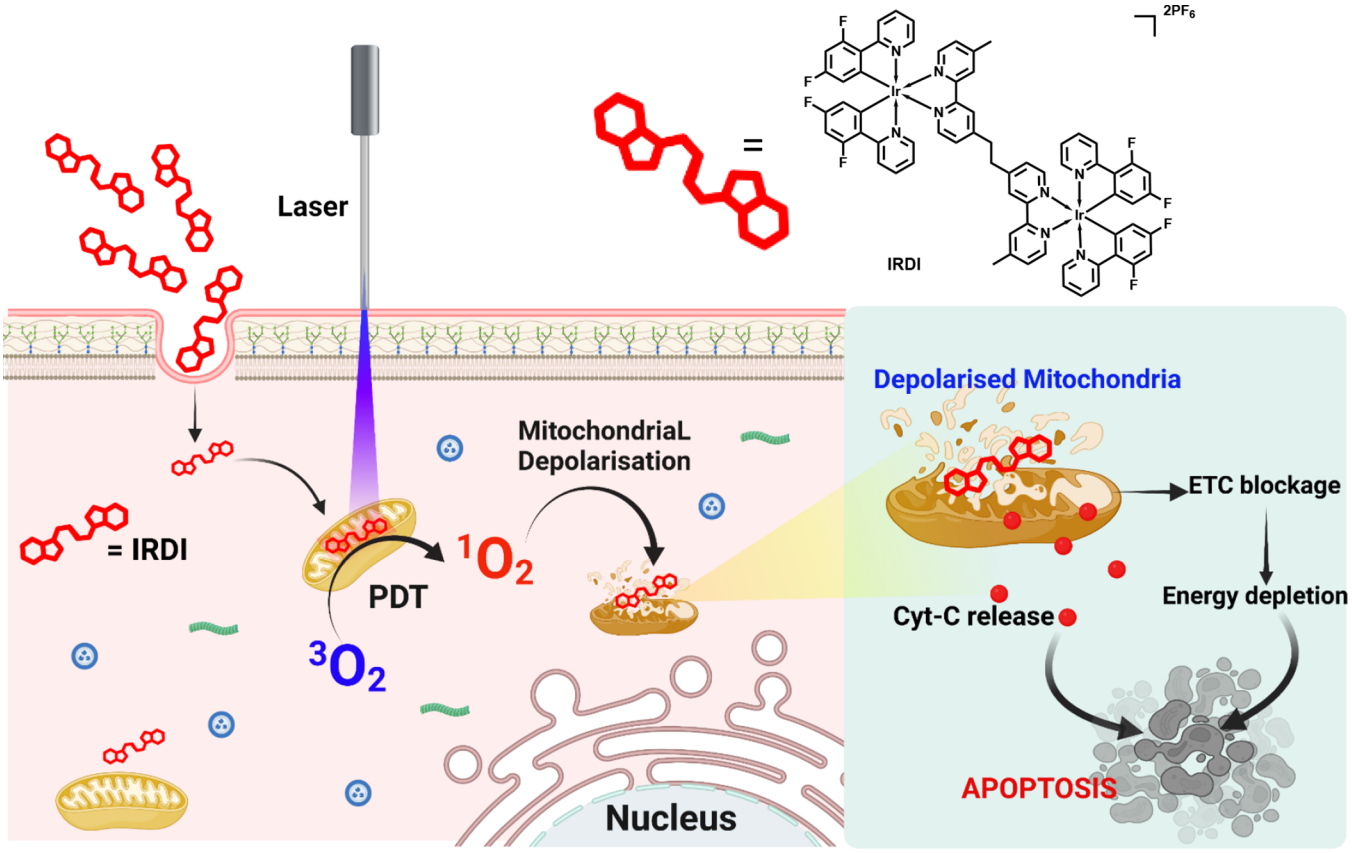

generating ROS upon interaction with oxygen, nontoxicity in its nonirradiated form, preferential absorption in a specific range, photochemical stability, and prompt clearance from the body to minimize the risk of long-term photosensitivity.[10] Although derivatives of porphyrin, chlorin, and phthalocyanine have traditionally been widely used as photosensitizers in PDT due to their favorable light absorption, fluorescence emission, and singlet oxygen generation, they often exhibit challenges such as synthesis and purification difficulties, poor water solubility, prolonged retention in the body, and potential hepatotoxicity. Metal complexes have emerged as promising photosensitizers for PDT, offering advantages such as long-lived triplet states, high ROS production, photochemical stability, and water solubility. The efficient room-temperature photoluminescence of metal complexes offers an additional advantage of cellular imaging, which makes them suitable for image-guided PDT compared to conventional photosensitizers.[11]

Recently, cyclometalated transition-metal complexes, particularly Pt(II) and Ir(III), have gained widespread attention due to their impressive luminescent properties and for their performance as a highly effective class of singlet oxygen photosensitizers.[12−16] Even though the success of cisplatin as an anticancer agent has ignited a pursuit for the development of several inorganic anticancer drugs, they generally induce cell death via the oxygen-independent type III pathway and are referred as photoactivated chemotherapeutic (PACT) agents rather than as PDT agents.[10,17,18] Despite numerous reported examples of Pt(II) complexes as efficient singlet oxygen sensitizers, only a few platinum complexes have demonstrated photosensitizing effects via a type I or type II mechanism.[10] Subsequently, it was found that iridium(III) complexes act as efficient photosensitizers through a type I or type II mechanism and are suitable for live-cell imaging-guided PDT applications.[10,19] In addition, iridium complexes show excellent photophysical and photochemical properties, such as a large Stokes shift, ease in color tuning, high triplet and singlet oxygen quantum yield, long luminescence lifetimes, and high chemical and photochemical stabilities.[20,21]

Several examples of mononuclear iridium complexes used as photosensitizers for PDT have been reported in recent years.[6,22−28] Thompson et al. reported two iridium complexes based on a cyclometalating ligand, phenylbenzothiazole with ancillary ligands pyridine and acac, respectively, showing singlet oxygen generation efficiencies as high as 100%.[29] Significant research efforts were also focused on organelle targeted PDT using iridium-based photosensitizers.[23,24,26] For example, endoplasmic reticulum targeted phenylquinoline-based iridium complexes for efficient ROS generation and rapid cell death were demonstrated by Kwon et al., where the phenylisoquinoline-based iridium enhanced ROS generation by tuning the photosensitizer energy level for efficient energy transfer to triplet oxygen.[25] Chao et al. reported a mitochondria targeting iridium complex for hypoxic tumors.[30] The overall positive charge and lipophilic nature of iridium complexes help them to get localized in the mitochondria of cells even without having any specific targeting group.[30,31] The subcellular localization plays a crucial role in the immunogenic response. As the energetic powerhouse of the cell, mitochondria act as ideal subcellular locations for the photosensitizer agent.[32−34] Efforts were also made in utilizing the iridium complexes for two-photon-based PDT and for extending the absorption of the complexes to the NIR region by substitution and conjugation to

https://doi.org/10.1021/acsabm.3c00883
ACS Appl. Bio Mater. 2023, 6, 5776−5788

overcome the inherent limitations of low wavelength absorptions for PDT.[35−38]

Despite the numerous reports on homoleptic and heteroleptic monomer iridium complexes for PDT applications, the study of di/multinuclear iridium complexes as photosensitizers remains less explored. Although the synthetic difficulties of dinuclear iridium complexes may be a reason for them being initially overlooked, reports on photophysical and device properties of di/multinuclear iridium complexes used for optoelectronic applications have highlighted their advantages over monomers.[39,40] Typically, multiple metal centers are expected to enhance spin−orbit coupling (SOC) in di/multinuclear iridium complexes, resulting in enhanced luminescence quantum yields and ROS generation.[41−44]

Herein, we have designed a mitochondria targeting dinuclear iridium complex with 2-(2,4-difluorophenyl)pyridine as the cyclometalating ligand and 4′-methyl-2,2′-bipyridine ancillary ligand joined through a flexible ethyl spacer (Scheme 1; **IRDI**) and investigated their photophysical and photocytotoxicity properties in comparison with the corresponding mononuclear iridium complex (**IRMO**). The flexible ethyl spacer ensures minimum through-bond electronic coupling while ensuring close proximity of the metal centers, leading to efficient spin orbital coupling without quenching of photoluminescence. Consequently, the dinuclear iridium complex shows enhanced triplet quantum yield and singlet oxygen generation efficiency compared to the monomer iridium complex. In addition to this, the dual positive charge of dinuclear complex (**IRDI**) enhances the mitochondria targeting properties. The *in vitro* analysis on the cellular internalization, mitochondrial localization, and photocytotoxicity of **IRDI** was conducted in the triple-negative breast cancer cell line MDA-MB-231. Finally, the investigation of the cell death mechanism deciphered the ROS-driven mitochondria mediated apoptotic pathway initiated by **IRDI** upon photosensitization. Thus, the dinuclear design can unleash the full potential of iridium-based photosensitizers in image-guided cancer photodynamic therapy.

2. MATERIALS AND METHODS

2.1. Materials and General Instruments. The chemicals used in this work, 2-bromopyridine, 2,4-difluorophenylboronic acid, 4,4′-dimethyl-2,2′-bipyridyl, 1,2-bis(4′-methyl-2,2′-bipyridin-4-yl)ethane, potassium carbonate, tetrabutylammonium bromide, $Pd(PPh_3)_4$, $IrCl_3{\cdot}xH_2O$, NH_4PF_6, and 2-ethoxyethanol, were purchased from Sigma-Aldrich and TCI Chemicals and used as received without further purification. Moisture- and oxygen-sensitive reactions were carried out under an argon atmosphere in dried solvents purchased from Sigma-Aldrich and Merck chemical suppliers. Thin layer chromatography (TLC) analysis was performed using aluminum plates coated with silica gel purchased from Merck. Silica gels (100−200 and 230−400 mesh) were used for column chromatography. ^{1}H NMR (500 MHz) and ^{13}C NMR (125 MHz) analyses were achieved using a Bruker Avance DPX spectrometer, with TMS as the internal standard (δH = 0 ppm and δC = 0 ppm). Acetonitrile-d_3 and DMSO-d_6 were used as solvents for NMR analysis. High-resolution mass spectra (HRMS) were obtained from a Thermo Scientific Q Exactive Hybrid Quadrupole-Orbitrap Electrospray Ionization Mass Spectrometer (ESI-MS).

2.2. Photophysical Measurements. The UV/vis absorption spectra were measured using a Shimadzu UV−vis spectrophotometer (UV-2600), and emission spectra were measured using a SPEX Fluorolog spectrofluorimeter. The photostability of **IRDI** was studied by recording absorption spectra with freshly prepared 10 μM solution in acetonitrile in the presence and absence of light irradiation on an Oriel optical bench model 11200 fitted with a 200 W xenon lamp using a 400 nm band-pass filter at regular time intervals. The pH-dependent study of **IRDI** was done by recording the emission spectra of 10 μM solution of **IRDI** in PBS buffer at different pH ranges from 5 to 9. Cyclic voltammetric analyses were done using a PARSTAT 4000A potentiostat under an argon atmosphere in dry and oxygen-free acetonitrile with 0.1 M tetrabutylammonium hexafluorophosphate (TBAH) as the supporting electrolyte. A standard three-electrode configuration utilizing a Ag/AgCl electrode and platinum wire counter electrode was used with the redox potentials referenced to the ferrocene/ferrocenium as standard for the measurement. Singlet oxygen generation quantum yields (Φ_s) were determined using 1,3-diphenylisobenzofuran (DPBF) as the singlet oxygen scavenger for **IRMO** and **IRDI**.[12] The DPBF undergoes a [4 + 2] cycloaddition with $^1O_2$ to form *o*-dibenzoylbenzene, which can be evaluated by a decrease in the absorbance of DPBF at 410 nm. The studies were done with a sample concentration ratio 1:10 of Ir(III) complexes and DPBF, irradiated using an Oriel lamp fitted with a 400 nm band-pass filter at regular time intervals followed by UV−vis measurement. The singlet oxygen quantum yields for **IRDI** and **IRMO** in acetonitrile were measured using the reference molecule $[Ru(bpy)_3]Cl_2$ in acetonitrile, (Φ_s = 0.57) using eq 1

$$\Phi_c = \Phi_s \frac{S_c \times F_s}{S_s \times F_c} \quad (1)$$

where S is the slope of a plot of the change in absorbance of DPBF (at 410 nm) with the irradiation time and F is the absorption correction factor, which is given by $F = 1 - 10^{-OD}$ (OD represents the optical density). The photoluminescence quantum yields of **IRDI** and **IRMO** were measured by a relative comparison method using $Ir(ppy)_3$ (Φ_p = 0.89 in dichloroethane) as the standard.[45] The fluorescence lifetime measurements were done using a picosecond single photon counting system (TCSPC) from Horiba (DeltaFlex), and a picosecond photon detection module (PPD-850) was used as the detector. The fluorescence decay profiles were analyzed using the EzTime software and fitted with a multiexponential decay model, with a chi-square value 1 ± 0.2.

2.3. *In Vitro* Studies. The MTT assay was performed using the MDA-MB-231 breast cancer cell line (purchased from ATCC). The cells were seeded in a 96-well plate at a density of 12,000 cells/well and maintained for 24 h in DMEM with 10% FBS. Then, the cells were incubated with **IRDI** at a concentration of 5−100 μM in different wells for 24 h. After the required incubation, the MTT assay was performed to get the cell viability. Internalization of **IRDI** was checked in MDA-MB-231 breast cancer cells. The cells were incubated with **IRDI** in plain DMEM at a concentration of 5−30 μM per well. The images were captured from 0 to 3 h in a time-dependent manner (FITC channel).

Mitochondrial colocalization experiments were conducted using the commercially available MitoTracker Red (Molecular probes). In these experiments, cells were first incubated with the **IRDI** molecule for approximately 3 h. After the incubation period, the cells were washed and then treated with a 100 nM concentration of MitoTracker Red. Following a 15 min incubation with MitoTracker Red, the cells were washed twice with PBS. Finally, images were captured using a confocal fluorescent microscope to study the colocalization of the **IRDI** molecule and MitoTracker Red within the mitochondria. Again, the mitochondrial localization of complex **IRDI** was confirmed using ICP-MS analysis. MDA-MB-231 breast cancer cells were seeded into a 16-well plate for 24 h. The medium was removed and replaced with **IRDI** (10 μM) in plain DMEM. After 3 h of incubation, the cells were scraped out, collected in PBS (3 mL), and counted. The cells were pelletized, and different subcellular fractions (nuclear, cytosolic, and mitochondrial) were collected by repeated centrifugation using the previously reported method.[46] HNO_3 (65%, 1 mL) was added to these fractions, and the mixture was incubated at room temperature for 24 h to digest entirely. The solution was then diluted to a final volume of 10 mL with Milli-Q water, and the cellular concentration of iridium was measured using the ICP-MS.

The singlet oxygen generation experiments were performed using Si-DMA (Sigma-Aldrich). Cells were incubated with **IRDI** for 3 h prior to the treatment with Si-DMA. After the required incubation, cells were

https://doi.org/10.1021/acsabm.3c00883
ACS Appl. Bio Mater. 2023, 6, 5776−5788

Scheme 2. (a) Structures of the Mononuclear Iridium Complex, IRMO, and Dinuclear Iridium Complex, IRDI. (b) Scheme Adopted for the Synthesis

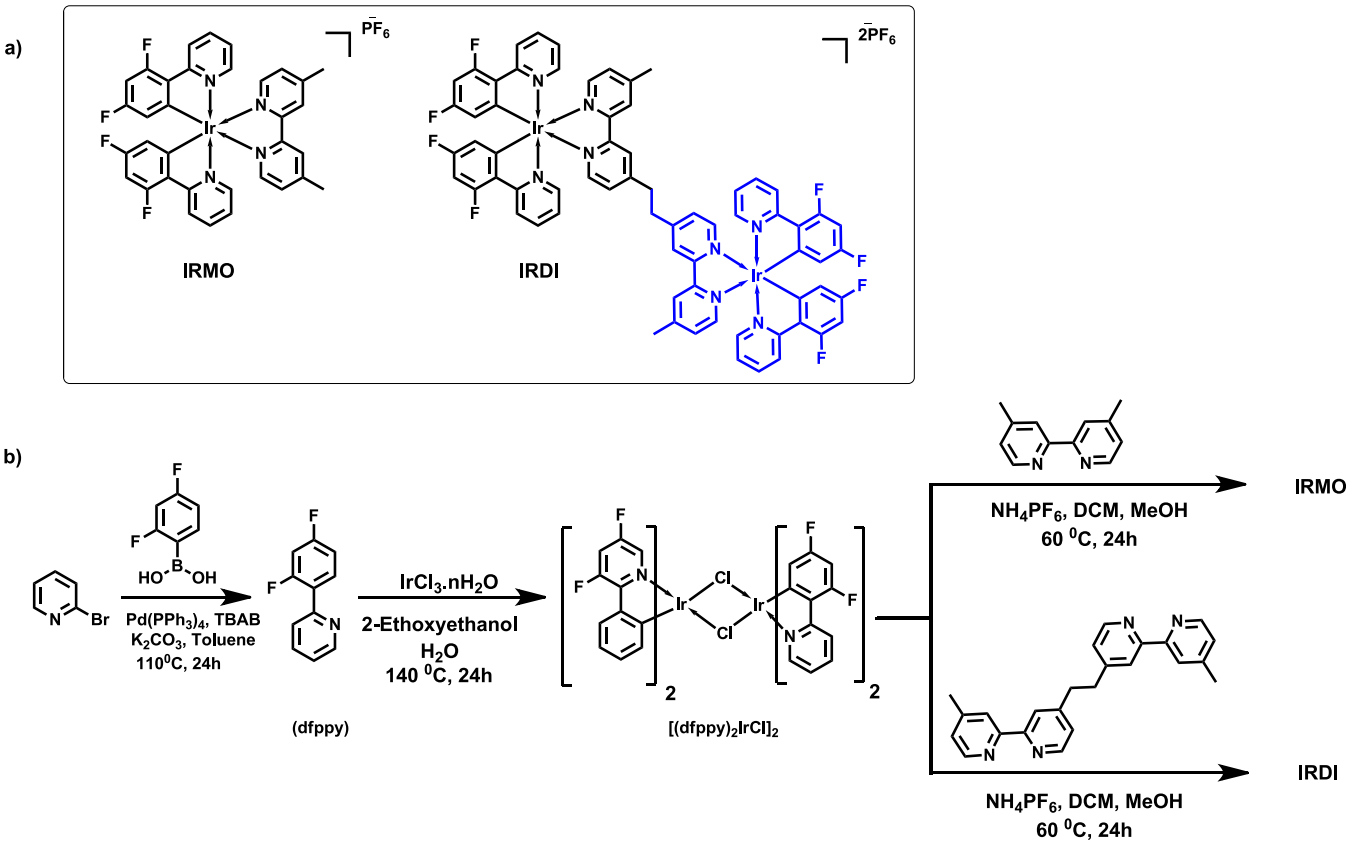

washed two times with PBS, and fluorescence images were taken in the inverted fluorescence microscope using the TRITC channel.

IRDI-driven cellular cytotoxicity and membrane damages were analyzed using various selective staining procedures. For these, MDA-MB-231 cells were seeded in a 96-well plate (10,000 cells/well), and after 24 h, the cells were incubated with **IRDI** (10 μM) for about 3 h, washed with PBS twice, and then irradiated with a 405 nm laser for 2 min (0.5 W laser power). Treatment groups like **IRDI**-treated/untreated cells with and without laser irradiation were included in all the studies. After 24 h, cells were washed and incubated with corresponding staining agents. A trypan blue dye exclusion study was performed by incubating the **IRDI**-treated laser-irradiated cells with 0.2% trypan blue solution in PBS for 5 min. Cells were washed, and bright field images were captured using an inverted microscope. For the acridine orange (AO)−ethidium bromide (EB) dual fluorescent staining assay, the live−dead assay cocktail (5 μg of each in 1 mL PBS) was incubated for 5 min with the treated and untreated cells, and the images were then captured in green and red fluorescence channels. AO will be taken up by all the cells giving green fluorescence, whereas the orange-red fluorescence of EB indicates membrane compromised dead cells. For the APOP assay, the cells were treated as mentioned above; after 24 h, the wells were washed, and the APOP reagent was added. Images were then captured in bright field mode. To examine the Hoechst nuclear staining assay, the cell lines were seeded in a 96-well plate for 24 h and incubated with/without **IRDI** for 3 h followed by laser irradiation using the 405 nm laser. After 24 h, the samples were washed with PBS and stained with Hoechst dye (10 μg/mL), and images were captured under the DAPI filter of the fluorescence microscope (UV range excitation, 340−390 nm and emission range, 430−490 nm; green channel images were taken with an excitation range of 460−495 nm and emission range of 510−550 nm, whereas the red channel images (MitoTracker) were taken with an excitation range of 530−550 nm and emission of 575 nm).

The cytochrome *c* release from mitochondrial membrane to cytoplasm was analyzed by protein expression studies using cytosolic and mitochondrial fractions. For this, MDA-MB-231 cells were cultured in six-well plates at a density of 1.5×10^5 cells/well, and after 24 h, cells were treated with and without **IRDI** for 3 h. Laser irradiation was given as mentioned above, and the plates were incubated for 8 h. Cells were then washed and scraped out to isolate the mitochondrial and cytosolic fraction as per the reported procedure, and Western blot analysis was performed for cytochrome *c* with GAPDH as the loading control.[47] The JC-1 assay was employed to analyze mitochondrial membrane depolarization in this study. Cells were cultured in 48-well plates at a density of 12,000 cells per well and subjected to various treatments as per the experimental requirements. The cells were then incubated for approximately 24 h to allow for cellular responses. After the treatment period, the cells were carefully washed to remove any residual substances and then incubated with JC-1 dye at a concentration of 2 μM for 15 min. Following the incubation with JC-1 dye, the cells were washed again with phosphate-buffered saline (PBS) to remove the excess dye. Finally, images of the cells were captured using a fluorescent microscope with separate channels for green and red fluorescence. The intensities of green and red fluorescence in the images indicate the extent of mitochondrial membrane depolarization, providing valuable insights into the mitochondrial health and function of the treated cells. Further, an annexin binding assay was carried out to confirm the cellular apoptosis. For this, cells were seeded in six-well plates (1.5×10^5 cells/well) and treated with or without **IRDI**. Laser irradiation was carried out for the required treatment groups. After 24 h of laser treatment, cells were harvested by trypsinization. The annexin V-FITC-PI staining was performed as per the manufacturer's instructions provided in the Apoptosis Detection Kit (BD Pharmingen), and flow cytometric analysis was carried out using FACS Aria (BD, USA).

https://doi.org/10.1021/acsabm.3c00883
ACS Appl. Bio Mater. 2023, 6, 5776−5788

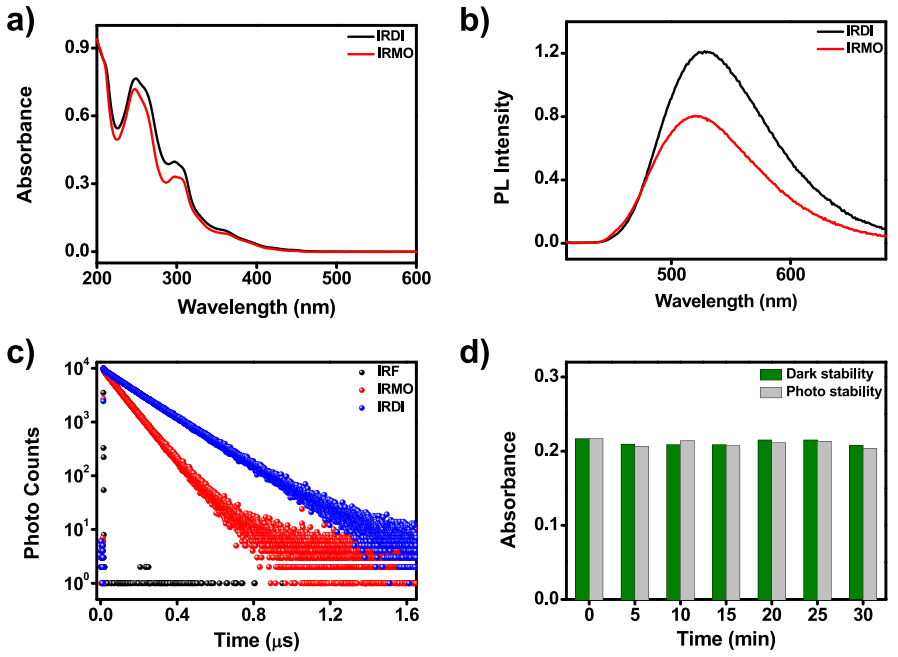

Figure 1. (a) UV−visible absorption spectra of **IRDI** and **IRMO** in acetonitrile. (b) Emission characteristics of **IRDI** and **IRMO** at 365 nm excitation. (c) Time-correlated single photon counting (TCSPC) measurement of **IRDI** and **IRMO**. (d) Photo and dark stability of **IRDI**.

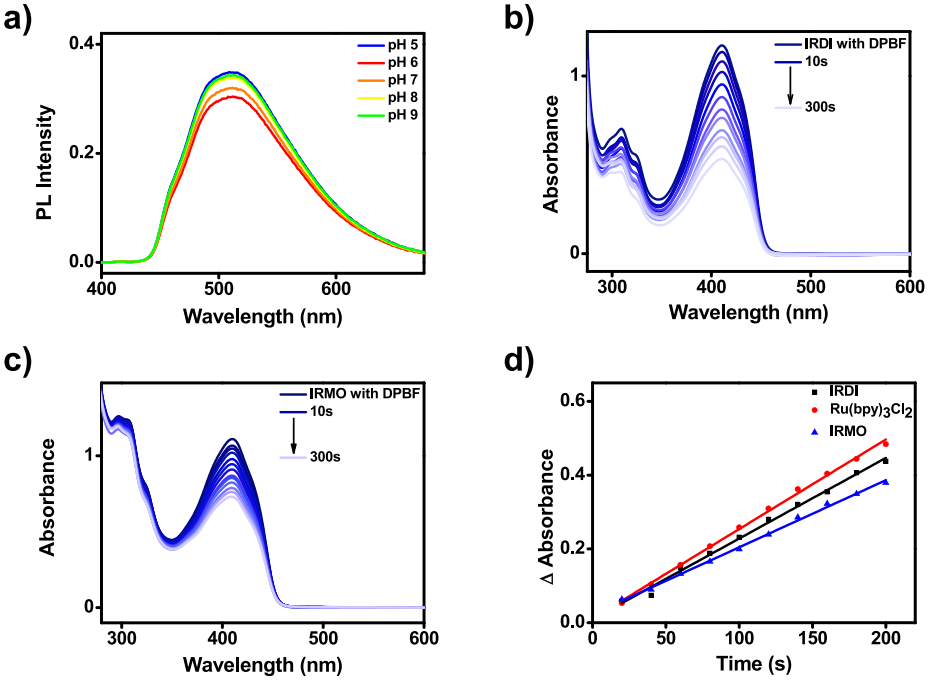

Figure 2. (a) pH-dependent emission spectral changes of **IRDI** at different pH values starting from 5 to 9 (excitation 365 nm). (b) Absorption spectra of the 1,3-diphenylbenzofuran (DPBF) mixture with the **IRDI** sample upon irradiation using a 200 W xenon lamp fitted with a 400 nm band-pass filter. (c) Absorption spectra of the 1,3-diphenylbenzofuran (DPBF) mixture with the **IRMO** sample upon irradiation using a 200 W xenon lamp fitted with a 400 nm band-pass filter. (d) Relative plot of decrease in absorption of DPBF at 410 nm in the presence of **IRDI, IRMO**, and reference $[Ru(bpy)_3]Cl_2$.

3. RESULTS AND DISCUSSION

3.1. Synthesis of IRMO and IRDI Complexes. Herein, we synthesized a dinuclear iridium complex (**IRDI**) and a structurally similar mononuclear iridium complex (**IRMO**) for comparative investigation of the photophysical properties, as shown in Scheme 2a. The cyclometalating ligand, 2-(2,4-difluorophenyl)pyridine (dfppy), was synthesized via a Pd-catalyzed Suzuki cross-coupling reaction using 2-bromopyridine and 2,4-difluorophenylboronic acid. Subsequently, the chlorine bridged iridium dinuclear complex, $[(dfppy)_2IrCl]_2$, was synthesized by coupling of the cyclometalating ligand with iridium(III) chloride ($IrCl_3 \cdot xH_2O$) via a Nonoyama reaction.[48] The syntheses of the dinuclear Ir(III) complex, **IRDI**, and the corresponding monomer Ir(III) complex, **IRMO**, were achieved by the final replacement of the bridged chlorine with respective ancillary bipyridine ligands. Finally, the chlorine counterions in the complexes were exchanged with hexafluorophosphate

https://doi.org/10.1021/acsabm.3c00883
ACS Appl. Bio Mater. 2023, 6, 5776−5788

Table 1. Photophysical and Electrochemical Properties of Ir(III) Complexes

complex	λ_{abs}[a] (nm)	λ_{ems}[b] (nm)	HOMO[c] (eV)	LUMO[d] (eV)	E_g[e] (eV)	Φ_p[f]	Φ_s[g]	lifetime[h] (ns)
IRDI	365	525	−6.12	−3.40	2.73	0.70	0.49	185
IRMO	365	519	−6.03	−3.11	2.92	0.47	0.28	97

[a]Absorption maxima. [b]Emission maxima. [c]HOMO determined by cyclic voltammograms in degassed acetonitrile (Figures S4 and S5). [d]LUMO determined by cyclic voltammograms in degassed acetonitrile (Figures S4 and S5). [e]$E_g = (E_{ox} - E_{red})$ [eV]. [f]Φ_p refers to the photoluminescence quantum yield, with $Ir(ppy)_3$ in dichloroethane ($\Phi_p = 0.89$) as the reference. [g]Φ_s refers to the singlet oxygen quantum yield, with $[Ru(bpy)_3]Cl_2$ in acetonitrile ($\Phi_s = 0.57$) as the reference. [h]Lifetime data (excitation wavelength 365 nm).

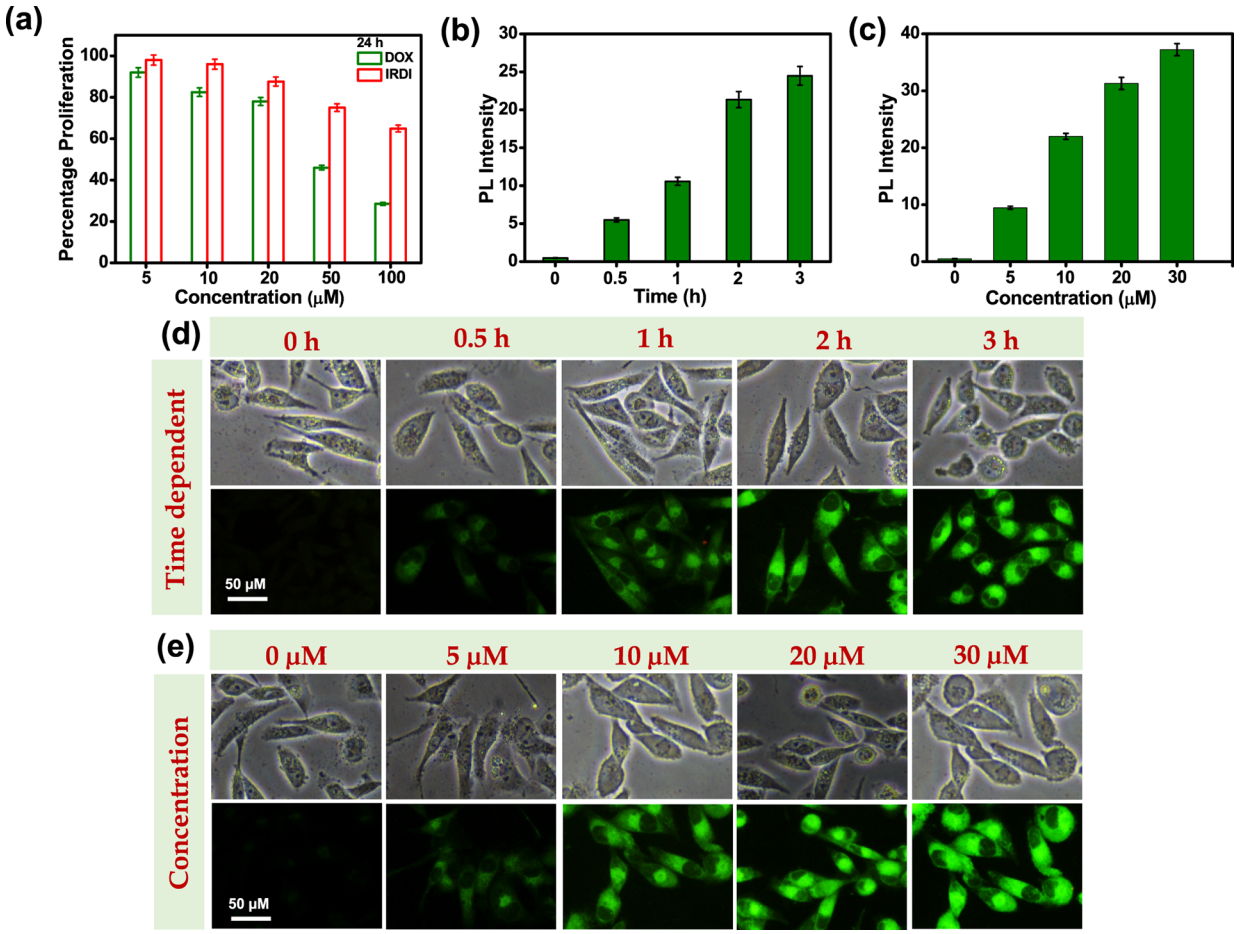

Figure 3. (a) *In vitro* cytotoxicity profiling of **IRDI** in MDA-MB-231 cells at 24 h using the MTT assay, with commercially available drug doxorubicin as the positive control. (b) Time-dependent fluorescent intensity quantification of **IRDI**-treated MDA-MB 231 cells. (c) Concentration-dependent fluorescent intensity quantification of **IRDI**-treated MDA-MB 231 cells. (d) Time-dependent fluorescent cell images from 0 to 3 h incubation. (e) Concentration-dependent internalization of **IRDI** from 0 to 30 μM probed using fluorescence microscopy.

anions through an anion exchange reaction with ammonium hexafluorophosphate (Scheme 2b). The synthesized monomeric and dinuclear complexes and all the synthetic intermediates were well-characterized using HRMS and NMR spectroscopic methods.

3.2. Photophysical Properties. The absorption spectra of the complexes in acetonitrile solution at room temperature are shown in Figure 1a. The UV−vis absorption spectra of both **IRMO** and **IRDI** exhibited an intense band around 200−300 nm, which can be assigned to spin allowed $^1\pi-\pi^*$ ligand centered transitions in 2-(2,4-difluorophenyl)pyridine and ancillary bipyridine ligands.[49] The less intense absorption bands in the range of 300−400 nm correspond to spin allowed and spin forbidden, mixed singlet and triplet metal-to-ligand charge transfer (^{1}MLCT and ^{3}MLCT) admixes with the ligand-to-ligand charge-transfer (LLCT) transitions.[49] The emission spectra of **IRMO** and **IRDI** in acetonitrile at room temperature under degassed conditions were documented in Figure 1b. An intense, broad, and featureless emission band with a maximum at 525 nm is observed for **IRDI**, which is slightly red-shifted compared to that of the monomer complex **IRMO** (λ_{em} = 519 nm). The broad and featureless emission bands are mainly attributable to charge-transfer (CT) states, whereas ligand-centered (LC) states typically give highly structured emissions.[50] The emission intensity of the dinuclear Ir(III) complex, **IRDI**, is nearly 2-fold compared to that of the mononuclear Ir(III) complex, **IRMO**, which is also reflected in the calculated photoluminescence quantum yields for **IRDI** (Φ_p = 0.70) and **IRMO** (Φ_p = 0.47) in acetonitrile, with reference to standard $Ir(ppy)_3$ in dichloroethane (Φ_p = 0.89).[51] The PL lifetime measurements of **IRDI** and **IRMO** using time-resolved single

https://doi.org/10.1021/acsabm.3c00883
ACS Appl. Bio Mater. 2023, 6, 5776−5788

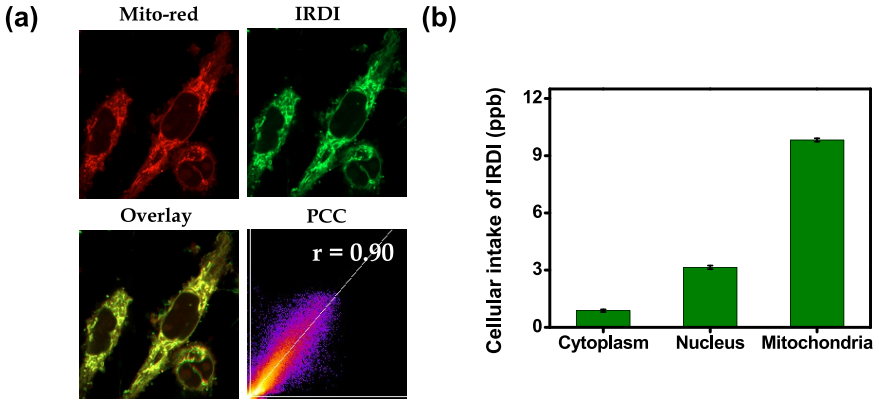

Figure 4. (a) The mitochondrial localization images of **IRDI**-treated cells with MitoTracker Red and the corresponding scatter plot. (b) The subcellular distribution of **IRDI** in the mitochondria, cytoplasm, and nucleus determined by ICP-MS.

photon counting techniques exhibited lifetimes of 185 and 97 ns, respectively (Figure 1c).

To investigate the photobleaching effect of the dinuclear Ir(III) complex **IRDI**, photostability measurements were conducted with and without irradiation using a 200 W xenon Arc lamp on an Oriel optical bench, and the results are shown in Figure 1d. The **IRDI** complex exhibited stable and reproducible absorption profiles in the presence and absence of irradiation in a time-dependent manner, indicating the excellent photostability of the complex **IRDI**. The pH-sensitive absorption and emission properties of **IRDI** were studied (Figure 2a, Figure S1), as the nature of the environment can perturb the electronic and photophysical properties of molecules. The absorption and emission profiles were recorded in PBS buffer by incubating **IRDI** at different pH values (5−9), which exhibited no significant sensitivity. The minimal impact of acidity on photophysical behavior allows **IRDI** to be stable under normal and acidic cell conditions.

The singlet oxygen generation efficiencies of the **IRDI** and **IRMO** complexes were investigated by employing 1,3-diphenylbenzofuran (DPBF) as the singlet oxygen scavenger and $[Ru(bpy)_3]Cl_2$ (Φ_s = 0.57 in acetonitrile) as reference (Figure S2).[12] The decrease in DPBF absorbance at 410 nm of **IRDI** and **IRMO** is depicted in Figure 2b,c. The reduction in absorbance was substantial upon light irradiation in the presence of the **IRDI** compared to **IRMO** complex, suggesting the higher singlet oxygen generation capacity of the dinuclear complex. To calculate and demonstrate the ROS capacity of iridium complexes using DPBF, we documented the linear correlation of change in absorption with time as in Figure 2d. The singlet oxygen quantum yields, Φ_s, of **IRDI** and **IRMO** were calculated as 0.49 and 0.28, respectively, which suggests that the dinuclear complex **IRDI** is a better photoactivatable ROS generator for PDT compared to **IRMO**. The singlet oxygen quantum yields obtained for **IRDI** and **IRMO** are comparable with earlier literature reports.[25,52] Further, the singlet oxygen generation capability of **IRDI** in aqueous media was confirmed using water-soluble singlet oxygen sensors ABDA and Si-DMA as shown in Figure S3.

The presence of two heavy metals in the dinuclear Ir(III) complex **IRDI** facilitates enhanced spin−orbit coupling, resulting in effective intersystem crossing (ISC) and high population of triplet excited states. As a result of their long-lasting triplet excited states, these iridium complexes can efficiently interact with oxygen, leading to high yields of singlet oxygen generation. The dinuclear **IRDI** reported in this work is designed, addressing the emission quenching exhibited by dinuclear systems in general, which marked them as a less potential candidate for PDT applications. Here the ethyl spacer in **IRDI** eliminates the chance of electronic coupling of monomer units via conjugation and the energy transfer by FRET, which happen to be the main reasons for the poor PL performance of dinuclear complexes.[41,43,52−54] Further, the extra positive charge also augments the mitochondria targeting ability of the dinuclear complex by utilizing the negative membrane potential.[55−58] As the dinuclear complex, **IRDI** exhibited better photophysical performance compared to **IRMO** in all aspects (Table 1). **IRDI** was subjected to detailed *in vitro* studies.

3.3. *In Vitro* Assessment of Photodynamic Therapy.

3.3.1. Cytotoxicity, Internalization, and Mitochondrial Targeting of IRDI in MDA-MB 231 Cells. The cytotoxicity of the dinuclear complex **IRDI** was evaluated in the triple-negative breast cancer cell line MDA-MB 231. To confirm the nontoxic nature of **IRDI**, we performed an MTT assay, as an ideal photosensitizer should have minimal dark toxicity and only be cytotoxic in the presence of light.[59,60] The complex **IRDI** demonstrated a proliferation of cells above 90% at a 10 μM concentration, confirming its nontoxic nature. Subsequent experiments involving varying concentrations of **IRDI** (ranging from 0 to 100 μM) at 12 and 24 h incubation revealed minimal dark toxicity up to 20 μM concentrations (Figure 3a). To assess the nontoxicity of **IRDI** in normal cells, an MTT assay was carried out in a normal breast epithelial cell line, MCF-10A. The results showed no significant dark toxicity at 10 μM concentration (Figure S6). To better understand the cellular uptake of **IRDI** in MDA-MB 231 cells, time- and concentration-dependent internalization studies were performed (Figure 3b,c). Cells were exposed to a 10 μM concentration of **IRDI** in plain DMEM, and the green fluorescence of **IRDI** was monitored in a time-dependent manner. The intensity of the green fluorescence increased from 0 to 3 h, indicating the progress of cellular uptake (Figure 3d). The green fluorescence signals were detectable from 30 min onward and reached their maximum intensity at 3 h, identifying the optimum internalization time as 3 h. Subsequently, concentration-dependent internalization experiments with various **IRDI** concentrations ranging from 0 to 30 μM exhibited a gradual increase in green fluorescence intensity with rising **IRDI** concentrations (Figure 3e). The IC_{50} value calculated for **IRDI** with laser is 5.31 μM and without laser is 48.3 μM by concentration-dependent cytotoxicity profiling of MDA-MB-231 cells using the MTT assay (Figure S7). Based on

https://doi.org/10.1021/acsabm.3c00883
ACS Appl. Bio Mater. 2023, 6, 5776−5788

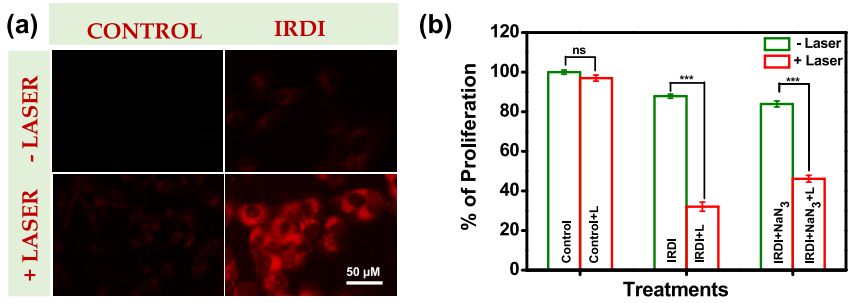

Figure 5. (a) The subcellular singlet oxygen generation study of **IRDI** using Si-DMA in MDA-MB 231 cells. (b) MTT assay showing the photodynamic effect of **IRDI**-treated and laser-irradiated cells with and without the singlet oxygen scavenger NaN_3; ns: $p > 0.05$ and ***: $p < 0.001$.

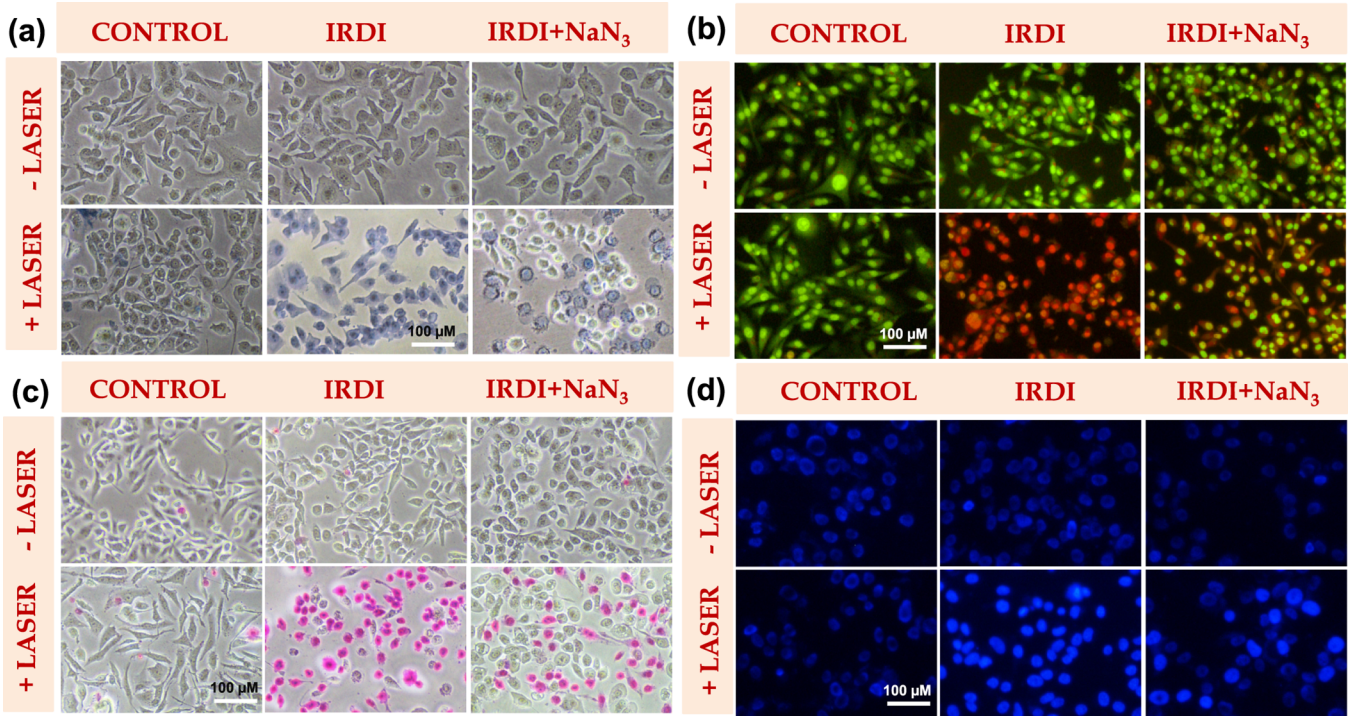

Figure 6. Apoptotic evaluation of the **IRDI**-treated cells followed by 405 nm laser excitation. (a) Trypan blue staining assay where apoptotic cells exhibit blue color. (b) Acridine orange-ethidium bromide dual staining assay where apoptotic cells stains in orange color. (c) APO percentage assay showing the dead cells in pink stain. (d) Hoechst staining assay demonstrating the nuclear damage induced by **IRDI** with enhanced blue emission.

these findings and considering the dark toxicity results, a 10 μM concentration of **IRDI** was selected as an ideal concentration for *in vitro* studies.

Mitochondria-targeted photodynamic therapy (PDT) is a cutting-edge approach that holds immense promise in the treatment of various diseases, particularly cancer.[23,61−64] This innovative technique involves using photosensitizing agents specifically designed to accumulate within mitochondria, the energy powerhouses of cells. The advantage of this targeting lies in its ability to selectively destroy mitochondria within diseased cells while leaving healthy ones unaffected, resulting in a more precise and less harmful treatment. By disrupting the crucial functions of the mitochondria, such as energy production and cellular signaling, this therapy can effectively impose cell death in the targeted diseased tissues. **IRDI** exhibits a unique dicationic structure that enables its specific accumulation in mitochondria. This phenomenon is attributed to the negative membrane potential found in these organelles, which actively attracts cationic species. Consequently, cationic iridium complexes are more prone to being internalized by the mitochondria.[63,65] To confirm the mitochondrial targeting properties of **IRDI** in MDA-MB-231 cells, coincubation experiments were performed with a mitochondria-specific dye, MitoTracker Red (Figure 4a). Fluorescence images displayed a high congruency with a Pearson's correlation coefficient (PCC) of 0.90, strongly indicating the localization of **IRDI** in the mitochondria.

To further verify the non-nuclear localization of the complex, colocalization studies were conducted with the nuclear-targeted dye Hoechst. Hoechst's blue fluorescence was clearly visible in the nuclear region, whereas the green fluorescence of **IRDI** was exclusively observed in the cytoplasm. This non-nuclear localization was confirmed with a Pearson's correlation coefficient (PCC) of 0.33 upon colocalization with Hoechst (Figure S8).The subcellular localization of **IRDI** was confirmed again with the inductively coupled plasma mass spectrometry (ICP-MS) technique. The extraction of subcellular fractions (i.e., mitochondrial, cytosolic, nuclear) after incubation with **IRDI** demonstrated 72% of the iridium content in the mitochondrial fraction, confirming mitochondria as the primary target (Figure 4b).

https://doi.org/10.1021/acsabm.3c00883
ACS Appl. Bio Mater. 2023, 6, 5776−5788

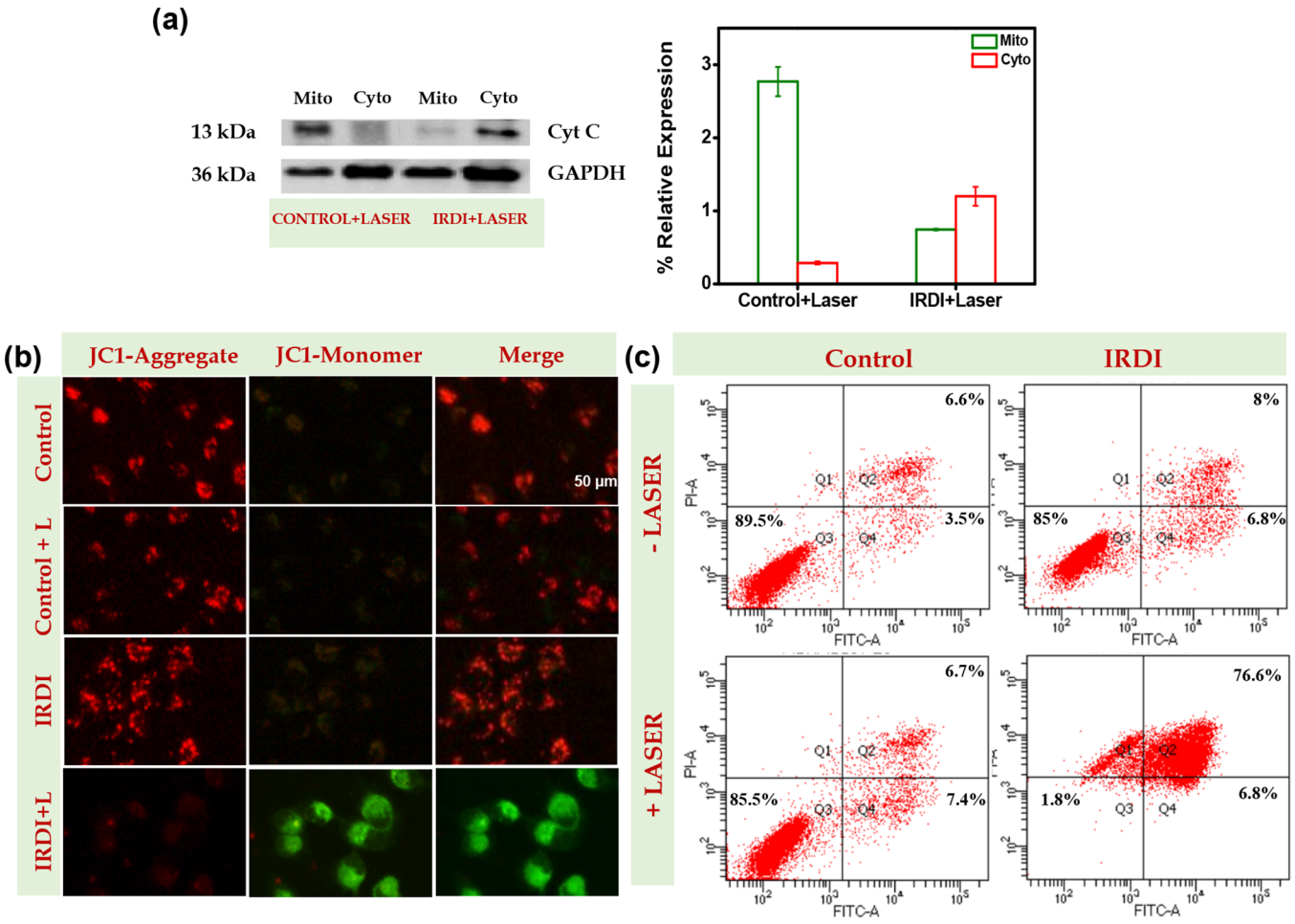

Figure 7. (a) Cytochrome *c* release from mitochondrial membrane to cytosol with **IRDI** + laser treatment confirmed with Western blot analysis. (b) Evaluation of the mitochondrial membrane potential using the JC-1 assay. The elevation of green color in the green panel indicates the reduction in membrane potential. (c) The extent of apoptosis was calculated via the annexin V-FITC method using flow cytometry.

3.3.2. Photoactivation and PDT Studies of IRDI in MDA-MB 231 Cells. The generation of singlet oxygen during the photoexcitation of the iridium dimeric complex (**IRDI**) in MDA-MB 231 cells was verified using a singlet oxygen red probe known as Si-DMA. The experimental procedure entailed the coadministration of **IRDI** and Si-DMA to the cells followed by exposure to light irradiation. The detection of a specific red fluorescence signal only in the presence of **IRDI** upon photoexcitation with a 405 nm laser demonstrated the photochemical capability of **IRDI** to produce singlet oxygen (Figure 5a).

To further substantiate these findings and establish **IRDI** as a promising type II photodynamic therapy (PDT) agent, we conducted an in-depth investigation of the photodynamic effect of laser irradiation on **IRDI**-treated cells in the presence of a singlet oxygen scavenger, sodium azide (NaN_3), using the MTT assay (Figure 5b). Under the influence of the 405 nm laser, cells treated with **IRDI** (10 μM) exhibited a remarkable decrease in viability up to 35% attributed to the robust generation of singlet oxygen during **IRDI** photoactivation. Notably, when **IRDI** was coincubated with 50 μM of NaN_3, a substantial recovery in cell viability was observed, amounting to an impressive 50% increase. This observation firmly established the potent singlet-oxygen-scavenging properties of NaN_3, leading to a marked enhancement in cell survival. These results provide strong evidence of **IRDI**'s exceptional capability to induce singlet oxygen production *in vitro*, substantiating its potential as a highly effective type II PDT agent.

3.3.3. Cell Death Mechanism of IRDI in MDA-MB 231 Cells. To investigate the mechanism of cell death and the potency of **IRDI** as a PDT agent, standard apoptosis assays were performed using MDA-MB-231 cancer cells. The live−dead assays were conducted in the presence of the singlet oxygen scavenger NaN_3 to ascertain the role of singlet oxygen and validate the type II pathway. Membrane changes associated with apoptosis were monitored through trypan blue dye exclusion assay, AO-EB dual fluorescent labeling assay, and APOP staining. Trypan blue can differently stain the dead cells only as the healthy cells with intact cell membrane are not permeable to trypan blue and will remain unstained. Figure 6a shows the results of the trypan blue assay where only a few stained cells with compromised membrane permeability were observed in the control group with **IRDI** treatment. In contrast, the cells in the laser-irradiated group with **IRDI** treatment displayed clear apoptotic features and significant trypan blue intake, indicating the efficacy of **IRDI** as a PDT agent.

Furthermore, the acridine orange/ethidium bromide (AO/EB) dual staining assay was utilized to evaluate distinct apoptosis features. AO, a green fluorescent dye, penetrated all viable cells, whereas the orange-red fluorescence of EB indicated a compromised cytoplasmic membrane integrity (Figure 6b). Cells treated with **IRDI** without laser irradiation exhibited green

https://doi.org/10.1021/acsabm.3c00883
ACS Appl. Bio Mater. 2023, 6, 5776−5788

fluorescence, whereas cells treated with **IRDI** after laser irradiation displayed red fluorescence, confirming the presence of apoptotic characteristics. To visualize apoptosis in a nonfluorescent platform, the APO percentage assay was employed. This assay demonstrated that **IRDI** and laser treatment induced the uptake of the dye, leading to the appearance of pink-stained dead cells, consistent with the expected apoptotic behavior (Figure 6c). This observation provides additional evidence of apoptosis occurrence in the experimental context. Additionally, a nuclear staining experiment was also conducted using Hoechst dye to study the nuclear condensation, yet another hallmark of apoptosis. The results revealed a striking enhancement of blue fluorescence in laser-treated **IRDI**-incubated cells, indicative of a robust interaction between Hoechst and condensed chromatin, providing strong evidence of DNA damage and apoptosis (Figure 6d). These findings were consistent with all of the live−dead staining assays performed, reinforcing the credibility of the observations. To further confirm the role of singlet oxygen in the apoptotic process triggered by **IRDI**, cells were pretreated with NaN_3, leading to a notable reduction in apoptotic features across all assays. This compelling evidence solidifies the classification of **IRDI** as a type II PDT agent, highlighting its ability to induce apoptosis through the generation of singlet oxygen.

Mitochondria play a critical role in cellular energy production, facilitated by the establishment of a substantial proton gradient across their lipid bilayer, creating a significant membrane potential of approximately 180 mV.[61] However, in the context of photodynamic therapy (PDT), the disruption of mitochondrial membrane potential becomes a pivotal event leading to apoptosis. The administration of **IRDI** and subsequent light exposure generate singlet oxygen, a highly reactive species that directly targets the mitochondrial membrane. This singlet oxygen interacts with crucial components of the mitochondrial inner membrane such as cardiolipin, resulting in their peroxidation and subsequent degradation. Consequently, the mitochondrial membrane potential is lost, causing depolarization. Furthermore, the singlet oxygen produced during **IRDI** photoactivation triggers lipid peroxidation, interfering with the proper functioning of electron transport chain complexes. This disruption leads to the leakage of electrons and additional ROS production, establishing a self-perpetuating cycle of ROS generation that further damages the mitochondrial membrane and exacerbates depolarization.[66,67] Cytochrome *c* (cyt *c*) is an intermitochondrial membrane residing protein that plays a crucial role in apoptosis induction.[47] Several proapoptotic stimuli like ROS can cause the release of cyt *c* from the mitochondria to the cytoplasm, leading to the initiation of apoptotic complex formation. Here, we also have analyzed the cyt *c* release into the cytoplasm by checking the levels in mitochondrial and cytosolic fractions. As depicted in Figure 7a, in the **IRDI**-treated laser-irradiated cells, cyt *c* is mostly found in the cytosolic fraction, and the relative expression of cyt *c* normalized with GAPDH is graphically represented. Meanwhile, the laser-exposed untreated cells show mainly mitochondrial homing of cyt *c*, confirming the mitochondria mediated cell death of **IRDI**-PDT. To further validate the claim, we conducted the widely used JC-1 assay for the direct monitoring of mitochondrial membrane potential. As a consequence of this mitochondrial membrane depolarization, the JC-1 dye, serving as an indicator of membrane potential, fails to accumulate in the mitochondria at the required concentration to form red-emissive J-aggregates in the laser treatment groups. Instead, the JC-1 dye predominantly exists in the green-emissive monomeric state, providing a clear indication of the loss of the mitochondrial membrane potential in **IRDI**-treated cells subjected to laser irradiation (Figure 7b).

Further, we aimed to understand the underlying mechanism of photodynamic therapy (PDT) using the **IRDI** compound, focusing on its impact on cell death in MDA-MB-231 cells. To evaluate this, we employed the annexin V-FITC/PI flow cytometric assay after subjecting the cells to a 24 h PDT treatment with **IRDI** along with laser irradiation. The results depicted in Figure 7c revealed a remarkable increase in late apoptosis, accounting for approximately 76% of the treated cell population, when **IRDI** was combined with laser activation. In contrast, using **IRDI** alone without laser exposure resulted in only 8% late apoptosis. Importantly, our study incorporated relevant controls, demonstrating that the activation of **IRDI** by the laser is critical in inducing significant cell death, as cells treated with **IRDI** without laser exhibited negligible late apoptosis. Furthermore, the control groups (with and without a laser) showed minimal apoptosis, reinforcing that the observed effects are specifically attributed to PDT treatment with **IRDI**. Overall, our findings offer evidence that **IRDI** predominantly induces apoptosis as the major form of cell death in MDA-MB-231 cells. This discovery holds promising potential for further exploration and potential therapeutic applications of **IRDI**-based PDT in cancer treatment.

4. CONCLUSIONS

In conclusion, we report the comparative investigation of the photophysical and biological properties of mononuclear and dinuclear Ir(III) complexes **IRMO** and **IRDI**. **IRDI** exhibited a higher singlet oxygen quantum yield of 0.49 compared to that of **IRMO** (0.28), demonstrating the potential of **IRDI** as a better PDT agent. The *in vitro* assessment of **IRDI** was carried out using the triple-negative breast cancer cell line MDA-MB-231. The mitochondrial localization of **IRDI** was confirmed using confocal fluorescence imaging with a mitochondria-specific dye, MitoTracker Red. An efficient laser-triggered apoptotic feature of **IRDI** on the MDA-MB-231 cancer cell line was demonstrated via live−dead assays such as trypan, acridine ethidium bromide, APOP, and Hoechst. **IRDI**-mediated PDT was found to trigger cytochrome *c* release from mitochondria, leading to apoptosome formation. Finally, the mitochondrial membrane potential was examined using the JC-1 assay, and the extent of apoptotic cell death was evaluated by the annexin flow cytometric assay, which reinforced **IRDI** as a potential image-guided PDT agent.

■ ASSOCIATED CONTENT

Supporting Information

The Supporting Information is available free of charge at https://pubs.acs.org/doi/10.1021/acsabm.3c00883.

Synthesis and characterization data, experimental data and figures of singlet oxygen generation, cyclic voltammetry, MTT assays, and nuclear Hoechst staining assay with scatter plot (PDF)

■ AUTHOR INFORMATION

Corresponding Authors

Kaustabh Kumar Maiti − *Chemical Sciences & Technology Division (CSTD), CSIR-National Institute for Interdisciplinary Science & Technology (CSIR-NIIST), Thiruvananthapuram, Kerala 695019, India; Academy of*

https://doi.org/10.1021/acsabm.3c00883
ACS Appl. Bio Mater. 2023, 6, 5776−5788

Scientific and Innovative Research (AcSIR), Ghaziabad 201002, India; orcid.org/0000-0003-3368-6929; Email: kkmaiti@niist.res.in

Joshy Joseph − *Chemical Sciences & Technology Division (CSTD), CSIR-National Institute for Interdisciplinary Science & Technology (CSIR-NIIST), Thiruvananthapuram, Kerala 695019, India; Academy of Scientific and Innovative Research (AcSIR), Ghaziabad 201002, India;* orcid.org/0000-0002-4592-8991; Email: joshy@niist.res.in

Authors

Nishna Neelambaran − *Chemical Sciences & Technology Division (CSTD), CSIR-National Institute for Interdisciplinary Science & Technology (CSIR-NIIST), Thiruvananthapuram, Kerala 695019, India; Academy of Scientific and Innovative Research (AcSIR), Ghaziabad 201002, India*

Shanmughan Shamjith − *Chemical Sciences & Technology Division (CSTD), CSIR-National Institute for Interdisciplinary Science & Technology (CSIR-NIIST), Thiruvananthapuram, Kerala 695019, India; Academy of Scientific and Innovative Research (AcSIR), Ghaziabad 201002, India;* orcid.org/0000-0003-1161-086X

Vishnu Priya Murali − *Chemical Sciences & Technology Division (CSTD), CSIR-National Institute for Interdisciplinary Science & Technology (CSIR-NIIST), Thiruvananthapuram, Kerala 695019, India; Academy of Scientific and Innovative Research (AcSIR), Ghaziabad 201002, India;* orcid.org/0000-0003-0759-991X

Complete contact information is available at: https://pubs.acs.org/10.1021/acsabm.3c00883

Notes

The authors declare no competing financial interest.

■ ACKNOWLEDGMENTS

We thank Rajashree R. Nair and Dr. S. Asha Nair for the annexin V-FITC study. We thank Roopasree O.J. for the confocal images. The financial support from the Council of Scientific and Industrial Research, DBT (GAP 1375), and DST Nanomission (GAP 162939) is gratefully acknowledged. N.N. gratefully acknowledges CSIR, Government of India, for the research fellowship and SERB Overseas Visiting Doctoral Fellowship 2018−19 supported by the Science and Engineering Research Board (SERB), Department of Science and Technology (DST) (SERB/F/6000/2019-20). S.J.S. acknowledges UGC for the research fellowship. V.P.M. acknowledges the ICMR-DHR young scientist program (R.12014/22/2021-HR/E-office: 8114716) for the funding provided. K.K.M. thanks the Council of Scientific and Industrial Research (CSIR), Govt. of India, and the Indian Council of Medical Research (ICMR), Govt. of India (5/4-5/3/01/DHR/NEURO/2020-NCD-I), for research funding.

■ REFERENCES

(1) Stritt, A.; Merk, H. F.; Braathen, L. R.; Von Felbert, V. Photodynamic Therapy in the Treatment of Actinic Keratosis. *Photochem. Photobiol.* **2008**, *84* (2), 388−398, DOI: 10.1111/j.1751-1097.2007.00276.x.

(2) Smits, T.; Moor, A. C. E. New aspects in photodynamic therapy of actinic keratoses. *Journal of Photochemistry and Photobiology B: Biology* **2009**, *96* (3), 159−169.

(3) Jiang, X.; Zhu, N.; Zhao, D.; Ma, Y. New cyclometalated transition-metal based photosensitizers for singlet oxygen generation and photodynamic therapy. *Science China Chemistry* **2016**, *59* (1), 40−52.

(4) Li, W.; Yang, J.; Luo, L.; Jiang, M.; Qin, B.; Yin, H.; Zhu, C.; Yuan, X.; Zhang, J.; Luo, Z.; Du, Y.; Li, Q.; Lou, Y.; Qiu, Y.; You, J. Targeting photodynamic and photothermal therapy to the endoplasmic reticulum enhances immunogenic cancer cell death. *Nat. Commun.* **2019**, *10* (1), 3349.

(5) Stritt, A.; Merk, H. F.; Braathen, L. R.; von Felbert, V. Photodynamic therapy in the treatment of actinic keratosis. *Photochemistry and photobiology* **2008**, *84* (2), 388−398.

(6) Bevernaegie, R.; Doix, B.; Bastien, E.; Diman, A.; Decottignies, A.; Feron, O.; Elias, B. Exploring the Phototoxicity of Hypoxic Active Iridium(III)-Based Sensitizers in 3D Tumor Spheroids. *J. Am. Chem. Soc.* **2019**, *141* (46), 18486−18491.

(7) Yaraki, M. T.; Liu, B.; Tan, Y. N. Emerging Strategies in Enhancing Singlet Oxygen Generation of Nano-Photosensitizers Toward Advanced Phototherapy. *Nano-Micro Lett.* **2022**, *14* (1), 123.

(8) Yu, H.; Chen, B.; Huang, H.; He, Z.; Sun, J.; Wang, G.; Gu, X.; Tang, B. Z. AIE-Active Photosensitizers: Manipulation of Reactive Oxygen Species Generation and Applications in Photodynamic Therapy. *Bionsensors* **2022**, *12* (5), 348 DOI: 10.3390/bios12050348.

(9) Sarbadhikary, P.; George, B. P.; Abrahamse, H. Recent Advances in Photosensitizers as Multifunctional Theranostic Agents for Imaging-Guided Photodynamic Therapy of Cancer. *Theranostics* **2021**, *11* (18), 9054−9088.

(10) McKenzie, L. K.; Bryant, H. E.; Weinstein, J. A. Transition metal complexes as photosensitisers in one- and two-photon photodynamic therapy. *Coord. Chem. Rev.* **2019**, *379*, 2−29.

(11) Pham, T. C.; Nguyen, V.-N.; Choi, Y.; Lee, S.; Yoon, J. Recent Strategies to Develop Innovative Photosensitizers for Enhanced Photodynamic Therapy. *Chem. Rev.* **2021**, *121* (21), 13454−13619.

(12) Shamjith, S.; Joseph, M. M.; Murali, V. P.; Remya, G. S.; Nair, J. B.; Suresh, C. H.; Maiti, K. K. NADH-depletion triggered energy shutting with cyclometalated iridium (III) complex enabled bimodal Luminescence-SERS sensing and photodynamic therapy. *Biosens. Bioelectron.* **2022**, *204*, No. 114087.

(13) Zheng, X.; Tang, H.; Xie, C.; Zhang, J.; Wu, W.; Jiang, X. Tracking Cancer Metastasis In Vivo by Using an Iridium-Based Hypoxia-Activated Optical Oxygen Nanosensor. *Angew. Chem. Int. Ed.* **2015**, *54* (28), 8094−8099, DOI: 10.1002/ange.201503067.

(14) Li, J.; Chen, T. Transition metal complexes as photosensitizers for integrated cancer theranostic applications. *Coord. Chem. Rev.* **2020**, *418*, No. 213355.

(15) Huang, T.; Yu, Q.; Liu, S.; Huang, W.; Zhao, Q. Phosphorescent iridium(iii) complexes: a versatile tool for biosensing and photodynamic therapy. *Dalton Transactions* **2018**, *47* (23), 7628−7633.

(16) Lee, L. C.-C.; Lo, K. K.-W. Luminescent and Photofunctional Transition Metal Complexes: From Molecular Design to Diagnostic and Therapeutic Applications. *J. Am. Chem. Soc.* **2022**, *144* (32), 14420−14440.

(17) Kelland, L. The resurgence of platinum-based cancer chemotherapy. *Nature Reviews Cancer* **2007**, *7* (8), 573−584.

(18) Su, S.; Chen, Y.; Zhang, P.; Ma, R.; Zhang, W.; Liu, J.; Li, T.; Niu, H.; Cao, Y.; Hu, B.; Gao, J.; Sun, H.; Fang, D.; Wang, J.; Wang, P. G.; Xie, S.; Wang, C.; Ma, J. The role of Platinum(IV)-based antitumor drugs and the anticancer immune response in medicinal inorganic chemistry. A systematic review from 2017 to 2022. *Eur. J. Med. Chem.* **2022**, *243*, No. 114680.

(19) Wang, F.-X.; Chen, M.-H.; Lin, Y.-N.; Zhang, H.; Tan, C.-P.; Ji, L.-N.; Mao, Z.-W. Dual Functions of Cyclometalated Iridium(III) Complexes: Anti-Metastasis and Lysosome-Damaged Photodynamic Therapy. *ACS Appl. Mater. Interfaces* **2017**, *9* (49), 42471−42481.

(20) Guan, R.; Xie, L.; Ji, L.; Chao, H. Phosphorescent Iridium(III) Complexes for Anticancer Applications. *Eur. J. Inorg. Chem.* **2020**, *2020* (42), 3978−3986, DOI: 10.1002/ejic.202000754.

(21) Lo, K. K.-W.; Zhang, K. Y. Iridium(iii) complexes as therapeutic and bioimaging reagents for cellular applications. *RSC Adv.* **2012**, *2* (32), 12069−12083.
(22) Huang, C.; Liang, C.; Sadhukhan, T.; Banerjee, S.; Fan, Z.; Li, T.; Zhu, Z.; Zhang, P.; Raghavachari, K.; Huang, H. In-vitro and In-vivo Photocatalytic Cancer Therapy with Biocompatible Iridium(III) Photocatalysts. *Angew. Chem. Int. Ed.* **2021**, *60* (17), 9474−9479, DOI: 10.1002/ange.202015671.
(23) Lv, W.; Zhang, Z.; Zhang, K. Y.; Yang, H.; Liu, S.; Xu, A.; Guo, S.; Zhao, Q.; Huang, W. A Mitochondria-Targeted Photosensitizer Showing Improved Photodynamic Therapy Effects Under Hypoxia. *Angew. Chem. Int. Ed.* **2016**, *55* (34), 9947−9951, DOI: 10.1002/anie.201604130.
(24) Zamora, A.; Vigueras, G.; Rodríguez, V.; Santana, M. D.; Ruiz, J. Cyclometalated iridium(III) luminescent complexes in therapy and phototherapy. *Coord. Chem. Rev.* **2018**, *360*, 34−76.
(25) Nam, J. S.; Kang, M.-G.; Kang, J.; Park, S.-Y.; Lee, S. J. C.; Kim, H.-T.; Seo, J. K.; Kwon, O.-H.; Lim, M. H.; Rhee, H.-W.; Kwon, T.-H. Endoplasmic Reticulum-Localized Iridium(III) Complexes as Efficient Photodynamic Therapy Agents via Protein Modifications. *J. Am. Chem. Soc.* **2016**, *138* (34), 10968−10977.
(26) Huang, H.; Banerjee, S.; Sadler, P. J. Recent Advances in the Design of Targeted Iridium(III) Photosensitizers for Photodynamic Therapy. *ChemBioChem* **2018**, *19* (15), 1574−1589, DOI: 10.1002/cbic.201800182.
(27) Manav, N.; Kesavan, P. E.; Ishida, M.; Mori, S.; Yasutake, Y.; Fukatsu, S.; Furuta, H.; Gupta, I. Phosphorescent rhenium-dipyrrinates: efficient photosensitizers for singlet oxygen generation. *Dalton Transactions* **2019**, *48* (7), 2467−2478.
(28) Prieto-Castañeda, A.; Lérida-Viso, A.; Avellanal-Zaballa, E.; Sola-Llano, R.; Bañuelos, J.; Agarrabeitia, A. R.; Martínez-Máñez, R.; Ortiz, M. J. Phosphorogenic dipyrrinato-iridium(III) complexes as photosensitizers for photodynamic therapy. *Dyes Pigm.* **2022**, *197*, No. 109886.
(29) Gao, R.; Ho, D. G.; Hernandez, B.; Selke, M.; Murphy, D.; Djurovich, P. I.; Thompson, M. E. Bis-cyclometalated Ir(III) Complexes as Efficient Singlet Oxygen Sensitizers. *J. Am. Chem. Soc.* **2002**, *124* (50), 14828−14829.
(30) Kuang, S.; Wei, F.; Karges, J.; Ke, L.; Xiong, K.; Liao, X.; Gasser, G.; Ji, L.; Chao, H. Photodecaging of a Mitochondria-Localized Iridium(III) Endoperoxide Complex for Two-Photon Photoactivated Therapy under Hypoxia. *J. Am. Chem. Soc.* **2022**, *144* (9), 4091−4101.
(31) Kuang, S.; Sun, L.; Zhang, X.; Liao, X.; Rees, T. W.; Zeng, L.; Chen, Y.; Zhang, X.; Ji, L.; Chao, H. A Mitochondrion-Localized Two-Photon Photosensitizer Generating Carbon Radicals Against Hypoxic Tumors. *Angew. Chem. Int. Ed.* **2020**, *59* (46), 20697−20703, DOI: 10.1002/anie.202009888.
(32) Wang, L.; Karges, J.; Wei, F.; Xie, L.; Chen, Z.; Gasser, G.; Ji, L.; Chao, H. A mitochondria-localized iridium(iii) photosensitizer for two-photon photodynamic immunotherapy against melanoma. *Chemical Science* **2023**, *14* (6), 1461−1471.
(33) Wang, D.; Huang, H.; Zhou, M.; Lu, H.; Chen, J.; Chang, Y.-T.; Gao, J.; Chai, Z.; Hu, Y. A thermoresponsive nanocarrier for mitochondria-targeted drug delivery. *Chem. Commun.* **2019**, *55* (28), 4051−4054.
(34) Yuan, L.; Wang, L.; Agrawalla, B. K.; Park, S.-J.; Zhu, H.; Sivaraman, B.; Peng, J.; Xu, Q.-H.; Chang, Y.-T. Development of Targetable Two-Photon Fluorescent Probes to Image Hypochlorous Acid in Mitochondria and Lysosome in Live Cell and Inflamed Mouse Model. *J. Am. Chem. Soc.* **2015**, *137* (18), 5930−5938.
(35) Tian, X.; Zhu, Y.; Zhang, M.; Luo, L.; Wu, J.; Zhou, H.; Guan, L.; Battaglia, G.; Tian, Y. Localization matters: a nuclear targeting two-photon absorption iridium complex in photodynamic therapy. *Chem. Commun.* **2017**, *53* (23), 3303−3306.
(36) Bolze, F.; Jenni, S.; Sour, A.; Heitz, V. Molecular photosensitisers for two-photon photodynamic therapy. *Chem. Commun.* **2017**, *53* (96), 12857−12877.
(37) Bi, X.-D.; Yang, R.; Zhou, Y.-C.; Chen, D.; Li, G.-K.; Guo, Y.-X.; Wang, M.-F.; Liu, D.; Gao, F. Cyclometalated Iridium(III) Complexes as High-Sensitivity Two-Photon Excited Mitochondria Dyes and Near-Infrared Photodynamic Therapy Agents. *Inorg. Chem.* **2020**, *59* (20), 14920−14931.
(38) Wang, L.; Yin, H.; Cui, P.; Hetu, M.; Wang, C.; Monro, S.; Schaller, R. D.; Cameron, C. G.; Liu, B.; Kilina, S.; McFarland, S. A.; Sun, W. Near-infrared-emitting heteroleptic cationic iridium complexes derived from 2,3-diphenylbenzo[g]quinoxaline as in vitro theranostic photodynamic therapy agents. *Dalton Transactions* **2017**, *46* (25), 8091−8103.
(39) Yang, X.; Xu, X.; Dang, J.-s.; Zhou, G.; Ho, C.-L.; Wong, W.-Y. From Mononuclear to Dinuclear Iridium(III) Complex: Effective Tuning of the Optoelectronic Characteristics for Organic Light-Emitting Diodes. *Inorg. Chem.* **2016**, *55* (4), 1720−1727.
(40) Zheng, Y.; Batsanov, A. S.; Fox, M. A.; Al-Attar, H. A.; Abdullah, K.; Jankus, V.; Bryce, M. R.; Monkman, A. P. Bimetallic Cyclometalated Iridium(III) Diastereomers with Non-Innocent Bridging Ligands for High-Efficiency Phosphorescent OLEDs. *Angew. Chem. Int. Ed.* **2014**, *53* (43), 11616−11619, DOI: 10.1002/anie.201407475.
(41) Shafikov, M. Z.; Zaytsev, A. V.; Kozhevnikov, V. N. Halide-Enhanced Spin−Orbit Coupling and the Phosphorescence Rate in Ir(III) Complexes. *Inorg. Chem.* **2021**, *60* (2), 642−650.
(42) Gao, T.-B.; Zhang, J.-J.; Wen, J.; Yang, X.-X.; Ma, H.-b.; Cao, D.-K.; Jiang, D. Single-Molecule MicroRNA Electrochemiluminescence Detection Using Cyclometalated Dinuclear Ir(III) Complex with Synergistic Effect. *Anal. Chem.* **2020**, *92* (1), 1268−1275.
(43) Congrave, D. G.; Hsu, Y.-t.; Batsanov, A. S.; Beeby, A.; Bryce, M. R. Synthesis, Diastereomer Separation, and Optoelectronic and Structural Properties of Dinuclear Cyclometalated Iridium(III) Complexes with Bridging Diarylhydrazide Ligands. *Organometallics* **2017**, *36* (5), 981−993.
(44) Lu, C.; Xu, W.; Shah, H.; Liu, B.; Xu, W.; Sun, L.; Qian, S. Y.; Sun, W. In Vitro Photodynamic Therapy of Mononuclear and Dinuclear Iridium(III) Bis(terpyridine) Complexes. *ACS Appl. Bio Mater.* **2020**, *3* (10), 6865−6875.
(45) Brouwer, A. M. Standards for photoluminescence quantum yield measurements in solution (IUPAC Technical Report). *Pure Appl. Chem.* **2011**, *83* (12), 2213−2228, DOI: 10.1351/PAC-REP-10-09-31.
(46) Dimauro, I.; Pearson, T.; Caporossi, D.; Jackson, M. J. A simple protocol for the subcellular fractionation of skeletal muscle cells and tissue. *BMC Res. Notes* **2012**, *5* (1), 513.
(47) Garrido, C.; Galluzzi, L.; Brunet, M.; Puig, P. E.; Didelot, C.; Kroemer, G. Mechanisms of cytochrome c release from mitochondria. *Cell Death & Differentiation* **2006**, *13* (9), 1423−1433.
(48) Nonoyama, M. Benzo[h]quinolin-10-yl-N Iridium(III) Complexes. *Bull. Chem. Soc. Jpn.* **1974**, *47* (3), 767−768, DOI: 10.1246/bcsj.47.767.
(49) Chen, Y.; Liu, C.; Wang, L. Effects of fluorine substituent on properties of cyclometalated iridium(III) complexes with a 2,2′-bipyridine ancillary ligand. *Tetrahedron* **2019**, *75* (47), No. 130686.
(50) Zhao, Q.; Yu, M.; Shi, L.; Liu, S.; Li, C.; Shi, M.; Zhou, Z.; Huang, C.; Li, F. Cationic Iridium(III) Complexes with Tunable Emission Color as Phosphorescent Dyes for Live Cell Imaging. *Organometallics* **2010**, *29* (5), 1085−1091.
(51) Brouwer, A. Standards for photoluminescence quantum yield measurements in solution (IUPAC Technical Report)*. *Pure Appl. Chem.* **2011**, *83*, 2213−2228.
(52) Liu, B.; Monro, S.; Lystrom, L.; Cameron, C. G.; Colón, K.; Yin, H.; Kilina, S.; McFarland, S. A.; Sun, W. Photophysical and Photobiological Properties of Dinuclear Iridium(III) Bis-tridentate Complexes. *Inorg. Chem.* **2018**, *57* (16), 9859−9872.
(53) Soliman, A. M.; Fortin, D.; Harvey, P. D.; Zysman-Colman, E. Intimate electronic coupling in cationic homodimeric iridium(iii) complexes. *Dalton Transactions* **2012**, *41* (31), 9382−9393.
(54) Li, G.; Zhu, D.; Wang, X.; Su, Z.; Bryce, M. R. Dinuclear metal complexes: multifunctional properties and applications. *Chem. Soc. Rev.* **2020**, *49* (3), 765−838.
(55) Davis, S.; Weiss, M. J.; Wong, J. R.; Lampidis, T. J.; Chen, L. B. Mitochondrial and plasma membrane potentials cause unusual accumulation and retention of rhodamine 123 by human breast

adenocarcinoma-derived MCF-7 cells. *J. Biol. Chem.* **1985**, *260* (25), 13844−13850.
(56) Chen, L. B. Mitochondrial Membrane Potential in Living Cells. *Annu. Rev. Cell Biol.* **1988**, *4* (1), 155−181, DOI: 10.1146/annurev.cb.04.110188.001103.
(57) Murphy, M. P. Selective targeting of bioactive compounds to mitochondria. *Trends Biotechnol.* **1997**, *15* (8), 326−330.
(58) Zhang, Q.; Cao, R.; Fei, H.; Zhou, M. Mitochondria-targeting phosphorescent iridium(iii) complexes for living cell imaging. *Dalton Transactions* **2014**, *43* (44), 16872−16879.
(59) Detty, M. R.; Gibson, S. L.; Wagner, S. J. Current Clinical and Preclinical Photosensitizers for Use in Photodynamic Therapy. *J. Med. Chem.* **2004**, *47* (16), 3897−3915.
(60) Juarranz, Á.; Jaén, P.; Sanz-Rodríguez, F.; Cuevas, J.; González, S. Photodynamic therapy of cancer. Basic principles and applications. *Clinical and Translational Oncology* **2008**, *10* (3), 148−154.
(61) Arya, J. S.; Joseph, M. M.; Sherin, D. R.; Nair, J. B.; Manojkumar, T. K.; Maiti, K. K. Exploring Mitochondria-Mediated Intrinsic Apoptosis by New Phytochemical Entities: An Explicit Observation of Cytochrome c Dynamics on Lung and Melanoma Cancer Cells. *J. Med. Chem.* **2019**, *62* (17), 8311−8329.
(62) Nair, J. B.; Joseph, M. M.; Arya, J. S.; Sreedevi, P.; Sujai, P. T.; Maiti, K. K. Elucidating a Thermoresponsive Multimodal Photo-Chemotherapeutic Nanodelivery Vehicle to Overcome the Barriers of Doxorubicin Therapy. *ACS Appl. Mater. Interfaces* **2020**, *12* (39), 43365−43379.
(63) Pathania, D.; Millard, M.; Neamati, N. Opportunities in discovery and delivery of anticancer drugs targeting mitochondria and cancer cell metabolism. *Adv. Drug Delivery Rev.* **2009**, *61* (14), 1250−1275.
(64) Singh, H.; Sareen, D.; George, J. M.; Bhardwaj, V.; Rha, S.; Lee, S. J.; Sharma, S.; Sharma, A.; Kim, J. S. Mitochondria targeted fluorogenic theranostic agents for cancer therapy. *Coord. Chem. Rev.* **2022**, *452*, No. 214283.
(65) Yoshihara, T.; Murayama, S.; Masuda, T.; Kikuchi, T.; Yoshida, K.; Hosaka, M.; Tobita, S. Mitochondria-targeted oxygen probes based on cationic iridium complexes with a 5-amino-1, 10-phenanthroline ligand. *J. Photochem. Photobiol., A* **2015**, *299*, 172−182.
(66) Lee, C.; Nam, J. S.; Lee, C. G.; Park, M.; Yoo, C.-M.; Rhee, H.-W.; Seo, J. K.; Kwon, T.-H. Analysing the mechanism of mitochondrial oxidation-induced cell death using a multifunctional iridium(III) photosensitiser. *Nat. Commun.* **2021**, *12* (1), 26.
(67) Zafon, E.; Echevarría, I.; Barrabés, S.; Manzano, B. R.; Jalón, F. A.; Rodríguez, A. M.; Massaguer, A.; Espino, G. Photodynamic therapy with mitochondria-targeted biscyclometallated Ir(iii) complexes. Multi-action mechanism and strong influence of the cyclometallating ligand. *Dalton Transactions* **2021**, *51* (1), 111−128.

https://doi.org/10.1021/acsabm.3c00883
ACS Appl. Bio Mater. 2023, 6, 5776−5788